

Selectivity in Hydrocarbon Conversions and  
Methanol Decomposition on a  
Pd/Fe<sub>3</sub>O<sub>4</sub> Model Catalyst.

A Molecular Beam Study.

DISSERTATION

zur Erlangung des akademischen Grades  
doctor rerum naturalium  
(Dr. rer. nat.)  
im Fach Chemie

eingereicht an der  
Mathematisch-Naturwissenschaftlichen Fakultät I  
Humboldt-Universität zu Berlin

von

Dipl.-Chem. Björn Brandt  
geboren am 23. Mai 1978 in Schleswig (Schleswig-Holstein)

Präsident der Humboldt-Universität zu Berlin:  
Prof. Dr. Dr. h.c. Christoph Marksches

Dekan der Mathematisch-Naturwissenschaftlichen Fakultät I:  
Prof. Dr. Lutz-Helmut Schön

Gutachter:

1. Prof. Dr. Hans-Joachim Freund
2. Prof. Dr. Klaus Rademann

Tag der mündlichen Prüfung: 11.12.2008



## Abstract

One of the most important objectives in chemistry is to understand and control the selectivity towards a desired reaction pathway. In catalysis, selectivity is thought to be governed by the catalyst's structure; many practical catalysts, however, have an inherently complex structure that obstructs their detailed understanding; therefore, simplified materials are studied instead. In order to advance the understanding of catalysis, we have applied a combination of *surface science* experimental techniques, centered around molecular beam methods to study surface reactions under vacuum on a well-characterized Pd/Fe<sub>3</sub>O<sub>4</sub> model catalyst; the reactions were followed by mass-spectrometric rate measurement and infrared-spectroscopic detection of adsorbates.

Our experiments focussed on the origins of selectivity in two reactions, the decomposition of methanol and the conversion of 2-butene with coadsorbed deuterium; additionally, both reactants may decompose on the Pd metal to carbonaceous species or carbon.

**Methanol decomposition** is a well-established model reaction in surface science and of high interest for application *per se*. We show in this work that methanol is dehydrogenated to formaldehyde and water by reaction with surface oxygen on pristine Fe<sub>3</sub>O<sub>4</sub> with high selectivity; the surface oxygen consumed by this reaction has to be replenished in order to sustain the reactivity. In the presence of Pd nanoparticles, support-related methanol and methoxy migrate quickly to the metal particles before formaldehyde could be formed on the oxide; on the Pd metal surface methanol decomposes in two pathways, forming carbon monoxide and hydrogen in the main pathway, and carbon in the minor pathway, which accumulates slowly on the Pd surface and poisons its catalytic activity.

**2-butene conversion** was studied as a model for hydrocarbon conversion reactions, focussing on mechanisms that induce selectivity between the three reaction pathways (hydrogenation, H/D-exchange/isomerization and decomposition). This work demonstrates that sustained reactivity can be obtained on the Pd/Fe<sub>3</sub>O<sub>4</sub> model catalyst at elevated temperatures (around 250 K); isomerization proceeds with sustained rates already on a clean catalyst, but sustained hydrogenation can only be induced in the presence of previously deposited, strongly dehydrogenated carbonaceous deposits (*carbon*); this induction of hydrogenation was explained by the ability of carbon to facilitate the formation of subsurface hydrogen under reaction conditions, which is necessary for hydrogenation. Additionally, we have compared the conversion rates with *cis*- and *trans*-2-butene; selectivity occurs under conditions where the reaction rates seem to be limited by the availability of butene; *cis*-2-butene gives higher yields in those cases, presumably because it reaches higher alkene surface coverages in adsorption-desorption equilibrium.



## Zusammenfassung

Eines der Hauptziele der Chemie ist das Verständnis und die Kontrolle über die Selektivität in bezug auf einen Reaktionspfad. In der Katalyse wird Selektivität oft in engem Zusammenhang mit der Katalysatorstruktur gesehen; da aber reale Katalysatoren eine komplexe mikroskopische Struktur besitzen, die ein tiefgehendes Verständnis erschwert, untersucht man in Studien oft vereinfachte Materialien; für diese Arbeit verwenden wir eine Kombination von Methoden der *Oberflächenforschung*, vor allem Molekularstrahlmethoden, zur Untersuchung von Oberflächenreaktionen auf einem gut charakterisierten Pd/Fe<sub>3</sub>O<sub>4</sub>-*Modellkatalysator* im Vakuum; die Reaktionen wurden durch massenspektrometrische Ratenmessungen und IR-spektroskopische Detektion von Adsorbaten verfolgt.

In dieser Arbeit untersuchen wir die Selektivität in zwei Reaktionen, Zersetzung von Methanol und Konvertierung von 2-Buten mit Deuterium; außerdem können beide Reaktanden auf metallischem Pd noch in stark kohlenstoffhaltige Verbindungen zerfallen.

**Methanol-Zersetzung** ist eine wichtige Modellreaktion in der Oberflächenforschung und schon an sich von großem praktischen Interesse. In dieser Arbeit zeigen wir, dass Methanol durch Reaktion mit Oberflächensauerstoff auf dem frisch präparierten Oxid Fe<sub>3</sub>O<sub>4</sub> sehr selektiv zu Formaldehyd und Wasser dehydrogeniert wird, wobei dieser Sauerstoff verbraucht wird und zur Aufrechterhaltung der Reaktivität nachgeführt werden müsste. In Anwesenheit von Pd Nanopartikeln diffundieren oxidgebundenes Methanol und Methoxy schnell zu den Metallpartikel, noch bevor sie auf dem Oxid zu Formaldehyd umgesetzt werden könnten. Auf Pd-Metallflächen werden sie stattdessen zu Kohlenstoffmonoxid und Wasserstoff zersetzt, und auch – in geringerem Umfang – zu Kohlenstoff, der langsam auf den Pd-Flächen aggregiert und deren katalytische Aktivität mindert.

**Konvertierung von 2-Buten** wurde als Modellreaktion für Kohlenwasserstoffkonvertierung untersucht; dabei interessierte uns vor allem die Selektivität zwischen den drei Reaktionspfaden (Hydrierung, H/D-Austausch/Isomerisierung und Zersetzung). Bei 250 K konnte anhaltende katalytische Reaktivität beobachtet werden; die Isomerisierung zeigt diese schon auf einem anfangs noch sauberen Katalysator, für die Hydrierung aber sind dafür zuvor abgelagerte, stark kohlenstoffhaltige Verbindungen nötig; solche Ablagerungen induzieren Hydrierung offenbar hauptsächlich dadurch, dass sie die Bildung von Wasserstoff unterhalb der Pd-Oberfläche (*subsurface*) erleichtern, welcher die Hydrierung offenbar erst ermöglicht. Außerdem haben wir die Raten mit *cis*- und *trans*-2-Buten verglichen und dabei eine Selektivität immer dann beobachtet, wenn die Reaktionsraten durch die Verfügbarkeit des Alkens limitiert waren; *cis*-2-Buten ergibt dann höhere Raten, vermutlich da es höhere Oberflächenbedeckungen im Gleichgewicht erreicht.

Diese Arbeit wurde im Zeitraum November 2004 bis Oktober 2008 am Fritz-Haber-Institut der Max-Planck-Gesellschaft, Berlin-Dahlem, Abteilung Chemische Physik, unter der Leitung von Prof. Dr. Hans-Joachim Freund angefertigt.



# Contents

<b>1</b>	<b>Introduction</b>	<b>1</b>
<b>2</b>	<b>Dynamic and Kinetic Processes on Surfaces and Surface Structure</b>	<b>7</b>
2.1	Gas Particles on Surfaces . . . . .	7
2.1.1	Gas-Surface Interactions . . . . .	7
2.1.2	Surface-Dynamics, Reactions and Adsorbate Interactions	12
2.2	Kinetic Effects on Complex Surfaces . . . . .	18
2.3	Particle-Related Effects . . . . .	21
<b>3</b>	<b>Experimental Setup and Techniques</b>	<b>23</b>
3.1	Preparation Chamber . . . . .	24
3.1.1	Sample, Sample Holder and Manipulator . . . . .	26
3.2	Scattering Chamber and Gas Inlet . . . . .	26
3.2.1	Gas Exposure by Molecular Beams . . . . .	29
3.3	Detection Techniques . . . . .	40
3.3.1	Gas Phase Detection (Mass Spectrometry) . . . . .	40
3.3.2	Detection of Surface Adsorbates (Infrared Spectroscopy)	46
3.4	Experiment Time Control . . . . .	55
<b>4</b>	<b>Pd/Fe<sub>3</sub>O<sub>4</sub>/Pt(111) as a Supported Model Catalyst</b>	<b>57</b>
4.1	Iron Oxide Fe <sub>3</sub> O <sub>4</sub> on Pt(111) . . . . .	58
4.2	Pd Nanoparticles supported on Fe <sub>3</sub> O <sub>4</sub> : Characterization and Treatments . . . . .	64
4.2.1	Sample Characterization by CO Adsorption . . . . .	65
4.2.2	The Pd/Fe <sub>3</sub> O <sub>4</sub> Model Catalyst: Stabilization . . . . .	67
4.2.3	Oxidation Behaviour of the Pd/Fe <sub>3</sub> O <sub>4</sub> Model Catalyst .	71
<b>5</b>	<b>Methanol Decomposition</b>	<b>73</b>
5.1	Introduction . . . . .	73

5.1.1	Methanol Decomposition- and Transformation Reactions on Surfaces under Vacuum . . . . .	75
5.2	Methanol Adsorption, Desorption and Reaction on Fe <sub>3</sub> O <sub>4</sub> . . .	86
5.2.1	Methanol Decomposition Investigated by Vibrational Spectroscopy . . . . .	86
5.2.2	Repeated Temperature-Programmed Reaction-Experiments . . . . .	96
5.2.3	Conclusions: Methanol Decomposition on Fe <sub>3</sub> O <sub>4</sub> . . . .	106
5.3	Methanol Adsorption, Desorption and Reaction on the Pd/Fe <sub>3</sub> O <sub>4</sub> Model Catalyst . . . . .	109
5.3.1	Methanol Decomposition Investigated by Vibrational Spectroscopy . . . . .	109
5.3.2	Repeated Temperature-Programmed Reaction-Experiments . . . . .	119
5.3.3	Kinetic Experiments . . . . .	123
5.4	Summary . . . . .	135
<b>6</b>	<b>Conversion of 2-Butene</b>	<b>141</b>
6.1	Introduction . . . . .	141
6.1.1	Conversion of 2-Butene on Pt-Group Metals (Group 10)	154
6.2	2-Butene on Fe <sub>3</sub> O <sub>4</sub> . . . . .	158
6.2.1	Surface Infrared Spectra of 2-Butene on Fe <sub>3</sub> O <sub>4</sub> . . . . .	158
6.2.2	Desorption of 2-Butene from Fe <sub>3</sub> O <sub>4</sub> . . . . .	160
6.2.3	Pulsed Molecular Beam Ad- and Desorption Experiments	164
6.3	2-Butene on the Pd/Fe <sub>3</sub> O <sub>4</sub> Model Catalyst . . . . .	167
6.3.1	Surface Infrared Spectra of 2-Butene on Pd/Fe <sub>3</sub> O <sub>4</sub> . . .	167
6.3.2	Desorption and Reaction of 2-Butene on Pd/Fe <sub>3</sub> O <sub>4</sub> . .	169
6.3.3	Chemoselectivity of 2-Butene-Conversion on Pd/Fe <sub>3</sub> O <sub>4</sub>	183
6.3.4	Selectivity in the Conversion of <i>cis</i> - and <i>trans</i> -2-Butene . . . . .	202
6.4	Summary . . . . .	218
<b>7</b>	<b>Summary</b>	<b>225</b>
7.1	Methanol Decomposition . . . . .	226
7.2	Conversion of 2-Butene with Deuterium . . . . .	229
7.3	Conclusions . . . . .	233
<b>A</b>	<b>Experimental Procedures</b>	<b>235</b>
A.1	Preparation of the Model Catalyst . . . . .	235
A.1.1	Preparation of the Pt(111) Single Crystal . . . . .	235
A.1.2	Cleaning of the Pt(111) Single Crystal . . . . .	236

A.1.3	Preparation of the Iron Oxides FeO and Fe <sub>3</sub> O <sub>4</sub> . . . . .	236
A.1.4	Preparation of Pd Nanoparticles . . . . .	237
A.1.5	Oxidation of the Model Catalyst for Experiments . . . . .	237
A.2	Chemicals: Handling and Beam Formation. . . . .	238
A.2.1	Purities and Suppliers of Chemicals . . . . .	238
A.2.2	Handling and Storage of Chemicals . . . . .	238
A.2.3	Beam Formation with Organic Reactants . . . . .	239
A.3	Data Correction . . . . .	240
<b>List of Abbreviations</b>		<b>245</b>
<b>Publications</b>		<b>251</b>
<b>Bibliography</b>		<b>255</b>
<b>List of Figures</b>		<b>277</b>
<b>List of Tables</b>		<b>281</b>





# Chapter 1

## Introduction

Heterogeneous catalysis is an established tool used in many important processes to control chemical reactions. Its main fields of application are in the *chemical industry* for conversion and synthesis of raw and basic materials, in *energy technology* for energy storage and conversion, and in *environmental technology* for pollutant detoxification [1, 2, 3]. Typical examples for catalyzed processes are the industrial production of ammonia from its elements, the cracking of *petroleum* into a defined composition of small hydrocarbons, the reduction of nitrogen oxides to molecular nitrogen in car exhaust catalysts, or the catalyzed oxidation of hydrogen to water in fuel cells.

In all its applications, catalysis is used to alter the *kinetics* of chemical reactions, *control reaction rates* and tune *selectivities* of chemical processes in order to increase the yield and purity of products; consequently, those aspects constitute the main challenge of catalyst development. A prerequisite for the achievement of these goals is to gain a detailed knowledge about the mechanism of the reactions that can occur, and for catalysis, this means to understand the correlation between structural parameters of the catalyst surface – regarding both its geometric and electronic structure – and the processes that occur on this template with the adsorbed reactants, products and side products. The structural parameters that are known to influence the mechanisms of catalyzed reactions include the chemical identities of the catalyst components<sup>1</sup>, the oxidation state of the components [4], the size, size distribution and morphology of the metal particles [5, 6, 7], the presence,

---

<sup>1</sup>Heterogeneous catalysts are typically composed of metal or metal oxide nanoparticles (the *active phase*) deposited on an oxide (the *support*) that helps to stabilize the high internal surface of the active metal phase under reaction conditions; sometimes, other substances are added to the catalyst which act as *structural* or *electronic* promoters. Some heterogeneous catalysts, however, also consist simply of metal sponges, *e.g.* platinum black.

characters and densities of defect sites, and the presence, identity and influence of promoter substances. Additionally, it is often not enough to understand the static catalyst structure alone, as the adsorbates may significantly alter the electronic structure of the catalyst; in some cases, this influence can be so high that it may even induce geometric surface restructurizations; these effects together give rise to a dynamic change on the catalyst which would need to be understood.

However, despite its enormous significance for economic wealth, such a *detailed*, maybe even *general* understanding of catalysis that would allow to design new catalysts based on theoretical insight, has not yet been reached; this is mainly due to the structural complexity of practical catalyst materials, the possible complexity of processes that can occur on their surfaces, and to the long-time unavailability of intrinsically surface-sensitive detection techniques. It is for this reason that researchers are still today in most cases bound to a primarily empirical approach (extensive catalyst *screening*) as the most promising way to find catalysts for new applications; those methods were introduced by Alwin Mittasch for the optimization of the Haber-Bosch process as early as 1909 [8, 9], and although they have proven efficient, they can only assay a limited amount of substances under a reduced set of conditions, and thus may only find a local optimum of a catalyst; consequently, this approach appears very unsatisfactory.

**The Surface Science Approach.** In order to enhance the understanding of catalysis, Langmuir suggested – based on his proof of a close connection between chemical adsorption (*chemisorption*) and catalysis [10, 11, 12, 13] – to simplify the study of catalysis and to start with experiments on the *well-defined surfaces of crystals* rather than the very complex materials applied in industrial processes [11]. Crystal structures had become experimentally accessible at that time by the introduction of crystallographic diffraction methods in 1912. Langmuir saw the necessity to gain control over the adsorbate population on the surfaces and to perform this research in high vacuum in order to reduce the collision frequency with background gases; he combined technologies available in his times and built the first *high-vacuum research* facility for the study of surfaces [14]. His approach is now termed the *surface science approach* [15]; its main elements are:

- Application of high-vacuum techniques to reduce and control surface adsorption.
- Surfaces of reduced and controllable complexity as model substances.

- Methods that allow to gain understanding at atomic resolution; use techniques which are intrinsically surface-sensitive.

A versatile set of surface-sensitive standard techniques is now available; an overview can be obtained from references [16, 17, 18].

In this work, we have studied surface reactions on a structurally well-defined model catalyst; in order to monitor the reactions, a set of surface-science techniques was applied, including vibrational spectroscopy of adsorbates (infrared reflection-absorption spectroscopy, IRAS) and gas-phase detection of desorbing and scattered products by mass-spectrometry during controlled gas exposures in ultra-high vacuum with molecular beams. The central aspect of the applied setup is the combination of molecular beams for gas (reactant) exposure and structurally well-defined model catalysts:

**Molecular Beam Experiments** are an established and versatile tool for studying kinetics and dynamics of reactions on surfaces and in the gas phase in ultra-high vacuum (UHV); their central advantage is that the species in the beam collide exactly one time with the surface, allowing to measure absolute reaction and sticking probabilities. Additionally, molecular beams allow for a precise time and intensity control of gas exposures, opening unparalleled opportunities for the study of elementary surface processes both under *transient* and *steady-state* conditions. Combined with the model catalyst approach, they possess a high potential to enhance the understanding of catalysis [19].

**The Model Catalyst Approach.** The most intensely studied samples in surface science are single-crystals; as a model for catalysts, however, those simple surfaces are not fully satisfactory, as many phenomena observed in real catalysis depend on structural properties which are not represented on such simple surfaces (some of those structural properties have been named above). As a strategy to overcome this complexity gap, *model supported catalyst systems* have been suggested and developed [20, 21], which mimick many aspects of the structural complexity of true catalysts, but can be prepared with good control over the structural parameters; additionally, they are accessible to most surface-sensitive standard techniques, including LEED, STM, or photoelectron methods [21]. These materials typically consist of thin, epitaxially grown oxide films of well-defined structures deposited on single-crystalline metal substrates; those oxide films then act as the deposition substrates for metal or metal oxide nanoparticles.

## Objective of this Work

In this work, we concentrated on investigating the origins of selectivity during surface reactions. Selectivity denotes the ability to guide the reactants through a network of possible reaction pathways, and selectively promote the formation of target products, while keeping the yield of undesired products as low as possible.

Two model reactions – decomposition of methanol and conversion of 2-butene with deuterium – have been chosen in this work as an object to study the origin of very different types of selectivities; both reactions can proceed *via* several different reaction pathways. **Methanol decomposition** is a relatively simple and well-established model reaction in surface science [22, 23] and of high interest for application *per se*, *e.g.* for industrial formaldehyde synthesis or for direct methanol fuel cells (DMFCs); it may proceed *via* C-H- and C-O-bond scission steps under formation of three distinct, important primary products – formaldehyde, carbon monoxide (CO) and surface carbonaceous species; in the present study, we concentrate on the decomposition reactions of methanol on both the pristine Fe<sub>3</sub>O<sub>4</sub> oxide support and the Pd nanoparticles, and the diffusion of species between those two components of the model catalyst. **2-butene conversion with deuterium** was studied as a prototype for catalytic hydrocarbon conversions, which is a central process in numerous industrial applications including petrochemical hydrotreating or fat hardening [24, 25]. Despite its economic significance and the extensive work that has already been done, however, key aspects of it remain nearly not understood – including the mechanisms that govern activity and chemoselectivity between the possible reactions pathways (which, in our case, are hydrogenation, H/D-exchange/isomerization and dehydrogenation/decomposition). It has been suggested that carbon – which is typically present during hydrocarbon conversion due to their rapid decomposition on many clean metal surfaces – may act as a critical modifier that may play a key role for the chemoselectivity in hydrocarbon conversion [26]. In this work, we will present detailed reactivity measurements on clean and carbon-precovered model catalysts for the study of the chemoselectivity between the reaction pathways; additionally, differences in the reaction rates with *cis*- and *trans*-2-butene as reactants have been studied.

**Outline of this Thesis:** But before the results part, an introductory part is provided. Chapter 2 will introduce general dynamic and kinetic processes that may take place on catalyst surfaces; the subsequent chapter 3 describes the setup of the applied molecular beam machine at the department of Chemical Physics of the Fritz-Haber-Institute, and the fundamental principles of the applied surface science molecular beam and detection techniques. Finally, chapter 4 describes the preparation and characterization of the Pd/Fe<sub>3</sub>O<sub>4</sub>/Pt(111) model catalyst used in this thesis, and the basic cleaning techniques applied to maintain an active surface.

Chapter 5 presents the systematic kinetic studies of methanol decomposition. At the beginning of this chapter, an overview over previous surface-science studies of methanol decomposition on reduced metals (of the groups VIII & IB) and metal oxides is provided, including an overview over the different reaction pathways. The subsequent results part separately presents our own experiments on both the pristine Fe<sub>3</sub>O<sub>4</sub> support and the model catalyst. Those experiments demonstrate that the main decomposition product of methanol on Fe<sub>3</sub>O<sub>4</sub> is formaldehyde, which is formed in an oxidative dehydrogenation under formation of water as a side product; since this reaction consumes surface oxygen from the oxide (*Mars-van-Krevelen* mechanism), the reaction can proceed with sustained reactivity only when surface oxygen is replenished. In the following, we provide evidence that support-related methanol and methoxy species quickly migrate to Pd metal nanoparticles in the model catalyst before they could be dehydrogenated to formaldehyde on the support; the main decomposition products on Pd are carbon monoxide and hydrogen; as a side reaction, C-O-bond scission leads to the formation of carbonaceous species, which accumulate slowly on the Pd surface and poison its catalytic activity.

Chapter 6 presents the systematic study of 2-butene conversion with deuterium. At the beginning of this chapter, the different reaction pathways and previously suggested mechanisms of hydrocarbon conversion are discussed; additionally, the literature of hydrocarbon conversion in surface science studies on Pt-group metals will be presented. The subsequent results part first demonstrates that the pristine iron oxide support is inactive towards 2-butene conversion or decomposition. However, we show that conversion reactions do indeed occur on the Pd nanoparticles in the model catalyst; at temperatures starting around 200 K, both hydrogenation and isomerization proceed on the initially clean surface, but with quickly vanishing activity due to the inhibition of dissociative deuterium adsorption by the accumulating hydrocarbon species; at elevated temperatures (around 250 K), truly catalytic reactivity can be observed. We show that the isomerization proceeds with sustained rates already on an initially clean model catalyst; sustained hydrogenation

rates, however, can only be induced in the presence of previously deposited carbon at the surface. The chapter will discuss possible explanations for this ability of carbon deposits to induce hydrogenation (*chemoselectivity*). Additionally, we present conversion rate measurements with *cis*- and *trans*-2-butene as reactants; different rates have been observed only under certain conditions – in which *cis*-2-butene always exhibits higher reactivity. The origins of this selectivity are discussed in a qualitative kinetic analysis of the rate-limiting steps under all conditions.

The thesis ends with a conclusion about the two projects and an appendix that succinctly lists all relevant experimental parameters, procedures and preparation conditions.

# Chapter 2

## Dynamic and Kinetic Processes on Surfaces and Surface Structure

As mentioned in chapter 1, this work focuses on an understanding of processes during heterogeneous catalysis at an atomic level. This chapter provides an overview over elementary dynamic and kinetic processes that often occur during heterogeneous catalysis on surfaces; it comprises four sections: the first of them gives an overview over processes of gas-surface interactions including adsorption, followed by a description of adsorbate dynamics and interactions on surfaces, including surface diffusion and reaction; the last two sections cover kinetic and dynamic processes on *complex* surfaces – such as diffusion between different surfaces or the influence of defects – and, finally, (metal) particle-related effects such as sintering and poisoning.

Most of the information in this chapter was compiled from references [26, 27, 28, 29].

### 2.1 Gas Particles on Surfaces

Fig. 2.1 gives an overview over the fundamental interaction processes between gas molecules and a surface discussed in this section.

#### 2.1.1 Gas-Surface Interactions

During their approach to a surface, gas phase molecules interact with the surface *via* the *surface potential* (see fig. 2.2). Initially, their kinetic energy

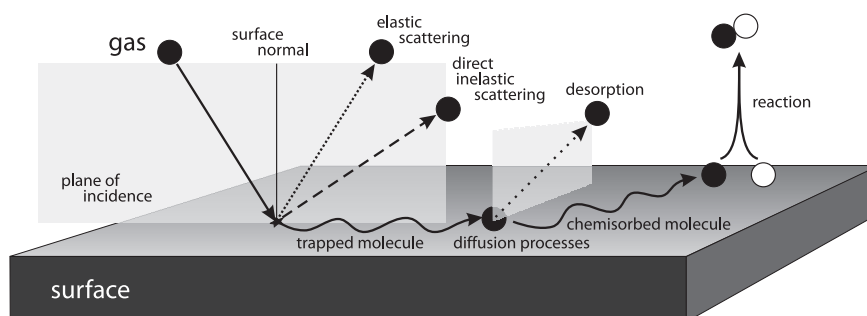


Figure 2.1: Elementary processes of gas-surface interactions.

is too high for them to get caught by the adsorbent<sup>1</sup>, but if they are able to transfer energy to the surface during their residence time close to the surface (while they bounce off from it), there is a certain probability for them to get caught on the solid surface; three processes may occur: scattering, trapping/desorption and sticking.

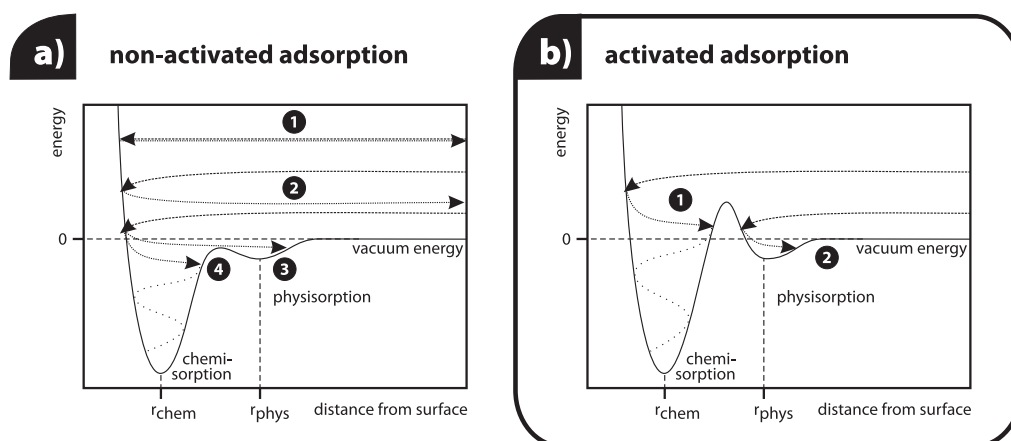


Figure 2.2: One-dimensional representations of possible trajectories on the potential energy surface for a) non-activated and b) activated adsorption processes.

**Scattering** occurs when the interaction period is too short for the adsorptive<sup>2</sup> to release enough of its kinetic energy to get bound in the surface potential; if no energy is lost at all to the surface (fig. 2.2 a) case 1), *elastic* scattering will be found, and the entrance and exit angles and velocity of the

<sup>1</sup> *Adsorbent* is a term for the solid surface on which adsorption takes place.

<sup>2</sup> *Adsorptive* is a term for the gas phase molecule before its adsorption.



molecule will be found identical if the surface is ideally flat. If however some momentum is lost (fig. 2.2 a) case 2) – or, reversely, if the molecule receives energy from the surface during its interaction –, *direct inelastic* scattering is the result and the exit angle and velocity of the molecule will be found to deviate from the entrance conditions.

**Trapping/Desorption and Sticking.** If the molecule loses all of its momentum normal to the surface, it gets *trapped* in the surface potential as an adsorbate (see fig. 2.2 a) cases 3 and 4); this adsorbate is typically still vibrationally excited, but it may lose its vibrational excitation during its residence time on the surface and thermally equilibrate with it, resulting in a stable adsorption state; this is termed *sticking*. Alternatively, the vibrationally excited, trapped molecule may as well overcome the desorption barrier again by energy transfer from the surrounding surface, or by intramolecular energy transfer; due to the possible processes, this desorption typically occurs with a certain energy-, and a cosine angular distribution; additionally, the desorption due to this process is significantly delayed with respect to the scattered molecules. This process of *indirect* inelastic scattering is often termed *trapping/desorption*.

**Sticking Coefficient:** The probability by which a molecule that impinges on a surface will get bound to the surface by sticking is termed the *sticking probability*  $S$ . It is a function of many parameters, including the surface coverage  $\theta$  of different species ( $\theta_1, \theta_2, \dots$ ), the surface structure, its electronic properties (which may be changed by electronic promoters), or temperature. It is defined as:  $S = dN_{\text{ads}}/dN$  (the differential quotient of adsorbing and impinging molecules). The remainder  $1 - S$  is the scattered ratio. The significance of the sticking coefficient is that it is an experimental observable, and it can be directly measured, *e.g.* by the so-called *King-and-Wells* method [30, 31].

**The Rate of Adsorption.** The rates of surface reactions depend on the surface coverages of the reactants; thus, those coverages need to be expressed mathematically for kinetic calculations. For this purpose, adsorption is treated as a chemical reaction  $A(g) + * \rightarrow A(\text{ads})$  between a gas phase particle  $A$  and a free surface adsorption site  $*$ . The rate of adsorption can then be expressed by the sticking coefficient  $S_A$ , the collision frequency  $Z_A$  of gas-phase species  $A$  with the surface (as obtained from kinetic gas theory) and the available free adsorption sites  $\theta_*$  as follows:

$$\frac{d\theta_A}{dt} = S_A(\theta_A, \theta_?, \dots) \cdot Z_A \cdot \theta_* \quad \text{with} \quad Z_A = p_A / \sqrt{2\pi \cdot m_A \cdot k_B \cdot T} \quad (2.1)$$

The sticking coefficient may need to be expressed as a function of (all) adsorbate coverages, and the amount of available adsorption sites  $\theta_*$  may also intricately depend on all coverages of the surface adsorbates. Finding a valid relation between the coverages of all surface species and the adsorption rate is a high demand on experiments and is usually the highest obstacle for an exact kinetic description of surface reactions.

**Chemisorption and Physisorption.** The adsorbate bond may be mediated by different types of interactions between the surface and the adsorbed species, and it may differ considerably in strength. As in condensed materials, dispersive or *van-der-Waals* forces may be responsible for the adsorbate-surface interaction; such adsorbates are relatively instable, and their adsorption energy is usually far less than  $\approx 50$  kJ / mole. This adsorption mode is typically found for closed-shell molecules, and is usually termed *physisorption*; it leaves the electronic structure of the adsorptive essentially intact (except for possible bond polarizations). The other type of adsorbate bonds forms by combination of unpaired electrons in adsorptive and surface, which leads to the formation of covalent *chemical* bonds; their typical character is their high directionality. Such adsorbates are called *chemisorbates* (see [1], vol. 3, p. 911-942). Chemisorption may lead to strong changes in the electronic structure of the adsorbate, and may even lead to the rupture of bonds and the dissociation of the molecule (*dissociative adsorption*).

**Activated and Non-Activated Adsorption.** The molecule approaching the surface may sense one of two very different types of potential energy surfaces, see fig. 2.2 a) and b). The two different cases can be discriminated by the temperature-dependance of the sticking coefficient  $S$  [27]: for *non-activated adsorption*, the sticking coefficient increases with decreasing temperature of surface and gas, while for *activated adsorption*, it increases with *increasing* temperature (at least at low temperatures). There is a certain relation between the terms activated or non-activated adsorption on one side and chemisorption or physisorption on the other: the chemisorption well in the potential energy surface always lies behind the activation barrier, if one is present (see fig. 2.2); physisorption on the other hand, is always non-activated.

**Direct and Precursor-Mediated Adsorption.** Adsorbing molecules may show a high mobility on the surface before they stick; this leads to the discrimination between *direct* and *precursor-mediated* adsorption. The ideal case of direct adsorption is when a molecule sticks during its first bounce with the surface and binds to the site where it lands. During precursor-mediated adsorption on the other hand, the molecule loses sufficient momentum normal to the surface to prevent it from returning into the gas phase (*i.e.*, it is trapped), but it still has sufficient energy to hop between adsorption sites (and thus shows a high mobility on the surface). This mobile state in which the molecule exists is called a *precursor-state*; it may simply be a physisorbed state, or a chemisorbed state in which the molecule may still possess enough (vibrational) energy to overcome the desorption barrier, but only in modes that are parallel to the surface; such a metastable precursor may later either lose its excess energy and stick, or gain enough energy by intramolecular energy transfer into the desorption coordinate, so that it may desorb. Precursor-mediated adsorption is observable in sticking coefficient-measurements, since the probability for a molecule to be trapped into a precursor state depends only weakly on surface coverage; thus, the sticking coefficient may be constant over an extended exposure range when the adsorption is precursor-mediated.

**Mono- and Multilayer adsorption, Condensation and Epitaxy.**

When the saturation coverage of an adsorbate is reached, no further gas phase particles can come into bonding interaction with the substrate surface; such a saturation layer of adsorbates is usually termed a *monolayer*. Nevertheless, at low enough surface temperatures, it is often observed that even beyond this point further molecules can adsorb, but they are not coordinated to the adsorbent surface; instead, they are bound by direct interaction with the already adsorbed layer(s) (*e.g.*, by *Van-der-Waals-forces*); in this way, infinite amounts of adsorbate layers may build up. This process is called *condensation*; typically, the particles in the *multilayers* are more weakly bound than the ones adsorbed by interaction with the metal surface (in the monolayer).

When the condensed layers form an ordered crystallite on the surface, the condensation process is called *epitaxy*. Epitactic growth also constitutes the basis for the preparation process of the model catalyst.

## 2.1.2 Surface-Dynamics, Reactions and Adsorbate Interactions

This section will discuss processes of adsorbed gas phase particles on surfaces.

### Diffusion

The seemingly random *Brownian* motion of a free gas phase particle characterized by alternating linear motion and collision processes is termed *diffusion*. It has an equivalent on surfaces, since adsorbed species are often also mobile on the surface; their linear migration may change direction each time the migrating molecule interacts with an adsorption site (where it may also reside for some time). The root mean square distance  $\bar{x}$  of a particle travelled within a time  $t$  from its original position is given by the particle's diffusion coefficient  $D$  as:  $\bar{x} = \sqrt{x^2} = \sqrt{2D \cdot t}$ ; the temperature-dependence of this coefficient can be expressed in Arrhenius form:  $D = D_0 \cdot \exp\left(-\frac{E_{\text{diff}}}{k_B \cdot T_s}\right)$ , where  $T_s$  denotes the surface temperature and  $E_{\text{diff}}$  the diffusion activation energy.

**Diffusion of Strongly Bound Species.** Strongly bound species have come into strong interaction with the substrate *via* formation of chemical bonds, and the potential energy diagram depicted in fig. 2.2 for the adsorption process suggests that the activation energy for migration from such an adsorption site to the next should also be high. In fact, the surface diffusion of chemisorbed species has to be described as a migration on a strongly corrugated potential energy surface with repeated troughs and hills; thus, the diffusion of strongly bound species does often follow certain pathways of minimal activation energy, which has an influence on the growth direction of adsorbate overlayers.

**Diffusion of Weakly Bound Species.** Trapped, physisorbed and also chemisorbed particles (at least at surface temperatures  $T_s$  with  $k_B \cdot T_s \gg E_{\text{diff}}$ ) diffuse rapidly and relatively freely in all directions, and may be described disregarding the surface corrugation; their motion may be compared to the *Brownian* motion of particles in a free gas; thus, such weakly bound species are sometimes said to form a *two-dimensional gas* or *lattice gas*. Their diffusion coefficient is  $D = v \cdot d^2/4$ , where  $v$  denotes the hopping frequency  $v$  and  $d$  the average travel distance per hop. The average distance that such a species can travel on the surface is mostly limited by its short surface residence time.

## Desorption

The residence time of an adsorbed particle ends with *desorption*; desorption is closely related to diffusion, but it denotes the process during which an adsorbed particle completely leaves the potential well that binds it to the surface; thus, the activation barrier for desorption is typically higher than for diffusion. The desorption rate of a species A is usually described by the following equation:

$$\frac{d\theta_A}{dt} = -(\theta_A)^n k_{\text{des}} \cdot \exp\left(-\frac{E_{\text{des}}}{k_B \cdot T_s}\right) \quad (2.2)$$

where  $k_{\text{des}}$  denotes the preexponential factor of desorption and  $E_{\text{des}}$  the desorption activation energy. The mathematical description, however, is more intricate than the above formula suggests, since both the preexponential factor and the desorption activation energy often strongly depend on all adsorbate(s) coverages. In simple cases, the desorption order  $n$  is identical to the molecularity of the elementary process and thus an integer value; it is 0 for coverage-independent desorption from condensed phases, and 1 or 2 for molecular and recombinative desorption, respectively. However, lateral interactions often show an influence on the desorption order as well, and in such cases, the desorption order usually becomes non-integer.

The desorption order, preexponential factor and activation energy can be obtained from careful evaluation of systematic thermal desorption experiments (TDS or TPD) with different initial coverages; a useful approach is the *Redhead*-method [32].

At reasonably low temperatures, the rate of desorption is low, so that desorption may be neglected from a kinetic treatment of the surface reactions.

## Adsorbate Bonding and Analogy to Metal Complexes

Adsorption sites with different coordination numbers can be occupied by adsorbates; fig. 2.3 depicts the sites occupied on many metal surfaces. Coordination to only one metal atom in the adsorbative is reached in *on-top*-sites, and 2-fold coordination in *bridge*-sites. The adsorbent may also be coordinated to a higher amount of metal atoms; the sketch depicts the adsorption on the (111) crystallographic plane of hcp or fcc metals, where these are threefold hollow sites; on the (100) plane of these metals, the adsorbate may get coordinated in a fourfold hollow site (not shown).

The bonding of adsorptives to the surface may be interpreted in analogy to the bonding in a metal complex, where the adsorptive acts as the ligand and the bonding atom(s) in the surface as the metal center. The molecular orbital

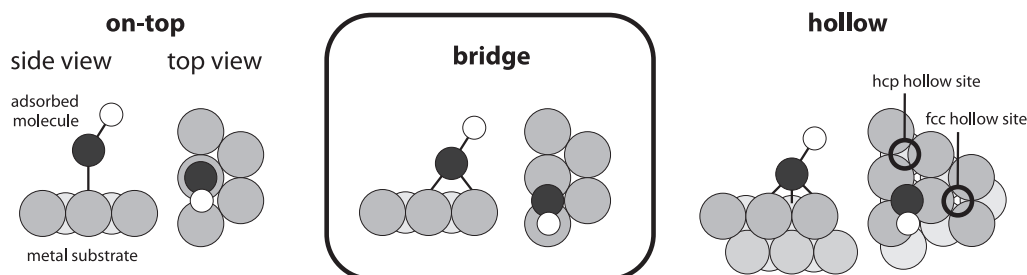


Figure 2.3: Different bonding modes of a diatomic model adsorbate on metals.

theory of bonding in complexes can also be applied in surface chemistry; this will be discussed in the following for the adsorption of carbon monoxide (CO) on palladium metal (Pd).

**The Bonding of CO to Pd.** The bond between carbon and oxygen in the free CO molecule is mainly mediated *via* the bonding  $3\sigma$  orbital and the two  $\pi$  orbitals  $1\pi_x$  and  $1\pi_y$  (also bonding); the four other valence electrons of the molecule that are not accommodated in these three bonding orbitals are situated in the two non-bonding orbitals  $4\sigma$  (energetically between  $3\sigma$  and the two  $1\pi$  orbitals) and  $5\sigma$ , which constitutes the highest occupied molecular orbital (HOMO) and is also non-bonding [33]. Blyholder introduced the model of CO adsorption on  $4d$ -metals based on molecular orbital theory [34, 35]: according to his model, the CO-metal interaction is mainly mediated by an interaction between the carbon-centered HOMO of CO and the metal's  $d$ - and  $sp$ -bands ( $\sigma$ -donation), and by *backdonation* from the metal's  $d$ - and  $sp$ -bands into the two unoccupied  $2\pi^*$  antibonding molecular orbitals of CO (its LUMO); backdonation into the two antibonding orbitals weakens the carbon-oxygen bond in CO. Since the extent of backdonation sensitively depends on the local bonding geometry and adsorption site, strong shifts in the vibrational frequency of adsorbed CO can be found when the molecule is bound on different surfaces, and also in different adsorption modes; a typical vibrational frequencies of CO bound on-top is  $2150 - 2050 \text{ cm}^{-1}$ , for bridge-sites it is  $2000 - 1920 \text{ cm}^{-1}$  and for CO bound in hollow-sites  $1920 - 1800 \text{ cm}^{-1}$ . Since the  $5\sigma$ -orbital is centered on the carbon atom in the molecule, CO is bound with carbon end-down on most metals [27].

### Adsorbate Overlayer Structures

At very low adsorbate coverages, the adsorbates may populate their specific binding sites on the substrate statistically. With increasing coverage, the

regular array of adsorption sites formed by the substrate's surface structure tends to coordinate the adsorbates into an ordered, *commensurate* overlayer equilibrium structure that reflects the substrate symmetry and structure. Then, with a further increase of coverage, the interaction between adsorbate particles on surfaces by direct physical contact and mediated *via* the electronic and geometric structure of the surface increases, leading to the formation of different, ordered structures, which may even be *incommensurate* (*i.e.*, they do not further represent the substrate structure). Very different well-defined overlayer structures may be formed on the same surface at different coverages. The full description of an overlayer structures includes a description of the structure's symmetry, which is usually denoted with respect to the substrate symmetry (*Wood's notation*), or – if the structure is incommensurate – by the *matrix notation*; additionally, a full description denotes the adsorption site.

Overlayer structures are equilibrium-structures, and they depend on thermodynamic parameters such as temperature and pressure. Their formation may be slow at low temperatures, and thus they may not be experimentally observed. The formation of an overlayer structure is observable with many experimental techniques such as LEED or IRAS. A change in adsorbate-adsorbate interaction may show up in the vibrational IRAS spectra of the adsorbates, because the lateral interaction may have influence on the extent of backdonation; this is observed in IRAS spectra of adsorbed CO [36]. The following two paragraphs will describe the overlayer structures of CO on the Pd(100) and (111) crystallographic planes under the conditions of the experiments described in this text. Since the Fe<sub>3</sub>O<sub>4</sub>-supported Pd nanoparticles – which are the subject of this thesis – expose only facets with (111) and (100) symmetry, the knowledge supplied in the following will also be valuable for the result chapters.

**CO on Pd(100).** On Pd(100), CO adsorbs only on bridge sites, regardless of coverage [37, 38]. At 300 K, the vibrational frequency shows a low-coverage limit of 1895 cm<sup>-1</sup> [38] and shifts linearly with increasing coverage to 1964 cm<sup>-1</sup> at the saturation coverage of 0.5, where it forms a  $c(2\sqrt{2} \times \sqrt{2})R45^\circ$  adsorbate overlayer structure [37, 38]. At temperatures below 200 K, this structure transforms into an incommensurate compression structure with a saturation coverage of 0.81; the vibrational frequency increases nonlinearly with exposure to a saturation value of 1989 cm<sup>-1</sup> [38]). The same saturation coverage is found when the CO is exclusively exposed at low temperatures (80 K), but no regular adsorbate overlayer structure is found under these conditions; the saturation vibrational frequency under these conditions is 1997 cm<sup>-1</sup> [38].

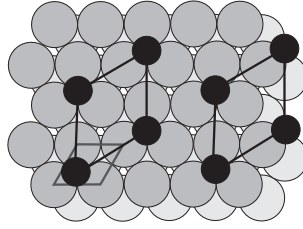


Figure 2.4: The  $(\sqrt{3}\times\sqrt{3})R30^\circ$  overlayer structure of CO on Pd(111), adsorbed in fcc hollow sites, after [39]. The black circles represent binding sites of CO; the dark grey trapezoid is the elementary cell of the metal lattice.

**CO on Pd(111).** A variety of ordered adsorption overstructures have been reported on Pd(111) [40]. At low coverages, CO adsorbed on this crystallographic plane does not form a closed adsorbate structure, but agglomerates in islands of an inner  $(\sqrt{3}\times\sqrt{3})R30^\circ$  structure; the islanding ends at a coverage of  $1/3$ , where CO forms a closed (saturated)  $(\sqrt{3}\times\sqrt{3})R30^\circ$  overstructure in which CO is bound in fcc hollow sites [39] (see fig. 2.4); this is in agreement with the observed vibrational frequency of CO of  $\approx 1840\text{ cm}^{-1}$  [37]. On further increase of the CO-coverage, an ordered  $c(4\times 2)$ -2CO overstructure is formed with a CO coverage of 0.5 and a single IR peak at a frequency of  $1936\text{ cm}^{-1}$  [37]; this structure defines the maximum equilibrium coverage for UHV studies at 300 K. The stretching frequency was first interpreted as an indication that CO is adsorbed in bridge sites [36]; later studies, however, assigned it to a structure in which CO is adsorbed in a combination of fcc and hcp hollow sites; this interpretation was originally deduced from photoelectron diffraction and STM results [41], and later supported by DFT calculations, which also demonstrated that the observed vibrational frequency of  $1936\text{ cm}^{-1}$  could actually be due to CO on hollow sites, although this is an exceptionally high value for the vibrational frequency of such a species: the shift of the vibrational frequency was explained by dynamic and static intermolecular interactions in this dense overstructure – the latter induced by coverage-dependent backdonation from the surface metallic atoms towards the antibonding  $2\pi$  molecular orbitals of the chemisorbed CO molecules [42]; furthermore, a combined HR-EELS and high-resolution core level photoemission spectroscopy study supported the interpretation [43]. Later, however, Rose and coworkers [44] have suggested that structures with both bridge-bonded and CO adsorbed in hollow sites can also coexist.

At temperatures as low as 120 K and below, CO coverages higher than 0.5 can be attained in a  $c(2\times 2)$ -3CO overlayer structure with a coverage of 0.75 [43, 44, 45] in which CO is adsorbed both on-top on Pd atoms ( $2110\text{ cm}^{-1}$ )



and in fcc and hcp hollow sites ( $1895 \text{ cm}^{-1}$ ) [46, 45]; this structure defines the CO saturation coverage below 120 K.

**Reconstructions.** The adsorption of molecules on a surface may even lead to a reconstruction of the substrate surface in order to minimize the whole system's free energy; such surface reconstructions are important phenomena in many catalytic systems, but were not found with CO-adsorption on supported Pd nanoparticles [45].

### Surface Reactions

In most cases, bimolecular reactions on surfaces occur between two fully accommodated adsorbates that encounter by surface diffusion; this process is called a *Langmuir-Hinshelwood* reaction [47] and is usually denoted by the following reaction scheme:  $A(\text{ads}) + B(\text{ads}) \rightarrow AB(\text{ads})$ . The reaction rate for this reaction is usually expressed as the change of product coverage per unit time and depends on the surface coverages of the reactants A and B:

$$\frac{d\theta_{AB}}{dt} = k \cdot \theta_A \cdot \theta_B \quad (2.3)$$

$$\frac{d\theta_A}{dt} = S_A(\theta_{AB}, \theta_A, \theta_B) \cdot Z_A \cdot \theta_* - k \cdot \theta_A \cdot \theta_B \quad (2.4)$$

$$\frac{d\theta_B}{dt} = S_B(\theta_{AB}, \theta_A, \theta_B) \cdot Z_B \cdot \theta_* - k \cdot \theta_A \cdot \theta_B \quad (2.5)$$

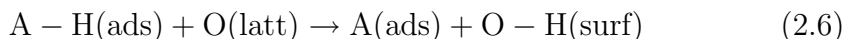
The surface coverages are functions of both reaction and adsorption rates, and typically depend on the availability of free surface sites  $*$  (of which different types may contribute); their valuable description usually complicates the description of surface reaction kinetics. Note that the rates of desorption were neglected in the above equations (which is a valid simplification at low temperatures).

In a few cases, reaction-dynamics experiments have indicated a *direct* reaction between an adsorbate and a gas phase particle during its impact on the surface [48]; this is called the *Eley-Rideal* mechanism. One example for the Eley-Rideal mechanism is the direct reaction between chlorine atoms adsorbed on Au(111) and hydrogen atoms in an atom beam, and it was observed by the angular distribution of the product HCl [49].

Examples for strictly unimolecular reactions on surfaces are scarce; in fact, many reactions that *seem* to be unimolecular (*e.g.* dissociation reactions) are truly bimolecular, because the fragments that are formed in the reaction have to be accommodated on the surface in additional binding sites

\*:  $A(\text{ads}) + * \rightarrow B(\text{ads}) + C(\text{ads})$ . The availability of new binding sites may be the rate-limiting factor in many surface-related dissociation reactions. Nevertheless and despite this complication of surface reactions as compared reactions in the gas phase, the mere possibility for the accomodation of a dissociation product on a surface typically leads to much higher rates of reactions with dissociative elementary step(s) on a surface as compared to the related gas-phase reaction.

The necessity of finding an additional binding site for dissociation products leads to a special situation on surfaces with increased heterogeneity such as oxides, where typically metal and oxygen are exposed; some dissociation reactions may require an oxygen site as a Brønsted base:



where A-H denotes the acid and O(latt) an exposed lattice oxygen atom at the oxide; the acid-base-reaction leads to the adsorbed conjugate base A and a surface hydroxyl group O-H(surf).

## 2.2 Kinetic Effects on Complex Surfaces

Real catalysts typically consist of metal particles supported on an oxide; in this thesis – as laid out in the introduction – we will attempt to understand catalysis by the study of processes on supported model catalysts, which typically consist of crystalline metal nanoparticles supported on an epitaxially grown oxide film, see fig. 2.5 as an example. The earlier sections of this chapter treated effects that would best be observable on well-defined surfaces of metal single-crystals; the following section will treat effects that can only arise when several different surfaces are in contact with each other; such a sample is termed a *complex surface*, and model catalysts are a one example for them.

### Diffusion between Different Surfaces and the Capture-Zone Effect.

Surface diffusion was described before; in a complex surface sample, diffusion processes can occur between *different* surfaces, and the surface species will tend to form the most stable adsorbate complex with the surfaces available. When the sample is heated, a weakly bound adsorbate – instead of desorbing – may quickly move to a surface on which it binds strongly, and where it may even react or dissociate. Thus, surface diffusion may lead to a sensible increase of reactant flux to the active parts of a catalyst [50, 51, 19]. The area around the active surface (usually the metal particle) that can increase the reactant flux to the active surface in such a way is often termed the *capture zone* (see fig. 2.5).

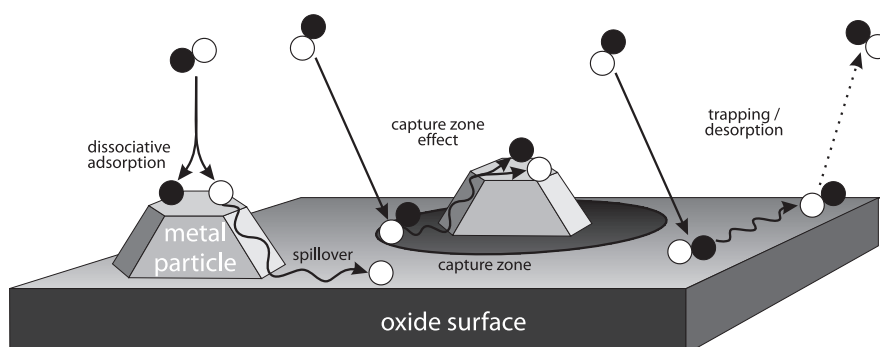


Figure 2.5: Elementary processes on the surfaces of model catalysts (as one example for a complex surface).

**Spillover.** *Spillover* denotes the migration of an active species formed on one surface (called the *donor*) to another surface (*acceptor*), on which it can not be formed and where it may react further ([1], volume 3, pp. 1064 - 1077). Such a set of events was found for the first time on real Pt/Al<sub>2</sub>O<sub>3</sub> catalysts, where hydrogen dissociates into hydrogen atoms on the platinum metal particles of this catalyst and then spills over to the oxide, where it reacted further [52, 53]. The inverse process of migration of active species from an oxide to a metal is often termed *inverse spillover*, since it is a less probable process.

**Reaction on the Support.** Although the oxide support in real catalysts was originally meant to stabilize the active metal phase of the catalysts and prevent it from sintering into a compact metal, it was in some cases found to be catalytically active itself; some catalysts even contain only oxidic phases; this thesis will discuss a chemical activity of the Fe<sub>3</sub>O<sub>4</sub> support in chapter 5. An example for the application of the oxidic support's chemical activity are the NO<sub>x</sub> storage materials used in automotive exhaust catalysts; in those materials, the harmful nitrogen oxides are stored in the oxide phases of the catalyst to be removed and reduced to nitrogen and oxygen at a later time [54].

**Strong Metal-Support Interactions.** Nanoparticles and their supporting oxides interact with one another in many ways, and the support may strongly influence the particles' electronic and geometric structure and *vice-versa*. This implies that two catalysts with metal nanoparticles of identical shapes may behave very different if the particles are supported on different oxides in the two cases, even if the support itself is chemically inert. As an example, an earlier work in our group [55] has shown that the  $\text{Fe}_3\text{O}_4$  support changes the reactivity of the supported Pd nanoparticles towards oxygen, leading to a preferential oxidation at the particle-support interface (see also chapter 4); a comparable effect has not been observed with the same particles supported on alumina  $\text{Al}_2\text{O}_3$ ; thus it was assigned to a strong metal-support-interaction (SMSI).

**Defects.** Defects are a well-known phenomenon in solid state chemistry and physics, and it is a common notion that catalytic action is strongly related with and considerably accelerated at defect structures [56, 57, 58]. Single crystal surfaces already show point defects (missing and ad-atoms, impurities, kinks) and line defects (steps, vicinal surfaces *etc.*). Complex model catalysts may expose an even bigger variety of non-equivalent sites; not only is their surface intrinsically more complex, but especially the oxides (which consist of at least two chemical species) may show additional structural imperfections such as *Schottky*- and *Frenkel* defects or colour centers; the metal nanoparticles expose facets of different crystallographic planes, and at the boundary of these facets, atoms with a higher degree of unsaturation are exposed at edges and steps. All of these and many other sorts of irregularities lead to a complex surface with a high degree of heterogeneity in which a multitude of different, non-equivalent possible reaction sites are exposed. Additionally, the ratio between regular and defect sites typically increases with decreasing dispersion<sup>3</sup>.

---

<sup>3</sup>In catalysis, *dispersion* denotes the ratio between surface *vs.* bulk atoms in metal clusters.

## 2.3 Particle-Related Effects

**Electronic Effects.** The electronic structure of a supported particle may differ from an extended metal surface, for example, due to its limited size leading to *electron confinement*, due to *lattice distortions* induced by the reduced dimensions or due to electronic influences of the support. Those differences may have implications for catalytic reactions; as an example, adsorption on transition metals arises by interaction between molecular orbitals in the adsorbed molecule and the band structure of the solid, and thus the adsorption bond may react on those differences in the electronic structure due to the limited size of isolated metal clusters; since surface-reactions occur between adsorbates, the dependence of the adsorbate-bond strength on cluster size may also have an influence on the reactivity, and small clusters may therefore show pronounced differences in adsorption and reaction behaviour compared to bigger clusters.

**Communication Effect.** Most heterogeneous catalysts consist of oxide-supported metal nanoparticles which typically expose adjacent facets of different crystallographic orientations; the reactions on a catalyst could thus be attempted to be understood as a simple sum of the processes that occur on the different exposed surfaces (the oxide surface and the different crystallographic facets of the nanoparticles); however, such a simple model does not account for the possibility of adsorbate-migration (diffusion) between the different surfaces of the complex catalyst, and in fact it is conceivable that reactions on a catalyst may occur stepwise on the different surfaces of the system. This possible synergism is known as *geometric* or *communication* effect.

**Particle Reshaping: Thermal Stability, Sintering and Stabilization.** Complex model catalysts expose different surfaces of metal and oxide. Surfaces generally tend to minimize their surface free energy by reduction of the surface area; another possibility for surfaces to minimize their energy is to interact with a different surface to form an interface. On a model catalyst, the interaction between the metal particles and the oxide support is meant to stabilize the particles and prevent them from sintering into one big metal agglomerate. For a given metal load on a defined oxide surface, the equilibrium structure is defined by the surface free energies of the metal and the oxide, and the free energy of the metal-support interface. It depends on temperature and may also depend on gas pressures, since surface free energies may differ with different adsorbate overlayers. As long as the surface free energy of

the oxide  $\gamma_{\text{oxide}}$  is lower than the sum of the surface free energies of the metal  $\gamma_{\text{metal}}$  and the metal-support interface  $\gamma_{\text{interface}}$  (*i.e.*,  $\gamma_{\text{oxide}} < \gamma_{\text{metal}} + \gamma_{\text{interface}}$ ), any additionally deposited metal atom will tend to form particles (*Volmer-Weber-growth*). In the rare case of very high surface free energies of the oxide ( $\gamma_{\text{oxide}} > \gamma_{\text{metal}} + \gamma_{\text{interface}}$ ), it can be energetically more favourable for the metal to cover the oxide completely (*Frank-van-der-Merwe-growth*).

Particle reshaping may result from thermal annealing, due to the increased surface mobility of the metal atoms at elevated temperatures; in other cases, particle reshaping occurs under different chemical conditions – *e.g.* for the case of the Pd/Fe<sub>3</sub>O<sub>4</sub>/Pt(111) model catalyst, reshaping has been observed only in an oxygen atmosphere (at elevated temperatures) [59], see chapter 4.

During deposition of metals on oxides, the sample is kept at low temperatures, because the metal atom mobilities on the support are low under these conditions, and many small clusters form by heterogeneous nucleation on the oxide surface. Thermal annealing induces a reshaping of the metal into bigger particles to reach thermodynamic equilibrium (*Ostwald ripening*).

**Catalyst Poisoning, Fouling and Coking.** In real catalysis, it is often observed that the efficiency of a catalyst material decreases slowly; this might be due to a loss of surface by particle reshaping under the reaction conditions, but it was often found that low-concentration contaminants of the reactant gases might bind so efficiently to the catalyst surface that they slowly accumulate and lead to a loss of active surface (see [1], volume 3, pp. 1263 - 1282); this process is called *poisoning*. In real catalysis, the accumulation of poisoning material may even lead to the formation of bigger agglomerates which not only block the surface of the catalyst, but block whole pores between grains of the catalyst material; this is often called *fouling*. Poisoning and fouling, since they lead to loss of catalyst activity, are severe problems, and the deactivated catalyst has to be exchanged or regenerated.

One example for catalyst poisoning is the deactivating effect of sulfur agglomerates on the active surface of the car exhaust catalyst; to prevent it, the fuels used in combustion engines with exhaust catalysts have to be hydrodesulfurized. Another example of a catalyst poison are carbon and small hydrocarbon species (*carbonaceous species*) that often agglomerate on catalysts used for conversion of organic reactants. The poisoning and fouling of real catalysts by carbon agglomerates is often termed *coking*. Though coking does often lead to deactivation, it was also found in some catalysts to be of minor relevance for the catalyst activity; as an example, heavy oil hydrotreating catalysts can tolerate enormous loads of accumulated carbon without significant loss of activity (see [1], volume 3, p. 1265).

# Chapter 3

## Experimental Setup and Techniques

The experimental setup used for this thesis allows to study surface processes (see chapter 2) on well-characterized model catalysts; it has been setup before and has also been previously described [60, 61]; the following chapter is aimed at supplying both a general overview of the setup, and an introduction into the applied measurement techniques.

Fig. 3.1 gives a schematic depiction of the setup; model catalysts can be directly prepared inside the setup in a dedicated *preparation chamber* using standard surface science techniques, including fast ion bombardment (*sputtering*), heating to elevated temperatures (*annealing*), metal physical vapor deposition (PVD), and controlled gas exposure; the preparations can then be examined by means of a surface crystallographic technique, low energy electron diffraction (LEED), as well as by Auger electron spectroscopy (AES).

The experiments on the such prepared model catalysts are conducted in a separate vacuum chamber, into which the sample can be transferred by means of a metal rod manipulator. In this *experimental- or scattering chamber*, the sample may be exposed to gases using up to three molecular beams, which cross on the sample surface. Surface processes such as scattering, adsorption and desorption, or reaction may then be studied by gas phase detection of species in the volume around the catalyst using quadrupole mass spectrometry (both in angle-resolved and angle-integrated mode), supplemented by infrared reflection-absorption spectroscopy (IRAS), which can be applied to detect species that are adsorbed at the surface.

Only the experimentally important details of the applied techniques and their setup will be described in this chapter; for further information about

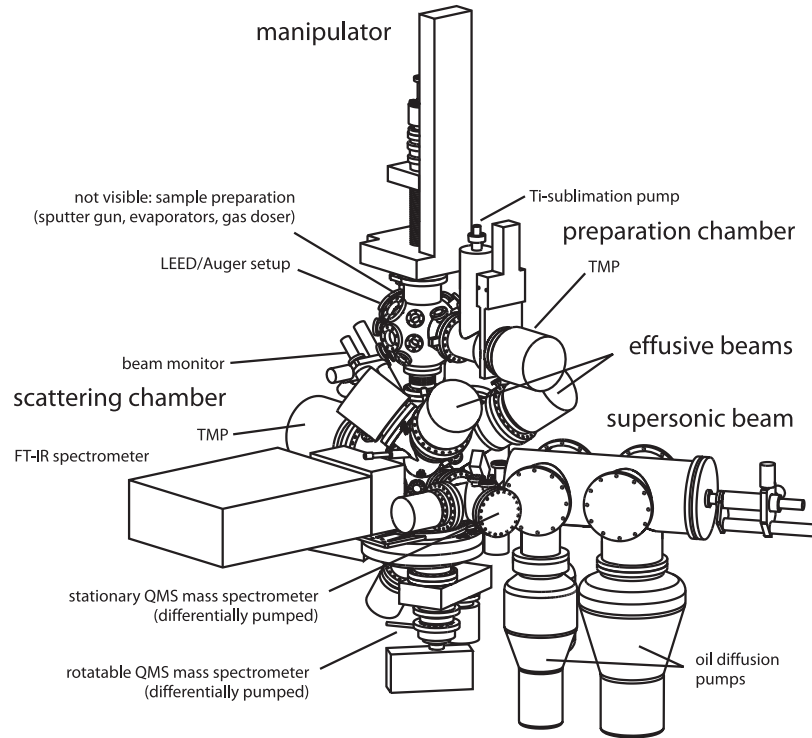


Figure 3.1: The molecular beam setup, schematically (from [60]).

the setup, we refer to [60] and [61] and the references given later in the text. The chapter is divided into four sections, one for each the preparation and the scattering chamber, the detection techniques, and the experiment time control.

### 3.1 Preparation Chamber

The preparation chamber is equipped with the machinery needed for the epitaxial growth of thin oxide films and preparation of metal nanoparticles by metal physical vapor deposition and controlled gas exposure. The base pressure in the chamber is kept below  $2 \cdot 10^{-10}$  mbar by means of both a turbomolecular pump (TMP, Pfeiffer TMU500MC, pumping capacity 500 L/s), and a titanium sublimation pump (Pfeiffer); the latter is mainly used to remove gases formed during sample preparation, most importantly water.

For sample cleaning, the preparation chamber is equipped with an ion gun for fast ion bombardment (*sputtering*, Omicron ISE10). Metals (iron (Fe) and palladium (Pd) for the purpose of this study) are deposited by means of two electron beam evaporators (Omicron Focus EFM3). The evaporator's ab-



solute deposition rate can be calibrated by means of a quartz microbalance (Caburn MDC, controller: Intellemetrics IL 150), which is also contained inside the preparation chamber. The evaporators output both ions and neutral particles (atoms and clusters); the flux of ionized particles in the beam is a good measure for the overall deposition rate, and it can be quantified during deposition on the sample based on the current that it induces in a wire loop around the evaporator's exit; this value is constantly monitored in order to keep the metal deposition rate constant during and in between preparations.

Additionally, the preparation chamber is equipped with a gas doser, which is simply a small tube filled with a reactant gas at a defined pressure and from which this reactant gas effuses into the preparation chamber through a small orifice; such a *gas doser* is often applied for oxygen dosage during the preparation of thin oxide films, but was not applied in this work.

For characterization of prepared samples, the preparation chamber is equipped with a LEED apparatus combined with an Auger spectrometer (AES) (Omicron ErLEED 150).

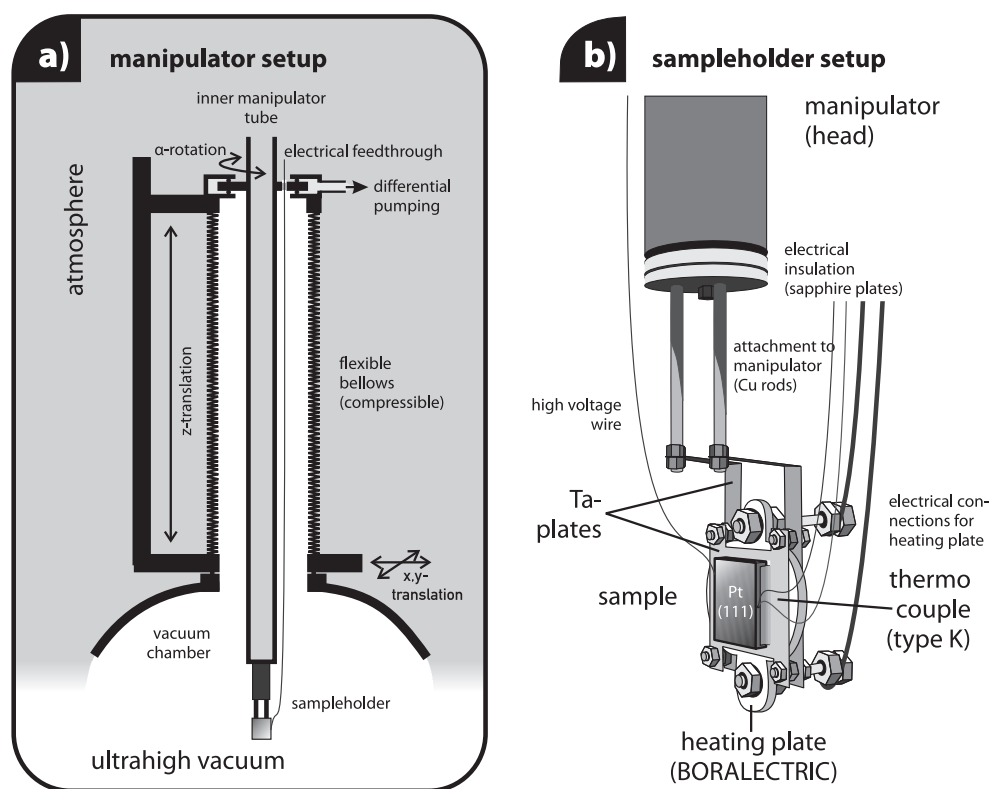


Figure 3.2: The setup of the manipulator and the sampleholder.

### 3.1.1 Sample, Sample Holder and Manipulator

For precise transfer between chambers and between different places in the same chamber, the sample is attached to a metal rod manipulator (Vacuum Generators, Omniax MX800) that allows to move the sample in the three directions  $x$ ,  $y$  and  $z$ , and also by rotation around the rod's long axis,  $\alpha$  (see fig. 3.2). The maximum translation in  $z$ -direction is approx. 70 cm. The manipulator shields the chamber volume against atmospheric pressure by means of flexible bellows and a differential pumping stage, which eliminates gases entering through the rotational bearing.

The sample is attached to the manipulator on the lower tip (*head*) of the manipulator's inner tube by means of a sample holder, as depicted in fig. 3.2 b). The sample holder is in contact with the manipulator's head *via* sapphire plates, which ensure electrical insulation and good thermal (heat) conductance between the manipulator and the sample holder at the same time; the latter is necessary to allow sample cooling to liquid nitrogen temperature. The inner manipulator tube can be filled with liquid nitrogen to cool the sample; the lowest possible sample temperature is  $\approx 110$  K in this setup. Additionally, the cold manipulator rod acts as a *cryo* pump.

The main aspect of the sample holder's setup is to ensure a good heat conductance between the ceramics heating plate and the sample single crystal to facilitate reaching the high temperatures necessary for thermal annealing ( $\approx 1300$  K); for this purpose, the Pt(111) single crystal used in these experiments is spot-welded onto a piece of tantalum foil<sup>1</sup>, and the heating plate (boron nitride, Advanced Ceramics Corp., Boralectric HT-01) is clamped to the setup from behind by a second tantalum foil. Electrical connections are made to the heating plate, and to the single crystal to ground it (esp. for LEED and AES) or set it to high offset potentials (for metal deposition). Additionally, a thermocouple (Ni/CrNi, type K) is directly spot welded to the single crystal's edge to allow precise measurements of the sample temperature.

## 3.2 Scattering Chamber and Gas Inlet

The scattering chamber is provided with all the equipment needed to conduct the kinetic experiments. The sample is brought into a well defined position

---

<sup>1</sup>Additionally, a piece of thicker molybdenum foil is put between Pt(111) sample and the tantalum foil to absorb possible over-time contamination from the heating plate.

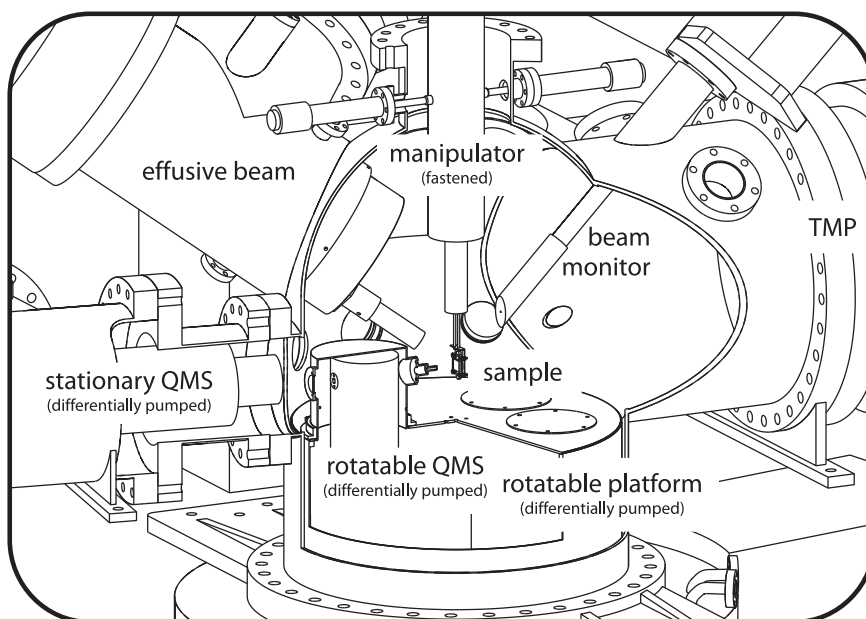


Figure 3.3: The components of the scattering chamber (from [60], modified). The IR source is attached at the backside of the chamber, and the IRAS detector to the cut-away part of the chamber wall in the front.

inside the scattering chamber where all the molecular beams and the infrared light from the IR-source cross (see fig. 3.3, and 3.4 for an overview over the scattering geometry). The scattering chamber is pumped with a high-capacity pump (TMP, Pfeiffer TMU1600MC, 1380 L/s) to keep the background pressure inside the chamber low even under molecular beam exposure; the base pressure of the chamber is approx.  $1 \times 10^{-10}$  mbar, and typically rises to values in the range of  $10^{-8}$  or low  $10^{-7}$  mbar under molecular beam exposure, while the pressure of the molecular beams on the sample surface is more than 100 times higher. Additionally, the kinetic experiments require a high pumping speed, because under such conditions, the momentary formation rate  $dn/dt$  of a species is practically identical to its momentary partial pressure in the chamber; the fulfillment of this requirement depends mainly on the ratio between the chamber volume and pumping speed.

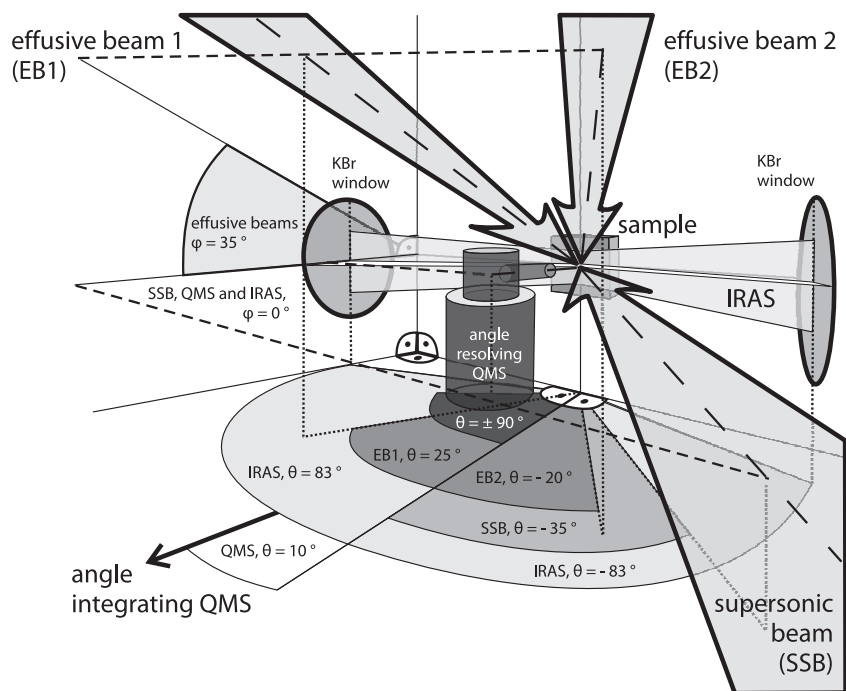


Figure 3.4: The scattering geometry.

Each molecular beam consists of two or even three differential pumping stages and enters the scattering chamber via small aperture tubes (effusive beam) or from a third, low-pressure differential pumping stage via a gate valve (supersonic beam). The beams can be interrupted by means of mechanical shutters in the beam pumping stages, and the amount of stray gas, which escapes into the main chamber from a shut beam, is negligible. The intensities of the beams are high (typical beam pressures on the sample are in the range of  $10^{-6}$  mbar) compared to the base pressure in the chamber (approx.  $1 \times 10^{-10}$  mbar).

**Detection Techniques.** The partial pressures of scattered or desorbing reactants and products around the sample is detected by two mass spectrometers, one of them stationary and angle-integrated, the other one rotatable around the sample surface, allowing to measure the angular distribution of desorbing or scattered species. The angle-resolved mass spectrometer is placed in a differentially pumped housing attached to the rotatable, differentially pumped platform. In addition to mass spectrometric detection, infrared vibrational spectroscopy is applied in the setup in the form of reflection-absorption spectroscopy (IRAS); in this spectroscopy, the IR light hits the sample under grazing incidence, and the reflected light is collected under the

same angle in an IR detector; both the IR light source and detector are positioned outside the scattering chamber, and the light is coupled into and out of the chamber by means of IR-transparent KBr windows.

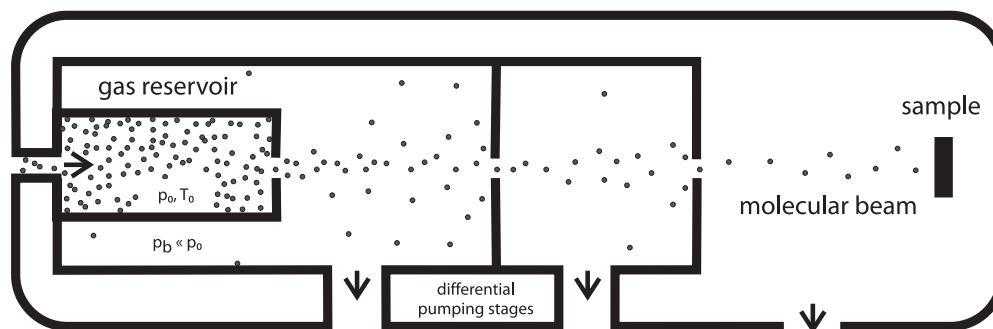


Figure 3.5: General scheme of a molecular beam: a gas expands from a high-pressure reservoir through a small opening into a region of lower pressure; a molecular beam is formed from the expansion by means of apertures.

### 3.2.1 Gas Exposure by Molecular Beams

A *molecular beam* (MB) is a spatially well defined, highly directed and collision-free flux of molecules [62, 63]. Molecular beams are prepared by an expansion of gas from a high pressure reservoir into a region with lower pressure (see fig. 3.5); the beam is formed from this expansion by cutting a small solid angle by means of apertures. The dynamic properties of such beams depend strongly on the pressure (and temperature) in the stagnation and also expansion stages, and on the dimensions and distances of the setup components. Two very different ways of beam formation have been established over the decades of molecular beams application; their fundamental difference is best understood by the ratio of the gas particles' mean free path  $\lambda$  in the gas reservoir and the width  $d$  of the expansion orifice; this ratio is known as the *Knudsen* number  $Kn = \lambda/d$ . As we will see in the following sections, beams operated at very low Knudsen numbers (indicating many collisions during the expansion: *supersonic beam* sources, SSB) and very low Knudsen numbers (practically no particle-particle collisions during expansion: *effusive beam* sources, EB) have very different dynamic characteristics.

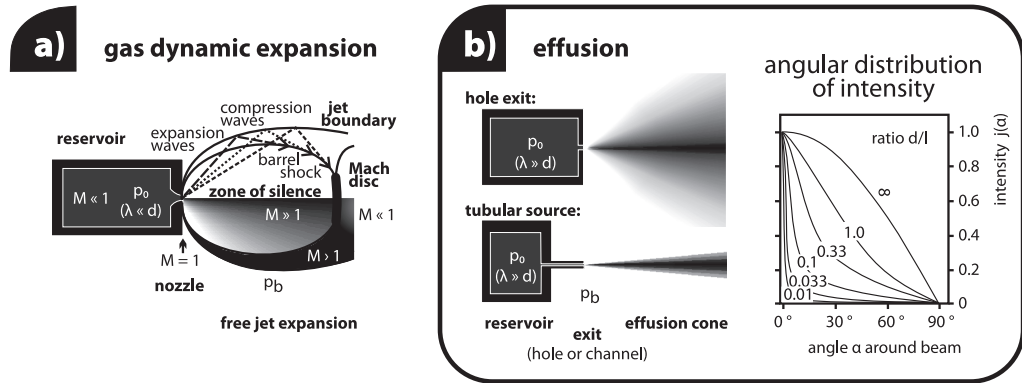


Figure 3.6: The two principles of molecular beam formation distinguished by the *Knudsen* numbers  $Kn$ : a) gas dynamic expansion (formation of a supersonic beam,  $Kn \ll 1$ ) and b) effusion (through a hole and a channel;  $Kn \gg 1$ ). Panel b) exhibits calculated angular intensity distributions around the exit (in the limit of infinite *Knudsen* numbers) obtained by effusion from a tubular source for different values of  $\beta = d/l$  (with channel diameter  $d$  and length  $l$ ) [63].

## Supersonic Beams

Gas particles in a free gas usually migrate arbitrarily into any direction in three-dimensional space, and in large numbers of free gas molecules the resulting momentum (*i.e.*, the sum over all individual momenta of all gas particles) is zero. When, however, a molecular beam is prepared from such a free gas under low *Knudsen* number-conditions, the many collisions in the source exit lead to an efficient energy and momentum transfer between gas particles from their random translation into the direction of lower pressure (flow direction, *i.e.*, towards the exit). The energy transfer into the translation in beam direction can be so effective that not only the translational degrees of freedom are affected, but also the internal degrees of freedom; especially the rotations are often effectively cooled in favor of a flow out of the reservoir. This leads to a breakdown of the equipartition of energy distribution over the degrees of freedom, and the regular Maxwell-Boltzmann distribution becomes invalid. The newly valid energy distribution for the translation into the beam direction is a sharply peaked Maxwell-Boltzmann distribution shifted towards higher energy. Due to the high collision-frequency in the nozzle, this type of molecular beam formation is usually termed *gas dynamic expansion*. It should be noted that this acceleration process is still adiabatic<sup>2</sup> – although

<sup>2</sup>It is more often described as *isentropic*.

the strong gain in velocity in one direction may appear as an indication for the opposite.

**Nozzles and Beam Acceleration.** The most effective accelerations are achieved in exits with convergent or convergent-divergent<sup>3</sup> shapes (*nozzles*), because the pressure and collision frequency increases in these devices with the decreasing cross section. The terminal beam velocity that can be reached at the nozzle exit increases with the pressure  $p_0$  in the stagnation stage, and will reach sonic<sup>4</sup> speed at some critical pressure  $p_{0,\text{crit}}$ , defined by the specific heat ratio  $\gamma = C_p/C_V$  of the expanding gas and the pressure  $p_b$  in the expansion volume (*backing pressure*); the condition is expressed by the *expansion coefficient*  $p_0/p_b$  as:  $p_0/p_b > G$  with  $G = (\frac{\gamma+1}{2})^{\gamma/\gamma-1}$ .  $G$  is smaller than 2.1 for any gas [62].

**Processes behind the Nozzle Exit.** When the gas particles reach sonic speed at the nozzle's point of constriction, they will be further accelerated to supersonic velocities in the region several exit diameters behind the nozzle, which is still collision-rich and which is termed *transition* region. The flow behind the nozzle builds up a *Prandtl-Meyer*-expansion fan originating at the rim of the nozzle exit.

As a consequence of the described processes, the flow *behind* the transition region is supersonic, has a highly unequilibrated energy distribution and expands symmetrically in form of an expansion fan around the beam's central axis (*free jet expansion*, see fig. 3.6); since this supersonic flow is nearly collision-free, its central part is often termed the *zone of silence*. The flow properties in the zone of silence can be estimated based on simple thermodynamic assumptions; table 3.1 lists some of the approximative formula.

The fact that the flow in the zone of silence is collision-free means that the molecules in this expansion cannot sense the downstream boundary conditions (*i.e.*, the backing pressure  $p_b$ , an equipartitioned energy distribution and the conservation of total momentum) by collisional transfer of informa-

---

<sup>3</sup>Convergent-divergent nozzles are known as *Laval* nozzles.

<sup>4</sup>Sonic speed is the maximum velocity by which pressure differences can travel through a medium by collision transfer. Collision processes are the main carrier of information transfer in a gas; thus, sonic speed is of high significance for many processes in gases, because it defines the point beyond which thermodynamic relaxation can only occur *via* shock waves. For an ideal gas, sonic speed is given by:  $c = \sqrt{\gamma \cdot p/\rho} = \sqrt{\gamma \cdot k_B \cdot T/m}$  (with the gas density  $\rho$ , the molecular mass  $m$  and gas temperature  $T$  before expansion). Note that the sonic speed depends on the local pressure  $p$  and temperature  $T$ . Different velocity regimes are discriminated by the *Mach* number  $M = v/c$ : subsonic ( $M \ll 1$ ), hypersonic ( $M < 1$ ), sonic ( $M \cong 1$ ), hypersonic ( $M > 1$ ) and supersonic ( $M \gg 1$ ) speed.

Table 3.1: Approximative formula and example values for the flow parameters in the zone of silence [62]. The example values are based on a nozzle pressure  $p_0 = 1$  bar and temperature  $T_0 = 25^\circ\text{C}$ , and a backing pressure  $p_b = 10^{-4}$  mbar.

property & approximative formula	example values for certain gases
terminal Mach number: $M_\infty = 1.17 \cdot (d/\lambda)^{(\gamma-1)/\gamma}$	8.3 (H <sub>2</sub> ), 8.3 (D <sub>2</sub> ), 8.7 (CO), 9.3 (O <sub>2</sub> ), 20 (Ar), 9.4 (2-butene)
terminal average velocity: $\langle v \rangle = v_{\text{max}} \cdot M_\infty \cdot \sqrt{M_\infty^2 + 2/\gamma - 1}$	2820 (H <sub>2</sub> ), 2000 (D <sub>2</sub> ), 755 (CO), 710 (O <sub>2</sub> ), 550 (Ar), 571 m/s (2-but.)
terminal beam temperature: $T_\infty = T_0 / (1 + (\gamma - 1) \cdot (M_\infty^2 / 2))$	20 (H <sub>2</sub> ), 20 (D <sub>2</sub> ), 18 (CO), 16 (O <sub>2</sub> ), 2 (Ar), 19 K (2-butene)

tion. Still, at some point, the unequilibrated, overexpanded and still further expanding flow has to adjust to the exterior boundary conditions. This adjustment can only happen by the formation of shockwaves, which form in a region termed the *free jet pressure boundary*, where reflected compression waves are turned into the direction of the supersonic flow (see fig. 3.6). These compression waves interfere and form a boundary known as the *barrel shock*; it terminates the zone of silence. The barrel shock boundaries meet at the central axis of the supersonic expansion in a distance  $x_M$  from the nozzle and form a shock structure known as the *Mach disc*; at this point, the free supersonic flow finally readjusts to the physical boundary conditions and gets subsonic.

**Consequences for Supersonic Beam Setups.** To obtain a stable, nearly collision free and thus well-directed supersonic beam, the compression waves have to be cut away from the zone of silence before the Mach disc by means of a skimmer. The position of the Mach disc can be estimated by the formula:

$$x_M = 2/3 \cdot \sqrt{p_0/p_b} \cdot d \quad (3.1)$$

where  $d$  is the nozzle's orifice diameter. In practice, the skimmer is placed much closer to the nozzle than equation 3.1 requires, and it is usually put shortly behind the transition region; the terminal surface of the transition region is known as the *quitting surface*; its position may also be estimated (for formula, see [62, 63]).



The position of the Mach disc depends very much on the backing pressure  $p_b$  in the expansion chamber. This constraint imposes high requirements on the pumping-speed in the expansion chamber. If high-capacity pumps are not available ( $p_b > 0.1$  mbar), the Mach disc is closer to the nozzle than the quitting surface, and very unstable beams with high collision numbers and thus high propensity for internal scattering will be obtained; this nowadays unusual type of supersonic beams is known as the *Campargue-type*. The use of high capacity pumps such as oil diffusion or turbomolecular pumps is therefore highly recommended and results in very reliable setups (*Fenn-type*).

**Properties of Supersonic Beams.** The gas dynamic expansion forms a flow with low collision number; thus, supersonic beams with a low divergence angle and a relatively homogeneous intensity over their cross-section may be formed (see fig. 3.9), if small solid angles are cut out from the highly divergent flow in the zone of silence, which has a nearly cosine angular distribution, by means of a skimmer and apertures. The intensities of supersonic beams are still high compared to effusive beams. Nevertheless, these two advantages of supersonic beams are often outbalanced by their disadvantages; the setups consume big amounts of gas in the expansion chamber (only a few percents of the gas pass the skimmer orifice), which makes their application very expensive for rare (esp. isotopically enriched) gases. Additionally, since big amounts of gases need to be pumped-off in the expansion chamber, high demands on pumping capacity increase the setup costs. Furthermore, it is difficult to change the beam intensity of supersonic beams<sup>5</sup>. Finally, because the pressure in the stagnation stage has to be in the range of atmospheric pressure, supersonic beams of substances with low saturation vapour pressure can only be formed by saturating a flow of a carrier gas, which may further shift the energy distribution of the beam and accelerate the particles.

For some experiments, the shift of the energy distribution towards higher values may be undesirable; however, this possible problem has turned out to be of no influence for surface kinetics experiments such as the ones described in this work, because the adsorbates thermalize very quickly on the surface, thereby losing their excess energy.

---

<sup>5</sup>One possibility for intensity adjustment in supersonic beams is to dilute the reactant in a carrier gas; another possibility – which is also used in the setup applied in this work – makes use of a mechanical chopper, which cuts the continuous beam into very short pulses to reduce the *average* beam flux to the sample.

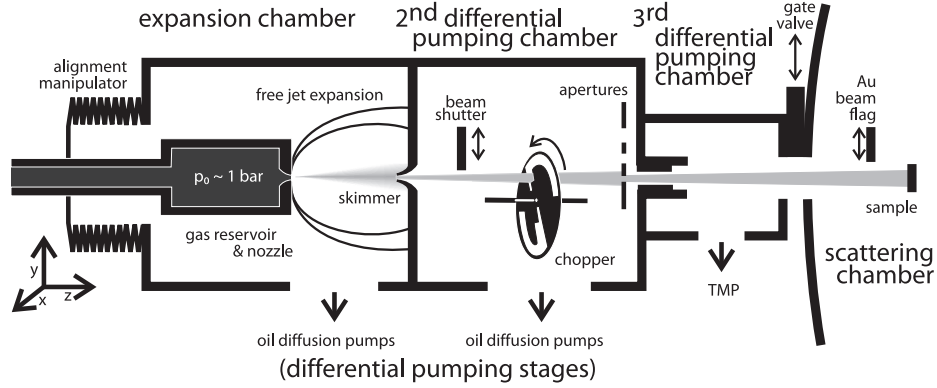


Figure 3.7: The setup of the supersonic beam used in this study (Fenn-type).

**The Setup.** The supersonic beam used in the described setup is a Fenn-type beam and comprises three differential pumping stages (see fig. 3.7); the expansion chamber and the second pumping stage are both pumped by oil diffusion pumps (expansion chamber: Edwards Diffstak 250/2000, 2000 L/s; second pumping stage: Edwards Diffstak CR 160/700, 700 L/s; pumping-oil: Santovac 5), and the third pumping stage is pumped by a turbomolecular pump (Pfeiffer, 50 L/s).

For all experiments described here, a solenoid-driven pulsed nozzle valve with an orifice diameter of  $100 \mu\text{m}$  was used (General Valve, Series 9) and driven by a dedicated pulse controller (General Valve, Iota One) to achieve a minimum pulse width of  $\approx 160 \mu\text{s}$ . A supersonic beam is stripped off from the expansion by means of a conical skimmer ( $0.7 \text{ mm}$  orifice). The beam is modified in the second pumping stage by means of a motor-driven beam shutter (steel flag); additionally, the continuous beam may be cut into short pulses by means of a motor driven, frequency-controlled chopper wheel (up to 200 Hz; 50 Hz used in all experiments described here), which was machined from an aluminum disc; this chopper offers duty cycles of 50, 3.3 and 1.5 %, and a light barrier (which produces TTL-signal) inside the chopper can be used to synchronize kinetic and dynamic measurements with respect to the chopper opening period; the minimum pulse length formed in the chopper is below 1 ms, which is below the time resolution of the detection setup. In effect, the chopper can be used in experiments to vary the average beam intensity.

The beam profile on the sample can be varied by the choice of one out of three different square metal frame apertures in the second pumping stage; due to the beam's inclination angle, the beam profile on the sample is rectangular with an axial ratio of 1.2; using these apertures, the longer edge of the beam profile can be chosen to be 7.6, 11.0 or 14.3 mm, respectively.

At the end of the beam path, a gold beam flag inside the scattering chamber right before the sample can be used to block the beam from the sample; this beam flag can be opened and closed from the air side by a computer controlled electronic stepper motor; it is a crucial component for sticking coefficient measurements.

### Effusive Beams

When a gas is allowed to expand through an orifice *smaller* than the average mean free path of the gas molecules (*i.e.*, at high *Knudsen* numbers), there will be virtually no particle-particle collisions in the source exit. Under such conditions, the particles that enter the exit will simply move on out of the reservoir instead of being reflected by a (missing) wall; thus, they will leave the reservoir and retain the equilibrium dynamic properties (velocity, angular and energy distribution) of the particles in the reservoir. This process is called *effusion*, and the flow behind the exit is known as *Knudsen* flow. Note that – unlike the case of gas dynamic expansion –, the gas particles in the source are not forced to expand into the vacuum by collision, but only the molecules with momenta into the exit direction can leave the source into the flow direction; thus, the molecules in the effusion flow retain the equilibrium thermodynamic properties of the free gas inside the source, and no shift of the Maxwell-Boltzmann-distribution occurs. For a perfect hole (infinite ratio  $\beta = d/l$  of diameter  $d$  and length  $l$  of the hole), the angular distribution of the effusing gas would be perfectly cosine (see fig. 3.6 b).

**Tubular Exits.** If the length  $l$  of the expansion orifice is increased, so that it gets tubular, an additional effect comes into play that strongly influences the angular distribution of the effusing particles: the tube walls are rough, and there is a finite probability that the gas particles that enter the tube in high inclination angles will be reflected back into the source during their collisions with the tube walls. If the tube is infinitely long, only those particles that enter the tube in axial direction do not strike the walls and will exit the tube on the low pressure side; this effect is usually referred to as the *tube focussing effect*. Generally speaking for finite tubes, this effect leaves the effusion's forward intensity untouched while removing most of the particles that enter the source tube off-angle from the centerline. The beam directionality is commonly denoted in terms of the *peaking factor*  $\kappa$ , which is the ratio of intensity  $I_0$  per unit area (steradian) in the forward direction (centerline intensity), and the total flow rate  $\dot{N}_0$  out of the source:  $\kappa = \pi I_0 / \dot{N}_0$ . For a tubular source, the peaking factor depends on the diameter-to-length ratio  $\beta$  of the tube as:  $\kappa = 3/4 \cdot \frac{l}{d} = 3/(4\beta)$ . In conventional sources,  $\beta$  is in the

range of 10 to 100; in the setup used for this study, it is 40, which results in a peaking factor of 15; compared to free jet expansions (peaking factors between 1.1 and 2), effusive beam formation imposes much smaller requirements on the pumping speed, and higher fractions of the expanding gas are actually transferred into the beam.

**Multichannel-Arrays.** Despite the strong centerline directionalization in tubular effusive sources, the flux in the effusion is orders of magnitudes lower than in a conventional supersonic beam due to the low source pressure. To reach beam intensities comparable with supersonic beams, an array of parallel tubes (*multichannel array*) is often used; all of these tubes build up their own strongly peaked effusion cone, which add up to form a much wider, more intense and very uniform flow field. A multichannel array (glass capillary array, GCA) is also used in this setup.

**Intensity Adjustment of Effusive Beams.** An essential feature of effusive beams is that their intensity depends linearly on the source pressure as long as the particle-particle collision number in the tube is low; this is usually expressed by means of the *channel Knudsen* number  $Kn_c = \lambda/l$ ; good effusive beams are obtained when the channel *Knudsen* number  $Kn_c$  is greater than the tube's length-to-diameter ratio  $\beta$ .

**Properties of Effusive Beams.** In summary, effusive sources form a comparably uncomplicated setup to form molecular beams of thermal energy distribution. The gas loss by the differential pumping stages is much smaller in effusive beam sources than in supersonic beams; thus, effusive beams are well suited to dose expensive gases, such as isotopes. Additionally, they need only a very low pressure in the reservoir, which extend their application to substances of low volatility. Effusive beams allow to easily vary the flux density in the beam by several orders of magnitude, and beams based on tube array sources can reach intensities that exceed the ones of typical supersonic beams. Their drawback is a high divergence angle compared to supersonic beams (see fig. 3.9), which results in a broader beam profile; therefore, the beam size was chosen to be much larger than the sample to ensure a homogeneous beam intensity over the entire sample.

**The Setup** The setup incorporates two effusive beam sources of identical construction, see fig. 3.8. Each of them contains two differential pumping stages evacuated by turbomolecular pumps (TMU520U, Pfeiffer); the first (inner) pumping stage is enclosed in the second (outer) pumping stage and

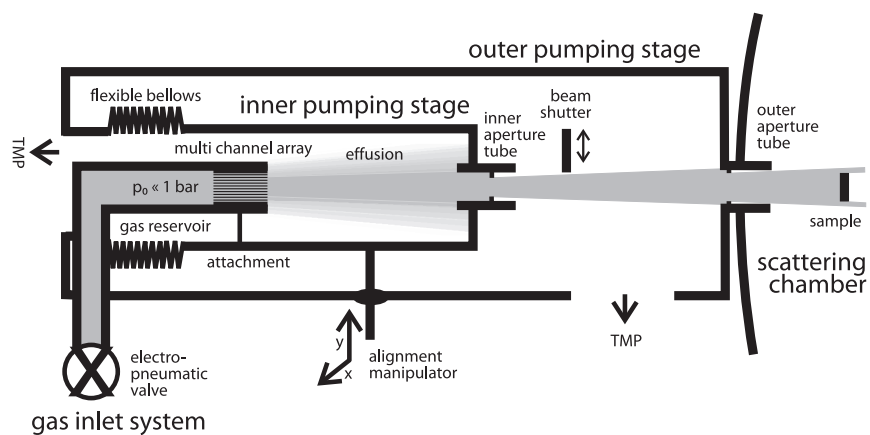


Figure 3.8: The setup of the effusive beams (both beams have identical construction).

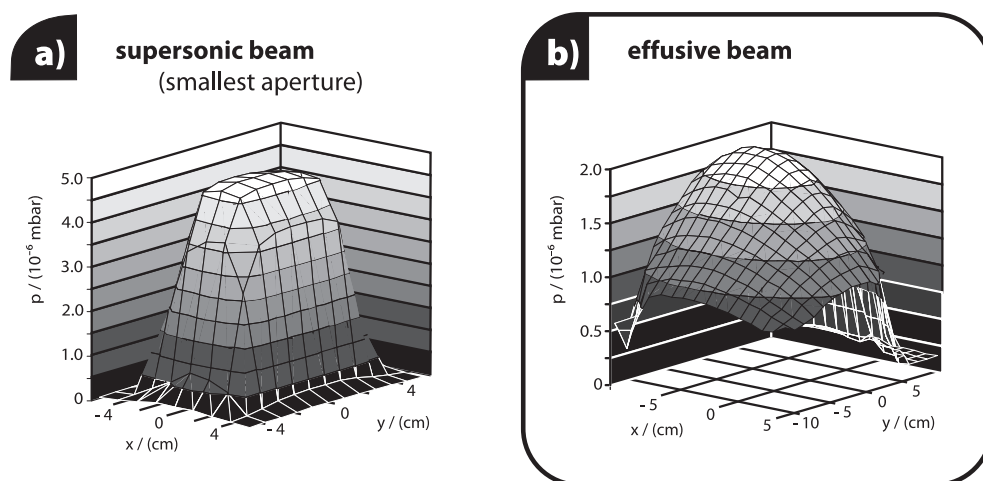


Figure 3.9: The beam profiles of a) the supersonic beam with the smallest aperture (7.6 x 6.3 mm) and b) the effusive beams.

contains the narrow gas reservoir tube that ends in a glass capillary array (Galileo, 50  $\mu\text{m}$  channel diameter, 1 mm length). The gas supply to the reservoir tube can be interrupted for beam modulation by an electropneumatic valve (EPN), and the reservoir pressure usually collapses within milliseconds due to the tube's small volume. The gas pressure admitted to the reservoir is controlled by a *gas inlet system* with a two-channel pressure regulation stage consisting of an upstream flow controller, a capacitance manometer and a bypass flow valve to minimize the controller's response time and pressure fluctuations. Stable effusion can be obtained with reservoir pressures between 0.001 and approx. 0.2 mbar (the upper limit is set by the *Knudsen* number).

The second differential pumping stage contains a mechanical beam shutter for beam modulation, which is driven by a UHV-motor (AML, B14.1; max. modulation frequency of 10 Hz). The beam enters the scattering chamber from the second pumping stage through an outer aperture tube, which ends close to the sample's surface. The beam alignment with respect to the sample can be adjusted by the inner pumping stage of the beam, which can be moved, together with the gas reservoir, with respect to the outer pumping stage by means of translation feedthroughs in  $x$ - and  $y$ -direction.

To allow a computer control of the beam modulation elements, both the electropneumatic valves and the beam shutters can be controlled by TTL signals. The reservoir pressure set by the gas inlet system can be controlled by the computer *via* an analog signal.

## Beam Monitor

For precise measurements of the beam pressure and intensity<sup>6</sup>, a tube with a small orifice of  $\varnothing$  1 mm (see fig. 3.10) can be used that acts as an accumulation detector; the molecular beam hits this tube and enters through the orifice, and the pressure in the tube rises until the beam flux into and out of the tube have reached equilibrium. Under these conditions, the pressure  $p_{\text{bm}}$  in the beam monitor and the dynamic pressure  $q$  of the beam are identical and can be measured with a pressure gauge inside the accumulation detector (the setup contains a Granville Phillips Stabillon 360 accuracy ion gauge calibrated for nitrogen as a reference gas). If strongly adsorbing gases are used in the beam, the pressure inside the accumulation detector will rise only very slowly due to gas adsorption on the tube's inner walls. Thus, the beam monitor is usually only used to measure the beam pressure with noble gas

---

<sup>6</sup>The beam intensity  $Z$  (in molecules/ $\text{cm}^2 \cdot \text{s}$ ) can be calculated from the beam pressure  $p$  using the kinetic gas theory:  $Z = p/\sqrt{2\pi mk_{\text{B}}T}$  with the mass of the gas particles  $m$  and the gas temperature  $T$ .

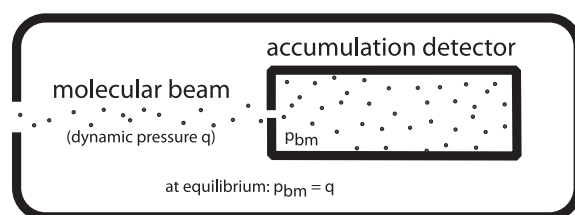


Figure 3.10: Principle of the beam monitor (accumulation detector).

beams, and other beam intensities are calibrated relative to noble gas beam intensities using the different pressures introduced by the different beams into the main chamber.

The beam monitor can be moved across the beam's cross section to measure the beam profile; fig. 3.9 displays measured beam profiles of the supersonic beam (with the smallest aperture, 7.6 x 6.3 mm) and the effusive beam with argon. The beam monitor can be exactly positioned at the sample position to allow an alignment of the beams with respect to the sample.

### Advantages of Molecular Beam Methods

Molecular beam setups have many advantages for the study of dynamic and kinetic processes on surfaces:

1. They allow to keep low background pressures to reduce the probability of uncontrolled collisions with these gases, and at the same time, they allow to reach a comparably high dynamic gas pressure of reactants in the beam. This potential is due to the high directionality of the beams and the high pumping capacity of the scattering chamber, which means that practically all gas particles in the molecular beam will hit the surface and then be pumped away very quickly if they do not stick to the sample's surface; in fact, the pressure ratio between the dynamic pressure on the sample and the pressure in the background is typically between 100 and 1000.
2. The fulfillment of the first point guarantees that all particles in the beam will hit the sample surface once and only once; this is usually termed *single scattering conditions*. This unique dynamic advantage allows us to directly infer sticking or reaction probabilities for each molecule from measurements of the chamber's background partial pressures.
3. An important prerequisite for kinetic experiments is the ability to exactly quantify and control the *flux* of reactant molecules on the sample

surface. Molecular beams (in combination with intensity detectors such as the described beam monitor) offer this possibility.

4. Molecular beams offer a superior time control of the reactant flux on the surface; the beams can be shut off within milliseconds by means of beam flags within the beams differential pumping stages. This allows to study transient kinetics with very high time resolution in addition to steady-state kinetics under continuous beam flux.

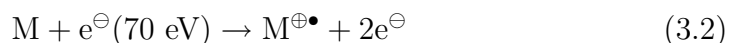
### 3.3 Detection Techniques

#### 3.3.1 Gas Phase Detection (Mass Spectrometry)

Mass spectrometry is one of the classical methods for the detection of chemical species in the gas phase, and it is widely applied in nearly all fields of chemistry, from isotope discrimination over chemical structure elucidation to analysis. Its outstanding feature is its high sensitivity even for species of low concentration in a complex mixture, as long as that species has a characteristic mass feature. One such examples is the detection of explosives in passenger luggage at the airport or of fire propellants at criminal analysis laboratories, because such compounds typically contain nitro groups that show up characteristically in the mass spectra of samples from those places.

The working principle of mass spectrometry is based on a separation of ions obtained from a mixture of species according to their individual mass-to-charge ratios  $m/z$  by their different motions in electrical fields. The separated ions are then detected and intensity-counted in an ion detector, and the detection count is typically proportional to the concentration of the detected species in the analyzed gas mixture; thus, mass spectrometry is a quantitative technique. The typical output data of a mass spectrometer is a plot of counting rate of the detector *versus* mass-to-charge ratio  $m/z$ ; this is termed a *mass spectrum* (or *mass profile*).

All mass spectrometers comprise at least four components (see fig. 3.11, which depicts the special case of a quadrupole mass spectrometer (QMS)). The first stage is an ion source; in most instruments, cations are formed by impact of high-energy electrons on the analyzed gas (*electron-impact ion source*) according to the following formula:



M denotes the molecule and  $M^{\oplus\bullet}$  denotes the molecule's (radical) cation. Because most substances show a maximum of their EI-ionization cross-section



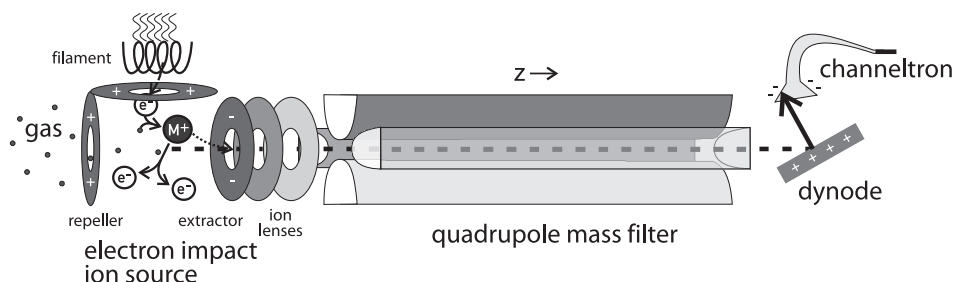
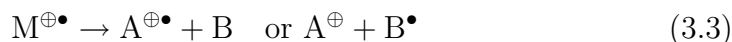


Figure 3.11: The setup of a QMS mass spectrometer.

close to an electron energy of 70 eV, most mass spectra are taken with this ionization potential; still, since the ionization cross sections differs between different substances, their mass spectrometric signals cannot be directly interpreted as the abundance of the respective species in the ion source, although it is often taken as an estimation. Formation of doubly charged cations is also possible by impact of high energy electrons, but for most substances it is less probable under the standard ionization potential; thus, the mass spectrum (signal *vs.* mass-to-charge-ratio) is usually interpreted as a signal-*vs.*-mass plot, and it is common to speak of *mass* for simplicity instead of *mass-to-charge-ratio*, when formation of multiply charged ions does not occur or is irrelevant in a certain experiment.

The relatively high energy of the electrons in the ionizer has another important implication: the cations formed in EI sources contain a relevant amount of excess energy and may undergo scission into smaller fragments to relax:



Those processes are relatively probably, and very often the mass spectrum of a substance contains many different peaks; in fact, this *fragmentation pattern* is one of the most important informations of a mass spectrum for substance identification.

The second component of a mass spectrometer setup, directly behind the ion source, is a combination of accelerating and focussing ion lenses that drive the ions into the continuously working mass filter, which constitutes the third component of any mass spectrometer. The mass filter allows only ions of a desired mass-to-charge ratio to exit and hit the last component of the mass spectrometer: the detector. The working principle of the mass filter will be described in the following section. The simplest setup for a detector would be a discharge electrode for the cations such as a *Faraday cup*; in most cases, however, more advanced detectors with significantly increased sensitivity are used, which even allow to count single ions. A typical ion-

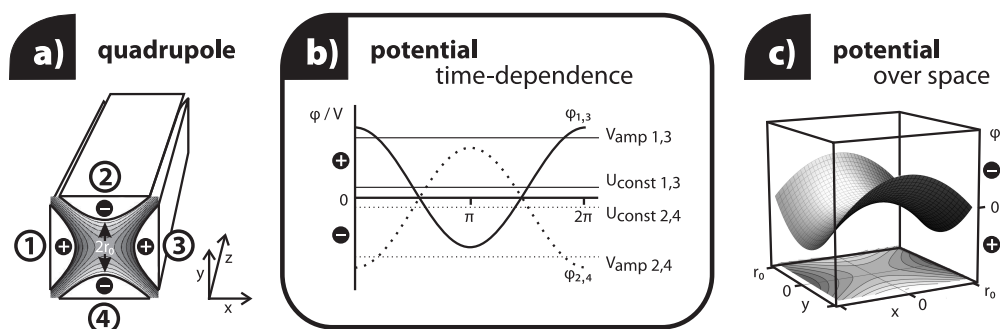


Figure 3.12: The principle of quadrupole mass spectrometry.

counting device is the channel-electron multiplier (*channeltron*, depicted in fig. 3.11); incoming ions are strongly accelerated onto a cathodic surface at the entrance of this device, and their impact onto the cathodic surfaces may release several electrons after the strong acceleration; the emitted electrons are deflected into the device by a potential that gradually increases over the channeltron surface; the impact of those electrons on the surface emits further electrons, leading to a strong amplification of the electrons towards the device's exit electrode, where a strong current pulse is detected for every incoming ion.

As an optional fifth component, many mass spectrometers contain a deflecting electrode (*dynode*) that is used to tune the flux of incoming ions on the detector entrance at wish and prevent detector overload.

Different setup types of continuous mass filters are known; the most common ones are sector field and quadrupole mass filters; they have different advantages: sector fields easily achieve much higher mass resolutions than quadrupoles and are capable to filter very heavy ions, but their disadvantage is their big size – which complicates pumping –, and the slow change of the permitted mass. Quadrupoles are usually capable of fast switching between mass ranges, so that they allow to follow many masses nearly continuously with high time resolution; other advantages of quadrupoles are their small sizes, their low prices and the fact that they are easy to pump. Their disadvantage is a principally lower mass-resolution compared to sector field instruments; for the purpose of this work, however, the mass resolution of the quadrupole does not constitute a considerable problem, and a quadrupole mass filter is clearly the preferred device.

## Working Principle of Quadrupole Mass Spectrometers

The application of alternating quadrupole fields for mass selection and filtering has originally been suggested by Wolfgang Paul and his coworkers from the university of Bonn in 1953 [64]. The first working instruments were described in 1955 [65] and 1958 [66], and since then the technique has become increasingly popular. Good literature is available describing the details [67], and only the essence is described here:

Briefly, those instruments accelerate the ions by an alternating quadrupole field in the  $x$ - and  $y$ -plane during their passage in  $z$ -direction (see fig. 3.12), and thus force them into a complicated oscillatory path which is instable for any ion except for the ones of the desired mass; the ions with instable paths exit the quadrupole transversely or hit its electrodes, and the desired ions leave the quadrupole regularly on the exit side.

The quadrupole field is established such that at any time, opposing electrodes of the quadrupole are on the same electrical potential, and their neighboring two opposing electrodes are on a potential with the same value, but with opposite polarity; this generates a saddle potential in the room between the electrodes with zero potential at the center (cross section with the quadrupole's central axis; see fig. 3.12 c). This potential is varied over time by an AC driver with a radio frequency  $\omega$  (typically several megahertz). One pair of opposing electrodes (say: electrodes 1 and 3) has a constant positive offset potential, while the other two opposing electrodes (2 and 4) have a constant negative offset potential. Thus, the potential on the apex of the electrodes may be written as

$$\begin{aligned}\phi_{1,3} &= U_{\text{const}1,3} + V_{\text{amp}1,3} \cdot \cos(\omega t) \\ \phi_{2,4} &= U_{\text{const}2,4} + V_{\text{amp}2,4} \cdot \cos(\omega t) \\ \text{with } U_{\text{const}1,3} &= -U_{\text{const}2,4} \quad \text{and} \quad V_{\text{amp}1,3} = -V_{\text{amp}2,4}\end{aligned}$$

The mass filtering effect of this field is based on the fact that the AC component  $V_{\text{amp}}$  will more effectively accelerate light ions and drive them into oscillatory paths leading transversely out of the quadrupole, while the DC component  $U_{\text{const}}$  will more effectively accelerate the heavier ions and slowly deflect them towards a cathode. Only for the ions of one specified mass (or, more precisely, mass-to-charge ratio), the two effects cancel, and these ions will remain on a stable (though complex) path around the quadrupole's central axis and leave it on the exit side into the detector; consequently, the quadrupole is intransparent for ions of the wrong mass.

**The Mass Resolution** depends mainly on the ratio between  $U_{\text{const}}$  and  $V_{\text{amp}}$ . The selection of the transparent mass is accomplished by a change of the absolute values of  $U_{\text{const}}$  and  $V_{\text{amp}}$  together, while keeping their ratio constant. However, for heavier ions, the resolution at the same  $U_{\text{const}}$ -to- $V_{\text{amp}}$  ratio is always lower than for lighter ions; thus, in order to keep the mass resolution constant over the full range of a mass spectrum, the ratio between  $U_{\text{const}}$  and  $V_{\text{amp}}$  is slightly changed for the higher masses together with the absolute values of these voltages; the correlation between mass and  $U_{\text{const}}$ -to- $V_{\text{amp}}$  ratio is called the *working line* of the mass spectrometer; it needs to be optimized to guarantee a constant instrument resolution over the full mass range. The exact dependance of the resolution and the quadrupole's electrical parameters is described by stability diagrams, which can be found in [67, 66]. Although change of the mass transparency could also be accomplished by a change of the AC frequency  $\omega$ , practical instruments do not attempt this, since a change of radiofrequency is hard to control.

**The Quadrupole's Transparency and Mass-Filtering Abilities** are limited by many factors. Most of all, the limited length of practical quadrupoles still allows some of the undesired ions to pass. On the other hand, also many ions of the desired mass get lost in the quadrupole during their passage – *e.g.* because they enter the mass filter at bad angles (*entrance conditions*) and the alternating field cannot drive them into a stable path before they get lost on the surfaces of the electrodes or pass between them. Thus, practical quadrupole mass filters do still suffer from imperfections, and they will always let some of the undesired ions pass and exclude some of the desired ions. For practical applications, it is necessary to find an optimum between mass resolution and transparency for any experiment; in most cases, the mass resolution is tuned to exactly fulfill a minimum desired value (typically such that the signal intensity between adjacent peaks is below 10 % of the peak value); the mass resolution should not be increased too much in order not to sacrifice too much transparency (and thus sensitivity).

### **Advantage of Mass Spectrometry for Molecular Beam Studies on Surfaces**

The use of mass spectrometry as a detection technique in a molecular beam setup has many advantages; most importantly, mass spectrometers have an outstanding sensitivity for even very low partial pressures of reactants or products, thus allowing to detect even small amounts of side products. This qualifies them as a detection technique for nearly any kinetic study, and although molecular beam studies of surface reactions yield only very little

amounts of products with low concentration in a vacuum chamber of relatively high volume, quadrupole mass spectrometry has proven to even allow detection in those experiments. The disadvantage of mass spectra is that they reflect structural differences (such as conformational differences) only indirectly if at all. Although it is often possible to discriminate products with the same mass by their fragmentation pattern, such discriminations can get very involved or impossible in some cases. In some other cases, it may be impossible to observe the molecule ion, so that only fragment ions can be detected<sup>7</sup>, which may further complicate the data evaluation.

### **The Setups of the Angle-Integrating and the Angle-Resolving QMS**

**The Stationary QMS Mass Spectrometer** flange is connected to the scattering chamber non-line-of sight with the sample and acts as a residual gas analyzer of the chamber background gases, which contain both beam molecules and reaction products. The flange-mounted mass filter assembly from ABB Extrel (MEXM0064) comprises an axial electron impact ionizer, ion lens and quadrupole (stainless steel, circular rods), a dynode and channel electron detector which can be operated in single ion counting mode (*digital counting mode*). The flange is differentially pumped by a turbo-molecular pump (TMP, Pfeiffer TMU 260, 210 L/s). The quadrupole rods are supplied with the voltages by a resonator (ABB Extrel 150 QC, 2.9 MHz resonance frequency) capable to set the quadrupole transparent only for molecules with small masses between 1 and  $\approx 55$  amu, but with very high transparency (*sensitivity*); this mass spectrometer is very well suited to perform sticking-coefficient measurements or direct reaction rate measurements. The channeltron discharge signals are converted into rectangular voltage pulses by a discriminator/comparator, and then are counted by an acquisition processor (ABB Extrel, Merlin Data Acquisition Setup, Series 5500), which also controls the whole measurement and is connected to a PC. The acquisition processor additionally provides digital (TTL) and analog in- and outputs, which can be controlled by a macro programming language, thus providing an interface that is used to control pulse sequence molecular beam experiments (see section 3.4). The interface and user communication is operated by standard software (ABB Extrel Merlin Data System, version 3.0).

**The Angular-Resolved Quadrupole Mass Filter** (Hiden HAL 501/3F-PIC) is kept in a doubly differentially pumped (2 x TMP Pfeiffer TMU 260)

---

<sup>7</sup>One important example is  $\text{H}_2\text{O}_2$ , which completely decomposes to  $\text{H}_2\text{O}^{\oplus\bullet}$  on EI ionization.

housing attached to the rotatable bottom platform of the scattering chamber; the rotatable platform's bearing is sealed with a viton gasket and differentially pumped. Gas molecules from the sample surface can reach the QMS detector through a small orifice tube in the top of the housing (orifice on the same level as the sample, see fig. 3.3) and then enter a second housing linearly, which is differentially pumped to further reduce gas load; the full acceptance angle of the rotatable QMS setup through the aperture tube is approx.  $6^\circ$ . The ionizer can be further cryopumped by a nearby cryoshield to avoid gas accumulation in the detector. The setup also serves for sample alignment: a window is built into the backside of the first pumping stage opposing the aperture tube, building up a viewport that serves as a deliberately positioned alignment reference for the sample. This setup allows to align the sample in scattering position with a precision of approx.  $\pm 1$  mm.

### 3.3.2 Detection of Surface Adsorbates (Infrared Reflection-Absorption Spectroscopy)

Infrared absorption spectroscopy for molecular structure examinations is one of the most frequently applied spectroscopic techniques [68, 69, 70], and it also offers many advantages for the study of the interaction between adsorbates and surfaces [36, 71, 16]. Chemical substances can absorb infrared light<sup>8</sup> if the substance offers internal energy states between which a transition can be excited by dipolar interaction with the electric field of the IR light; this precondition is met by many transitions between vibrational states. The exact energy of the transition depends on the physical properties of the excited vibrational mode, and allows to conclude on the chemical identity of the substance (or parts of it); if the sample is an adsorbated molecule, the absorption frequency also contains information about the interaction between adsorbate and substrate.

**Spectral Intensities.** The rate  $W$  of a transition between two quantum states  $i$  (initial state) and  $f$  (final state with an energy difference  $E_{\text{fi}}$  to the initial state  $i$ ) induced by dipolar interaction with electromagnetic radiation of the energy  $E_{\text{fi}}$  can be approximated by *Fermi's Golden Rule* [72]:

$$W = 2\pi\hbar |V_{\text{fi}}|^2 \rho(E_{\text{fi}}) \quad (3.4)$$

---

<sup>8</sup>The range of infrared radiation is defined as 800 - 500000 nm (12500 - 20  $\text{cm}^{-1}$ ); it borders on the range of visible radiation, and is further split – referencing to the range of visible radiation – into near (NIR, 800 - 2500 nm), mid (MIR, 2500 - 50000 nm; 4000 - 200  $\text{cm}^{-1}$ ) and far (FIR, 50000 - 500000 nm) infrared. The experiments in this thesis concentrate on the MIR range.

with  $|V_{fi}|^2$  being the square modulus of the transition matrix element  $V_{fi} = \langle f|\hat{\mu}|i\rangle$  and  $\rho(E_{fi})$  the density of states at the transition frequency  $E_{fi}$ . This transition rate is connected with the *Beer-Lambert* law (and thus the spectral intensities) over the *Einstein* coefficient of absorption; consequently, an understanding of the transition dipole moment allows to understand the gross selection rule of IR spectroscopy:

**The Gross Selection Rule of IR Vibrational Spectroscopy.** The transition dipole moment of a vibrational excitation  $v' \leftarrow v$  between vibrational states with quantum numbers  $v$  and  $v'$  within an electronic state with quantum number  $\varepsilon$  is:  $\mu = \langle \varepsilon, v' | \hat{\mu} | \varepsilon, v \rangle$ ; in this formula,  $\hat{\mu}$  denotes the dipole moment operator  $\hat{\mu} = R \cdot \delta q$  (with the bond length  $R$  and the magnitudes of the oscillating partial charges  $\delta q$ ) [72, 68, 73].

This formula will be shortly inspected for a diatomic molecule: During vibrations, the charged nuclei change their distances around the equilibrium positions. This motion of positive charges causes an adaption of the electron density; thus, the electronic wavefunction also changes during the vibration. However, because the electrons are so much lighter and faster than the nuclei, they can be assumed to adjust quickly to nuclear displacements (*Born-Oppenheimer* approximation), so that the electron motion can be separated from the nuclear motion, and the expression for the transition moment simplifies to  $\mu = \langle v' | \hat{\mu} | v \rangle$ . For small displacements, the dipole moment may be assumed to change linearly with displacement:  $\mu = R \cdot \delta q = (R_e + x) \cdot \delta q \equiv \mu_0 + x \cdot \delta q$  (with the equilibrium bond length  $R_e$  and the displacement  $x$ ). Thus, the expectation value for the transition dipole moment can be written as:  $\mu = \langle v' | \hat{\mu} | v \rangle = \mu_0 \langle v' | v \rangle + \langle v' | x | v \rangle \cdot \delta q$ . Since vibrational wave functions with different  $v$  are orthogonal, the integral  $\langle v' | v \rangle$  vanishes (is zero), and the formula for the transition dipole moment of the molecule simplifies further to  $\mu = \langle v' | x | v \rangle \cdot \delta q$ , demonstrating that the transition dipole moment depends only on the quantity  $\delta q = d\mu/dx$  within this linear approximation. This allows the conclusion that the transition dipole moment is zero and the vibration can not be excited by IR light, unless the dipole moment varies with the vibrational displacement.

**Group-Theoretical Description for Fundamental Transitions.** Under normal conditions, most molecules are in their vibrational ground state ( $v = 0$ ). The fundamental vibrational transition is from the ground state to the first excited state ( $1 \leftarrow 0$ ); higher excitations (*overtones*) are only allowed by *anharmonicity* of the vibrational potential, and only possess a negligible transition dipole moment in most cases.

The transition dipole moment of the fundamental transition has a component in  $x$ -direction of:  $\mu_x = \langle 1 | \hat{\mu}_x | 0 \rangle = -e \int \Psi_1^* x \Psi_0 d\tau$  (with the electron's elementary charge  $-e$ ); similar expressions hold for the other two spatial directions  $y$  and  $z$  [73]. The vibrational wave functions are *Hermitian* polynomials and possess simple symmetry properties: the ground state vibrational wave function is of the form  $e^{-x^2}$  (and symmetrical in  $x$ ); thus, the product  $x \cdot \Psi_0$  is *antisymmetric* in  $x$ . Then, to yield a nonvanishing integral  $\int \Psi_1^* x \Psi_0 d\tau$  in  $x$ -direction, the wave function  $\Psi_1$  needs to be proportional to  $x$ ; this will be the case if the vibrational mode has the same symmetry species as the translation mode  $x$  is  $x$ -direction (as compiled in the group table). The full vibrational mode (in all three spatial directions) will be IR-active if at least one of the three components of its transition dipole moment in the three directions  $x$ ,  $y$  and  $z$  is non-vanishing; this condition can be expressed according to the above treatment as a selection rule: **If the symmetry species of a vibrational (normal) mode is the same as any of the symmetry species of the translations in  $x$ ,  $y$  or  $z$ -direction, then the mode is infrared active.** [74]

**Polyatomic Molecules.** Molecules with more than one bond have several vibrational modes<sup>9</sup>. In this case, the potential energy of the molecule can be expressed as a function of all atomic coordinates in the form of internal coordinates called *normal coordinates*<sup>10</sup>  $Q$ . The vibrational modes are linear combinations of these normal coordinates called *normal modes*; they can be constructed by a lengthy procedure called *normal coordinate analysis* [74, 75, 76]. The decision whether or not one of these normal modes is IR active can then be conducted in the same way as demonstrated above for the case of a vibration in a diatomic molecule.

### Principle of IRAS

Conventional infrared spectroscopy is most often done in transmission mode; this means that the sample (*e.g.* a gas or a fine powder) is penetrated by the IR light. The thick metal substrates used in this study reflect the IR light instead of transmitting it and do not allow a study in transmission mode; in this case, infrared spectroscopy has to be performed in reflection mode [77], see fig. 3.13: the light is directed onto the sample's surface where it gets reflected; during its reflection on the metal surface, the light can

<sup>9</sup>Linear molecules have  $3N - 5$  vibrational modes and non-linear molecules  $3N - 6$  ( $N$  is the number of atoms in the molecule).

<sup>10</sup>The normal coordinates  $Q$  replace the bond length (atom distance)  $R$  used above in the treatment of a vibration in a diatomic molecule.



interact with the adsorbates and get absorbed. The reflected intensity is then collected, spectrometrically analyzed and compared to a reference spectrum taken without adsorbates (see fig. 3.14). This mode of IR spectroscopy is termed *Infrared Reflection Absorption Spectroscopy* (IRAS or IRRAS; sometimes also: Reflection-Absorption Infrared Spectroscopy, RAIRS). For IRAS, the sample is usually kept under ultrahigh vacuum, and the IR source and detector are positioned outside the UHV chamber. The IR light has to be coupled into and out of the sample chamber through IR-transparent windows made of potassium bromide (KBr, transparent above  $\approx 800\text{ cm}^{-1}$ ).

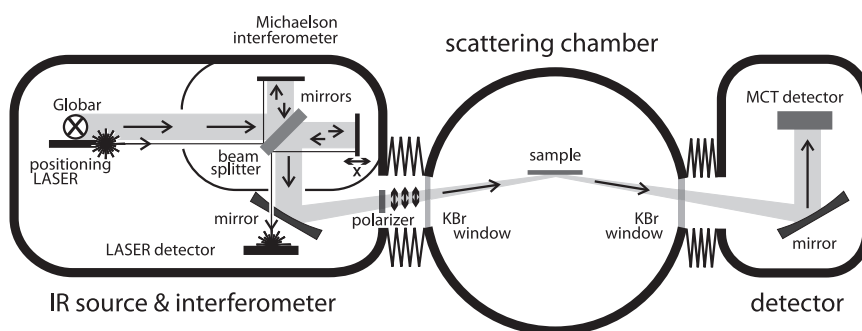


Figure 3.13: The principle of IRAS spectroscopy.

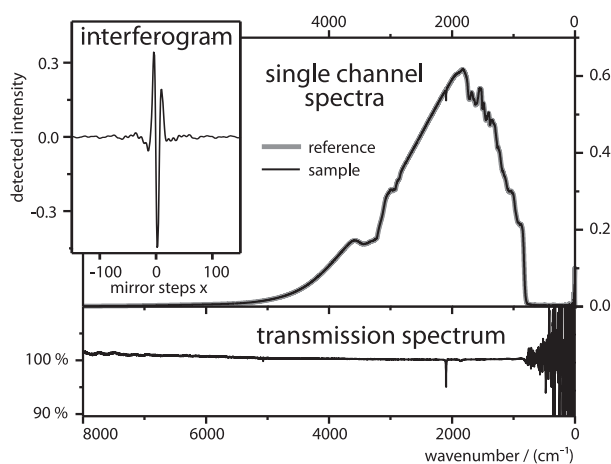


Figure 3.14: The calculation of IRAS spectra (example: CO on clean Pt(111),  $\approx 115\text{ K}$ ).

The intensity of the IR light is not homogeneous over the spectral range due to absorptions in the beam path and KBr windows before and after the sample and the peculiarities of the IR source (a Globar in the case of this work). In order to discriminate these effects from absorptions by the sample,

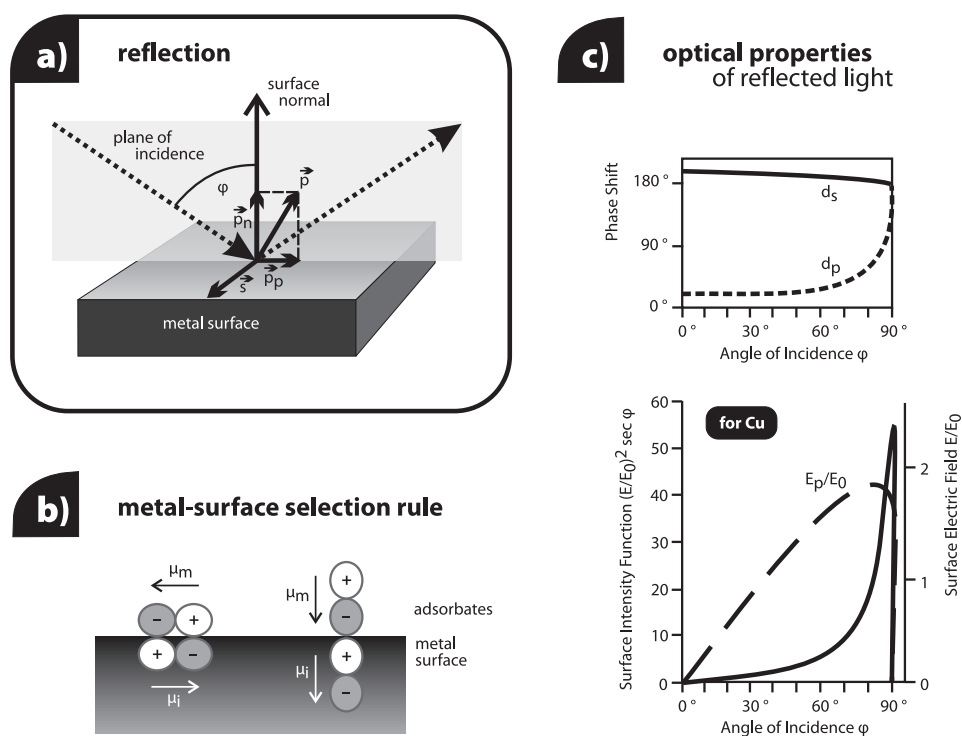


Figure 3.15: Physical foundations of IRAS spectroscopy, after [36].

a reference measurement with zero absorption in the sample compartment needs to be taken directly before the IR experiment. Fig. 3.14 shows the single channel spectra of the reference and sample (CO on Pt(111)); it underlines the necessity of reference experiments for the case of IRAS, since the absorptions caused by the sample (around  $2000 \text{ cm}^{-1}$  in the example) are extremely small compared to the intensity variations of the source over the MIR range. Thus, for presentations of IRAS experiments, the ratio between the two single channel spectra is plotted; this is termed a *transmission* spectrum (see fig. 3.14). The example demonstrates that typical IRAS absorptions lie in the range of a few percent and often below, because the absorber in IRAS is only a thin layer of adsorbates: IRAS has to detect very little amounts of substance compared to conventional transmission-mode spectroscopy.

**Fourier-Transform IRAS spectroscopy:** The low amount of absorber substance requires relatively long acquisition times in order to obtain a reasonable signal-to-noise ratio; to facilitate this, IRAS is usually performed using *Fourier-Transform* instruments (FT-IRAS) instead of dispersion-type

instruments. The principles<sup>11</sup> of *Fourier* transform spectroscopy will not be discussed here, but it shall be emphasized that *Fourier* transform spectroscopy offers many advantages over conventional spectroscopy in dispersive instruments known as the *Fellgett*<sup>12</sup>-, *Jacquinot*<sup>13</sup>- and *Connes*<sup>14</sup>-advantages (see [70]).

**Peculiarities of Light Reflections on Metal Surfaces.** The dependency of IRAS spectroscopy on IR light reflection on the metal surface has several severe implications for the interaction of light with the adsorbates [36, 71]. Fig. 3.15 a) depicts the reflection process: the IR-light strikes the surface under an angle  $\phi$  and gets reflected. The plane between the surface normal and the projection of the light beam on the surface is the *plane of incidence*. The IR beam's polarization is usually decomposed in reference to the plane of incidence into the component  $\vec{p}$  parallel and the component  $\vec{s}$  normal to it (s from German *senkrecht* = perpendicular); the parallel component  $\vec{p}$  is further decomposed into the component parallel to the surface,  $\vec{p}_p$ , and normal to it,  $\vec{p}_n$ ; of these two, only the latter is discussed in the following (the contribution from  $\vec{p}_p$  is small under grazing incidence and behaves like the perpendicular component  $\vec{s}$ ). The two components  $\vec{s}$  and  $\vec{p}_n$  experience very different phase shifts during their interaction with the surface (see fig. 3.15 c): the perpendicular component  $\vec{s}$  experiences a phase shift of nearly 180° under all angles, and the parallel component  $\vec{p}_n$  shows a very

---

<sup>11</sup>Briefly, in *Fourier* transform spectroscopy the full range of wavelengths interacts with the sample at the same time, and the dispersion analysis is conducted with the interference pattern caused by the mirror movement in a *Michaelson* interferometer; the full spectral information (transmitted intensity *vs.* wavelength) is contained in the interferogram (transmitted intensity *vs.* path difference in the Michaelson interferometer), and can be obtained from the interferogram by a mathematical procedure known as *inverse Fourier transform* (see fig. 3.14). Under certain precautions, the result of this procedure is identical to conventional spectroscopy.

<sup>12</sup>The *multiplex*- or *Fellgett*-advantage denotes the big time saving in *Fourier* transform spectroscopy as compared to conventional spectroscopy facilitated by the simultaneous recording of all wavelengths (the dispersive information in an FT spectrum comes from the interferogram obtained during the mirror movement; this can be performed much faster than the monochromator adjustment in a conventional spectrometer).

<sup>13</sup>The *Jacquinot*-advantage: the recording time for an FT-spectrum is much shorter compared to a conventional spectrum because it is recorded with a light beam of larger cross section. In an FT spectrometer, the whole source radiation can strike the sample; in conventional spectrometers the light has to be monochromatized, with the resolution depending on gratings and slits; thus, for a high resolution conventional spectrum, only very narrow light beams hit the sample at any time.

<sup>14</sup>The *Connes*-advantage: The wavelength in the result spectrum can be very precisely calculated based on the mirror displacement, which in turn can be very precisely measured based on the interference maxima of a reference HeNe-LASER beam, whose wavelength is very well known.

strong dependence of the phase shift on the incidence angle, with the phase shift ranging from nearly 0 up to  $180^\circ$ . This phase shift has a very important implication for IRAS: owing to its long wavelength, the interference length of IR radiation is very long compared to the interaction region between the light and the molecules. When incoming and reflected wave have a phase shift of  $180^\circ$ , these two waves will interfere destructively in the region of the surface, and the light intensity in that region is close to zero, resulting in low interaction with the adsorbates. Thus, the only component that could excite vibrations in adsorbates on the surface is the  $\vec{p}_n$  component (under certain angles); detailed calculations of the surface electric field for this component using Fresnel's equations (see fig. 3.15 c) and [36]) yield that the effective field on the surface is highest for angles around  $83^\circ$ ; for this reason, IRAS is usually done under grazing incidence using only  $\vec{p}$ -polarized IR radiation.

**Adsorbed Molecules and the Metal-Surface Selection Rule.** For IRAS-spectroscopy, it is not enough to consider the vibrations of the adsorbed molecule as an isolated species, because the oscillating dipoles associated with the adsorbate vibrations induce image-dipoles in the electron distribution within the metal substrate (see fig. 3.15 b). This image dipole and the dipole in the molecule interfere either constructively (if the dipole moment of the molecule stands perpendicular on the surface) or destructively (molecular dipole moment parallel to the surface, see fig. 3.15 b). Thus, even if a normal mode of a molecule possesses a high transition dipole moment, the vibration mode may still be unobservable in IRAS spectroscopy of the adsorbed molecule if the dipole moment of the molecule lies parallel to the surface.

Actually, two effects add up for vibrations with dynamic dipole moments parallel to the surface, which both obstruct their IRAS spectroscopic detection. The first of those reasons is that such dipoles could only be excited by interaction with  $\vec{s}$ -polarized light, but it was shown above that such light has only very low field strength on the surface due to the reflection process (and is therefore usually filtered out anyway in the source to reduce gas-phase contributions to the spectrum). The second obstacle is the deletion of the dipole moment of vibrations parallel to the surface due to interaction with their antiparallel image dipoles in the metal substrate. These two effects together lead to a very efficient reduction of spectral intensity of vibrations with dipole moments parallel to the surface, and are known as the *metal-surface selection rule* (MSSR).

The MSSR has further important implications: for vibrations that change the molecular dipole moment in a direction that is not exactly parallel nor perpendicular to the surface, only the component perpendicular to the surface

can interact with IR radiation on the surface and absorb energy; thus, the IR-intensity of different vibrational modes may considerably differ from the gas phase spectra. This fact has an implication for (model) catalysts: the side facets of model catalysts usually have a high inclination angle with respect to the metal substrate; thus, for molecules adsorbed on these facets, the components of their dipole moment perpendicular to the metal substrate may differ considerable from the molecules adsorbed on the top facet. This leads to different intensity contributions of the same molecule when it is adsorbed on the top or the side facets.

### Surface-Related Effects on Adsorbate Spectra

The molecule-substrate interaction creates new vibrational modes<sup>15</sup> of which some are IR-active. The loss of rotational fine structure and the coupling with surface modes leads to considerable line broadening of the IR peaks.

The interaction of adsorbed molecules with the substrate surface does also lead to frequency shifts in the internal modes of the adsorbed molecule with respect to their gas-phase values: a considerable shift to higher energies is due to *mechanical renormalization* by the formation of a bond to the substrate – which is a very heavy body; this is known as the *wall effect*. Additionally, the formation of the new bond does also change the electronic structure and thus bond strengths of the internal bonds in the adsorbed molecule (*chemical or electrostatic effect*). The extent of this shift depends very much on the bond strength and possibly also the adsorption site, and allows to use adsorbed molecules as *surface probes*; this work will apply carbon monoxide (CO) in this way. In addition to the mechanical renormalization and chemical shift, another type of interaction occurs with the image dipole, which changes the electrical field at the adsorbed molecule and gives rise to a red shift of the absorption frequency; this is typically termed *coupling with the image dipole* or *polarization effect*.

A second group of frequency shifts is caused by the interaction between adjacent adsorbates; these effects increase in magnitude with increasing surface coverage. The oscillating dipoles of adjacent molecules can interact directly or mediated by image dipoles in the substrate; such a *dipole coupling* leads to blue shifts of the frequencies. Additionally, the proximity of a coadsorbate can have an influence on the *chemical or electrostatic shift* that an adsorbed molecule experiences, due to a change of the electronic structure of the substrate by the close-by coadsorbate [36].

---

<sup>15</sup>Note that the adsorption of a molecule eliminates its translational and rotational modes and might also lead to a coupling of the molecular vibrational modes with the phonons of the solid.

The intensities of IR absorptions on surfaces are influenced by three mechanisms; the effect of the MSSR has already been treated in the preceding section. The second mechanism is caused by the interaction of dipoles of different neighboring molecules; these can couple together effectively when they have similar vibrational frequencies. The consequence for the IR spectra is an increase in the absorption intensity of the mode with higher vibrational frequency at the expense of the lower-frequency vibrational mode; this is called *intensity transfer* or *intensity borrowing by dipole coupling* [71]. Finally, the dynamic dipoles of the adsorbed molecules interact more and more destructively with increasing density of the adsorbate structure, leading to *depolarization* and a decrease of the spectral intensities [71]. The three aforementioned effects together lead to a more and more non-linear (and probably also non-monotonous) intensity variation with increasing coverage.

All of these effects are treated in detail based on experiments in references [36] and [71].

## The Setup

For the acquisition of IRAS data, a commercially available high-resolution FT-IR spectrometer (Bruker IFS 66 v/s) was applied as infrared source and interferometer. The IR source is a hot SiC rod (*Globar*). The spectrometer was modified for the purpose of IRAS spectroscopy (see fig. 3.13): the beam is deflected from the internal beam path,  $\vec{p}$ -polarized, coupled into the scattering chamber through a KBr window and focussed onto the sample under grazing incidence ( $83^\circ$ ); the IR light spot on the sample is smaller than the sample with a size of approx. 8 x 6 mm. The light reflected from the sample passes a second KBr window and is focussed onto a high-sensitivity wide-range infrared MCT detector (mercury-cadmium-telluride, HgCdTe); this detector needs to be cooled with liquid nitrogen. Source and detector are independent vacuum systems ( $p_{\text{source}} < 1 \text{ mbar}$ ,  $p_{\text{detector}} < 0.01 \text{ mbar}$ ).

The source/interferometer and detector are controlled by an acquisition processor (AQP) that transfers the data to a PC after the end of the measurement series for data storage and display; its reduced memory limits the amount of spectra that can be acquired per acquisition sequence. The personal computer acts as the user interface and is equipped with standard software (Bruker OPUS, version 3.0); it allows to program measurement macros for time resolved measurements (TRS-macros), and also to program TTL out- and respond to TTL inputs; they are mainly applied to synchronize IR measurements to beam pulse sequences controlled by the Extrel Merlin AQP.

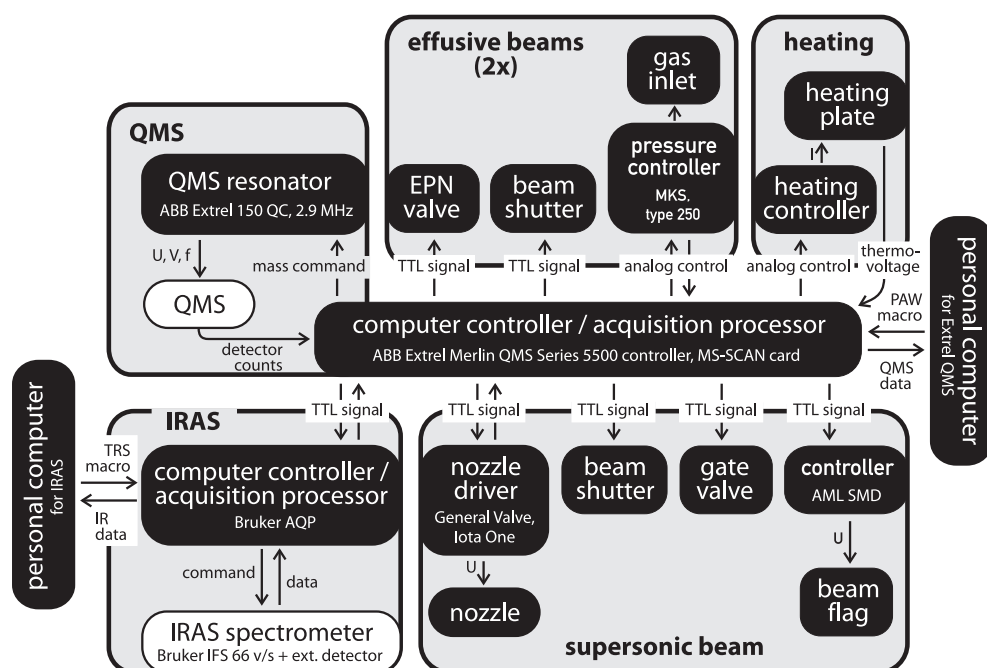


Figure 3.16: The block diagram of experiment control (for the usual case of time control by the QMS acquisition processor).

### 3.4 Experiment Time Control

For the experiments displayed in this thesis, well-controlled, complex molecular beams pulse sequences had to be produced; the central experiments are pulse-sequence molecular beam (PSMB) experiments to measure adsorption and reaction rates both under *steady-state* and *transient* conditions, sometimes with synchronized IRAS measurements. Typical beam-on and -off times are in the range of seconds, and the beam exposures have to be repeated many times for each study to allow for averaging. The experimental setup allows to generate these complex sequences by a precise computer time control (rather than by hand) in order to improve the comparability between kinetic experiments under controlled variation of single conditions (like beam intensity or temperature).

Many elements of the setup can be remote controlled (see fig. 3.16), including the three molecular beams (all valves and shutters and the pressure regulation of the effusive beams), the Au beam flag inside the scattering chamber, the measurement sequences of infrared spectrometer and the sample temperature; the sample temperature (thermovoltage) can be recorded simultaneously by the mass spectrometer, so that it is synchronized with the QMS experiments, which is important *e.g.* for TPD experiments.

All necessary signals (digital TTL as well as analog in- and outputs) are given by the acquisition processor of the mass spectrometer (ABB Extrel, Merlin QMS Series 5500 controller), see fig. 3.16. It offers up to 8 TTL in- and also 8 TTL outputs, 6 analog inputs (1 x  $\pm 1$  V, 5 x  $\pm 10$  V, 12 bit) and 5 analog outputs (4 x  $\pm 10$  V, 1 x 0-10 V, 12 bit); up to 6 internal clocks can be used for time control.

### **Macro Control**

The Extrel AQP can be programmed by macros written in a C-like macro language (Extrel PAW); this language is relatively complex and offers a possibility to start and stop measurements, control all in- and outputs at wish, control and reset the internal clocks and react on input data like the sample temperature, including performing simple calculations. These possibilities allow, as an example, to arbitrarily change the intensity of the effusive beams, or to adjust the heating power for the sample according to a temperature difference (and control temperature curves for isothermal experiments).

Apart from the ABB Extrel acquisition processor, also the IR spectrometer offers 3 TTL in- and one output that can be controlled by its own macro program language (OPUS TRS macro language). These (limited) possibilities allow to run exposure-synchronized IR experiments with a very high time resolution.



## Chapter 4

# Pd/Fe<sub>3</sub>O<sub>4</sub>/Pt(111) as a Supported Model Catalyst

It was laid-out in the introduction that real heterogeneous catalysis is in most cases conducted on materials that essentially consist of metal particles grown on metal oxides (*supports*) with minor components added occasionally which act as *promoters*; however, their structural complexity obscures the desired detailed understanding of catalysis by these systems, and such a deep insight could more easily be obtained on systems of *reduced* and *controlled* complexity. Based on the availability of a multitude of studies conducted on the very simple single crystals, the model catalyst approach was put forward as a promising concept to overcome the *materials gap* to real catalysts. This thesis is based on this approach and discusses effects observed during molecular beam experiments conducted on a Pd/Fe<sub>3</sub>O<sub>4</sub>/Pt(111) system as a model catalyst.

**Choice of Pd/Fe<sub>3</sub>O<sub>4</sub> as a Model Catalyst.** Pd nanoparticles as the active metal phase of the model system were chosen because they have shown high catalytic activities towards a multitude of reactions including CO oxidation [78], hydrocarbon conversion [79] or methanol decomposition [80]. Pd particles supported on Al<sub>2</sub>O<sub>3</sub> have been most extensively studied, but various other oxidic supports have also been investigated (see [81] and references therein). The choice of the mixed iron(II, III) oxide Fe<sub>3</sub>O<sub>4</sub> (*ferrous-ferric oxide, magnetite*) as a support in the model catalyst was originally based on three ideas; extensive studies have shown that this oxide is partly terminated by iron ions [82, 83], and not only oxygen ions; pure oxygen termination could make it chemically inert, but the Fe-termination suggested that the oxide itself would offer free valences for gas adsorption allowing for direct interactions of the oxidic support with the gas phase. More notably, Fe<sub>3</sub>O<sub>4</sub>

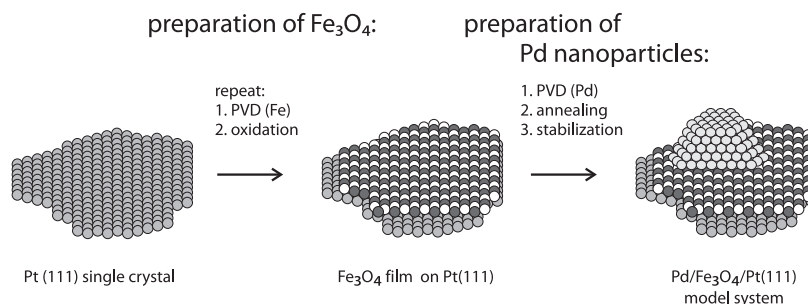


Figure 4.1: Preparation of the Pd/ $\text{Fe}_3\text{O}_4$ /Pt(111) model catalyst, schematically.

contains both  $\text{Fe}^{2+}$  and  $\text{Fe}^{3+}$  ions and can both be oxidized and reduced; thus, it was expected that it may get directly involved in reactions by the supply of lattice oxygen [81] (*Mars-van-Krevelen*-mechanism, [84, 85]).

Additionally, the epitaxial  $\text{Fe}_3\text{O}_4(111)$  film can be grown relatively thick (around 100 Å in this work); this property is one of the reasons for the high thermal (and chemical) stability of the Pd/ $\text{Fe}_3\text{O}_4$  system – compared with other typical model system, especially Pd/ $\text{Al}_2\text{O}_3$  – as evidenced by previous studies in our group [55].

The current chapter addresses the preparation and characterization of the  $\text{Fe}_3\text{O}_4$  film and the Pd/ $\text{Fe}_3\text{O}_4$ /Pt(111) model system, including a short outline over its oxidation and reduction behaviour, which has been the topic of a previous study of our group; finally it will be shown that it can be oxidized to clean the catalyst from carbonaceous deposits in order to allow extensive measurement series on one single preparation.

The principle for the preparation of the Pd/ $\text{Fe}_3\text{O}_4$ /Pt(111) model system is schematically displayed in fig. 4.1. The (111) face of a Pt single crystal mounted on the sample holder of the measurement setup (see chapter 3.1.1) acts as a preparation substrate for the epitaxial growth of the oxide film by repeated PVD and oxidation; this oxide then acts as the support for deposition of Pd metal nanoparticles by PVD. The detailed preparation procedure including all parameters is listed in the appendix A.1.

## 4.1 Iron Oxide $\text{Fe}_3\text{O}_4$ on Pt(111)

The epitaxial growth of iron oxide films has been extensively studied, initiated by Somorjai and coworkers [86, 87, 82] and continued in detail by Weiss and coworkers [83] (more references given below). These studies have shown that the three iron oxides FeO (*wüstite*, oxidation state of iron: +II),  $\text{Fe}_3\text{O}_4$

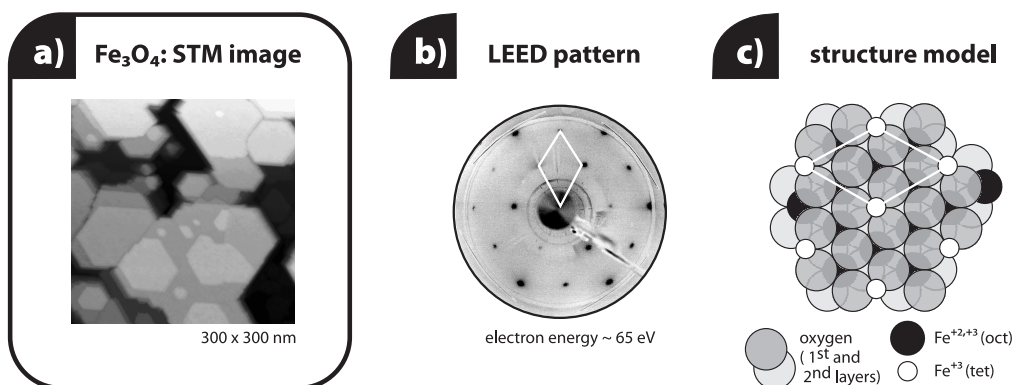


Figure 4.2: Surface structure of Fe<sub>3</sub>O<sub>4</sub> as observed by a) STM (from [92]) and b) LEED. c) Surface structure model in (111) direction according to the investigations described in [93, 82] (sizes not representative of ionic radii).

(*magnetite*, mixed iron oxidation states +II and +III) and Fe<sub>2</sub>O<sub>3</sub> (*hematite*, Fe<sup>3+</sup>) can all be obtained on the Pt(111) surface by PVD and oxidation, depending on the preparation conditions (thickness of deposited Fe-layer, and surface temperature and oxygen pressure during oxidation).

According to these studies, the first deposited monolayer of iron is fully covered by an oxygen overlayer after oxidation ( $p_{\text{O}_2} = 1 \times 10^{-6}$  mbar, 1000 K), forming a polar iron and oxygen bilayer similar to the rock salt-structure found in bulk FeO in the (111) direction [86, 87, 88]; this bilayer covers the preparation substrate Pt(111) completely. Further repetitions of iron deposition ( $\approx 4$  ML) and oxidation (same pressure, 875 K) result in the nucleation and growth of flat, three-dimensional Fe<sub>3</sub>O<sub>4</sub> islands – *i.e.*, the iron oxides FeO and Fe<sub>3</sub>O<sub>4</sub> on Pt(111) grow together in the *Stranski-Krastanov* growth mode [89, 90]. The Fe<sub>3</sub>O<sub>4</sub> islands coalesce with increasing coverage, forming a closed Fe<sub>3</sub>O<sub>4</sub> oxide with very broad, flat terraces, see fig. 4.2 a); the Fe<sub>3</sub>O<sub>4</sub> films prepared for this study were  $\approx 100$  Å thick (the details of the preparation conditions are compiled in the appendix A.1.3 of this work for reference). According to STM results, the step height between individual terraces is  $\approx 4.8$  Å or a multiple thereof, which corresponds to the distance between equivalent Fe<sub>3</sub>O<sub>4</sub>(111) surface terminations; this was interpreted to be indicative of identical surface terminations on all terraces [91].

The Fe<sub>3</sub>O<sub>4</sub> thin film has been shown to have the same volume crystal structure as naturally occurring, bulk Fe<sub>3</sub>O<sub>4</sub> (*magnetite*) [89]. Magnetite crystallizes in the cubic inverse *spinel* structure  $[\text{Fe}^{3+}]_{\text{tet}}[\text{Fe}^{2+}, \text{Fe}^{3+}]_{\text{oct}}\text{O}_4^{2-}$ , where the oxygen anions are arranged in hexagonal close-packed (111) layers forming a cubic *ABCABC...* (fcc) stacking sequence along the [111] direction

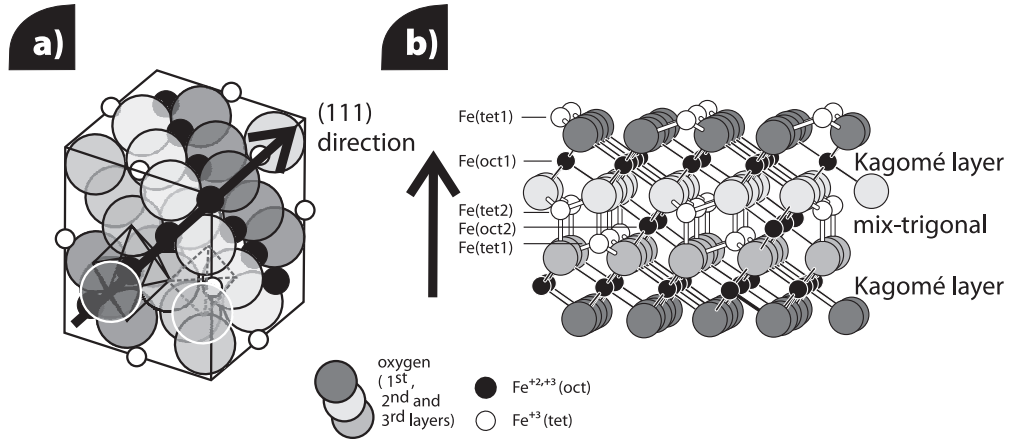


Figure 4.3: Inverse spinel bulk structure of  $\text{Fe}_3\text{O}_4$ : a) unit cell, and b) as viewed parallel to the (111) surface (after [89, 83]) – sizes not representative of ionic radii.

[94], see fig. 4.3 and 4.2 c). The iron ions occupy both tetrahedral (tet, A-type) and octahedral (oct, B-type) interstitial sites in the oxygen sublattice; the tetrahedral sites are occupied by  $\text{Fe}^{3+}$  exclusively and the octahedral sites are occupied by equivalent amounts of both  $\text{Fe}^{2+}$  and  $\text{Fe}^{3+}$ , forming layers of iron ions between the fcc oxygen layers (fig. 4.3 b); these layers are denoted in fig. 4.2 c) and 4.3: some of the octahedrally coordinated iron ions (black) form a layer with *Kagomé* structure; the other ions form a mix-trigonal layer together [83]. Since only  $1/4$  of the tetrahedral and  $3/8$  of the octahedral<sup>1</sup> sites are occupied, the iron ions form two-dimensional hexagonal superstructures on the oxygen layers with a lattice constant of  $5.92 \text{ \AA}$  [91]. Those structures are assumed to be responsible for the protrusions observed in high-resolution STM images [95] and the  $(2 \times 2)$  LEED structure (fig. 4.2 b).

**Surface Termination of  $\text{Fe}_3\text{O}_4$ .** It was proposed that the surface termination of magnetite crystals can be derived from the bulk structure when it is cleaved in (111) direction [82]; based on this assumption, dynamic LEED experiments were evaluated by comparison with predicted  $I$ - $V$ -LEED curves for a multitude of different possible relaxed surface terminations derived from the bulk crystal structure; this procedure indicated a termination by the tetrahedrally coordinated  $\text{Fe}^{3+}$  denoted Fe(tet1) in the mix-trigonal layer in

<sup>1</sup>Remember that a hexagonal close-packed (fcc) structure contains one tetrahedral and two octahedrally coordinated interstitial sites between the close-packed layers per lattice particle. Thus,  $1/3$  of the Fe ions are in tetrahedral, and  $2/3$  are in sites that are octahedrally coordinated by oxygen.

fig. 4.2 c) as the most probable surface structure [82]; those ions have a coverage of  $1/4$  with respect to the underlying close-packed oxygen layer.

Another study by Shaikhutdinov *et al.* was based on TPD experiments and infrared spectra (IRAS) of CO adsorbed on the  $\text{Fe}_3\text{O}_4$  film at 90 K [92]. These authors distinguish between three different CO species on the surface based on three IRAS peaks observed at 2207, 2141 and 2080  $\text{cm}^{-1}$  (fig. 4.5 a), spectrum 1). These species are related to three TPD desorption features, and were denoted, according to their desorption sequence, as  $\alpha$  (2141  $\text{cm}^{-1}$ , 110 K),  $\beta$  (2080  $\text{cm}^{-1}$ , 180 K) and  $\gamma$  (2207  $\text{cm}^{-1}$ , 230 K). Based on its desorption temperature and vibrational frequency close to the value of gas-phase CO, the  $\alpha$ -species was assigned to a weakly bound (physisorbed) species. The discussion of the vibrational frequency of the other two CO species resulted in the following assignment: the  $\beta$ -species was interpreted to be CO adsorbed on the octahedrally coordinated  $\text{Fe}^{2+}$  ions, and the  $\gamma$ -species as CO on  $\text{Fe}^{3+}$  ions in the tetrahedral interstitial sites. Most of the CO was found to be adsorbed as the  $\beta$ -species; thus, the surface was suggested to be terminated by an outmost  $1/4$  ML consisting of octahedral  $\text{Fe}^{2+}$  ions situated above an  $1/4$  ML of tetrahedral  $\text{Fe}^{3+}$  ions<sup>2</sup>; note that this surface termination can also be derived from the mix-trigonal layer shown in fig. 4.2 b).

For this thesis, both static LEED experiments (at  $\approx 65$  eV) and IRAS spectra of CO adsorbed at  $\approx 115$  K were conducted to characterize the quality of each newly prepared  $\text{Fe}_3\text{O}_4$  film. The LEED pattern of all accepted samples showed the clear  $(2 \times 2)$  structure as displayed in fig. 4.2 b). However, the CO-IRAS spectra showed a considerable variability (despite constant and clear LEED patterns): many of the spectra resembled the type described by Shaikhutdinov *et al.* (as shown in fig. 4.5 a), spectrum 1), but several preparations showed a strongly increased  $\alpha$ -peak together with a minor decrease in the  $\beta$ -peak (spectra 2 and 3); the  $\gamma$  peak was sometimes slightly increased. It is not so surprising that the  $\alpha$ -peak shows intensity variations between different spectra measurements, since it was assigned to a weakly bound species that desorbs at temperatures close to the gas exposure temperature [92]; its peak intensity could even be easily increased by further CO exposures (grey curve in spectrum 3). The variations in the other peaks, however, are less understandable. Moreover, some preparations showed even *strongly* decreased intensities in the peaks assigned to adsorption on the Fe ions ( $\beta$ -

---

<sup>2</sup>It is worth noting that both suggested surface terminations would mean a concentration of cations above the anionic oxygen layers; thus, these surfaces would be polar. It was suggested by the authors of both surface termination models that the bonding between the oxygen and iron has a strong covalent component and that the iron oxides are *not* purely ionic solids (salts).

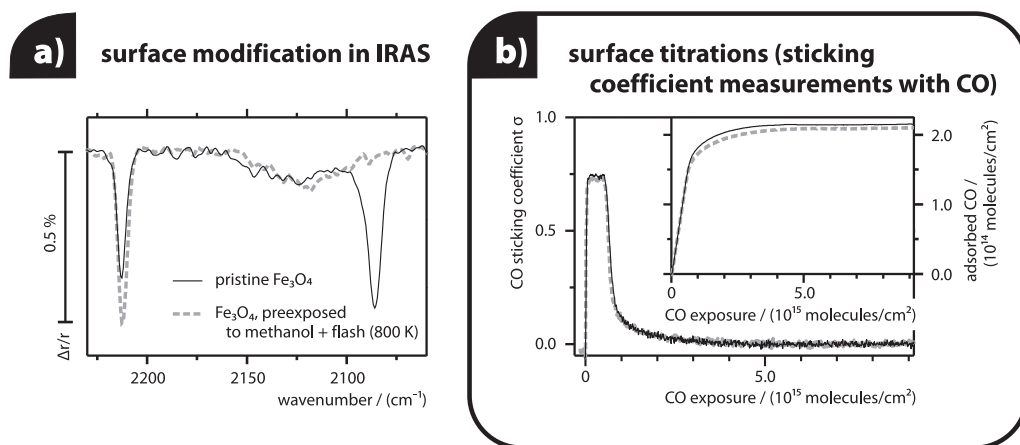


Figure 4.4: Fe<sub>3</sub>O<sub>4</sub>-surface titrations with CO as a probe molecule before and after methanol exposure (19 L at 115 K) and annealing (at 800 K). a) IRAS experiments, b) sticking coefficient measurements and integration.

and  $\gamma$ -peaks), so that the  $\alpha$ -peak was the main IRAS feature in these cases (and slightly shifted, spectra 4 and 5).

Very similar variabilities in the spectra were also previously observed in our group in preparations conducted with the gas doser of the preparation chamber instead of chamber backfilling for oxygen exposures, which may result in lower reproducibility of the oxygen partial pressure on the sample between preparations [55]. The associated change in the spectra might thus simply indicate that the growth of Fe<sub>3</sub>O<sub>4</sub> responds very sensitively on the preparation temperature and pressure; indeed, investigations by another group suggest that an increase of the preparation *temperature* by only 30 K can result in a loss of the  $\beta$ - and  $\gamma$ -peaks in TPD [96] – again, without observable differences in the (2×2) LEED pattern. Thus, the seemingly high sensitivity of the surface termination to the preparation conditions might be a possible explanation for the two different surface terminations derived by the groups of Weiss [83] and Shaikhutdinov [92].

**An alternative interpretation** for the variability of the CO-spectra is suggested in this work: our experiments suggest that the observed high variability of the IRAS peaks – which are in no case related with a significant change of the LEED pattern (as a possible indication for the formation of a different surface termination in different preparations) – may be understood assuming that the  $\beta$ -species (and probably also the  $\gamma$ -species) relate to minority surface sites or defect structures of the iron oxide films. This interpretation is deduced from observations made during the study of me-

methanol decomposition on the pristine oxide, which will be the topic of chapter 5.2; briefly, those experiments have shown that some of the adsorbed methanol dehydrogenates to formaldehyde on the pristine oxide, and that the hydrogen atoms formed in this decomposition step are accommodated in surface hydroxyl groups formed on exposed surface oxygen species of the oxide; those surface hydroxyl groups desorb from the oxide in the form of water, which leads to the loss of some of the surface oxygen from the oxide. Those changes in the oxide seem to be reflected in the IRAS spectra of CO adsorbed on the oxide (19 L adsorbed at 115 K); fig. 4.4 displays such spectra for a pristine oxide and an oxide after methanol adsorption (11.7 L at 115 K) and annealing to 800 K (*i.e.*, after surface oxygen depletion). The pristine film (black line) shows the typical  $\alpha$ -,  $\beta$ -,  $\gamma$ -structure discussed above, but after methanol-exposure and annealing at 800 K the  $\beta$ -peak (around  $2080\text{ cm}^{-1}$ ) has completely vanished, while the  $\gamma$ -peak showed a slightly increased intensity; similar intensity changes were also observed by Sun, Kaya and Shaikhutdinov [96] in related TPD-surface titrations with CO according to the above discussed recipe given by Lemire *et al.* (see [92]) after similar treatments. Interestingly, the observed loss of CO adsorption capacity in the sites related to the relatively intense IRAS- and TPD- $\beta$ -peak is *not* reflected by CO-sticking coefficient-measurements conducted at 115 K on a freshly prepared  $\text{Fe}_3\text{O}_4$  film and one that was treated with methanol and annealed as described above, see fig. 4.4 b): the results of both experiments are identical or differ only insignificantly, suggesting that the loss of adsorption capacity in the  $\beta$ -peak observed in the IRAS spectra is not associated with a significant loss in the total CO-adsorption capacity of the oxide as detected by the sticking coefficient measurements. This observation indicates that the sites related to the  $\beta$ -peak do not account significantly for the adsorption capacity in the sample, and that most CO must be adsorbed in other sites; additionally, taking into account that also the  $\gamma$ -peak may exhibit a considerable intensity variation between preparations, we may tentatively assume that also this peak is related to a minority, possibly a defect site (and not a regular surface site).

Another indication for the interpretation that the  $\beta$ - and  $\gamma$ -peaks observed in the IRAS spectra are related to defect sites on the iron oxide preparations may be seen in the fact, that LEED spots in preparations with low  $\beta$ - and  $\gamma$ -intensities typically were observed to be sharper and showed lower background intensities than the preparations with higher  $\beta$ - and  $\gamma$ -intensities (no example LEED patterns shown here); since the presence of irregular (defect) sites may lead to higher background intensities, the high background intensities (which go together with intense  $\beta$ - and  $\gamma$ -peaks) also suggest that the  $\beta$ - and  $\gamma$ -sites are defect sites. This observation also renders an alternative

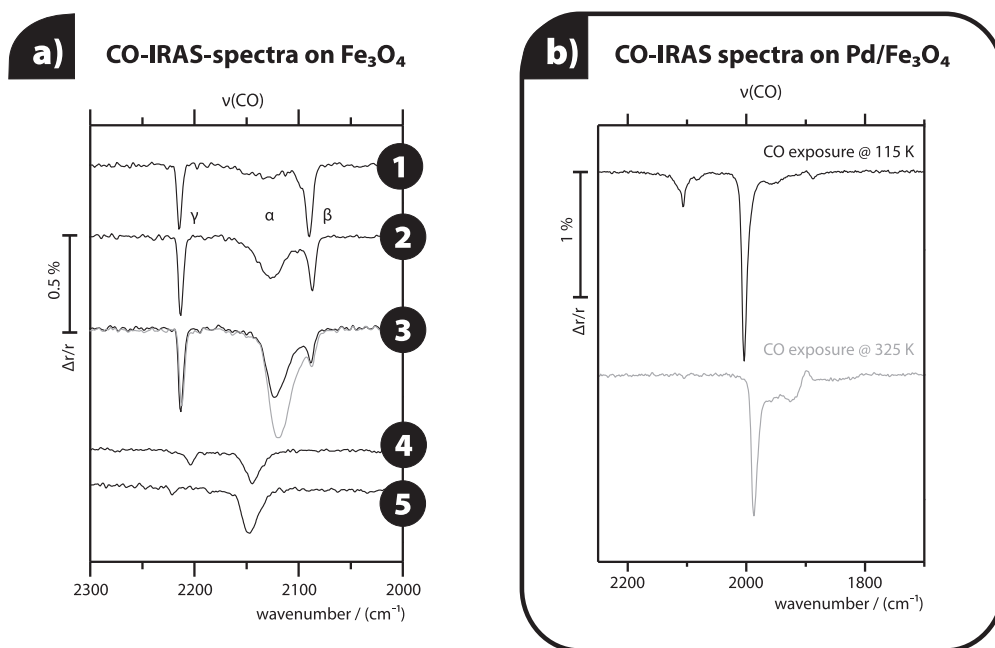


Figure 4.5: Characterization of Fe<sub>3</sub>O<sub>4</sub> and Pd/Fe<sub>3</sub>O<sub>4</sub> by IRAS of CO, adsorbed at 115 K (and also at 325 K on the model catalyst, fig. b). Exposures were  $\approx 19$  L in all spectra except for the grey spectrum 3 on Fe<sub>3</sub>O<sub>4</sub> ( $\approx 171$  L), and the spectrum with exposure at 325 K ( $\approx 13$  L). All spectra taken at 115 K.

possible explanation for the changes induced by methanol-reactions – that the sites responsible for the  $\beta$ -peak transform into the  $\gamma$ -species during water desorption – less probable.

## 4.2 Pd Nanoparticles supported on Fe<sub>3</sub>O<sub>4</sub>: Characterization and Treatments

The epitaxial Fe<sub>3</sub>O<sub>4</sub> film described in section 4.1 acts as a substrate for the deposition of the active Pd metal phase, as displayed in fig. 4.1. The growth behaviour and morphology of metals deposited on (oxide) surfaces is controlled by the interaction energy  $\gamma_{\text{interface}}$  between the oxide and the metal, and by the surface free energies of the metal  $\gamma_{\text{metal}}$  and the oxide  $\gamma_{\text{oxide}}$ ; those properties govern whether the deposited metal will wet the oxide surface, be covered by the oxide and get integrated into it, or if it will segregate and agglomerate to particles (see chapter 2.3). Pd on Fe<sub>3</sub>O<sub>4</sub> is known to form nanoparticles [81, 59] (*i.e.*,  $\gamma_{\text{oxide}} < \gamma_{\text{metal}} + \gamma_{\text{interface}}$ , *Volmer-Weber*-growth).



Thus, the growth of Pd nanoparticles on magnetite is a spontaneous process and occurs as soon as the metal is deposited on the oxide, given that the atomic mobility is high enough. For all experiments shown in this thesis, a nominal coverage of  $\approx 4 \text{ \AA}$  of Pd was deposited on the magnetite film by PVD at 115 K under a flux of  $\approx 4.5 \times 10^{12} \text{ atoms} \cdot \text{cm}^{-2} \cdot \text{s}^{-1}$ ; the detailed preparation conditions are listed in the appendix A.1.4. Under these conditions, the mobilities of the Pd atoms are low, and numerous Pd particles with relatively poor crystallinity were formed. To advance the healing process and form crystalline nanoparticles by *Ostwald ripening*, the deposited material was annealed at 600 K for 60 s after preparation. An STM micrograph of the obtained nanoparticles is shown in fig. 4.6 a) together with a close-up image displaying the shape of the particles. The particles appear to be well-ordered and show a very narrow size-distribution with an average diameter of  $\approx 4 \text{ nm}$  ( $\approx 700$  atoms); they expose mainly (111)-facets. The Pd-dispersion (*i.e.*, the fraction of Pd surface atoms) is  $\approx 40 \%$ , and the particle density on these preparations was found to be  $\approx 3.8 \times 10^{12} \text{ cm}^{-2}$ .

#### 4.2.1 Sample Characterization by CO Adsorption

It was described before that adsorbed CO can act as a surface probe for the identification of available adsorption sites or the surface condition; this was exemplified in chapter 2.1.2 by IRAS spectra of CO adsorbed on the(100)- and (111)-crystallographic planes of Pd single crystals. The application of adsorbed CO as a surface probe can also be utilized on Pd nanoparticles, as has been shown in many studies, *e.g.* [97, 98, 45]; however, these spectra are complicated by the increased heterogeneity of these samples as compared to single crystals, by coupling effects and intensity transfer; additionally, the steep inclination angle of the particles' side facets leads to a decreased spectral intensity for CO adsorbed at these sites due to the small perpendicular component of the dynamic dipole moment for those species with respect to the surface (see chapter 3.3.2).

Fig. 4.5 b) shows IRAS spectra of CO adsorbed on the model catalyst; four main absorption features can be identified in those spectra and assigned as follows: the feature around  $2100 \text{ cm}^{-1}$  are CO species bound linearly (on-top) on (111)-facets and at defect sites of the nanoparticles. The feature at  $\approx 2000 \text{ cm}^{-1}$  are bridge-bound CO species at steps and edge-sites, and additionally – but only as a minor contribution due to the steep inclination angle of those facets – on the (100)-facets. Finally, the broad feature between  $\approx 1970$  and  $\approx 1800 \text{ cm}^{-1}$  with peaks at  $\approx 1950$  and  $1880 \text{ cm}^{-1}$  are CO species adsorbed on the (111)-facets at hollow sites; the feature around  $1950 \text{ cm}^{-1}$  may also contain a minor contribution by CO in bridge sites. It is

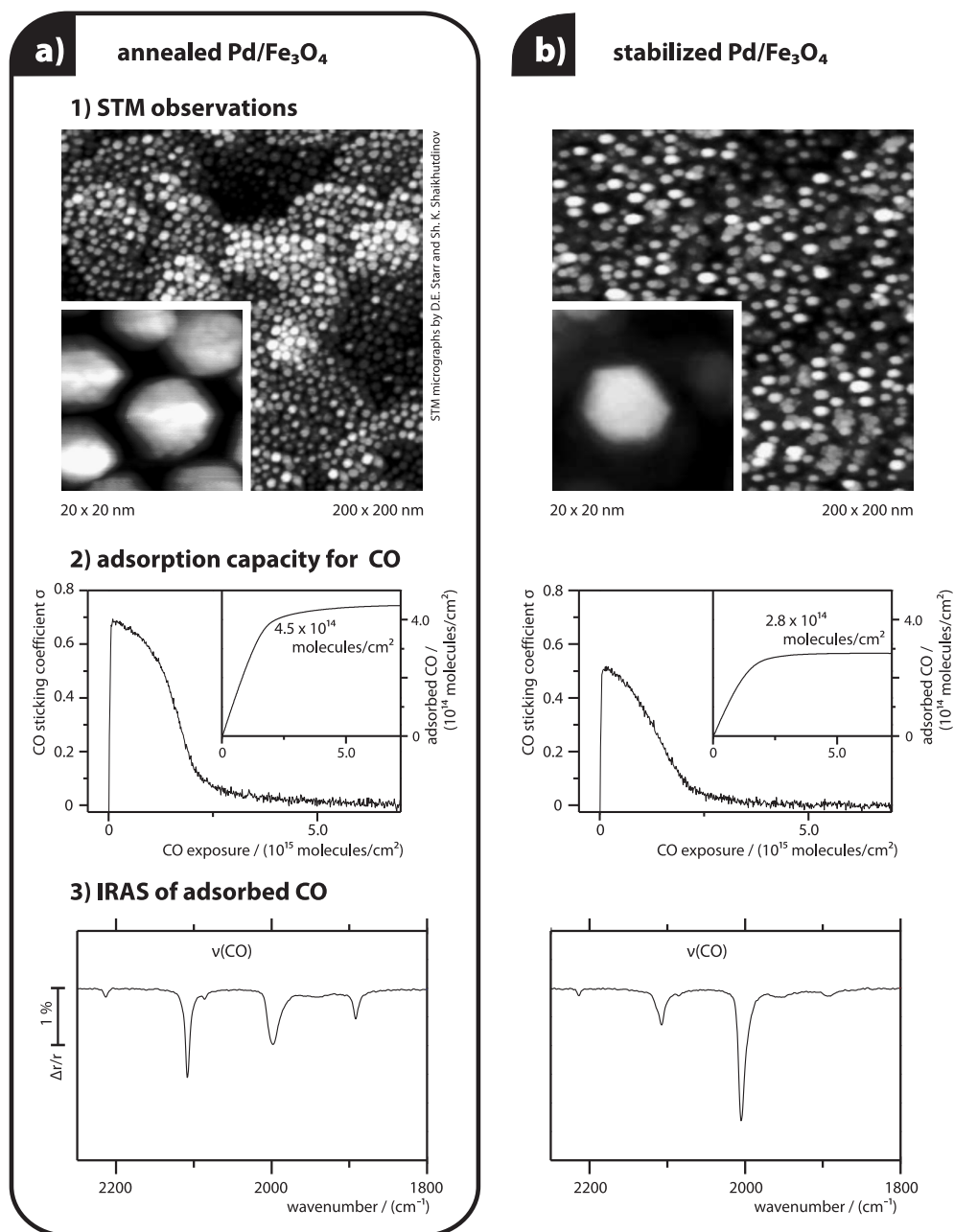


Figure 4.6: Experimental observation of particle sintering (*stabilization*) on the Pd/Fe<sub>3</sub>O<sub>4</sub> model catalyst by different techniques; STM micrographs were taken from reference [59].

important to notice that the intensities of those features do not simply represent the abundances of the respective species on the surface due to strong dipolar coupling interactions between adjacent adsorbates, which lead to intensity transfer towards the species with the higher vibrational frequency (see chapter 3.3.2), and additionally due to possible differences in the dynamic dipole moments of the different species. The efficiency of such effects gets apparent from spectra taken after CO exposure at different temperatures, see fig. 4.5 b): due to the decrease of the saturation coverage between 115 (upper spectrum) and 325 K (lower spectrum) to approx. 0.5, the influence by coupling and intensity transfer is decreased in the spectrum taken after exposure at the higher temperature. This results in higher absorption intensities between  $\approx 1970$  and  $1800 \text{ cm}^{-1}$  than in the low-temperature spectrum, although the CO-surface coverage is lower. Note that the feature around  $2100 \text{ cm}^{-1}$  is absent in the lower spectrum, since no Pd-on-top adsorption sites are occupied by CO at 325 K (see chapter 2.1.2).

#### 4.2.2 The Pd/Fe<sub>3</sub>O<sub>4</sub> Model Catalyst: Stabilization

It has been established during the earlier work of our group in cooperation with Shaikhutdinov and coworkers that the annealed nanoparticles are initially not stable in oxygen atmosphere ( $p_{\text{O}_2} \approx 10^{-6} \text{ mbar}$ ) at elevated temperatures of 500 K [55, 59]; instead, the particles undergo extensive reshaping during the first cycles of oxygen treatment and subsequent reduction by CO, until they have reached an equilibrium shape and the reshaping process has become insignificantly slow [59]. The effect of particle reshaping can be followed by many experimental techniques (see fig. 4.6 a and b):

- STM images (by D. Starr and Sh.K. Shaikhutdinov) clearly reflect the change of particle density and morphology during oxygen-induced sintering. The stabilized particles were found to be much bigger (diameter  $\approx 7 \text{ nm}$ , approx. 3300 atoms per particle) than the freshly prepared system, and their density is strongly decreased by 80 % to a new value of  $\approx 8.3 \times 10^{11} \text{ cm}^{-2}$ . A possible migration of Pd into the iron oxide support or a segregation of Fe onto the Pd particles as an alternative explanation for the observations could be excluded, because the calculated Pd coverage on the support before and after the treatments does not change.
- The surface area of the particles was quantified by a CO-sticking coefficient-measurement at 300 K, see fig. 4.6 a) and b), panel 2: the sticking coefficient is very high initially on both annealed and stabilized surface and stays relatively constant over a longer time due to precursor-mediated adsorption, and then drops to zero quickly. The integration

over the experiments yields an adsorption capacity of  $4.5 \times 10^{14}$  molecules per  $\text{cm}^2$  on the annealed and  $2.8 \times 10^{14}$  on the stabilized sample, indicating that the sintering process reduces the surface area by approx.  $1/3$ .

- The IRAS spectra of CO adsorbed at 115 K on the annealed and stabilized particles do also sensitively reflect the change in particle morphology. Both spectra show the four main features described in section 4.2.1: CO in on-top coordination ( $\approx 2100 \text{ cm}^{-1}$ ), bridge-bonded at steps and edge-sites and – as a small contribution – on the (100)-facet ( $\approx 2000 \text{ cm}^{-1}$ ), and CO at hollow- (and some bridge-) sites on the Pd(111) facets (between  $\approx 1950$  and  $1880 \text{ cm}^{-1}$ ). The most notable differences between the two spectra are the relatively high abundance of linearly coordinated CO molecules on the *unstabilized* sample, and the increased intensity and slight blue-shift in the peak around  $2000 \text{ cm}^{-1}$  in the stabilized sample. Both can be understood by the sintering process: the reshaping leads to an increased crystallinity and a decreased defect density in the stabilized sample. On the unstabilized sample, CO gets linearly and bridge-bonded at the many defect sites. During stabilization, the (100) and (111) facets grow and heal, leading to an increased availability of regular adsorption sites such as (100) bridge- and (111) hollow-sites; thus, less species are adsorbed in on-top sites, which is also reflected in the intensity-loss around  $2100 \text{ cm}^{-1}$ . The strongly increased intensity around  $2000 \text{ cm}^{-1}$  is due to the increased efficiency of intensity-transfer from regular adsorption sites to the bridge-bonded CO species at the edge and corner sites.

Concluding, all experiments have shown that the Pd/Fe<sub>3</sub>O<sub>4</sub> model catalyst system is initially unstable in oxygen atmosphere at and above 500 K and shows a strong propensity for particle reshaping/sintering, which, however, nearly stops after approx. five of the oxidation cycles (as described in the appendix A.1.4). Since the oxidation treatment could also be used to remove carbon deposits – as will be shown in the following section –, all experiments discussed in this thesis had to be conducted on a stabilized system; therefore, stabilization was performed as a routine treatment.

### Long Term Stability and Cleaning Procedure

The projects described in this work focused at reactions of methanol and 2-butene on the model catalyst, both of which – as many other organic reactants – have a tendency to decompose on many transition metal surfaces and leave behind strongly dehydrogenated carbonaceous species or even carbon

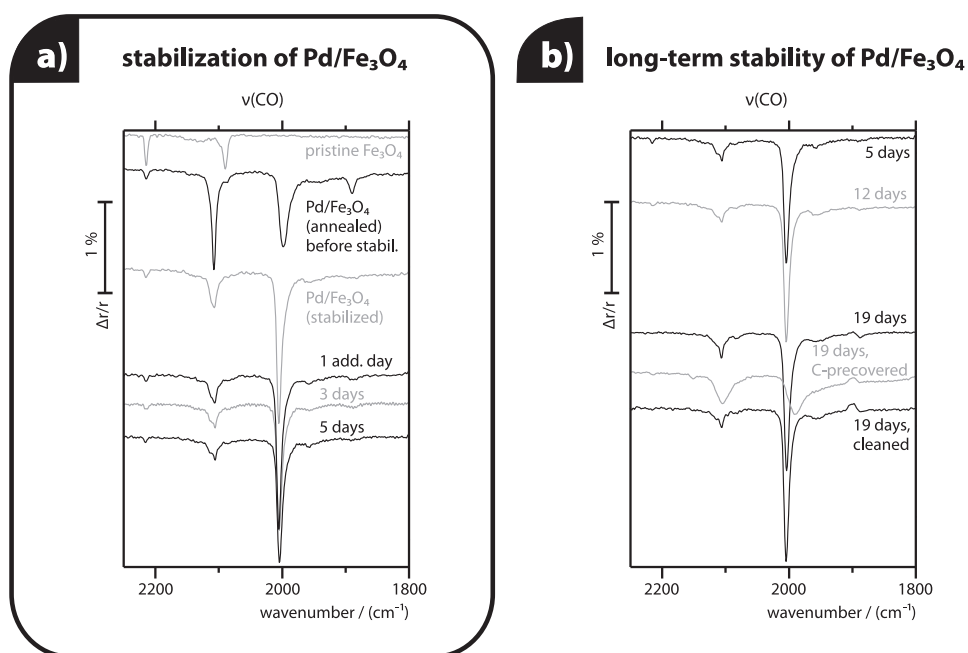


Figure 4.7: Long-term stability of Pd/Fe<sub>3</sub>O<sub>4</sub>; additionally, the ability of the stabilization procedure to remove carbonaceous deposits resulting from the decomposition of organic reactants during experiments is demonstrated (panel b).

[80, 99], which potentially block and deactivate the catalyst surface; thus, they need to be removed before the next experiments. Unfortunately, those surface remainders have very high desorption temperatures and can often not be removed by thermal desorption without serious changes of the particle morphologies (sintering). Note that also the alternative preparation of a fresh model catalyst after each experiment that has left such species is not a good solution for extended experimental series, since it is known that different preparations of a model catalyst may differ considerably in their morphologies, and since such a difference in morphology may have a significant influence on kinetic measurements; therefore it is generally desirable to conduct series of kinetic experiments on the same catalyst preparation. Thus, a procedure to clean the model catalyst from carbonaceous deposits is needed; the commonly applied method is to burn those species by a treatment in oxygen; however, such oxidation treatments at high temperatures do also often alter model catalyst surfaces.

It was possible to show in this work that the stabilization procedure discussed above can be successfully applied to remove carbonaceous deposits

from the surface of the Pd/Fe<sub>3</sub>O<sub>4</sub> model catalyst; this can be demonstrated by IRAS spectra of adsorbed CO as displayed in fig. 4.7: the third trace from the top in panel a) exhibits the IRAS spectrum of the sample directly after the initial stabilization procedure; this sample was then applied in a large number of kinetic experiments with 2-butene, and after each of those butene-exposures, the sample was cleaned by the stabilization procedure (often over night – 10 to 15 cycles –, although one cycle is typically sufficient to clean the sample); the lower part of the panel shows CO-IRAS spectra obtained after those cleaning treatments over the following experimental days; their correspondence with the spectrum of the freshly stabilized sample demonstrates the efficiency of this treatment.

Fig. b) shows that the many repetitions of the stabilization procedure for sample cleaning doesn't lead to further particle reshaping on the once stabilized sample. Moreover, this panel shows another important observation: although the stabilization procedure was automatically conducted over night by computer control of the setup to remove carbon deposits, it was also established that one stabilization cycle is enough to remove experimental carbonaceous deposits (see the three spectra in the lower part of fig. 4.7 b).

### 4.2.3 Oxidation Behaviour of the Pd/Fe<sub>3</sub>O<sub>4</sub> Model Catalyst

The sintering behaviour of freshly prepared samples of the Pd/Fe<sub>3</sub>O<sub>4</sub> model catalyst in oxygen atmosphere (*vide supra*) was discovered during an earlier project of our group that was set up to investigate the interaction with and incorporation of oxygen into the Fe<sub>3</sub>O<sub>4</sub>-supported Pd nanoparticles [55]. Some of those results are of significance for the project discussed in this thesis, and will be briefly reviewed in this section; references to the original literature will be given. Fig. 4.8 graphically concludes the most important aspects of this behaviour. The project was initiated based on an earlier investigation by Meyer and Shaikhutdinov which suggested that the oxidation of CO to CO<sub>2</sub> on this model catalyst might involve oxygen from the oxide support [81].

Our experiments have shown that large quantities of oxygen can be incorporated into the Pd particles in the form of palladium oxides; particles of the size used in this work can store approximately four times more oxygen during oxidation at  $\approx 500$  K than an ordinary saturated overlayer of chemisorbed oxygen could accommodate, as revealed by oxygen titration experiments with a pulsed CO-beam [100]. The formation of dense Pd-oxide phases in the Pd nanoparticles could be experimentally confirmed with high-resolution core-level spectra (HR-CLS, XPS); these experiments have also established that those oxide phases form preferentially at the interface between the Pd particles and the Fe<sub>3</sub>O<sub>4</sub>-support [100, 101]. Additional IRAS surface titration experiments with CO as a probe molecule as well as a more detailed analysis of the HR-CLS spectra have shown that Pd oxide phases form not only at the particle-support interface, but also on the particles' surface, although the interface oxide is thermodynamically favoured [101].

The formation of the interface oxide is kinetically limited by the diffusion of oxygen into the particles' bulk; this could be inferred from the different oxidation behaviours of particles with different sizes [102, 103] as well as from the decomposition kinetics of the oxide phases as observed in transient (pulsed) molecular beam experiments [104].

CO does not adsorb on the Pd surface oxide, and thus it can not react there [101]; consequently, surface-oxidation leads to a strong deactivation of the catalyst. Dynamic oxidation-reduction experiments with mixtures of different relative amounts of oxygen and CO were performed; in those experiments, both the deactivation of the catalyst by surface-oxidation under oxygen-rich conditions, as well as the recovery of catalytic activity by reduction of the surface oxides under CO-rich conditions could be observed by the change of the reaction rates as well as the surface area that could be titrated by *in-situ*-IRAS experiments with CO as a surface-sensitive probe molecules

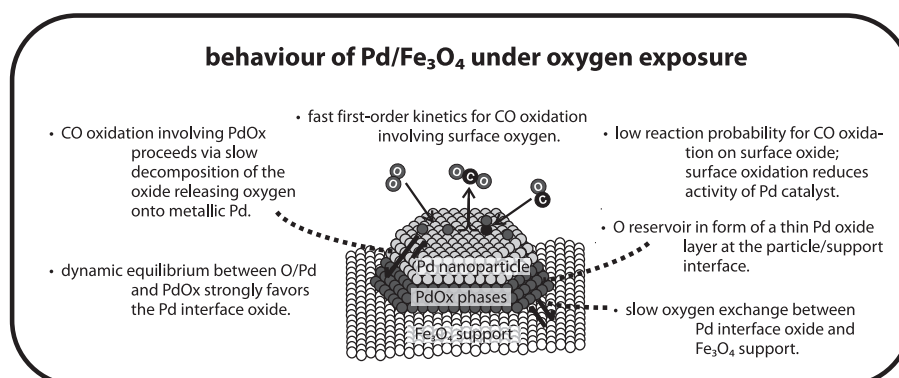


Figure 4.8: Abstract: oxidation behaviour of Pd/Fe<sub>3</sub>O<sub>4</sub> and influence on activity.

[105]. In other transient kinetic experiments, the equilibrium between the oxide phases and chemisorbed oxygen (which are converted into each other) could be studied in detail and was also simulated by a simple microkinetic mechanism [104].

Additionally, it could be shown by pulsed molecular beam CO titration experiments on a model catalyst with an isotopically labelled support that only minor amounts of oxygen are exchanged between the particles and the support and that no CO oxidation occurs on the support. Thus, the Fe<sub>3</sub>O<sub>4</sub> oxide support does not effectively contribute to the oxygen storage capacity of the Pd/Fe<sub>3</sub>O<sub>4</sub> model catalyst.

Finally, it was shown that the Pd nanoparticles sinter during the first oxidation-reduction cycles; it could be established that this sintering is induced by oxygen during the oxidation process; thus, it is *not* simply a thermal process (*Ostwald ripening*) [59].



# Chapter 5

## Methanol Decomposition

### 5.1 Introduction

As a first model reaction system, we focus on the decomposition of methanol (fig. 5.1). Methanol is one of the main products in synthetic chemical industry, where it is typically formed from *synthesis gas* ( $\text{CO} + \text{H}_2$ ). It has applications as a substance, but most of the methanol production is transformed into secondary raw chemicals, most importantly formaldehyde and fuels (see next page). As a consequence, both the formation of methanol from *synthesis gas* and its dehydrogenation to formaldehyde are important industrial reactions.

The methanol decomposition reaction may proceed under formation of formaldehyde or CO, and CO-formation from methanol is the reverse process to methanol formation from *syngas*; this relation to important industrial processes may be one of the reasons why methanol decomposition has become one of the most frequently studied model reactions on surfaces. It constitutes a relatively complex model reaction for the context of fundamental research aiming at an understanding of chemical reactions on a microscopic level, since it may already comprise numerous intermediate steps; on the other hand, the reaction has already been studied on various materials, and the existing reports constitute a very good basis for the evaluation of experiments on new surfaces; additionally, the multitude of references facilitates to conclude on correlations between the materials' structures and their reactivities and selectivities. Finally, the methanol molecule and reaction products are still simple enough to allow for studying by many of the standard analytical techniques, including IRAS and mass spectrometry.

In this work, methanol decomposition was studied both on the pristine oxide  $\text{Fe}_3\text{O}_4(111)$  as well as on the model catalyst  $\text{Pd}/\text{Fe}_3\text{O}_4$ ; both materials

possess different chemical activities and selectivities in methanol decomposition, and will be discussed in two separate sections of this chapter. Before the results part, however, an overview over reported studies of methanol decomposition on metals and oxides (mainly in UHV) will be given.

**Methanol in Industrial and Technical Applications.** Molecular methanol is one out of the ten most-produced synthetic organic raw chemicals (approx. 35 million tons *per annum*, with increasing tendency [106]). It was first obtained by dry distillation (*pyrolysis*) of wood<sup>1</sup>, which remained the main source of methanol until the first decades of the 20<sup>th</sup> century, when an extension of the production was made possible by a newly developed process based on fossil materials (Mathias Pier, BASF); in this process, the fossil materials (originally mainly coal) are first converted into synthesis gas (*syngas*, CO + H<sub>2</sub>) by reaction with balanced amounts of water and oxygen at elevated temperatures and pressures; the purified syngas is then transformed into methanol in a second reaction step at the surface of a zinc-chromium catalyst at very high pressures and temperatures (300 bar, 350°C). The process was later improved by ICI in the 1960ies to obtain methanol from syngas under lower pressure; this process makes use of a different catalyst (copper-zinc-aluminum oxide) [107]. Coal has by now mostly been replaced by natural gas (methane) as a source for syngas, but nevertheless, methanol production is still largely based on syngas conversion, although it is an energetically very inefficient process. Newer approaches for methanol formation are based either on direct conversion of methane into methanol (without detour over the highly oxidized CO), electrochemical conversion of carbon dioxide from exhaust gases (inverse fuel cell-process) [108], or – for some agricultural areas – the conversion of biological materials such as plant fibers.

New scenarios conceived for energy storage focus on methanol as one central fuel substance with high versatility [108]; on one hand, methanol can be applied directly as a hydrogen carrier in fuel cells (DMFCs), or in

<sup>1</sup>The name originally given to methanol, *methylene* (Dumas and Peligot in 1834), was meant to denote „alcohol obtained from wood“ (greek „méthy“ = wine, and „hylé“ = wood).

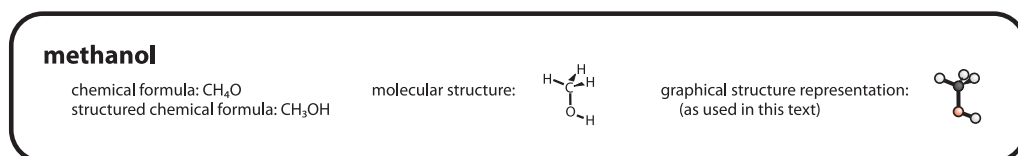


Figure 5.1: The methanol molecule.

combustion engines (both pure or as an additive). Additionally, several secondary products obtained from methanol are already today used as fuels or fuel additives, most notably *tert*-butyl-methyl-ether (MTBE), fatty-acid methyl esters (FAMEs, *biodiesel*), dimethyl ether (DME) or hydrocarbons (prepared by the *methanol to gasoline*-process (*Mobil*-process); *e.g.* *Shell V-power*). Approximately one third of the methanol production is transformed into MTBE, which is currently mostly applied as a gasoline additive to increase the *octane number* of the fuel and decrease its propensity for *engine knocking*.

More than another third of the methanol is converted catalytically into formaldehyde (CH<sub>2</sub>O, annual production: approx. 11 million tons). Formaldehyde is an important building block in the synthesis of many complex chemical compounds and materials; most of it is used in the production of polymers and artificial resins. Two processes are applied for formaldehyde production, both of them conducted at atmospheric pressure; the older process is the dehydrogenation on metallic silver<sup>2</sup> according to  $\text{CH}_3\text{OH} \rightarrow \text{CH}_2\text{O} + \text{H}_2$  around 600°C (often in the presence of oxygen) [110, 111, 112], but it is less energy-efficient and the catalyst less stable, although easier to regenerate *on-site*. A newer process is the oxidative dehydrogenation on iron molybdate (Fe<sub>2</sub>(MoO<sub>4</sub>)) around 350°C according to  $\text{CH}_3\text{OH} + 1/2 \text{O}_2 \rightarrow \text{CH}_2\text{O} + \text{H}_2\text{O}$  [113]; this catalyst has a longer duration, but the degenerated catalyst can not be easily regenerated *on-site*.

### 5.1.1 Methanol Decomposition- and Transformation Reactions on Surfaces under Vacuum

On adsorption on metals or metal oxides, methanol undergoes a series of different possible decomposition and transformation reactions, which have been previously studied and discussed in literature. An overview over the main pathways discussed up to date will be given in the following two sections to supply a basis for discussion of the results obtained in this work; the first section covers decomposition on metals (limiting the discussion to the technically relevant metals of the groups VIII and IB), and is followed by a section addressing methanol decomposition and transformation on oxides.

#### Methanol Decomposition on Transition Metals (groups VIII & IB)

The typical decomposition steps of methanol on the surfaces of groups VIII- or IB-transition metals as discussed in literature are summarized in fig. 5.2.

---

<sup>2</sup>Earlier, also copper was used as a catalyst, but silver was found more active [109].

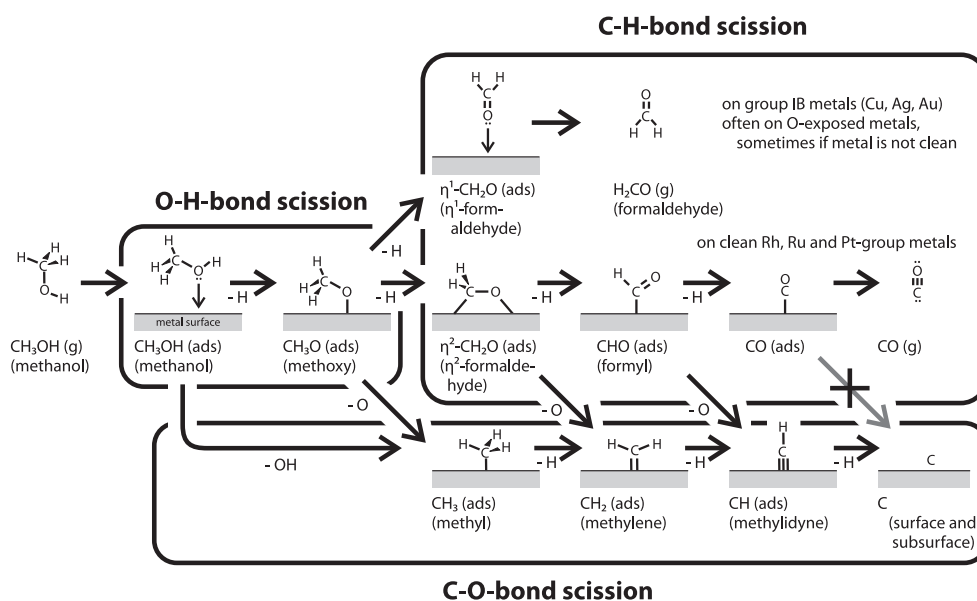


Figure 5.2: Possible methanol decomposition pathways and products on metal surfaces; see discussion in the text for references.

A good overview over the subject has been given by Mavrikakis and Barteau [22].

It is generally accepted that molecularly adsorbed methanol experiences its first bond rupture at the hydroxylic O-H bond at temperatures as low as 100 or 200 K, which leads to the formation of a methoxy (or *methoxide*) fragment. This process has been observed on different metal surfaces, including Pd(111) [114], defect-enriched Pd(111) [115], Pd(100) [116], Ni(111) [117], Ni(100) [118], Rh(111) [119], Rh(100) [120], Fe(100) [121], Ru(001) [122], Ag(110) [123], Cu(111) [124] (only in the presence of oxygen as a H-scavenger) or Cu(110) [125] (at 270 K); in most cases, methoxy formation has been observed by vibrational spectroscopy (HR-EELS or IRAS), and sometimes also by XPS.

The second fragment of methanol dissociation is a hydrogen atom, which is usually easily accommodated on metals, either at the surface, subsurface or in the bulk; for the group IB-metals Cu and Ag, however, it was argued that coadsorbed oxygen or sulfur atoms are necessary to accommodate the H-atoms as a scavenger [126, 127]. Coadsorbed oxygen was also described to facilitate the formation of methoxy on other metals, including Pd(111) [128]; in this paper, Davis and Barteau discuss different roles of surface oxygen, including its effect as a Brønsted base, or stabilization of methoxy on the surface. The detailed mechanism of H-abstraction by coadsorbed oxygen on Pd(100)

has been described by Jørgensen and Madix, who argue based on TPD and EELS experiments that the hydrogen atom is transferred through-space from the methanolic hydroxy-group to the surface oxygen atom [129].

Alkoxide-formation may generally be considered the first step in alcohol decomposition on metals; according to Mavrikakis and Barteau, several observations argue for this conception [22]; first, alcohols bind to metal surfaces by donation of lone-pair electrons centered at the oxygen atom in the hydroxyl group [125], so that an activation of methanol *via* the O-atom in the hydroxy group appears also very probable. In agreement with this expectation, great difficulties have been observed to activate ethers as compared to their respective alcohols [130]; additionally, even in this case, alkoxy groups are always the first decomposition products, indicating that activation starts on the O-atom.

Consequently, the methoxy fragment is often considered a key compound in methanol decomposition. Methoxy contains only two types of bonds, which undergo scission in two different pathways (see fig. 5.2). The three C-H-bonds in the methyl group are broken step-by-step in the *C-H-bond scission*-pathway (*dehydrogenation*) by  $\alpha$ -hydrogen abstraction; this pathway typically leads to the formation of CO as the ultimate reaction product, since CO does not undergo a possible further decomposition (by C-O-bond scission to carbon and oxygen atoms) on many metals, including Pd [115]. The second pathway proceeds additionally under rupture of the methanolic C-O-bond, and in combination with additional C-H-bond scission steps, different compounds (*carbonaceous species*) can be formed in this pathway (see fig. 5.2); carbon is usually the final product in this sequence. C-O-bond scission is usually found to be the less probable of the two processes, and the difference is so large that many earlier investigations of methanol decomposition in UHV systems failed to observe it (*e.g.* [131, 116]). The first UHV-observation of C-O-bond cleavage was presumably obtained by Hoffmann *et al.* on Ru(001) [132]; later it was also found on other metals, including Pd(111) [133, 134].

**C-H-Bond Scission.** The product of the first C-H-scission is a compound with the same stoichiometry as *formaldehyde*. It is well established that this compound can be accommodated on the surface in two different geometries, see fig. 5.2. One of them binds to the surface through an interaction of the lone-pair orbital of the oxygen atom (*monodentate*) and is often denoted  $\eta^1(\text{O})\text{-CH}_2\text{O}$  [22]; this relatively weakly bound species is anticipated to desorb quickly from the surface, thus making formaldehyde the final decomposition product. This monodentate bonding geometry is particularly expected to be

favoured by poor electron-donor metals such as the group IB-metals, or by metals with coadsorbed electrophiles (such as oxygen or sulfur). As a consequence, formaldehyde is usually obtained as the final decomposition product on Ag and Cu, and even on Pd in the presence of coadsorbed oxygen [128]; note also that Ag and Cu are used as catalysts in the industrial production of formaldehyde from methanol.

The second bonding mode of formaldehyde is *bidentate* (*chelating*) and denoted  $\eta^2(\text{C},\text{O})\text{-CH}_2\text{O}$ . In this mode, formaldehyde is bound by interaction between the  $\pi$ -orbital in the carbonyl group, and back donation of electron density from the metal to the carbonyl's  $\pi^*$ -orbital; only metals with high electron density available for back donation such as clean Pd(111) can support this bonding mode [22, 131].  $\eta^2(\text{C},\text{O})\text{-CH}_2\text{O}$  formaldehyde easily decomposes further by stepwise rupture of the remaining C-H-bonds, thereby intermediately forming the acyl-species HCO (*formyl*), and ultimately leading to carbon monoxide. Note how the surface intermediate changes from exclusively bonded *via* the oxygen atom (in methoxy) over the bidentate intermediate  $\eta^2(\text{C},\text{O})\text{-CH}_2\text{O}$  to one that is exclusively bonded *via* the carbon atom (in formyl and CO) during these processes. It was argued that the rate limiting step in the C-H-bond scission sequence of methanol is the transition from methoxide to the formaldehyde intermediate, and that the following steps occur so quickly, that direct spectroscopic evidences of surface-formaldehyde are rare [135, 131].

**C-O-Bond Scission.** It is unclear whether the C-O-bond scission-pathway is exclusively entered from the methoxy-intermediate, or if also the later intermediates in the C-H-bond scission pathway may decompose by C-O-bond scission. However, it is well established that the final product of the C-H-bond-scission pathway, carbon monoxide, does *not* undergo C-O-bond rupture to carbon and oxygen atoms on Pd, as it can do on some other metals such as Rh; this was *e.g.* shown for defect-enriched Pd(111) [115].

It was argued that C-O-bond scission can only happen above a certain limiting coverage of methanol on the surface [114], or that it might exclusively occur on defect sites [134, 136]. Yudanov, Neyman and Rösch [137] have predicted theoretically by DFT calculations that methanolic C-O-bond scission is an overall exothermic process on Pd nanoparticles, but not on Pd(111) single crystals; the authors argue that only the nanoparticles offer the opportunity to adsorb the resulting methyl group in strongly binding, unique on-top-sites at the edges between adjacent (111)-facets in the clusters, and that the high adsorption enthalpy released during adsorption of methyl on the cluster edges compensates for the activation energy of the

overall reaction, thereby rendering it exothermic; still, the activation energy for C-O-bond scission was calculated to be much higher than the barrier for the C-H-bond scission pathway, which allows to understand why C-O-bond scission is so slow compared to C-H-bond scission. In fact, it was experimentally shown that carbonaceous deposits from C-O-bond scission accumulate preferentially at the edges of Pd nanoparticles: Schauermaun *et al.* have studied the buildup of carbonaceous species formed by methanol decomposition on a Pd/Al<sub>2</sub>O<sub>3</sub> model catalyst by titrations with CO as a surface-sensitive probe molecule, and observed that the IRAS-signal for CO on the edge- and defects sites was significantly decreased on the methanol-exposed system as compared to a clean model catalyst; this was taken as an indication that the strongly dehydrogenated carbonaceous species initially accumulate – and most probably also form – at these sites [80]. Further IR experiments conducted by this group allowed to measure the rates of CO-formation from methanol (*i.e.*, the rate of C-H-bond scission) and the rate of C-O-bond scission (accumulation of strongly dehydrogenated carbonaceous species) individually; those experiments have shown that the rate of C-O-bond scission strongly decreases on the carbon-contaminated particles [138], unlike the kinetics of C-H-bond scission, which stays essentially identical (although, of course, the total CO yield decreases slightly due to the loss of some active surface by carbonaceous deposits). This observation indicates that C-O-bond scission on Pd nanoparticles is a structure-sensitive reaction and occurs preferentially on the particles' edges – in agreement with the theoretical calculations by Yudanov *et al.* [137] –, while C-H-bond scission may be structure insensitive.

Additional results on methanol decomposition on Pd nanoparticles were obtained by Kaichev, Morkel *et al.*, who have studied the decomposition of methanol on the alumina-supported Pd nanoparticles using XPS and SFG spectroscopy both in UHV and at elevated pressures. In these experiments, larger XPS-C1s-signals have been observed after prolonged exposure of methanol at 0.1 mbar and 400 K than what could be explained by a deposition of a monolayer of CH<sub>x</sub>; as an explanation, the authors have suggested that parts of the strongly dehydrogenated carbonaceous species may accumulate in the form of carbon in the bulk of the nanoparticles [139]. This hypothesis would be in a good agreement with recent theoretical calculation by Yudanov *et al.* [140], who suggest that migration of carbon from the surface hollow-sites on the Pd nanoparticles to certain subsurface octahedral sites is nearly isoenergetic, and thus a thermodynamically feasible process.

In addition to the formation of strongly dehydrogenated carbonaceous species or carbon, methane-formation has been observed and reported as another possible pathway during methanol-decomposition on a (1×1)-recon-

structed Pt(110) surface (together with carbon and hydrogen) [141, 142]; other reports of methane formation on metal during methanol decomposition under UHV conditions are unknown to us though.

**As a Summary,** the main aspect of methanol decomposition on transition metals may be seen in the antagonism between C-H- and C-O-bond scission. According to the results discussed in literature, C-H-bond scission in adsorbed methoxy seems to be the main route, and may lead to the formation of two products: formaldehyde (which is the typical product on group IB-metals) and – after rupture of additional C-H-bonds – carbon monoxide (CO), which is typical for group VIII-metals. The products from the less probable pathway including C-O-bond rupture are carbonaceous species or carbon; they accumulate on the surface or in the subsurface region and may lead to an observable blocking of the surface.

## Methanol Decomposition and Transformation on Metal Oxides

**Metal Oxides Differ from Reduced Metals** in many aspects of their stoichiometry and structure [23]. They are built up of two or more chemical species – one of them oxygen, the other(s) metal(s) –, and usually have very ionic characteristics (such as polarity), although some oxides also show covalent characters<sup>3</sup>.

The structure of oxides is often described as consisting of cation-anion site pairs, the cations being metal ions that may act as Lewis acids, and the oxygen anions acting as Lewis- and Brønstedt bases [23]. This concept of oxides helps to understand many of the reactions occurring on their surfaces, and the differences observed between oxides may be found in the different abilities of their active centers to act as acids or bases [23]. Due to this site-pair character, metal oxide surfaces possess an intrinsically higher level of structural complexity than those of reduced metals. Oxides may be terminated by metal cations of different charge states (such as in the spinel structure, see chapter 4.1) and by bridging or terminal oxygen species; they may also be completely oxygen terminated, exposing no metal centers to the vacuum side, or their surfaces may be polar when either cationic or anionic charges concentrate on the surface due to ion layering (as in FeO [144] and Fe<sub>3</sub>O<sub>4</sub> [82]). Finally, the higher complexity of metal oxide structures is also represented in a higher complexity of possible surface defects.

---

<sup>3</sup>A typical example for an oxide with largely covalent bonding is mercury(II) oxide (HgO) [143].



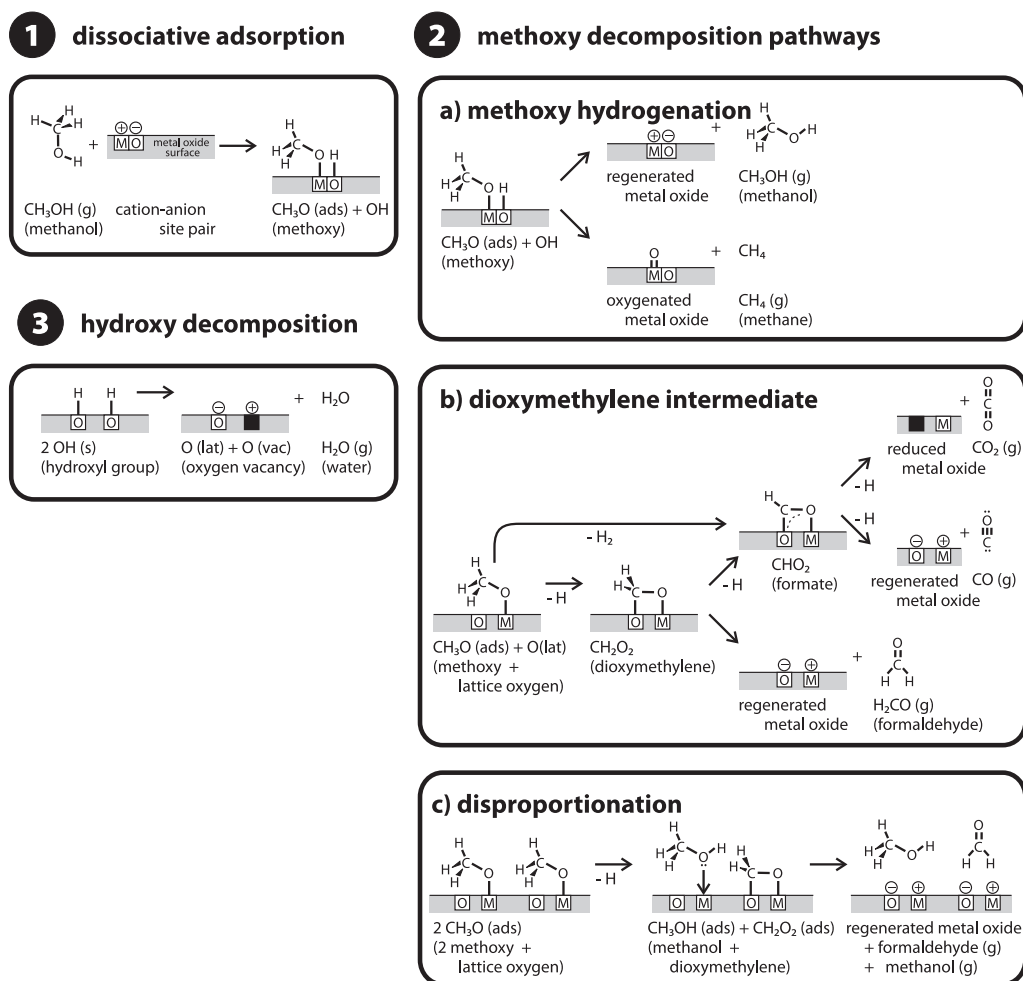


Figure 5.3: Methanol decomposition pathways and products as discussed for different metal oxides (see the discussion in the text for details and references). Tertiary reaction pathways – which may lead to the formation of coupled products such as ethers or esters – are not shown.

**Methoxy formation.** Because they are cations, the metal centers in oxides can not accommodate hydrogen *atoms* as reduced metals can do after a homolytic O-H-dissociation of methanol to methoxy; nevertheless, O-H-bond dissociation is also the initial activation step of methanol on metal oxide surfaces, but it exclusively proceeds *heterolytically* on oxides, as a Brønsted acid-base reaction between methanol and a cation-anion site pair exposed on the metal oxide surface (see fig. 5.3, sketch 1) [23, 145, 146, 147, 148, 149]. The proton that forms during this process is accommodated on oxygen anion sites in the form of surface hydroxyl groups; in fact, hydroxyl groups formed during heterolytic methanol dissociation could be experimentally detected, *e.g.* in vibrational spectra such as HR-EELS [148]. The conjugate base anion formed during the heterolytic dissociation is the methoxy ion, which coordinates to a coordinatively unsaturated metal center exposed at the oxide surface; its formation has been experimentally confirmed in numerous previous studies; before concentrating on the suggested mechanism of methanol decomposition reactions on oxides, some references for methoxy observations on different oxides are compiled in the following two paragraphs (together with the observed decomposition products):

Kim and Barteau have studied methanol adsorption and reaction on TiO<sub>2</sub>(001) single crystals by XPS and TPD experiments [145]; they have observed by XPS that methoxy formation occurs at the deposition temperature (200 K) and is related to proximate, coordinatively-unsaturated Ti cations and adjacent oxygen anions on the surface; several reaction channels have been observed on this surface: some of the methoxy species recombine with surface-related hydrogen to molecular methanol (which desorbs at 365 K); other parts of them decompose; different decomposition products have been observed, including methane, dimethylether, formaldehyde and CO; interestingly, the selectivity towards formaldehyde formation was observed to increase parallel to the surface oxygen concentration. In another study, Peng and Barteau have studied the dissociation of methanol (and other Brønsted acids) on magnesium oxide by XPS and ion-scattering spectroscopy (ISS) [147]; the authors report that methanol (and all the other Brønsted acids) dissociate on the MgO surface (based on XPS experiments), and that the conjugate base anion methoxy adsorbs on the exposed Mg<sup>2+</sup> ions on the oxide surface; at 300 K, methoxy was found to be the only surface species (and no molecular methanol was observed); the decomposition reactions of methoxy were not studied in this work. As the next example, Mensch, Byrd and Cox have studied methanol decomposition on stoichiometric and O-terminated chromium oxide ( $\alpha$ -Cr<sub>2</sub>O<sub>3</sub>(10 $\bar{1}$ 2)) using TPD experiments [149]; an earlier work with IRAS by Kittaka *et al.* had previously shown that methanol dissociates into methoxy when methanol is adsorbed on this surface at 300 K

[150]; Mensch *et al.* could show by a detailed product analysis in TPD experiments that many different methanol decomposition products form on this surface, including methane, formaldehyde, CO, CO<sub>2</sub> and H<sub>2</sub> at elevated temperatures; as the central reaction intermediates, dioxymethylene and formates have been detected (see next paragraphs). As a final example, Dilara and Vohs have studied methanol reactions on the zirconia (ZrO<sub>2</sub>) (100)- and (110)-surfaces using HR-EELS and TPD [148]; in this study, dissociative methanol adsorption (formation of methoxy) has been observed on both surfaces at the deposition temperature (125 K); in addition to the recombination to methanol (which occurs between 230 K and approx. 450 K and is the primary reaction pathway), CO and CH<sub>4</sub> have been observed as decomposition products on the (100) surface (at 630 K), and formaldehyde on the (110) surface (at 450 K).

Studies of methanol-dissociation on tin oxide SnO<sub>2</sub> by Gercher *et al.* [151] using TPD and XPS have shown that the surface methoxy yield depends strongly on the density of oxygen vacancies on the surface, and it has been observed to be maximal at an intermediate amount of those vacancies (defects); the authors see this observation as an indication that both oxygen vacancies (exposed metal ions) and surface oxygen species (*i.e.*, the availability of anion-cation site pairs) are necessary to allow for methoxy-formation on this oxide surface; also the yield of formaldehyde (a later decomposition product of methoxy that forms in two channels at 450 and 540 K) shows the same dependance on surface composition; consequently, SnO<sub>2</sub> has the highest activity for methanol decomposition to formaldehyde at intermediate amounts of oxygen vacancies. A similar observation has been made on two differently terminated surfaces of ZnO(000 $\bar{1}$ ) by Vohs and Barteau, who have applied a combination of TPD and XPS for their experiments [146]; methoxy has been observed by XPS to form between 160 and 400 K; interestingly, the two surfaces have shown different reactivities towards methoxy in TPD experiments: on a surface terminated both by oxygen- and metal ions, methoxy was found to decompose to formaldehyde and formate, while no decomposition products could be obtained from a surface that is exclusively O-terminated (and polar, as it is termed in the study).

**The Methoxy Intermediate.** As on reduced metal surfaces, the surface-bound methoxy species can also be seen as the central intermediate compound on metal oxides. Different possible reaction pathways of methoxy on oxides that have been discussed in the literature are depicted in fig. 5.3, part 2 (in three panels). The simplest possible reaction is the recombination of methoxy and a hydroxyl-hydrogen to molecular methanol (panel a), and in

fact, this reaction has been observed on mostly any oxide, and in some cases it was even described to be the main reaction pathway (*e.g.* for  $\text{ZrO}_2$  [148] and  $\text{TiO}_2$  [145]). Alternatively, recombination may also proceed in connection with C-O-bond scission, resulting in methane-formation and oxidation of the oxide (see fig. 5.3 part 2, panel a); this reaction has been observed on oxygen-deficient metal oxide surfaces of  $\text{TiO}_2$  [145],  $\alpha\text{-Cr}_2\text{O}_3$  [149] or  $\text{ZrO}_2$  [148].

**The Dioxymethylene Intermediate.** In analogy to the decomposition of methanol on metal surfaces, C-H-bond scission is also a major reaction pathway on oxides; but, possibly due to the lower ability of oxides to accommodate hydrogen [152], C-H-bond scission on metal oxides typically proceeds with higher selectivity towards formaldehyde than CO (which is the main product on many transition metals, see above); formation of formaldehyde has been observed on  $\text{ZrO}_2(110)$  [148],  $\text{TiO}_2(001)$  [145],  $\alpha\text{-Cr}_2\text{O}_3(10\bar{1}2)$  [149],  $\text{ZnO}(0001)$  [146],  $\text{Cu}_2\text{O}(100)$  [153],  $\text{CeO}_2(111)$  [152] or  $\text{SnO}_2$  [151]; Mullins and coworkers have studied methanol decomposition (and formation of formaldehyde) on ceria ( $\text{CeO}_2$ ) [152], and the groups of Shaikhutdinov and Kuhlenbeck in our department have studied formaldehyde yield during methanol decomposition on the vanadium oxides  $\text{V}_2\text{O}_3(0001)$  [154] and  $\text{V}_2\text{O}_5(001)$  [155] (thin films, both on  $\text{Au}(111)$ ), as well as on  $\text{V}_2\text{O}_3$  particles grown on silica [156] and ceria [157]. Mullins *et al.* have observed that formaldehyde forms on a pristine  $\text{CeO}_2(111)$  oxide (and desorbs at 560 K in TPRS experiments), but this reactivity towards formaldehyde formation has been observed to decrease in the later repetition cycles; instead, more and more CO and hydrogen desorb as decomposition products; this change in selectivity towards different products of C-H-bond scission was ascribed to the loss of surface oxygen from the surface of the oxide. The experiments on the vanadium oxides show that formaldehyde can be obtained as a product on mildly reduced vanadium oxides, which were either obtained by electron exposures [154, 155], or a mild oxidation treatment [157]; formaldehyde can not be obtained both on the fully oxidized  $\text{V}_2\text{O}_3(0001)$  and  $\text{V}_2\text{O}_5(001)$  films, and also not on too strongly reduced oxide surfaces. Those results were taken as an indication that both the exposed metal and oxygen ions (*i.e.*, cation-anion site pairs) are necessary for the reaction. In many of those studies, also a deactivation has been observed, which has been ascribed to surface oxygen loss in the course of formaldehyde formation, and indicates that reoxidations of the oxide are required in order to obtain a sustained reactivity.

Fig. 5.3, sketch 2 b) shows how formaldehyde is thought to be formed on metal oxides [23]: an intermediate *dioxymethylene* compound – which is

structurally identical to the  $\eta^2$ -formaldehyde species found on metals – is formed by C-H-bond scission on oxides; it contains lattice oxygen from the oxide and has been suggested as reaction intermediate based on the observation that oxygen exchange between the oxygen of the oxide and the adsorbed methoxy can occur (as can be proofed by isotope labeling experiments) [149]; note that this oxygen exchange with the lattice could not be explained by a dehydrogenation of methoxy under formation of formaldehyde that is coordinated exclusively *via* the molecular O-atom (as in the  $\eta^1$ -formaldehyde species on metals). Additionally, dioxymethylene has also been spectroscopically detected by HR-EELS and XPS [148]. As a rationale, it has been suggested that the formation of formaldehyde on oxide surfaces would require a bi-functional acid-base surface, which contains both a mildly basic oxygen species to accept protons released during methoxy formation, and more weakly acidic cationic sites that bind methoxy strong enough, but still allow desorption of later decomposition products (formaldehyde) [158].

Interestingly, it has been repeatedly observed in TPRS experiments of methanol from oxides that methanol and formaldehyde desorb virtually simultaneously (*e.g.* from  $\text{CeO}_2$  [152] or  $\text{V}_2\text{O}_3$  [156]). This behaviour has been interpreted as an indication that the reaction of surface-bound methoxy to dioxymethylene is the rate-limiting step [152]; thus, as soon as dioxymethylene formation by nucleophilic attack of lattice oxygen on the methoxy-carbon atom followed by  $\alpha$ -H-abstraction is activated, the hydrogen would be quickly transferred to another methoxy species to form molecular methanol. If the formation of dioxymethylene is the rate limiting step and occurs only at temperatures above the desorption limit of the products, both formaldehyde and methanol may desorb simultaneously, as it has been observed.

Another observed fate of the dioxymethylene intermediate is dehydrogenation to formate (see fig. 5.3, 2 b), which is the analogous compound to the formyl species on metal surfaces; formate can either desorb as formic acid (not shown in fig. 5.3), or dehydrogenate further to CO, or – under incorporation of a lattice oxygen and reduction of the metal oxide – to  $\text{CO}_2$ . Vohs and Barteau have identified surface formates from methanol decomposition on  $\text{ZnO}(0001)$  by XPS and by comparison of TPRS experiments with adsorbed methanol, formaldehyde or formic acid [146]; their experiments indicate that the relative yields of CO and  $\text{CO}_2$  during decomposition of adsorbed formaldehyde depends on the extent of surface reduction of the  $\text{ZnO}(0001)$ : oxygen-deficient oxide surfaces favour the formation of the less oxidized product CO.

**Decomposition of Hydroxyl-Groups.** Surface hydroxyl groups decompose by at least two reactions, see fig. 5.3: in addition to recombination with methoxy to methanol, two surface hydroxyl groups may disproportionate into water and surface oxide (panel 3).

**Concluding,** the following products have been observed during the decomposition of methanol on metal oxides: molecular methanol, formaldehyde, methane, formic acid, CO and CO<sub>2</sub>; side products are water and H<sub>2</sub>. Surface hydroxyl groups formed during the heterolytic dissociation of methanol on the oxide act as a hydrogen storage, but can also desorb by a disproportionation into water and lattice-oxygen on the surface. Note that tertiary products were not discussed here; they may form by condensation of surface intermediates, and include dimethylether, dimethoxymethane, methylformate, or hydrocarbons (such as ethylene or acetylene) – see [23] for further information.

## 5.2 Methanol Adsorption, Desorption and Reaction on Fe<sub>3</sub>O<sub>4</sub>

### 5.2.1 Methanol Decomposition Investigated by Vibrational Spectroscopy

Fig. 5.4 a) shows IRAS spectra of fully deuterated methanol (methanol-*d*<sub>4</sub>, CD<sub>3</sub>OD) adsorbed at 115 K on the Fe<sub>3</sub>O<sub>4</sub>(111) thin film in the coverage range between 0 to 11.7 L (multilayer exposures); note that the methanol sticking coefficient at the low adsorption temperature of 115 K is 1 over infinite exposures (see [159]).

At low exposures (0.8 L), three peaks appear simultaneously at  $\sim 2076$ , 2045 and 1127 cm<sup>-1</sup>; with further increasing exposure, additional peaks emerge at  $\sim 2242$ , 2214, 1064 and 983 cm<sup>-1</sup> (those values are the peak positions at the highest coverage); additionally, a very broad feature appears, which shows a strong peak shift with increasing coverage from  $\sim 2250$  cm<sup>-1</sup> at 1.6 L to  $\sim 2446$  cm<sup>-1</sup> at 11.7 L.

#### Peak Assignments

The peaks in the spectrum were assigned by reference to literature data; those references are summarized in table 5.1. The labels for vibrational modes are

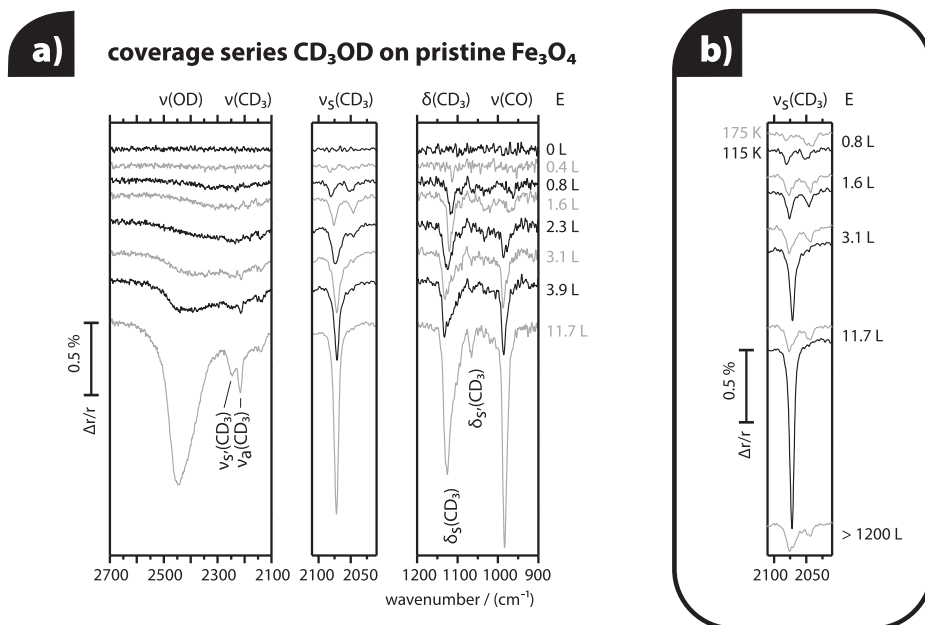


Figure 5.4: a) Coverage series of deuterated methanol on pristine  $\text{Fe}_3\text{O}_4$  at 115 K. b) Comparison of coverage series at 115 and 175 K at low and very high coverages for the  $\nu_s(\text{CD}_3)$ -region.

based on the point groups  $C_{3v}$  for methoxy and  $C_s$  for methanol to represent the highest possible symmetries for those adsorbates<sup>4</sup>.

Fig. 5.5 shows the peak-assignment for two spectra at coverages of 1.6 and 11.7 L together with simplified graphical representations of the vibrational modes. According to this assignment, the main peaks in the low-coverage spectra can be assigned to the symmetric stretching mode  $\nu_s(\text{CD}_3)$  in the methyl group of molecular methanol ( $\sim 2076 \text{ cm}^{-1}$ ) and methoxy ( $\sim 2045 \text{ cm}^{-1}$ ), and to the methyl group's symmetric deformation mode  $\delta_s(\text{CD}_3)$  at  $1127 \text{ cm}^{-1}$ . This unambiguous assignment based on literature data clearly states that both molecular methanol and methoxy accumulate on the surface of the model catalyst even at the low exposure temperature of 115 K, indicating that the oxidic support  $\text{Fe}_3\text{O}_4$  is capable to dissociate methanol to methoxy.

It is apparent that the spectrum at the higher coverage (11.7 L) shows additional peaks compared to the spectrum at the lower coverage, including the asymmetric methyl stretching mode  $\nu_a(\text{CD}_3)$  and the hydroxyl group's

<sup>4</sup>Note that the surface as part of the adsorbate is neglected in these assignments, since an analysis of spectra has shown that they can be understood based on the *local* symmetry of the adsorbate [160].

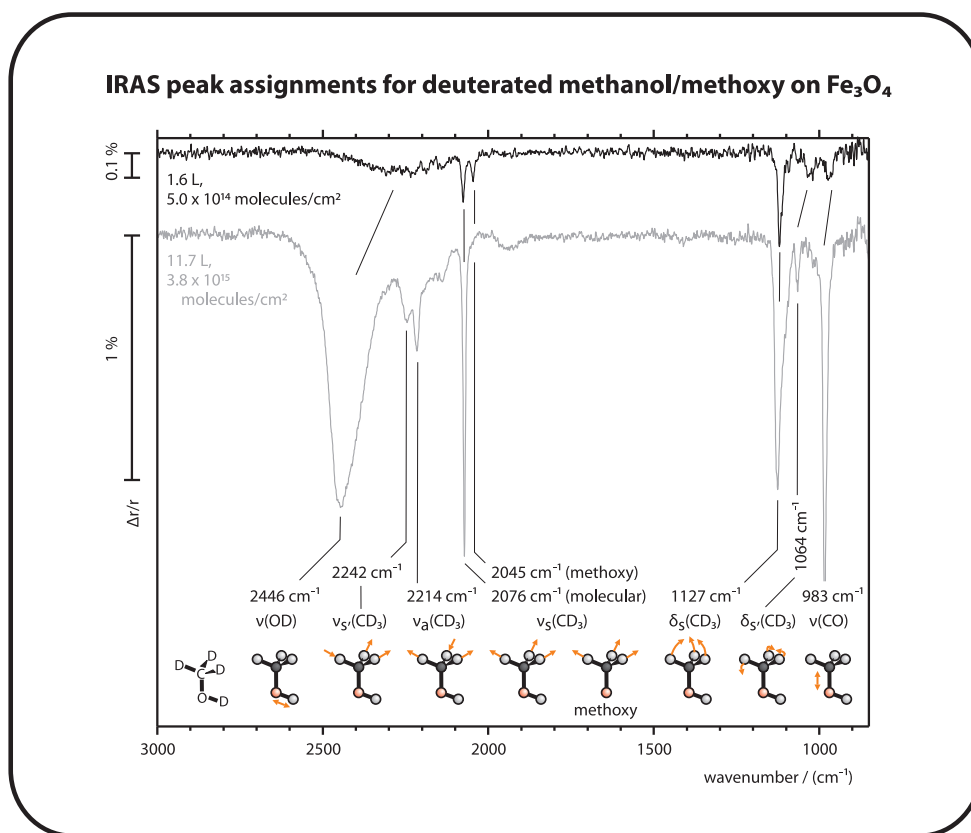


Figure 5.5: Peak assignments for deuterated methanol and methoxy, after [118]. Adsorbed on  $\text{Fe}_3\text{O}_4$  at 115 K, exposures: 1.6 (mono-) and 11.7 L (multilayer).

stretching mode  $\nu(\text{O-D})$ ; it is important to note that these modes differ remarkably in their symmetry properties from the modes observed in the low-coverage spectra ( $\nu_s(\text{CD}_3)$  and  $\delta_s(\text{CD}_3)$ ), which only have a dynamic dipole moment parallel to the C-O-bond; the modes  $\nu_a(\text{CD}_3)$  and  $\nu(\text{O-D})$  that emerge only at higher coverages on the other hand change the molecular dipole moment mainly in a plane *perpendicular* to this bond. In consideration of the metal-surface selection rule (MSSR), those differences may be seen as indications that the molecules in the low-coverage spectra are oriented with the C-O-bond perpendicular to the surface, so that the modes  $\nu_a(\text{CD}_3)$  and  $\nu(\text{O-D})$  could not be observed; at high coverages, on the other hand, the molecules seem to adopt also other orientations with respect to the surface, allowing for an observation of these modes. However, those interpretations should be seen with a precaution because the modes which are unobservable in the low coverage spectra are modes with small transition dipole moments, and thus their spectral intensities may simply be too low to be observed.



Table 5.1: Assignment between methanol CD<sub>3</sub>OD vibrational modes and observed peaks in IRAS sub-monolayer and multilayer spectra (on Fe<sub>3</sub>O<sub>4</sub>, fig. 5.5).

vibrational mode	observed energy / (cm <sup>-1</sup> )			
	this work	Ar matrix (15 K), [161]	Ni(100), [118]	Cu(100), [162]
$\nu(\text{O-D})$	2446	2705	2446	2441
$2\delta_s(\text{CD}_3)$		2266	2245	2218
$\nu_{s'}(\text{CD}_3)$	2242	2254	–	–
$\nu_a(\text{CD}_3)$	2214	2218	2218	2218
$\nu_s(\text{CD}_3)_{\text{methanol}}$	2076	2078	2073	2073
	$\nu_s(\text{CD}_3)_{\text{methoxy}}$ 2045	–	2059	2054
$\delta_s(\text{CD}_3)_{\text{methanol}}$	1127	1133	1125	1126
	$\delta_s(\text{CD}_3)_{\text{methoxy}}$ 1090	–	1096	1095
$\delta_{s'}(\text{CD}_3)$	1064	1080	1070	1066
$\nu(\text{C-O})$	983	983	983	983

The assignment of the peak at 2242 cm<sup>-1</sup> is unclear. Serrallach *et al.* list two bands observed at 2266 (weak) and 2254 cm<sup>-1</sup> (medium intensity) in spectra of fully deuterated methanol embedded in an Ar matrix at 15 K, and assign the peak at higher energy to the overtone  $2\delta_s(\text{CD}_3)$  of the symmetric deformation mode, and the peak at lower energy to the stretching mode  $\nu_{s'}(\text{CD}_3)$  based on a detailed normal coordinate analysis [161]. Camplin and McCash [162], who studied methanol adsorbed on oxidized Cu(100), list only one spectral feature in this region, at 2218 cm<sup>-1</sup>; it was assigned to the overtone of the symmetric deformation *and* the *asymmetric* stretching mode  $\nu_a(\text{CD}_3)$  (*i.e.*, the two modes overlap). Finally, Huberty and Madix – who studied methanol multilayers on Ni(100) – observed only one peak around 2245 cm<sup>-1</sup>, which was assigned to the overtone of the symmetric deformation mode. Those authors have also discussed the possibility of a Fermi-resonance between the symmetric stretching mode  $\nu_s(\text{CD}_3)$  and the overtone of the symmetric deformation mode,  $2\delta_s(\text{CD}_3)$ , because such a Fermi-resonance was observed in isotopically normal methanol; however, due to the larger frequency difference of the respective modes in the deuterated methanol compared to the case in the isotopically normal isotopomer, the authors argue that this Fermi-resonance is reduced – thus, the peak was assigned to  $2\delta_s(\text{CD}_3)$ . As a

consequence of those references, a clear assignment of the peak observed at  $2242\text{ cm}^{-1}$  in our work based on literature values is impossible; most probably, the peak either needs to be assigned to the overtone of the symmetric deformation mode  $\delta_s(\text{CD}_3)$  or to the stretching mode  $\nu_{s'}(\text{CD}_3)$ .

One of the reasons for us to apply deuterated methanol  $\text{CD}_3\text{OD}$  instead of isotopically normal methanol  $\text{CH}_3\text{OH}$  is that the strong *Fermi*-resonances observed between the overtone  $2\delta_s(\text{CH}_3)$  and the mode  $\nu_s(\text{CH}_3)$  in normal methanol are neglectable in the deuterated isotopomer. However, a different resonance has to be considered though, which establishes in the deuterated molecule between the symmetric deformation  $\delta_s(\text{CD}_3)$  and the C-O-stretching mode  $\nu(\text{C-O})$ , since they are sufficiently close in energy to enable a strong coupling; this coupling results – together with shifts of the vibrational frequencies – in a strong intensity transfer from the C-O-stretching mode into the otherwise relatively weakly absorbing deformation mode [162], making it the most prominent mode in low-coverage spectra of methanol or methoxy; therefore, it can be used as a sensitive probe for the presence of those species.

Methoxy was often described in literature to be oriented with the C-O-bond perpendicular with respect to the adsorbent surface; this notion is supported by many experiments, including IRAS [163, 118] and photoelectron diffraction experiments [164, 165]. Assuming perpendicular orientation of methanol and methoxy, only the modes  $\nu(\text{C-O})$ ,  $\delta_s(\text{CD}_3)$  and  $\nu_s(\text{CD}_3)$  possess a dipole moment that is oriented exactly perpendicular to the surface and should be IRAS-active. Additionally, the modes  $\nu(\text{O-D})$  and  $\delta_{s'}(\text{CD}_3)$  have *small* components of the dynamic dipole moment perpendicular to the surface and thus may give rise to weak vibrational features. In fact, this is exactly what has been detected in the submonolayer-spectrum displayed in fig. 5.5: the symmetric stretching mode of the methyl group  $\nu_s(\text{CD}_3)$  and the symmetric deformation mode  $\delta_s(\text{CD}_3)$  are the strongest modes in the spectrum, and the mode  $\delta_{s'}(\text{CD}_3)$  and the O-D-stretching mode (which appears as a broad, relatively weak feature between  $2100$  and  $2500\text{ cm}^{-1}$ ) contribute only weakly.

The spectral feature in the sub-monolayer spectrum that is most important for our purpose is the peak observed at  $2045\text{ cm}^{-1}$ , which is assigned to the symmetric methyl-stretching mode  $\nu_s(\text{CD}_3)$  in the methoxy fragment, while the same mode in *molecular* methanol gives rise to the peak observed at  $2076\text{ cm}^{-1}$ ; those peaks are so important for us since they allow us to discriminate between methanol and methoxy. The red-shift of the frequency for the methyl group’s symmetric stretching mode in the methoxy fragment with respect to molecular methanol is well established in literature [118, 162, 163].

**Coverage-Dependance of Methanol IRAS Spectra.** Looking again at the detailed coverage-dependence of the spectra as displayed in fig. 5.4 a), it is apparent that the peak for the symmetric deformation mode is the first feature that emerges clearly. Then, the symmetric methyl stretching mode  $\nu_s(\text{CD}_3)$  appears at frequencies of  $\sim 2076$  and  $2045 \text{ cm}^{-1}$ ; the simultaneous appearance of those features indicates that molecularly adsorbed methanol and methoxy accumulate simultaneously on the surface at low coverage. This parallel accumulation of methanol and methoxy may be explained by two different models; for one, it may be due simply to the presence of different adsorption sites on the oxide surface, of which only one possesses the ability to decompose methanol into methoxy at 115 K; this explanation, however, may be problematic, because molecularly adsorbed methanol might be considerably mobile on the oxide surface, even at this temperature [166] – in which case, all molecularly adsorbed methanol would be expected to quickly migrate to the dissociation-active sites to dissociate into methoxy, until the surface is saturated with this species, and only then molecular methanol would begin to accumulate. The alternative explanation for the simultaneous buildup of methanol and methoxy spectral features does not possess this complication: the two species are conjugated Brønstedt acids and bases, and their simultaneous presence on the surface may simply reflect the acid-base equilibrium.

With increasing coverage and the buildup of multilayers (from approx. 1.6 L), the intensity of the  $\nu_s(\text{CD}_3)$  mode in methoxy is transferred more and more into the same mode in molecular methanol, so that the distinct peak for methoxy observed in low-coverage spectra shifts into a shoulder of the further increasing peak of molecular methanol, until it finally disappears in it.

Exposure-dependant IRAS experiments were also conducted at the higher temperature of 175 K; fig. 5.4 b) shows the  $\nu_s(\text{CD}_3)$  spectral region after different identical exposures at 115 and 175 K. While the peak positions and spectral intensities at low, (sub)monolayer coverages (0.8 and 1.6 L) are nearly identical at the two temperatures, strong differences evolve as soon as the monolayer is saturated (3.1 and 11.7 L): while the intensity in the experiments at low temperature keeps to rise, the spectra obtained at 175 K stay essentially identical to the spectrum obtained at 1.6 L (approx. one monolayer), and even after an exposure of 1200 L, no significant difference is observed. This behaviour clearly indicates that multilayers of methanol (*methanol ice*) do not build up on the surface at 175 K and above, as they do at 115 K above an exposure of  $\sim 1.6$  L.

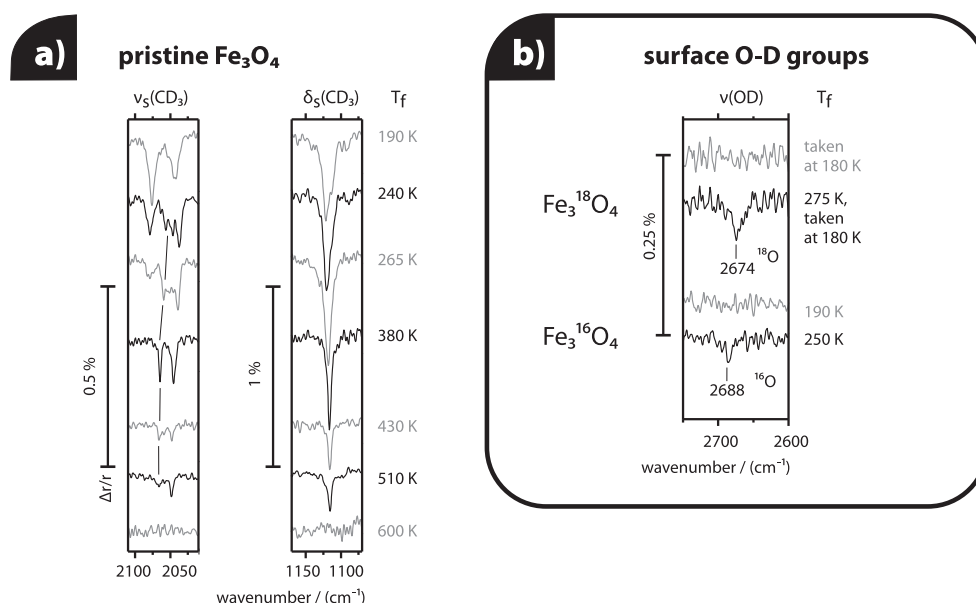


Figure 5.6: IRAS spectra obtained as a function of annealing temperature  $T_f$  of a multilayer of  $\text{CD}_3\text{OD}$  (11.7 L) adsorbed on pristine  $\text{Fe}_3\text{O}_4$  at 115 K. a) Region of the  $\nu_s(\text{CD}_3)$  and  $\delta_s(\text{CD}_3)$ -mode in methanol and methoxy. b) O-D stretching mode region of surface O-D groups on  $\text{Fe}_3\text{O}_4$  and  $^{18}\text{O}$ -labelled  $\text{Fe}_3^{18}\text{O}_4$ .

### Molecular Transformations in IR Experiments as a Function of Temperature

In order to study the thermally induced transformations of methanol on  $\text{Fe}_3\text{O}_4$ , and also the desorption of this reactant and possible transformation products, the following IRAS experiments have been conducted: 11.7 L of deuterated methanol  $\text{CD}_3\text{OD}$  were adsorbed on the pristine iron oxide at 115 K, and then the sample was repeatedly heated to different, increasing temperatures (190, 240, 265, 380, 430, 510 and 600 K) for short times and then cooled again to 115 K in each cycle to record an IRAS spectrum of the newly formed and remaining surface species. The results of this experiment series is displayed in fig. 5.6 a).

After heating to 190 K, the multilayers have desorbed (see previous section) and the spectrum shows the typical structure of coadsorbed methanol and methoxy with clearly distinguished peaks for the  $\nu_s(\text{CD}_3)$ -mode at  $\approx 2076$  (molecular methanol) and  $\approx 2045 \text{ cm}^{-1}$  (methoxy), and additionally the peak at  $\approx 1125 \text{ cm}^{-1}$  ( $\delta_s(\text{CD}_3)$ ), as it was also observed in the submonolayer spectrum at 115 K discussed previously.

Upon heating to 240 K and 265 K, the signal of molecularly adsorbed methanol at  $2076\text{ cm}^{-1}$  attenuates, and a new feature *emerges* at  $\approx 2056\text{ cm}^{-1}$  (marked in fig. 5.6 a) with a line). Between 265 and 380 K, the peak for molecular methanol ( $2076\text{ cm}^{-1}$ ) vanishes completely. The following heating steps in the flash series (380, 430 and 510 K) did not induce further spectral features – which could be indicative of other decomposition intermediates such as dioxymethylene<sup>5</sup>; however, the intensities in all features drop with each heating step. After annealing to 600 K, the spectrum shows a surface free of any IR-active adsorbate, suggesting a desorption of surface species between 510 and 600 K.

Fig. 5.6 b) shows the spectral region of surface O-D-groups as observed in temperature-dependant IRAS experiments with methanol  $\text{CD}_3\text{OD}$  on isotopically normal  $\text{Fe}_3\text{O}_4$  and  $^{18}\text{O}$ -labelled  $\text{Fe}_3^{18}\text{O}_4$ . For those experiments, multilayers of deuterated methanol were adsorbed; the spectra on the isotopically labelled  $\text{Fe}_3^{18}\text{O}_4$  were recorded at 180 K, the spectra on the normal  $\text{Fe}_3\text{O}_4$  were taken at 115 K. The spectrum obtained on the isotopically labelled  $\text{Fe}_3^{18}\text{O}_4$  directly after adsorption at 180 K did not exhibit any spectral signatures for O-D-groups; the same is true for the isotopically normal  $\text{Fe}_3\text{O}_4$  after heating to 190 K and cooling back to the exposure temperature (115 K); note that heating to 180 K is sufficient to desorb the multilayers of methanol. This situation changed after heating the sample to 250 K (isotopically normal oxide) or 275 K (isotopically labelled oxide), which induced the appearance of peaks at  $2688\text{ cm}^{-1}$  (on the isotopically normal oxide) or  $2674\text{ cm}^{-1}$  (on the  $^{18}\text{O}$ -labelled oxide). However, those features have disappeared again from the spectrum after heating the sample to 380 K (only tested on the isotopically normal oxide; spectrum not shown).

**Interpretation.** The transformations occurring in the  $\nu_s(\text{CD}_3)$ -region between 240 and 265 K can be interpreted – based on the assignments of vibrational modes in methanol and methoxy comprised in table 5.1 – as the formation of a second type of methoxy from methanol that has been molecularly adsorbed at the surface up to this temperature; the occurrence of two spectral features for methoxy species in the  $\nu_s(\text{CD}_3)$ -region might be explained by methoxy-species adsorbed at two different surface sites; the appearance of one of those species only at an elevated temperature around 250 K might further indicate that also its formation is associated with a certain site (presumably the adsorption site) with a different activity towards methanol dissociation than the sites which decompose methanol already at the deposition temperature (115 K) into the first observed methoxy species.

---

<sup>5</sup>Dioxymethylene possesses two O-C-O modes  $\nu_a$  and  $\nu_s(\text{O-C-O})$  that could be expected to give rise to intense peaks around  $\sim 1000$  and  $1150\text{ cm}^{-1}$  [148].

The spectral intensity for molecularly adsorbed methanol decreases completely between 265 and 380 K; this might be understood by the transformation into the second methoxy species discussed in the last paragraph, but it may be additionally related to a desorption in this temperature range; the issue will soon be further discussed based on the TPRS experiments. Also the spectral intensity of the two methoxy species decreases between 265 and 510 K, but significant parts of them remain present on the surface up to a temperature between 510 and 600 K, which is a relatively high temperature for a methoxy species adsorbed on the surface – in many cases, methoxy species desorb from oxide surfaces by recombinative desorption (see fig. 5.7) at considerably lower temperatures<sup>6</sup> [23]; thus, it seems that not all of the adsorbed methoxy fragments have the option to recombine and desorb. This observation will be explained in the following paragraphs:

**Formation of Fe<sub>3</sub>O<sub>4</sub>-related O-D-Groups.** The appearance of the O-D-groups took place in the same temperature region as the formation of the second type of methoxy species (between 240 and 265 K). Remember that methoxy formation on oxides is generally understood as a heterolytic dissociation (Brønstedt acid-base reaction, see fig 5.3, sketch 1), after which the methoxy species formed are coordinated to an exposed metal ion of the oxide, while the proton is accommodated on surface oxygen in the form of a surface O-D-group. Those hydroxyl groups stand relatively upright on the surface and should contribute strongly to IR spectra – however, in many cases they are found to be undetectable in IR experiments due to their high propensity for hydrogen bonding with other surface species which leads to strong line broadening. Thus, there are in fact two possible reasons that could explain why the O-D-groups appear in the spectra only after heating to approx. 250 K, but that they are invisible after heating to 190 K: they may either be formed in an activated process at a temperature between 190 and 250 K, or they may be present on the surface before, but their spectral feature may be so broad due to formation of hydrogen bonds with other species (methanol or methoxy), that it is not observable in IRAS spectra – this situation might only change when the surface is heated to 250 K due to the onset of molecular methanol-desorption. In fact, we believe that both processes have an influence on our observations: for one, we do know from the observations discussed in the previous paragraph that fractions of the adsorbed methanol have already dissociated into methoxy at the low exposure temperature of 115 K, so that surface-hydroxyl groups should be present at the surface al-

---

<sup>6</sup>Note that methoxy can not desorb into the gas phase unreacted, because it is an unsaturated species.

ready after the methanol dosage at 115 K; however, it is very possible that these species are invisible in IRAS spectra due to the high surface coverage with methanol in multi- and monolayers at 115 K, and probably also – even after desorption of the multilayers – above 190 K (because molecular methanol is still adsorbed); only with the onset of methanol desorption from the monolayer (around 250 K), the coupling *via* hydrogen bonds decreases. On the other hand, the above discussed IRAS spectra clearly indicate the dissociation of further amounts of the molecularly adsorbed methanol starting around 240 K; of course, this process produces further O-D-groups, thereby increasing the surface coverage with hydroxyl groups. Thus, this complex interplay of processes might account for the observation of surface-hydroxyl groups at the elevated temperature.

The assignments for the spectral features of O-D-groups were made according to literature data for  $\text{Fe}_3\text{O}_4$  [167, 168]. Leist, Ranke and Al-Shamery studied adsorption of deuterium oxide ( $\text{D}_2\text{O}$ ) on the epitaxially grown  $\text{Fe}_3\text{O}_4$  film [167] by TPRS and IRAS and found different adsorption states for water: multilayer, physisorbed and chemisorbed water (denoted  $\alpha$ ,  $\beta$  and  $\gamma$ ). The thermodynamically most stable species (chemisorbed water,  $\gamma$ -species) desorbs from the surface at  $\sim 290$  K at lowest exposures, where it is the only water surface species. It was found to give rise to two intense IRAS peaks at 2712 and 2691  $\text{cm}^{-1}$ ; since these values are typical for free O-D-groups, the authors concluded that the  $\gamma$ -species must be a dissociated water species as shown in fig. 5.7 sketch 3. In combination with the results of the earlier work by Joseph, Ranke and Weiss [168] – who studied water adsorption on the same oxide film by photoelectron spectroscopies (UPS and XPS) as well as TPD –, the authors proposed to assign one of the spectral features to an O-D-group that contains the oxygen of the dissociated water and coordinatively binds to an exposed Fe ion on the surface, and the other one to a surface O-D-group formed by the Brønstedt-acid-base-reaction between a basic oxygen ion on the  $\text{Fe}_3\text{O}_4$ -surface and the deuteron  $\text{D}^\oplus$  released during water dissociation; however, an unambiguously clear assignment was impossible. By reference to our data as shown in fig. 5.6 b), we suggest to assign the feature observed on the isotopically normal oxide film at 2688  $\text{cm}^{-1}$  to an O-D-group formed in the Brønstedt-acid-base-reaction between methanol and a basic oxygen site exposed on the oxide film, because the spectral feature at 2712  $\text{cm}^{-1}$  described by Leist *et al.* could not be observed in our work. Note that the observed disappearance point of the O-D-groups from the spectra between 275 and 380 K is also in agreement with the literature data [167, 168].

Another fact supports the assignment of the observed vibrational mode to a surface O-D-group containing oxygen from the oxide lattice: the observed

vibrational frequencies for this species are different for an isotopically normal film (mainly  $^{16}\text{O}$ ) and for an  $^{18}\text{O}$ -labelled  $\text{Fe}_3\text{O}_4$ -film. The vibrational frequency of this group can be roughly estimated using the literature value for the frequency of the isotopically normal O-D-group  $E_{16\text{O}}=2691\text{ cm}^{-1}$ ; assuming the behaviour of a harmonic oscillator and identical force constants for the isotopomers, the calculated vibrational frequency  $E_{18\text{O}}$  for the  $^{18}\text{O}$ -D-group would be  $E_{18\text{O}} = E_{16\text{O}} \cdot \sqrt{\mu_{16\text{O}}/\mu_{18\text{O}}} = 2691\text{cm}^{-1} \cdot \sqrt{\frac{16 \cdot 2}{(16+2)}/\frac{18 \cdot 2}{(18+2)}} = 2674\text{cm}^{-1}$ . In fact, similar values were experimentally observed, as shown in fig. 5.6 b).

### surface hydroxy decomposition

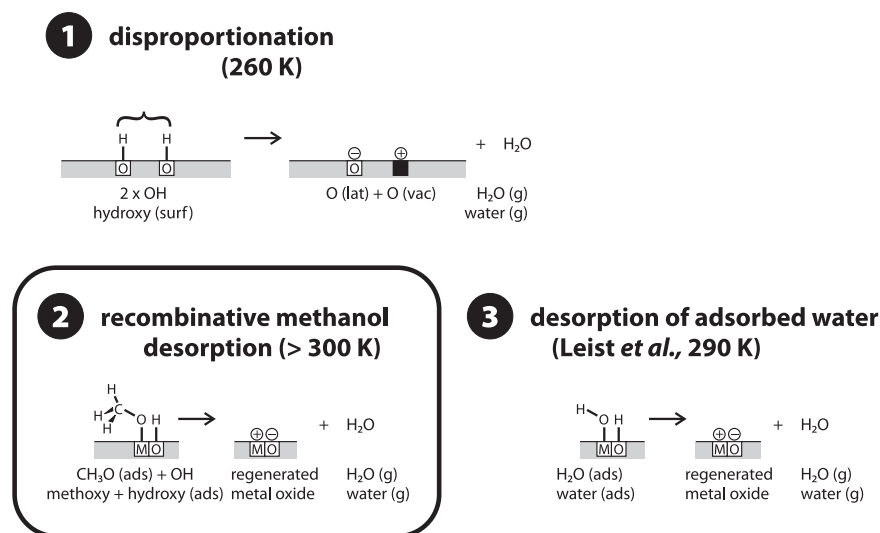


Figure 5.7: Different processes for the decomposition of  $\text{Fe}_3\text{O}_4$  oxide-related O-D-group during desorption experiments (see text for details).

## 5.2.2 Repeated Temperature-Programmed Reaction-Experiments

In the next step, we studied the decomposition of methanol  $\text{CD}_3\text{OD}$  on  $\text{Fe}_3\text{O}_4$  in repeated temperature-programmed reaction-desorption experiments (TPRS); a total of four repetition cycles was conducted without intermediate treatments of the oxide such as cleaning or reoxidation to allow studying a possible change of the oxide support during the experiments, *e.g.* by carbon deposition or loss of surface oxygen. For those studies, a sample of freshly prepared, annealed  $\text{Fe}_3\text{O}_4$  was first exposed to multilayers (11.7 L) of deuterated methanol at 115 K, followed by the TPRS experiment with a heating



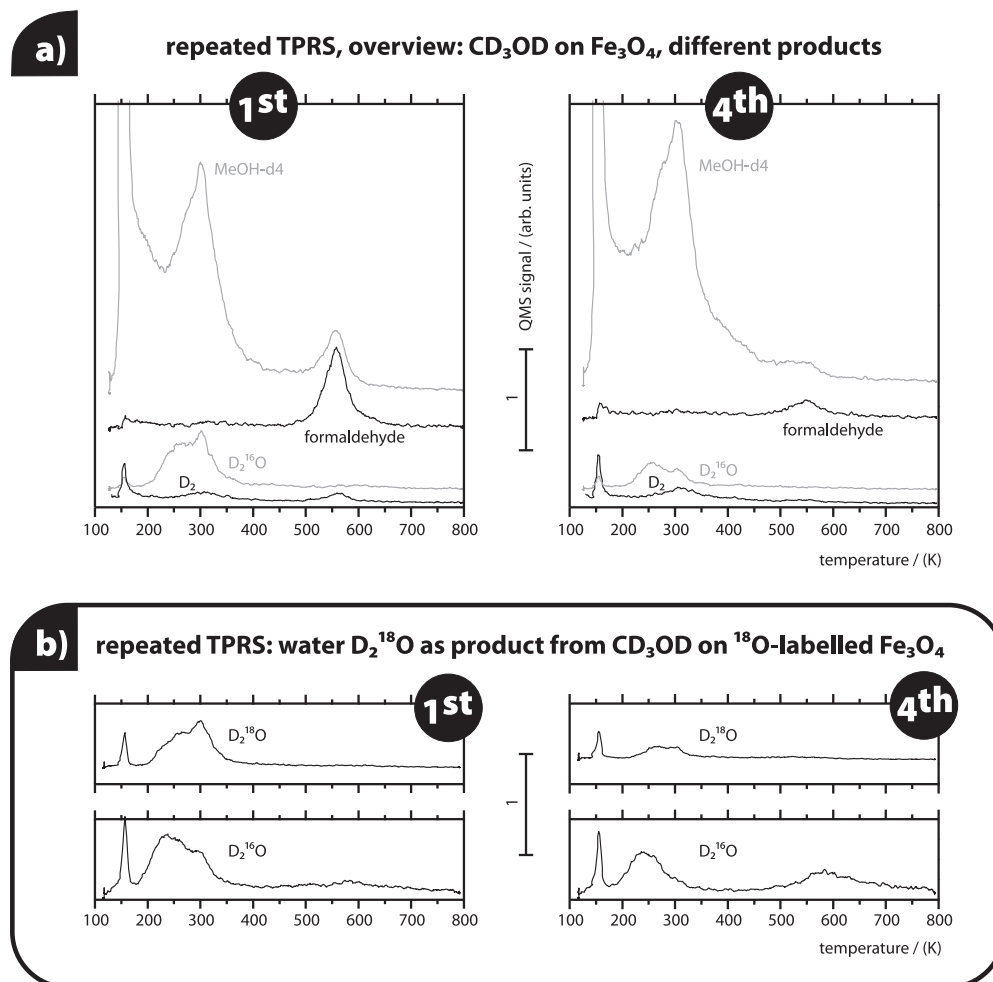


Figure 5.8: Repeated temperature-programmed reaction-desorption (TPRS) experiments of CD<sub>3</sub>OD (11.7 L) adsorbed on Fe<sub>3</sub>O<sub>4</sub> at 115 K: a) on the isotopically normal oxide, b) on the <sup>18</sup>O-labelled oxide (only for water-desorption). Signals of formaldehyde and D<sub>2</sub> were corrected for contributions by the fragmentation component of molecular methanol (formaldehyde by 9 %, and D<sub>2</sub> by 0.3 % of the signal of molecular methanol, mass 34).

repeated TPRS: evolution of desorption signals of reactants and products

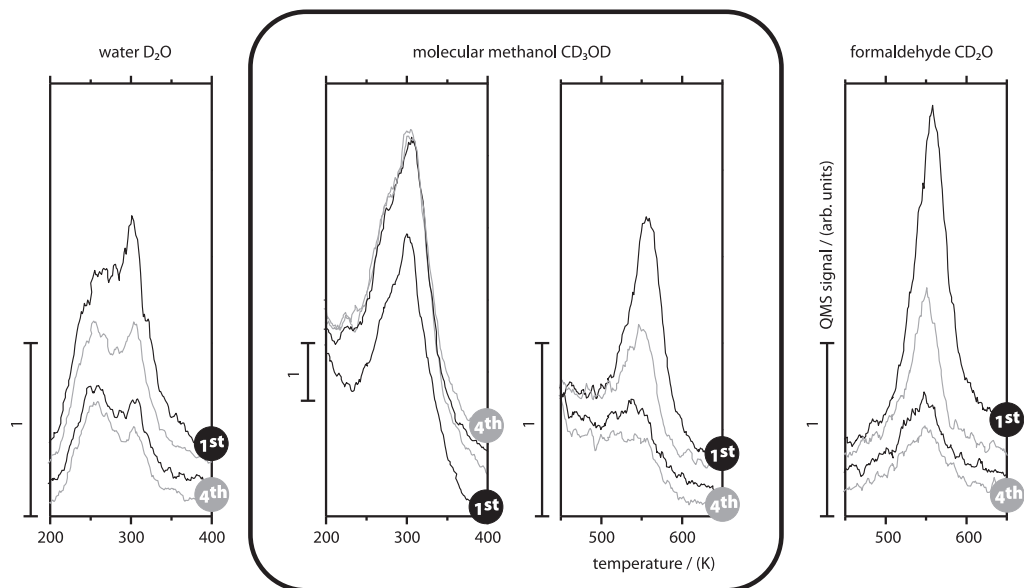


Figure 5.9: Evolution of temperature-programmed reaction-desorption (TPRS) experiments of  $\text{CD}_3\text{OD}$  (11.7 L) on  $\text{Fe}_3\text{O}_4$  with experiment repetition cycles. The signal of formaldehyde was corrected for contributions by the fragmentation component of molecular methanol (9 % of the signal of molecular methanol, mass 34 – see also the appendix A.3).

rate of  $\sim 3.5$  K/s and a peak temperature of 800 K; then, the sample was cooled to the deposition temperature again (115 K), and a second deposition/TPRS cycle with the same deposition temperature, exposure, heating rate and peak temperature was conducted; this procedure was repeated four times. Such repeated TPRS experiments with four cycles were conducted both on isotopically normal and on  $^{18}\text{O}$ -isotopically labelled  $\text{Fe}_3\text{O}_4$ . During the experiments, the quadrupole mass spectrometer was set to record the following masses simultaneously to monitor the desorption of the following species: mass 4 (deuterium from decomposition), 20 and 22 (20 for  $\text{D}_2^{16}\text{O}$  on the isotopically normal  $\text{Fe}_3\text{O}_4$  and 20 and 22 for  $\text{D}_2^{16}\text{O}$  and  $\text{D}_2^{18}\text{O}$  on the isotopically labelled  $\text{Fe}_3^{18}\text{O}_4$ ), 32 (formaldehyde) and 34 amu (molecular methanol); additionally, mass 28 (carbon monoxide) was followed (signal not shown in plots). Signals of formaldehyde and  $\text{D}_2$  were corrected for contributions by the cracking fraction of molecular methanol (formaldehyde by 9 %, and  $\text{D}_2$  by 0.3 % of the signal at mass 34), see the appendix A.3.

The results of those experiments are displayed in fig. 5.8 and 5.9 (note that the signals were offset for presentation); fig. 5.8 gives an overview over

all of the detected signals during the first and last cycles on the isotopically normal oxide (panel a), and comprises the desorption-signals for  $\text{D}_2^{16}\text{O}$  and  $\text{D}_2^{18}\text{O}$  from the  $^{18}\text{O}$ -labelled oxide (panel b); in addition to the overview plots, fig. 5.9 summarizes the evolution of certain desorption peaks with repetition cycle, concentrating on the desorption of water  $\text{D}_2\text{O}$ , molecular methanol  $\text{CD}_3\text{OD}$  (in two different temperature regions), and formaldehyde  $\text{D}_2\text{CO}$ . Note that no signals on the masses of  $\text{D}_2^{16}\text{O}$  and  $\text{D}_2^{18}\text{O}$  have been detected in blind experiments (not shown), where the TPRS experiment was conducted *without* prior gas exposure, indicating that the signals observed on those masses in the reaction experiments could not be ascribed to the desorption of species that originate from the chamber background.

From a freshly prepared oxide (first TPRS cycle), molecular methanol desorbs in three desorption peaks around 155, 300 and 555 K; the peak at 155 K has the highest intensity, followed by the peak at 300 K and the peak at 555 K with the smallest relative intensity. In subsequent TPRS cycles, the peak at 555 K decreases strongly with every repetition – most significantly between the first and the second cycle –, while the peaks around 155 and 300 K change only little. Formaldehyde was observed to desorb from the pristine oxide at 555 K, but the formaldehyde yield vanishes rapidly in the following experiment cycles, parallel to the high-temperature desorption of molecular methanol at the same temperature. Water desorbs at two temperatures (260 and 300 K) from the pristine oxide (*i.e.*, in the first cycle). Isotopically normal water  $\text{D}_2^{16}\text{O}$  desorbs from the isotopically normal oxide film, and  $\text{D}_2^{16}\text{O}$  and  $\text{D}_2^{18}\text{O}$  desorb from the isotopically labelled film  $\text{Fe}_3^{18}\text{O}_4$ ; the desorption behaviour (*i.e.*, yields and peak temperatures) of  $\text{D}_2^{16}\text{O}$  from the isotopically normal oxide film and  $\text{D}_2^{18}\text{O}$  from the  $^{18}\text{O}$ -labelled oxide film – *i.e.*, species that presumably contain oxygen from the oxide – are nearly identical, and additionally, the desorption signals of those two species on those two differently labelled oxides both decrease considerably with each experiment repetition cycle. On the other hand, the desorption signal of  $\text{D}_2^{16}\text{O}$  from the  $^{18}\text{O}$ -labelled oxide – *i.e.*, the species that does obviously *not* contain oxygen from the oxide – behaves different than the other two water species: it exhibits a different intensity ratio between the two peaks at 235 and 300 K, and additionally, only the signal at 300 K vanishes over the repetition cycles, while the signal at 235 K stays essentially identical.

Deuterium desorption was not observed. However, a desorption peak for CO (mass 28) was found around 530 K (not shown), but on a background component that increases strongly at and above 500 K, so that we chose not to evaluate this signal.

**Interpretation.** The methanol desorption at  $\approx 155$  K is due to the disaggregation of the condensed methanol multilayers; this desorption point is also in very good agreement with the multilayer desorption observed in the temperature-dependant IRAS experiments discussed above, and also with literature data for multilayer-desorption, *e.g.* from  $\alpha$ -Cr<sub>2</sub>O<sub>3</sub>(10 $\bar{1}$ 2) [149] or Al<sub>2</sub>O<sub>3</sub> [169]; after this desorption, the surface is only covered with methanol and methoxy species directly coordinated to the oxide surface. A second desorption of molecular methanol occurs around 300 K, with an onset at 240 K; this observation is in agreement with the disappearance of the IRAS signal for molecular methanol around 2075 cm<sup>-1</sup> observed in the same temperature region<sup>7</sup>, and thus it appears reasonable to assign this desorption to the disaggregation of the methanol monolayer, which has also previously been described on other oxides (see the literature overview in the introduction, section 5.1.1). Additionally, recombinative desorption of methoxy species (by reaction with surface hydroxyl groups as displayed in fig. 5.7, panel 2) in the same temperature region has also been described previously on several other oxides (see also section 5.1.1), including MgO(100) (between 300 and 350 K, [147]), ZrO<sub>2</sub>(100) (between 230 and approx. 450 K, [148]), or TiO<sub>2</sub>(001) single crystals (at 365 K, [145]). Since water desorption from disproportionation of surface hydroxyl-groups (as displayed in fig. 5.7, panel 1) is observed in approx. the same temperature region (see the discussion in the paragraph on water desorption below), it appears that recombinative desorption of methoxy as methanol – which is an alternative pathways to hydroxyl decomposition into water – might also be a possible reaction pathway on Fe<sub>3</sub>O<sub>4</sub>; indeed, also the intensities of the IR-signatures of methoxy decrease slightly in the temperature region between 265 and 380 K. Clearly, we can not unambiguously clarify based on our data whether or not recombinative desorption of methoxy contributes to the molecular methanol desorption around 300 K; the complete disappearance of IR-signatures of molecular methanol in the same temperature region indicates that the desorption of molecular methanol from the monolayer is the main source of this signal, but we believe – based on the above given indications from other studies and our IR-signals – that recombinative desorption should be kept in mind as a possible additional contribution to this signal. In any case, remember that no signatures for surface hydroxyl groups on Fe<sub>3</sub>O<sub>4</sub> could be found in the IRAS spectra at and above 380 K (see above).

Finally, a third desorption of molecular methanol occurs around 555 K – but with yields that decrease with every repetition cycle; this desorption

---

<sup>7</sup>Note, however, that not all of the molecularly adsorbed methanol desorbs, but that a fraction of it dissociates into a second type of methoxy species in the same temperature window (between 250 and 300 K), as demonstrated by the IRAS spectra discussed above.

is related to formaldehyde desorption, and will be explained below (in the section about formaldehyde formation).

**Water Desorption.** In fact, the TPRS experiments show the desorption of water from the sample at two temperatures (260 and 300 K) both on the isotopically normal and labeled oxide film. The desorption of  $D_2^{18}O$  from the  $^{18}O$ -labelled  $Fe_3^{18}O_4$  proves that the generated water contains lattice oxygen of the iron oxide. This result is also in good agreement with the previously discussed IR-experiments on the isotopically labelled oxide, which have shown that the surface O-D-groups formed during methanol dissociation incorporate lattice oxygen  $^{18}O$ . Those two results together suggest that surface O-D-groups desorb by disproportionation into lattice oxygen and water around 260 K as shown in fig. 5.7, sketch 1. The desorption temperatures are in good agreement with the values reported by Leist *et al.* [167] for the  $\gamma$ -species (see the discussion of the IRAS results in section 5.2.1), although the desorption mechanism in our and their experiments might be slightly different (see fig. 5.7, sketch 1 and 3).

The disproportionation of surface O-D-groups into water and lattice oxygen results in a loss of surface oxygen, as displayed in fig. 5.7, sketch 1 – and since this oxygen was not replenished in between the TPRS cycles (*e.g.* by reoxidation), the deficiency of surface oxygen persists throughout the discussed repeated TPRS experiments. Since surface oxygen is necessary to accommodate hydrogen in hydroxyl groups during the dissociation of methanol into methoxy, we believe that less hydroxyl groups and methoxy species can form in the later TPRS cycles; this decrease could explain both the observed smaller yields of formaldehyde and water in the later TPRS cycles, as will be explained in more detail in the paragraph about formaldehyde formation.

Interestingly, a desorption of  $D_2^{16}O$  was also observed from the  $^{18}O$ -labelled  $Fe_3O_4$ . The only explanation for this signal – which, according to the blind experiments, is clearly not due to desorption of water species adsorbed from the background – can be found in a possible C-O-bond scission in adsorbed methanol/methoxy, which would deliver the  $^{16}O$  inside methanol to the surface, where it may further react to form water; methanolic C-O-bond scission was only rarely described on oxides, and where it was observed, it was assigned to a high affinity of the oxide surface towards oxygen (see in the introduction 5.1.1); as one example, methane (in addition to molecular methanol) was reported to desorb from oxygen-depleted  $ZrO_2$  surfaces [148]. Since examples for C-O-bond scission on metal oxides are rare and no further investigation of this phenomenon was attempted in this work, the observed desorption of  $D_2^{16}O$  will not be further discussed here.

**Formaldehyde Formation.** We have observed the desorption of formaldehyde as a reaction product from a pristine oxide at a temperature of 555 K simultaneous with desorption of molecular methanol – and both with a yield that decreases with every TPRS cycle. As discussed above, no hydroxyl groups seem to be present at the surface at and above the temperature of 380 K; thus, the methoxy species remaining at the surface above this temperature could not leave the surface by recombinative desorption into molecular methanol, and thus are forced to remain adsorbed at the surface until an alternative pathway gets activated – which, obviously, occurs at 555 K; since the IRAS spectra obtained after heating to 600 K did not detect any adsorbates at the surface, we believe that the processes that lead to the desorptions around 555 K remove all of the remaining methoxy species from the surface.

The simultaneous desorption of methanol and formaldehyde suggests that they are also formed simultaneously (see section 5.1.1 and fig. 5.3, panel 2 c); those products desorb immediately after their formation, because the reaction temperature is far above their desorption point. As mentioned briefly in the discussion of IRAS spectra, no other spectroscopic signatures than the ones for methoxy could be observed in the spectrum at 510 K; particularly, no spectroscopic signatures could be detected of the often-discussed intermediate for formaldehyde formation from methoxy, dioxymethylene (see in the introduction to this chapter), which would be expected to give rise to two intense IRAS-features for the  $\nu_a$  and  $\nu_s(\text{O-C-O})$  modes around 1000 and 1150  $\text{cm}^{-1}$  [148]; based on this lack of other features, we believe that methoxy is the only surface species up to 510 K (and possibly even up to the reaction temperature of 555 K), suggesting that the rate-limiting step for formaldehyde formation on  $\text{Fe}_3\text{O}_4$  may be the activation of methoxy to a reaction intermediate, which might be – based on the studies described in literature (see in the introduction) – dioxymethylene. In any case,  $\text{Fe}_3\text{O}_4$  has been previously demonstrated to be very inactive in C-H-bond scission towards ethylbenzene (to form styrene) [170], and this low activity is possibly also the reason why the activation of methoxy decomposition to formaldehyde – which must include a C-H-bond scission step – needs such a high temperature.

The hydrogen transfer between the two methoxy species that disproportionate into formaldehyde and methanol might occur in two ways, either *via* the surface – presumably *via* surface hydroxyl-groups –, or in a direct transfer process between two methoxy species on an encounter. We cannot clearly distinguish between these two possibilities, but it shall be stated here that surface-hydroxyl groups – if they were responsible for this transfer – at such high temperatures might be expected to not only recombine with methoxy to molecular methanol, but that some of them would also recombine to water

as an alternative reaction (as discussed in the paragraph on water desorption); since water desorption, however, was not observed experimentally, the reaction by a direct hydrogen transfer between two methoxy species on an encounter may appear more convincing.

As a summary of the previous discussion, the factors that are responsible for formaldehyde formation may be described as follows: formaldehyde forms on  $\text{Fe}_3\text{O}_4$  from those oxide-related methoxy species that do not find hydroxyl-groups to recombine into molecular methanol and – as a consequence – are thus forced to remain at the surface until an alternative reaction pathway gets activated; this happens to be the disproportionation into formaldehyde and molecular methanol at relatively high temperatures. Hydroxyl-groups form on the oxide during the dissociation of molecularly adsorbed methanol into methoxy, so that in principle enough hydroxyl-groups should be available to allow any methoxy species to recombine again into methanol later; however, some of the surface O-D-groups leave the surface by an alternative process: they disproportionate into water (and a surface oxide and oxygen vacancy, as displayed in fig. 5.7, panel 1) at relatively low temperature (around 260 K).

This may be more succinctly summarized: formaldehyde formation depends on the loss of surface hydroxyl groups by water desorption, which leaves some methoxy species *locked* to the surface until the alternative disproportionation into formaldehyde and methanol gets activated at much higher temperatures.

**Surface Oxygen.** Based on this interpretation, the strong decrease in the yields of water at 260 K, and of formaldehyde and methanol at 555 K in the later TPRS cycles may now be ascribed to the water desorption from the oxide in the earlier TPRS cycles, which leaves oxygen vacancies on the oxide that were not replenished between the TPRS cycles (*e.g.* by a reoxidation of the oxide); as a consequence, less O-D groups and methoxy can form on the oxide in the later experiment cycles. Additionally, we believe that those methoxy and hydroxy species that still do form on the oxide in the later cycles (as evidenced by IR experiments, not shown) disaggregate mostly by recombination into methanol at elevated temperatures, instead of alternatively disproportionating into water (as at least some hydroxyl species obviously do in the first cycle).

The provided interpretation for the experiments is further supported by additional experiments conducted by Sun, Kaya and Shaikhutdinov [96], which demonstrate that the reactivity of the  $\text{Fe}_3\text{O}_4(111)$  film towards formaldehyde formation can be fully recovered by a simple reoxidation of the oxide according to the oxide's preparation recipe (see appendix A.1.3) after several TPRS cycles with methanol. This observation corroborates that the loss of surface oxygen is the origin for the observed decrease in reactivity towards formaldehyde formation in the later TPRS cycles. In additional experiments, Shaikhutdinov *et al.* have shown that even a simple coadsorption of oxygen and methanol at 150 K on a *preexposed*  $\text{Fe}_3\text{O}_4$  film can fully regenerate the reactivity of the oxide towards water and formaldehyde formation; moreover, this procedure was surprisingly found to even increase the formaldehyde yield significantly beyond the values found on pristine oxide preparations [96].

In their experiments, Sun, Kaya and Shaikhutdinov [96] have also investigated the possible formation of other methanol decomposition products that have been found on other oxides (see the discussion in the introduction to this chapter), including methane,  $\text{CO}_2$ , dimethylether or formic acid, using both TPRS and GC (the latter at atmospheric pressures); however, none of those possible products could be experimentally observed on  $\text{Fe}_3\text{O}_4$ . Together with our own observations, we thus may conclude that the main decomposition products of methanol on the  $\text{Fe}_3\text{O}_4(111)$  thin film are formaldehyde and water, but that most of the methanol desorbs undecomposed (molecularly).

As an explanation for the overall relatively low yield of formaldehyde and its fast collapse during repeated TPRS cycles, we believe that the hydroxyl groups that leave the surface in the form of water in the first cycle instead of recombining into methanol are presumably related mainly to a certain, very reactive minority oxygen species on the oxide surface (*i.e.*, presumably a point defect); note that this interpretation is not necessarily in contradiction with the observation by Shaikhutdinov *et al.* that this oxygen species can be fully recovered by reoxidation of the preexposed oxide according to its preparation recipe, since the concentration of point defects may depend on a thermal equilibrium – so that similar amounts of those minority species may be regenerated by reoxidation of the oxide surface under the same conditions as during its preparation.

At this stage, it is interesting to point back to the discussion of the surface termination of  $\text{Fe}_3\text{O}_4(111)$  in chapter 4.1, where two literature models were presented, which are both based on the bulk structure of  $\text{Fe}_3\text{O}_4$ ; in one of those models,  $\text{Fe}_3\text{O}_4$  is terminated by  $1/4$  ML of  $\text{Fe}^{3+}$  (tet1) ions above a close-packed layer of oxygen ions, and in the other model it is terminated



by  $1/4$  ML of  $\text{Fe}^{2+}(\text{oct}2)$  above  $1/4$  ML of  $\text{Fe}^{3+}$  (tet1). The latter model was suggested based partly on IRAS- and TPD-experiments with CO as a surface sensitive probe molecule, in which two sharp and one broad feature have been observed; the broad feature is associated with the lowest-temperature desorption of CO (at 110 K, associated with an IRAS-peak around 2115-2140  $\text{cm}^{-1}$ ; it was termed the  $\alpha$ -peak) and was assigned to a weakly bound CO species; the other two peaks, one desorbing at 180 K (associated with an IRAS peak around 2080  $\text{cm}^{-1}$ ) and termed  $\beta$ , the other one desorbing at 230 K (associated with an IRAS peak around 2207  $\text{cm}^{-1}$ ) and termed  $\gamma$ , are associated to strongly binding species;  $\beta$  was assigned to CO adsorbed on  $1/4$  ML of octahedral  $\text{Fe}^{2+}$ ,  $\gamma$  to CO adsorbed on  $1/4$  ML of  $\text{Fe}^{3+}$  (tet1) ions [92].

This assignment was reevaluated in chapter 4.1 based on IRAS spectra of CO adsorbed on a freshly prepared  $\text{Fe}_3\text{O}_4$ , and again after methanol adsorption and reaction/desorption (at 800 K); in the latter spectrum, the  $\beta$  peak was observed to have disappeared completely, while the  $\gamma$ -peak has grown slightly, and the  $\alpha$ -peak exhibited no significant changes; despite those considerable changes in the IRAS-spectra of adsorbed CO, however, related sticking coefficient measurements with CO on the freshly prepared oxide and the oxide after methanol adsorption and heating to 800 K exhibited no significant differences; this was interpreted as an indication against assigning the  $\beta$ - and  $\gamma$ -peaks to regular adsorption sites, and alternatively, an assignment to adsorption on defect sites, which do not account significantly to the adsorption capacity, was suggested.

Interestingly, those changes were also found by Shaikhutdinov *et al.* in the related TPD spectra of adsorbed CO [96] during the above named experiments; during those experiments, it has also been shown that the reoxidation of the iron oxide film after methanol adsorption and reaction – which regenerates the reactivity of the oxide towards formaldehyde formation (see above) –, results also in a full regeneration of the  $\beta$ - and  $\gamma$ -peaks in the TPD-spectra of adsorbed CO; thus, it appears reasonable at this point to combine all observations – the complete loss of formaldehyde formation during repeated TPRS experiments with methanol, the loss of the  $\beta$ -peak in the IRAS and TPD spectra of adsorbed CO, and the regeneration of formaldehyde formation and the  $\beta$ -peak by reoxidation – : since the loss of formaldehyde-yield was assigned to surface-oxygen-depletion, it appears possible that the  $\beta$ -peak in the IRAS- and TPD-spectra of adsorbed CO is related to this surface oxygen. Since this surface oxygen gives rise to one discrete peak in both IRAS (at 2080  $\text{cm}^{-1}$ ) and TPD (at 180 K) of adsorbed CO, it appears to be reasonable to speak of a specific, defect-oxygen *species* that gives rise to this peak; of course, the CO that is associated with the  $\beta$ -IRAS- and TPD-spectra

would not directly adsorb on those surface-oxygen species, but merely on Fe ions near those sites. Note that this interpretation would corroborate further that the oxygen species responsible for water desorption and formaldehyde formation is a minority (defect) oxygen species.

### 5.2.3 Conclusions: Methanol Decomposition on $\text{Fe}_3\text{O}_4$

In the preceding section, we have discussed methanol-adsorption and decomposition experiments on the  $\text{Fe}_3\text{O}_4(111)$  oxide film. At a temperature of 115 K, methanol was found to adsorb both molecularly and dissociated into methoxy; both adsorbates accumulate simultaneously at the surface. The second product of methanol dissociation into methoxy are hydrogen ions, which are accommodated on the oxide surface in the form of hydroxyl groups containing lattice oxygen of the iron oxide. At an exposure of approx. 1.6 L, the monolayer of methanol/methoxy species saturates; on further exposure at this temperature, methanol condenses into multilayers, which desorb around 155 K.

Around 260 K, water desorbs from the surface due to the decomposition of unstable surface-hydroxyl groups; isotope-labelling experiments have revealed that those desorbing water molecules contain lattice oxygen from the oxide (and also a contribution of methanolic oxygen, which might indicate that methanolic C-O-bond scission may occur on the oxide); thus, water-desorption leads to a depletion of surface oxygen on the oxide. Around 300 K, a large amount of methanol desorbs; this desorption may have two conceivable sources: methanol that has been molecularly adsorbed on the oxide, and recombinative desorption of methoxy (and surface-hydroxyl groups); the desorption of molecularly adsorbed methanol clearly accounts for the major part of the signal, but we believe that recombinative desorption between some of the methoxy species and the remaining hydroxyl groups on the surface may constitute a minor contribution to this desorption. In any case, no remainders of hydroxyl groups could be spectroscopically detected on the surface at 380 K, but considerable amounts of methoxy-species were still detected up to a temperature between 510 and 600 K. We have discussed that one factor for this remarkable thermal stability of the methoxy species may be seen in the previous loss of the surface hydroxyl-groups by water desorption, which otherwise could supply hydrogen for a recombinative desorption of methoxy as methanol. The methoxy species that remain at the surface after the desorption of hydroxyl groups can leave the surface only when an alternative reaction pathway gets activated, which occurs around 555 K with the simultaneous formation of molecular methanol and formaldehyde in a reaction between two methoxy species; the products desorb simultaneously

at this high temperature as soon as the reaction has occurred. The hydrogen transfer between two methoxy species may either proceed under participation of surface-hydroxyl groups or directly between two methoxy species on an encounter; the lack of water desorption at this temperature may imply that hydroxyl groups are not the carriers for this transfer.

Thus, the loss of surface hydroxyl groups by water desorption in the experiments on a freshly prepared film appears to be responsible for the fact that formaldehyde can form on the surface at higher temperature; however, less water desorbs from the surface in the later TPRS experiments, presumably because most of the oxygen species responsible for water desorption from a freshly prepared  $\text{Fe}_3\text{O}_4$  film have disappeared during only one TPRS experiment on the fresh film; this oxygen may be a special species that forms particular, very labile hydroxyl-groups – possibly even a defect species. Experiments from a cooperating group support those interpretations and demonstrate that a simple reoxidation of the iron oxide can reactivate the surface for formaldehyde formation.

A high thermal stability of methoxy species was detected by IRAS spectra, in which methoxy was observed up to a temperature of 510 K. For the sake of completeness, we have to add here that *two different methoxy* species were detected spectroscopically in our experiments: one of them already forms during methanol exposure at 115 K, and the second species around 240 to 265 K; both species exhibit the high thermal stability.

**Comparison and Discussion.** The main result of this work is to show that formaldehyde can form on the iron oxide  $\text{Fe}_3\text{O}_4$ , and that its formation depends on the availability of certain surface oxygen species, which have a tendency to desorb from the surface as water. The methoxy species that remain on the surface after water desorption can not recombine into methanol, and thus are forced to disproportionate into formaldehyde and methanol.

Those results are in very good agreement with experiments conducted by other groups on various reducible oxides. In a recent paper about methanol decomposition on ceria ( $\text{CeO}_2$ ), Mullins, Robbins and Zhou have reported on a surface oxygen loss from fully oxidized  $\text{CeO}_2$  due to water formation and desorption at 200 K during TPRS experiments on a surface covered with methanol [152]. Like our experiments, the authors observed a simultaneous desorption of methanol and formaldehyde around 560 K; unlike our results, an additional decomposition pathway was found in the later repetition cycles of the experiments (*i.e.* on the partially reduced oxide), where increasing CO and hydrogen yields (and decreasing water yields) were observed with increasing extent of reduction. The results indicate that surface oxygen is necessary to obtain the decomposition reaction to formaldehyde.

Recent work conducted in our department further corroborate our model; those studies concentrated on the reactions of methanol on different vanadium oxide thin films and particles – including  $V_2O_3(0001)$  [154] and  $V_2O_5(001)$  [155] thin films (both grown on Au(111) ), and  $V_2O_3$  particles grown on silica [156] and ceria [157]. The general result from those experiments is that formaldehyde can be obtained as a product on mildly reduced vanadium oxides, which were either obtained by electron bombardment [154, 155], or a particular oxidation treatment [157]; formaldehyde can not be obtained on the fully oxidized  $V_2O_3(0001)$  and  $V_2O_5(001)$  films, and also not on too strongly reduced oxide surfaces. Those results were interpreted as an indication that both exposed metal ions and oxygen species (cation-anion site pairs) are necessary for the reaction, which is also in general agreement with our observations; note that, if it is true that those site pairs are necessary for the reaction,  $Fe_3O_4$  seems to expose those site pairs right after its preparation, since no particular pretreatment of  $Fe_3O_4$  was necessary to induce formaldehyde formation. In many of the studies on vanadium oxides also a deactivation due to surface oxygen loss in the course of formaldehyde formation has been observed, indicating that reoxidations are required for sustained formaldehyde yield. In most of the cases, a simultaneous formaldehyde and methanol desorption was observed at temperatures between 500 and 600 K; interestingly, Romanyshyn and coworkers [154] have reported on a disproportionation into formaldehyde and *methane* instead on  $V_2O_3(0001)$ .

## 5.3 Methanol Adsorption, Desorption and Reaction on the Pd/Fe<sub>3</sub>O<sub>4</sub> Model Catalyst

After the reaction study on the pristine iron oxide film, we examined methanol decomposition on the Pd/Fe<sub>3</sub>O<sub>4</sub> model catalyst. According to the observations discussed in the last section and the earlier studies in our group on methanol decomposition on Pd/Al<sub>2</sub>O<sub>3</sub> [159, 80, 138], we expected to find a reactivity towards methanol of both components of the model catalyst – the Fe<sub>3</sub>O<sub>4</sub> support and also the active Pd metal particles. To start this study, we conducted exactly the same IR- and TPRS-experiments on the model catalyst as described in the previous section about the pristine Fe<sub>3</sub>O<sub>4</sub> support. They were complemented with isothermal molecular beam reaction rate studies to measure the rates of C-H- (CO-formation) and C-O-bond scission (carbon formation).

Additionally, experiments were conducted not only on the clean, stabilized model catalyst, but also on a Pd/Fe<sub>3</sub>O<sub>4</sub> system *pretreated with oxygen* at 550 K. This approach was inspired by the earlier project of our group on the oxidation behaviour of the Pd/Fe<sub>3</sub>O<sub>4</sub> system (see section 4.2.3 and [55]), which lead to the conclusion that the Pd nanoparticles can oxidize extensively – initially at the interface to the Fe<sub>3</sub>O<sub>4</sub> support, but later also on the Pd surface; surface oxidation was found to severely deactivate the catalyst towards the CO oxidation reaction [105]. The experiments of methanol decomposition on the oxidized system aimed at extending our understanding about the implications of catalyst oxidation for the activity the Pd/Fe<sub>3</sub>O<sub>4</sub> system.

### 5.3.1 Methanol Decomposition Investigated by Vibrational Spectroscopy

#### Coverage-Dependance of IRAS Spectra

Fig. 5.10 a) shows IRAS spectra of deuterated methanol CD<sub>3</sub>OD adsorbed on clean Pd/Fe<sub>3</sub>O<sub>4</sub> at 115 K at exposures<sup>8</sup> between 0 and 3.9 L; note that the experimental procedure is identical to the experiments on the pristine support discussed in section 5.2.1 (see fig. 5.4); based on the assignments from the previous discussion, the spectra show the following behaviour: the first peaks appear at a coverage of 0.4 and 0.8 L at 2074 and 2046 cm<sup>-1</sup>

---

<sup>8</sup>Note that exposure and surface coverage are equivalent in those experiments, because the sticking coefficient for methanol is essentially 1 at the temperature of 115 K.

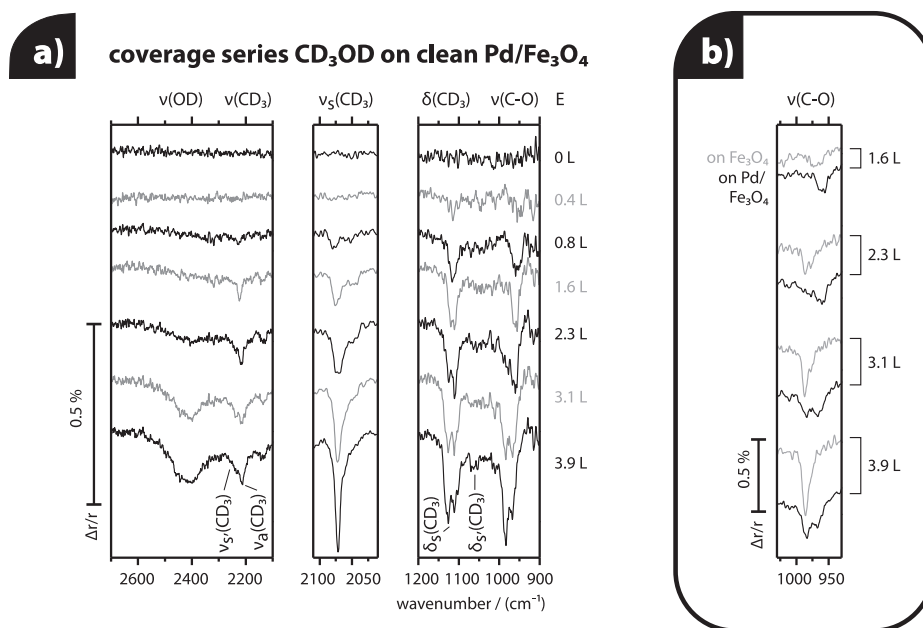


Figure 5.10: a) Coverage series of deuterated methanol on initially clean Pd/Fe<sub>3</sub>O<sub>4</sub> at 115 K. b) Comparison of coverage series on the model catalyst with coverage series on the pristine support Fe<sub>3</sub>O<sub>4</sub> at 115 K (only  $\nu(\text{C-O})$ -region).

( $\nu_s(\text{CD}_3)$  in molecularly adsorbed methanol and methoxy, respectively) and at  $1114\text{ cm}^{-1}$  ( $\delta_s(\text{CD}_3)$ ) and  $959\text{ cm}^{-1}$  ( $\nu(\text{C-O})$ ), which is in good agreement with the adsorption behaviour observed on the pristine support. With increasing coverage, additional peaks appear, which were also observed on the pristine support, including the  $\nu(\text{O-D})$ -mode at  $2410\text{ cm}^{-1}$  (3.9 L), the  $2 \times \delta_s(\text{CD}_3)$ - or  $\nu_{s'}(\text{CD}_3)$ -mode (appears as a shoulder at  $2440\text{ cm}^{-1}$  – as discussed in section 5.2.1, an unambiguous assignment based on literature data is impossible), and the  $\nu_{\text{as}}(\text{CD}_3)$ -mode (at  $2414\text{ cm}^{-1}$ ); the signature for the symmetric methyl-stretching mode  $\nu_s(\text{CD}_3)$  in methoxy, which is clearly visible in the low-coverage spectra around  $2046\text{ cm}^{-1}$ , disappears in the strongly increasing signature of the corresponding mode in molecularly adsorbed methanol around  $\sim 2071\text{ cm}^{-1}$  with the buildup of multilayers (between 1.6 and 2.3 L coverage). Additionally, a weak peak for the  $\delta_{s'}(\text{CD}_3)$ -mode appears around  $1061\text{ cm}^{-1}$  with increasing coverage. Interestingly, the signatures for the  $\delta_s(\text{CD}_3)$ - and  $\nu(\text{C-O})$ -modes behave different in these experiments on the model catalyst as compared to the pristine Fe<sub>3</sub>O<sub>4</sub>, and split with increasing coverage: the  $\delta_s(\text{CD}_3)$ -mode shows two peaks at  $1125$  and  $1110\text{ cm}^{-1}$  in the spectrum with 3.9 L exposure, and the  $\nu(\text{C-O})$ -mode at  $984$  and  $966\text{ cm}^{-1}$ .

These spectra are similar to the ones obtained with deuterated methanol adsorbed on the pristine support. Qualitatively, they show that methanol dissociates into methoxy also on the model catalyst at 115 K, and that methoxy and molecularly adsorbed methanol are formed simultaneously (this interpretation is inferred from the simultaneous growth of the spectral features of  $\nu_s(\text{CD}_3)$  in molecular methanol (at 2074) and in methoxy (at 2046  $\text{cm}^{-1}$ ), see section 5.2.1). At an exposure between approx. 1.6 and 2.3 L, methanol begins to condense, leading to a strong growth of the peak at 2074  $\text{cm}^{-1}$ . As discussed for the spectra observed on the pristine support, the multilayer spectra exhibit more features than the monolayer spectra due to the different orientation of the molecules in methanol ice, which allows additional modes to fulfil the metal-surface selection rule, including the methyl stretching modes  $\nu_{s'}$  and  $\nu_{\text{as}}(\text{CD}_3)$ .

**Discrimination between Support- and Pd-Related Species.** The most interesting observation in those spectra as compared to the spectra on the pristine support is observed in the spectral region of the C-O-stretching mode  $\nu(\text{CO})$ ; fig. 5.10 b) compares some of the spectra obtained at identical exposures on the pristine support and on the Pd/Fe<sub>3</sub>O<sub>4</sub> model system. It is apparent that the spectra obtained on the pristine support exhibit only one feature (around 967  $\text{cm}^{-1}$ ) that blue-shifts with increasing coverage (to 986  $\text{cm}^{-1}$ ), while the spectra obtained on the model catalyst exhibit two different features, one of them around 966  $\text{cm}^{-1}$  and the other around 984  $\text{cm}^{-1}$ ; the feature at 966  $\text{cm}^{-1}$  appears first. Two possible explanations may account for this observation:

- Since the C-O bond in methanol/methoxy is close to the adsorbent surface, it may be anticipated that its vibration frequency could be affected by the local geometry and electronic properties of the adsorbent surface, and thus would allow to discriminate whether an adsorbate is bound on the support or on the Pd metal surface; in fact, in earlier studies in our group it has been possible to distinguish between methanol species adsorbed at the Pd nanoparticles and the oxide support based on the  $\nu(\text{C-O})$  frequency (in those experiments, Al<sub>2</sub>O<sub>3</sub> was used as a support; the nanoparticles had a similar morphology, size and density as the ones on the Pd/Fe<sub>3</sub>O<sub>4</sub> model catalyst used in this work) [159]; based on those experiments, it was argued that the methanol/methoxy coverage builds up on the Pd metal surface initially before the first support-related methanol/methoxy species can be observed (which happened at coverages exceeding  $5 \cdot 10^{14}$  molecules/ $\text{cm}^2$ ). Building on this earlier report and the comparison made in fig. 5.10 b),

it would be tempting to also assign the spectral feature observed in our spectra at  $966\text{ cm}^{-1}$  to Pd-bound methanol/methoxy, and the other feature at  $984\text{ cm}^{-1}$  to support-related methanol/methoxy; also the shifts of metal- and oxide-related species would be in agreement with the earlier reports [159]. Based on this assignment, the spectra would indicate that at the beginning of the experiment, all methanol/methoxy species accumulate on the Pd nanoparticles due to a rapid surface diffusion from the support to the Pd metal, and only after a critical coverage on the Pd metal has saturated, support-related methanol/methoxy can begin to accumulate – which, according to our spectra, would begin at a coverage slightly above 1.6 L.

- The splitting occurs at around the same coverage where also the formation of multilayers commences. Sometimes, band splitting due to molecules in symmetrically inequivalent crystal sites has been observed in molecule crystals (for example, it has been observed in the crystals of methyl halides [171]). Based on the onset of multilayer formation at around the same coverages where the splitting is first observed in our spectra, it might be thought that it could be due to methanol in different lattice sites of the multilayers [166].

The first interpretation would indicate that methanol rapidly diffuses from the support to the Pd nanoparticles, because it is more strongly adsorbed there; the saturation coverage of methanol/methoxy on the Pd particles (approx. 1.6 L,  $5.6 \cdot 10^{14}$  molecules/cm<sup>2</sup>) would be in a good agreement with the measurements by Schauermaun *et al.*; additionally, it is also in a good agreement with the amount of the exposed Pd surface atoms in the Pd/Fe<sub>3</sub>O<sub>4</sub> model catalyst (approx.  $5.4 \cdot 10^{14}$  cm<sup>-2</sup>, [55]). The other conceivable interpretation – splitting due to methanol molecules in symmetrically inequivalent sites in the accumulating multilayers – appears inappropriate due to the fact that no such splitting was observed in the methanol coverage series on the pristine Fe<sub>3</sub>O<sub>4</sub>, but only on the model catalyst – although multilayers of methanol do form on both the pristine support and the model catalyst. Note that the nearly simultaneous onset of methanol/methoxy accumulation on the support and buildup of methanol multilayers between 1.6 and 2.3 L is not a contradiction, because multilayers may begin to form first on the Pd particles.

**Experiments on the *Partially Oxidized* Model Catalyst.** Fig. 5.11 shows the results of a coverage-dependant IRAS experiment on the *partially oxidized* Pd/Fe<sub>3</sub>O<sub>4</sub> model catalyst between 0 and 3.9 L; this experiment



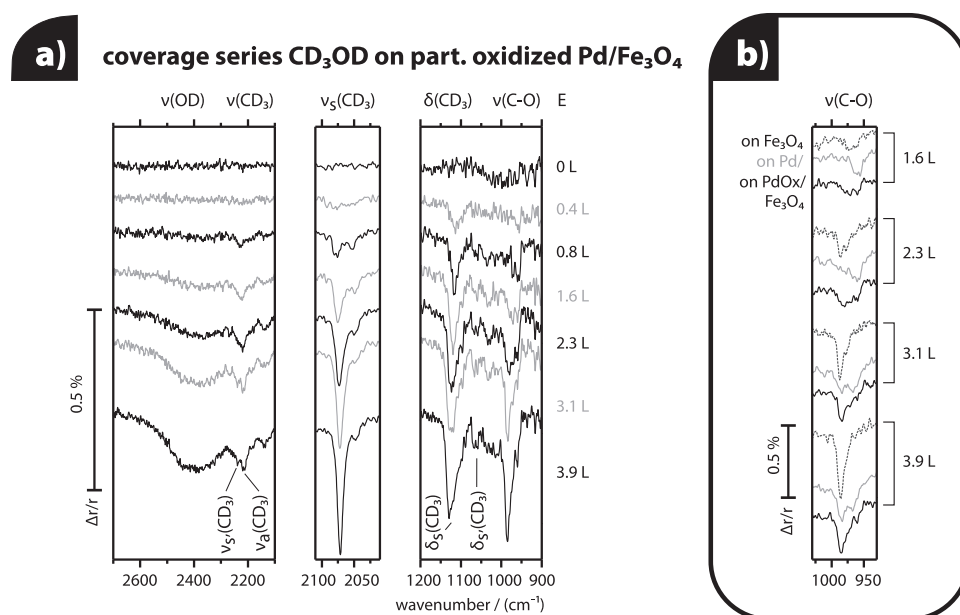


Figure 5.11: a) Coverage series of deuterated methanol on *partially oxidized* Pd/Fe<sub>3</sub>O<sub>4</sub> at 115 K. b) Comparison of series on the oxidized and unoxidized model catalyst with experiments on pristine Fe<sub>3</sub>O<sub>4</sub> (115 K, only ν(C-O)-region).

was conducted in the same way as the previously described experiments on the clean, stabilized model catalyst (see last section) and the support. The Pd/Fe<sub>3</sub>O<sub>4</sub> system was oxidized directly before the experiments with methanol according to the following procedure: first, the model catalyst was exposed to oxygen ( $p_{\text{O}_2} = 8 \times 10^{-7}$  mbar) at 550 K for 1000 s (650 L); subsequently, it was quickly cooled down in oxygen to  $\sim 505$  K and shortly exposed to CO ( $p_{\text{CO}} = 4 \times 10^{-6}$  mbar) for approx. 8 s (5.2 L) at  $\sim 500$  K to remove chemisorbed surface-oxygen; finally, the system was cooled in UHV to the methanol adsorption temperature (115 K). IRAS Pd-surface titration experiments using CO as probe molecule show approx. 60 % less integrated spectral intensity in the ν(CO) region than an unoxidized system [101]; this value may be taken as an estimate for the surface loss due to Pd surface oxidation.

Again, we apply the assignments discussed in section 5.2.1: At low-coverages (0.4 and 0.8 L), the exposure series exhibits peaks at 2075 and 2051 cm<sup>-1</sup> (ν<sub>s</sub>(CD<sub>3</sub>) in molecularly adsorbed methanol and methoxy, respectively), and at 1114 (δ<sub>s</sub>(CD<sub>3</sub>)) and 960 cm<sup>-1</sup> (ν(C-O)). At coverages above  $\sim 1.6$  L (*i.e.* approx. monolayer coverage), additional peaks at 2400

( $\nu(\text{O-D})$ ), 2239 ( $2 \times \delta_s(\text{CD}_3)$  or  $\nu_{s'}(\text{CD}_3)$ ), and 2212  $\text{cm}^{-1}$  ( $\nu_{\text{as}}(\text{CD}_3)$ ) appear. Additionally, the peak for  $\nu_s(\text{CD}_3)$  in molecularly adsorbed methanol at 2075  $\text{cm}^{-1}$  grows with the buildup of multilayers, incorporating the peak of methoxy as a shoulder.

This behaviour agrees well with the observations obtained on both the pristine support and the model catalyst; most importantly, it also demonstrates the presence and simultaneous accumulation of both molecularly adsorbed methanol *and* methoxy on the surface at very low coverages – and also the buildup of multilayers was found to commence at a coverage between 1.6 and 2.3 L, just as on the two other samples (see above).

Again, it is interesting to inspect the region of the C-O-stretching mode  $\nu(\text{C-O})$  in the spectra obtained at identical exposures on the pristine support and on the *unoxidized* and partially oxidized Pd/Fe<sub>3</sub>O<sub>4</sub> model catalyst – several of those spectra are displayed together in fig. 5.11 panel b). It is apparent at the first glance that all spectra obtained on the *oxidized* model system compare well in frequency and intensity with the respective experiments on the pristine *support*, and that the additional feature at 966  $\text{cm}^{-1}$  obtained on the *unoxidized* model system (and assigned to methanol/methoxy adsorbed on the Pd metal surface, see previous section) does only occur as a weaker shoulder in the experiments on the *oxidized* system. Based on our assignment to support- and Pd-related species (see above), those spectra indicate that the surface oxidation leads to a decrease of methanol/methoxy adsorption capacity on the Pd metal surface in the *oxidized* metal nanoparticles as compared to the *unoxidized* system; this interpretation would also be in good agreement with the explanation for the decrease of CO adsorption capacity observed on *oxidized* Pd/Fe<sub>3</sub>O<sub>4</sub> in the earlier study of our group [55]. Moreover, the feature for support-related methanol/methoxy (around 985  $\text{cm}^{-1}$ ) is more intense at any exposure in spectra obtained on the partially oxidized system than in the respective spectra on the *unoxidized* model system, indicating that support-related methanol/methoxy begins to accumulate at much lower coverages on the partially oxidized model system. This observation may be understood based on the rapid diffusion of methanol/methoxy from the support to the Pd metal particles, where it binds preferentially and which, thus, saturate before the support; if, however, the Pd metal surface is decreased by surface oxidation, the Pd nanoparticles' adsorption capacity towards methanol/methoxy is also reduced, resulting in an earlier onset of methanol/methoxy accumulation on the oxide.

It was speculated in our earlier project – based on a detailed evaluation of the IRAS spectra of CO adsorbed on the oxidized model system – that the Pd particles' surface might oxidize initially on the part that is close to the oxide support (the *perimeter*); if this is true, and if methanol/methoxy does

not adsorb on the Pd oxide, the surface oxide on the perimeter between the particles and the support could also act directly as a barrier for the diffusion of methanol/methoxy from the support to the Pd metal phase.

On the other hand, the observed differences in the spectra might also be ascribed to a coincidence of the peak positions for methanol/methoxy adsorbed on  $\text{Fe}_3\text{O}_4$  and – hypothetically – on Pd-oxide, so that the single peak observed at  $985\text{ cm}^{-1}$  on the oxidized model catalyst may thus simply be due both to methanol/methoxy adsorbed on the support and also on Pd surface oxide. The linewidths (FWHM) of this peak on the partially oxidized catalyst and the pristine support, however, are nearly identical (14 and  $13\text{ cm}^{-1}$ , respectively), so that the vibration frequencies on  $\text{Fe}_3\text{O}_4$  and the hypothetical Pd-oxide would need to coincide exactly – which, however, appears very unlikely.

### Molecular Transformations in IR Experiments as a Function of Temperature

The following experiments were conducted to study the thermally induced transformations of deuterated methanol  $\text{CD}_3\text{OD}$  adsorbed at 115 K on a *clean*, stabilized and on a *partially oxidized* Pd/ $\text{Fe}_3\text{O}_4$  model catalyst (the oxidized sample was obtained using the same oxidation method as described in the previous section and in appendix A.1.5). For those experiments, the reactant  $\text{CD}_3\text{OD}$  was adsorbed at 115 K (exposure: 11.7 L), and then the two samples were repeatedly heated to gradually increasing peak temperatures (190, 245, 275, 345 (only on the unoxidized sample), 380, 510 and 600 K); in between the heating steps, the sample was cooled back to the deposition temperature (115 K) to measure an IRAS spectrum referenced to the background spectrum taken before methanol deposition; note that these experiments are identical to the series that was conducted on the pristine support and discussed in section 5.2.1. Fig. 5.12 a) displays the results obtained on the clean (*unoxidized*) Pd/ $\text{Fe}_3\text{O}_4$  model system, and panel b) exhibits the results obtained on the *partially oxidized* sample.

The following observations were obtained on the *unoxidized* system (panel a): After annealing at 190 K (*i.e.*, after multilayer desorption), the spectrum shows signatures for a combined monolayer of molecularly adsorbed methanol and methoxy, as it has also been observed on the pristine support – *i.e.*, the peaks for the symmetric methyl stretching mode  $\nu_s(\text{CD}_3)$  at 2074 (molecular methanol) and  $2045\text{ cm}^{-1}$  (methoxy), and the symmetric deformation mode  $\delta_s(\text{CD}_3)$  at  $1120\text{ cm}^{-1}$ . On heating to 245 and 275 K, the signature for molecularly adsorbed methanol at  $2074\text{ cm}^{-1}$  disappeared slowly, and simultaneously another signature around  $2059\text{ cm}^{-1}$  appeared,

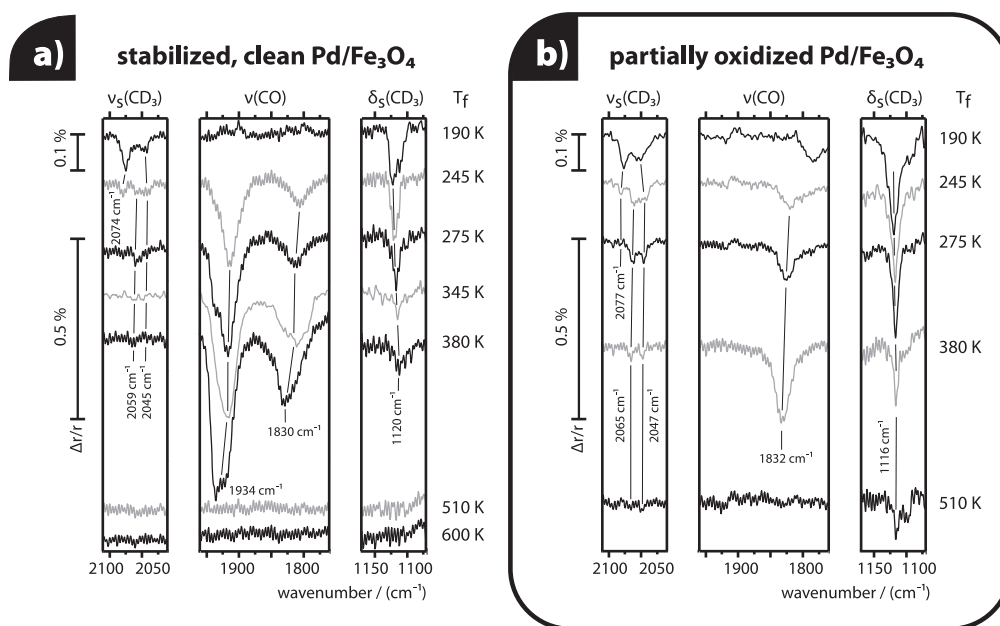


Figure 5.12: IRAS spectra of  $\text{CD}_3\text{OD}$  (11.7 L) on a)  $\text{Pd}/\text{Fe}_3\text{O}_4$  and b) partially oxidized  $\text{Pd}/\text{Fe}_3\text{O}_4$  as a function of annealing temperature.

indicating formation of a second methoxy species; those observations are completely parallel to the pristine support (see section 5.2.1). Unlike the pristine support, two additional and very intense spectral signatures at 1915 and  $1806\text{ cm}^{-1}$  occurred after flashing to 245 K. Even more interestingly, on further heating to 345 and 380 K, the spectral signatures at 2059, 2045 and  $1120\text{ cm}^{-1}$  – which, at this temperature, would be the spectral signatures for methoxy – disappeared slowly, and no indications for the presence of methoxy is observed in the spectra after heating to 510 K – unlike the experiments on the pristine support. During the heating step to 380 K, the intense spectral signatures at 1915 and  $1806\text{ cm}^{-1}$  – the ones that were observed on the model catalyst, and not on the pristine support – gained further in intensity and shifted slightly (to 1934 and  $1830\text{ cm}^{-1}$ , respectively); they have disappeared completely from the spectra after heating to 510 K. Both the spectra after heating to 510 and 600 K do not show any spectral signatures (peaks).

On the *partially oxidized* system (panel b), we have observed the following transformations: After annealing at 190 K, also the spectra obtained from the oxidized system exhibited the signatures for both molecularly adsorbed methanol and methoxy at 2077 ( $\nu_s(\text{CD}_3)$  in molecular methanol) and  $2047\text{ cm}^{-1}$  ( $\nu_s(\text{CD}_3)$  in methoxy), and at  $1116\text{ cm}^{-1}$  ( $\delta_s(\text{CD}_3)$ ); again, on heating to 245 and 275 K, the signature for  $\nu_s(\text{CD}_3)$  in molecularly adsorbed

methanol at  $2077\text{ cm}^{-1}$  transformed into a signature at  $2065\text{ cm}^{-1}$ , characteristic of the second type of methoxy species. Additionally, an intense spectral signature at  $1817\text{ cm}^{-1}$  develops after heating to 245 K, similar to the observations on the clean model catalyst; however, the second feature observed on the clean model catalyst at  $1915\text{ cm}^{-1}$  did not appear on the partially oxidized system. Even more interestingly – and again unlike the observations obtained on the clean model catalyst –, the spectral signatures at  $\sim 2065$ ,  $2047$  and  $1116\text{ cm}^{-1}$  (indicative of methoxy at this temperature) did *not* disappear on heating to 380 or even 510 K, as they have been found to do on the clean model catalyst; however, they do disappear on heating to 600 K; note that this behaviour is very similar to the behaviour of the methoxy peaks observed on the pristine support. Finally, the intense feature around  $1817\text{ cm}^{-1}$  gained further in intensity on heating to 380 K and shifted slightly to  $1832\text{ cm}^{-1}$ , but it has disappeared from the spectra after heating to 510 K, just as in the experiments on the clean model catalyst.

**Interpretation.** We may easily understand the disappearance of the spectral signature for molecularly adsorbed methanol ( $2075\text{ cm}^{-1}$ ) and the simultaneous appearance of another peak around  $2060\text{ cm}^{-1}$ , since it occurs in the experiments on the model catalyst (clean and partially oxidized Pd/Fe<sub>3</sub>O) as well as in the previously described experiments on the pristine Fe<sub>3</sub>O<sub>4</sub> when it is heated to  $\sim 265\text{ K}$ : it is due to the transformation of molecularly adsorbed methanol into a second type of methoxy (in addition to the one that forms already during methanol exposure at 115 K).

The peaks observed between  $1800$  and  $2000\text{ cm}^{-1}$  during the same heating step clearly are signatures for the reaction product CO adsorbed on the Pd nanoparticles, which is the main product from C-H-bond scission on Pd metal. The peak at  $1934\text{ cm}^{-1}$  may be CO-species at Pd(111) hollow sites, and additionally on edge and corner sites; the species around  $1830\text{ cm}^{-1}$  are CO-species in Pd(111) hollow sites (see chapter 4.2.1). Those peaks appear already after heating the sample to 190 or 245 K, indicating that the decomposition of methanol/methoxy to CO on Pd is activated in this temperature window; CO desorbs from the Pd(111) facets at a temperature around 475 K [46]. Interestingly, the spectrum obtained from the *partially oxidized* model catalyst shows only the signature at  $1832\text{ cm}^{-1}$  for CO adsorbed on Pd(111) hollow sites, but not the peak at  $1934\text{ cm}^{-1}$  observed in the experiments on the unoxidized model catalyst. Two explanations may account for this behaviour: 1) The peak around  $1930\text{ cm}^{-1}$  in IRAS spectra has been assigned based on literature values for CO adsorbed on Pd(111) at a coverage of 0.5, where it was assigned to CO adsorbed in hollow sites; this peak shifts strongly

with coverage, and at a lower coverage of 0.25, it appears at  $1830\text{ cm}^{-1}$  [37]. Based on this assignment, it appears that the best explanation why no peak around  $1930\text{ cm}^{-1}$  is observed in the spectra on the partially oxidized system, is that oxidation of the system leads to a lower coverage of the reaction product CO on the Pd metal surface – either because the oxidized system is less active in CO-formation of methanol/methoxy, or because CO is more weakly bound on this system and reaches lower saturation coverages. 2) Since the peak at  $1934\text{ cm}^{-1}$  may partly also be due to CO adsorbed at edge sites, the absence of this peak may be related in part to an oxidation of those sites (remember that CO does not adsorb on Pd surface oxides [104]).

In any case, the more interesting information from the IRAS spectra obtained on the model catalyst, however, is not related to the spectral features for CO – the ones with highest intensity –, but it is contained in the different behaviours of the  $\nu_s(\text{CD}_3)$  and  $\delta_s(\text{CD}_3)$  features, which are indicative for methoxy species in this temperature range: while those IRAS spectral signatures were observed on the pristine support up to an annealing temperature of 510 K, they clearly disappear from the spectra obtained on the *unoxidized* model catalyst between 345 and 510 K – *i.e.* at significantly lower temperatures; moreover, those signatures remain in the spectra of the *partially oxidized* model catalyst up to a temperature of 510 K and disappear only after heating to 600 K. Thus, in summary the partially oxidized model catalyst behaves more like the pristine support in this respect, and interestingly less like the clean, unoxidized model catalyst. The obvious explanation for the behaviour observed on the unoxidized model catalyst is that the support-related methoxy species diffuse to the Pd nanoparticles at temperatures between 275 and 345 K, where they rapidly decompose to CO and  $\text{D}_2$ .

**Transformations on the *Partially Oxidized* Model System.** The observed enhanced thermal stability of methoxy on the *partially oxidized* model system as compared to the unoxidized system suggests that support-particle diffusion is inhibited in the oxidized system. As discussed during the interpretation of the IRAS spectra, two factors may be responsible for this inhibition: for one, the partially oxidized nanoparticles have a significantly smaller metallic surface area than the unoxidized particles due to the formation of Pd surface oxides, and it is anticipated that methanol/methoxy – as the reaction product CO [104] – do not adsorb on the surface oxides; additionally, certain experiments suggest that the surface oxidation of the Pd nanoparticles might start at the parts of the surface close to the interface with the support (the perimeter) – and if this is the case, the surface ox-

ide could additionally act directly as a diffusion barrier for methoxy species from the support to the Pd particles. In either case, surface-oxidation of the Pd particles seems to strongly influence the activity of the model catalyst towards CO-formation, presumably because only metallic Pd may facilitate C-H-bond scission.

### 5.3.2 Repeated Temperature-Programmed Reaction-Experiments

Next, we studied methanol transformation and decomposition on the clean Pd/Fe<sub>3</sub>O<sub>4</sub> model catalyst by repeated temperature-programmed reaction- and desorption-experiments (TPRS, peak temperature: 600 K). For those experiments, 11.7 L of deuterated methanol were adsorbed on the initially clean, stabilized model catalyst at a temperature of 115 K, and then the TPRS experiment was conducted to a peak temperature of 600 K. Subsequently, the sample was cooled back to the exposure temperature (115 K) without any intermediate cleaning or other treatment, and the gas exposure and TPRS experiment was repeated; a total of four such methanol exposure/TPRS cycles was conducted. This procedure is identical to the experimental series conducted on the pristine support discussed in section 5.2.2, and the observations obtained on the model catalyst may thus be compared to the results obtained on the pristine support.

Fig. 5.13 compares all desorption signals (molecular D<sub>2</sub>, water D<sub>2</sub><sup>16</sup>O, formaldehyde D<sub>2</sub>CO, carbon monoxide CO and molecular methanol CD<sub>3</sub>OD – see the appendix A.3 about the monitored masses and data correction) obtained during the first and last TPRS cycle on the model catalyst, and fig. 5.14 displays the signal evolution for the desorption signals of water (D<sub>2</sub>O), molecular methanol, deuterium D<sub>2</sub> and carbon monoxide with the experiment repetition cycles. The following observations were made: in the first TPRS cycle, we have observed the desorption of water at 265 K (with a shoulder around 295 K), the desorption of molecular methanol around 155 and 295 K, deuterium around 325 K (and a broad feature around 490 K), and carbon monoxide at 470 K. The following changes were determined in the following cycles: the yields of deuterium (around 325 K), and carbon monoxide (around 470 K) were found to be strongly decreased, and also the yield of water (around 265 K) has diminished. On the other hand, the molecular desorption of methanol around 300 K increases slightly with the cycles, while the desorption of molecular methanol around 155 K shows no systematic variation.

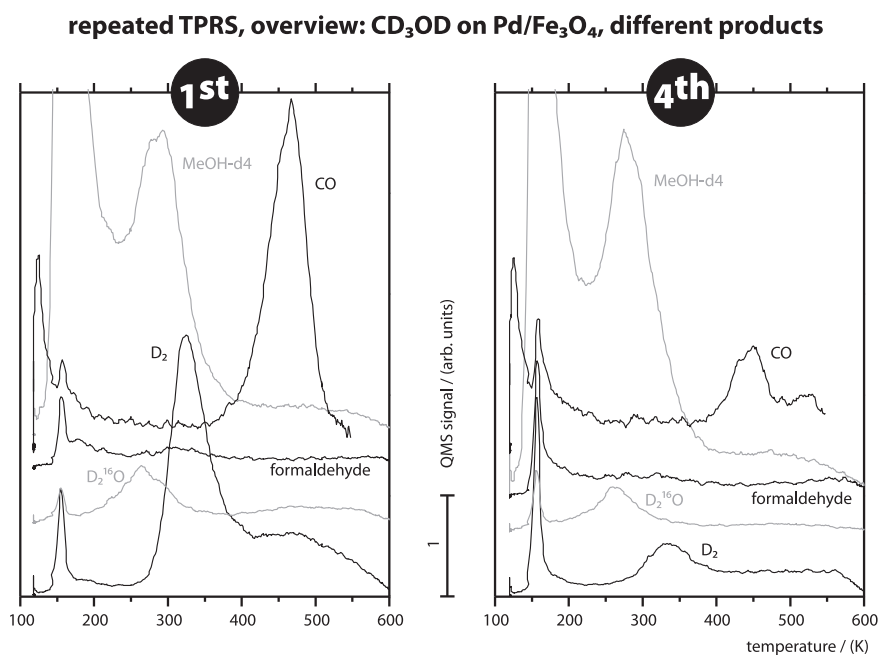


Figure 5.13: Repeated temperature-programmed reaction-desorption TPRS experiments of CD<sub>3</sub>OD (11.7 L adsorbed at 115 K) on Pd/Fe<sub>3</sub>O<sub>4</sub>. Signals of formaldehyde and D<sub>2</sub> were corrected for contributions by the fragmentation component of molecular methanol (formaldehyde by 9 %, and D<sub>2</sub> by 0.3 % of the signal of molecular methanol, mass 34).

**Interpretation.** Compared to the experiment on the pristine support (see section 5.2.2), significant differences as well as similarities were observed in the experiments on the model catalyst; before starting a detailed discussion, we may state by comparison that the methanol desorption observed around 155 K is identical to a desorption feature observed on the pristine support, and may also be assigned to the desorption of methanol from multilayers (for assignment references, see section 5.2.2); because the molecules in those multilayers are not directly bound to the catalyst surface, but instead to previously adsorbed layers of methanol/methoxy, they understandably may exhibit very similar desorption temperatures in experiments on the oxide and the model catalyst.

The main products obtained during methanol decomposition on the clean model catalyst are CO (which desorbs around 475 K, in accordance to experiments on Pd(111) [46]) and D<sub>2</sub> (desorbing around 330 K [172]); the yields of those products decrease with every repetition cycle, while the amount of molecularly desorbing methanol around 300 K increases slightly. Unlike the case on the pristine support, the high-temperature simultaneous desorption



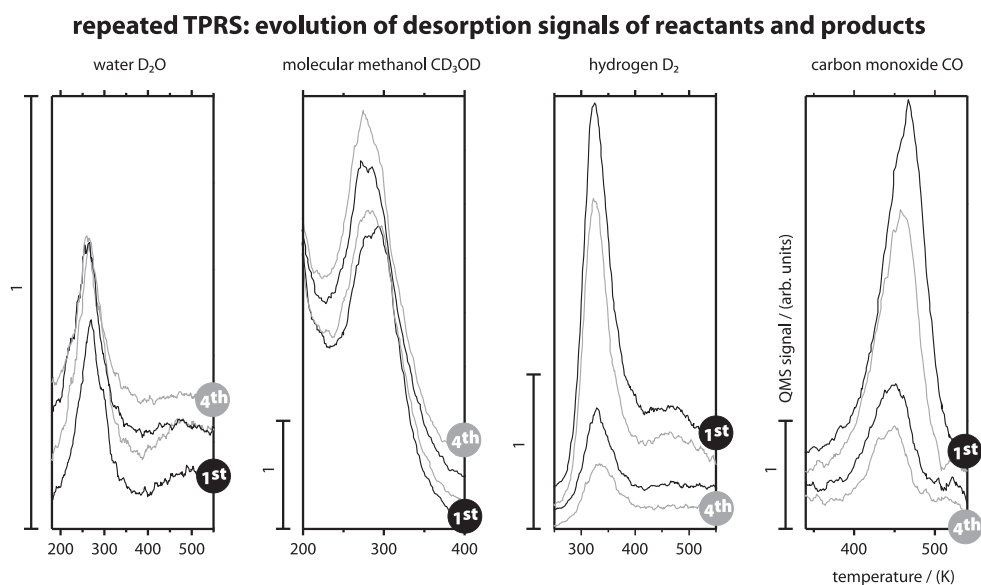


Figure 5.14: Evolution of temperature-programmed reaction-desorption TPRS experiments of  $\text{CD}_3\text{OD}$  (11.7 L adsorbed at 115 K) on  $\text{Pd}/\text{Fe}_3\text{O}_4$  with experiment repetition cycles. Signals of formaldehyde and  $\text{D}_2$  were corrected for contributions by the fragmentation components of molecular methanol (formaldehyde by 9 %, and  $\text{D}_2$  by 0.3 % of the signal of molecular methanol, mass 34 – see also the appendix A.3 for more details).

of molecular methanol together with formaldehyde does not occur on the model catalyst, and formaldehyde as a decomposition product is clearly not formed.

All of those observations can be combined with the results of the IRAS experiments discussed in the previous sections to give a conclusive model: First of all, it is important to notice that the Pd nanoparticles have a different final product of the C-H-bond scission pathway than the pristine support ( $\text{CO}$  and  $\text{D}_2$  instead of formaldehyde and water). The fact that formaldehyde does not form as a decomposition product on the model system – although it might, since formaldehyde forms on the pristine support, and a large fraction of approx. 70 % of the support is also exposed on the model catalyst –, could be understood based on a rapid diffusion of support-related methoxy species in the model catalyst onto the Pd metal phase, where they decompose quickly into  $\text{CO}$  and  $\text{D}_2$  instead; alternatively, an explanation could also be found in different adsorption properties and reactivities of the support in the model catalyst and the pristine oxide, which may be due to the deposition of the Pd nanoparticles and the stabilization procedure –

some earlier STM results from our group do in fact indicate modifications at the surface of the iron oxide support during the stabilization procedure of the model catalyst [173]. Nevertheless, we are lead to believe that such possibly occurring structural modifications of the  $\text{Fe}_3\text{O}_4$  support during the stabilization treatment do not principally affect the reactivity of the support towards formaldehyde formation; this understanding is based on our observation that two methoxy species form on the model catalyst as well as on the pristine support (and with nearly identical IRAS peaks), and that those species exhibit a high thermal stability on the partially oxidized model catalyst – in which support-particle diffusion is limited by the Pd surface oxides – similar to the one observed on the pristine support (both observations were discussed in the temperature-dependance of IRAS spectra on the oxidized model system, see section 5.3.1). Consequently, we believe that decomposition of methoxy to formaldehyde does not occur at the support in the stabilized, *not* oxidized model catalyst, simply because support-related methoxy species rapidly diffuse to the Pd nanoparticles at temperatures below the activation temperature for decomposition to formaldehyde on the support – as already suggested above.

Decreasing yields of the decomposition products CO and hydrogen were observed over the repetition cycles; this may be understood as follows: in addition to C-H-bond scission, also C-O-bond scission occurs on the Pd nanoparticles, which leads to the formation of carbonaceous species (or carbon) on the Pd surface that do not desorb and thus accumulate over the cycles, thereby slowly deactivating the catalyst by surface blocking. In fact, carbon accumulation after methanolic C-O-bond scission is a well-known phenomenon on Pd nanoparticles; as an example, it has been verified by XPS spectra on a Pd/ $\text{Al}_2\text{O}_3$  model catalyst [174]. We have followed the buildup of carbon and the related surface site blocking by IRAS surface titrations with CO:

**Carbon Accumulation and Surface Poisoning.** We have titrated the free metal surface area of an initially clean model catalyst and of the same model catalyst after each of four TPRS cycles with methanol (using the procedure described in the previous paragraphs) by IRAS using CO as a surface-sensitive probe molecule. For those experiments, 13 L of CO were exposed to the model catalyst at 325 K, and the spectra were recorded at 115 K; those spectra are displayed in fig. 5.15. The spectra exhibit an intense peak around  $1970\text{ cm}^{-1}$  with a broad shoulder around  $1935\text{ cm}^{-1}$ ; additionally, a broad peak appears around  $1850\text{ cm}^{-1}$ , and two weak features around  $2085\text{ cm}^{-1}$  (related to CO adsorbed in on-top sites on Pd). It is apparent

that the methanol decomposition first leads to a decrease in the intense peak at  $1970\text{ cm}^{-1}$ , while the other spectral features are relatively constant during the first experiments; however, over the following methanol exposure/flash cycles, also the peak at  $1935\text{ cm}^{-1}$  is more and more attenuated, while the intensity of the broad peak around  $1850\text{ cm}^{-1}$  is still only weakly affected.

Qualitatively, those experiments demonstrate a gradually decreasing free surface available for CO adsorption with each methanol exposure/desorption cycle. The fast decrease of the feature at  $1970\text{ cm}^{-1}$  demonstrates that the carbon-accumulation first affects the edge-, bridge- and defect sites of the nanoparticles, which are related to this peak. Of course, the experiments can only show that carbon accumulates preferentially on these surface sites, but it is not clear from this assignment whether or not the carbon formation reaction (C-O-bond scission) also preferentially occurs at the same sites – or if carbon forms also on other sites at the surface, and only diffuses to the edge sites after its formation; however, it could be shown in an earlier work of our group for the Pd/Al<sub>2</sub>O<sub>3</sub> model catalyst that the carbon-oxygen bond scission occurs preferentially at particle step and edge sites, whereas the dehydrogenation pathway does not exhibit such a structure sensitivity [80, 138] (this interpretation was based on surface titration experiments and individual reaction rate measurements for the C-O- and C-H-bond scission pathways on clean and carbon-precovered model catalysts by molecular-beam experiments). It appears very probable that the C-O-bond scission pathway shows a very similar structure sensitivity also on the Fe<sub>3</sub>O<sub>4</sub>-supported Pd model catalyst, since the Pd nanoparticles in the two model catalysts have very similar morphologies.

**To conclude,** we have observed that different products form during methanol decomposition on the Pd nanoparticles and on the pristine oxide: on the model catalyst, the products of the C-H-bond scission pathway are CO and D<sub>2</sub>, while formaldehyde and water are the products on the pristine support; additionally, C-O-bond scission occurs on the Pd metal surfaces on the model catalyst, and leads to the formation of carbonaceous species or carbon, which do not desorb from the model catalyst, and thus slowly accumulate at the Pd surfaces. Due to this accumulation of carbon, the reactivity of the model catalyst declines with every TPRS cycle.

### 5.3.3 Kinetic Experiments

We have shown in the previous sections that the two products of methanol decomposition on the Pd/Fe<sub>3</sub>O<sub>4</sub> model catalyst are carbon monoxide (and hydrogen as a side product) – which are formed by C-H-bond scission –, and

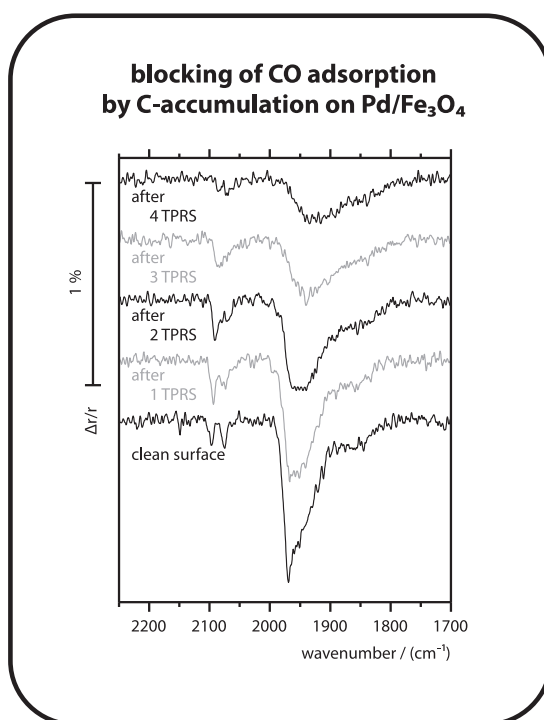
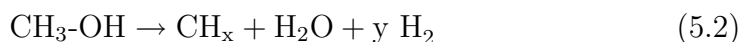


Figure 5.15: Buildup of carbon during TPRS-experiments (peak-T: 600 K) with methanol (11.7 L adsorbed at 115 K) on Pd/Fe<sub>3</sub>O<sub>4</sub> as observed in IRAS spectra of adsorbed CO (13 L adsorbed at 325 K, spectrum taken at 115 K).

carbonaceous species or carbon, which form by a combination of C-H- and C-O-bond scission steps; as discussed in the introduction of this chapter and displayed in the reaction scheme in fig. 5.2, principally any combinatorial sequence of those steps finally leads to carbonaceous species or carbon, and the only definite knowledge we have about the real sequence is that carbon can *not* be formed by C-O-bond scission from CO on the Pd nanoparticles (see the introduction to this chapter for references).

Those two reaction pathways may be simplified to the following two net reactions:



Equation 5.1 describes CO formation, and reaction 5.2 the formation of carbonaceous species or carbon.

The following two sections describe isothermal measurements of the rates in these two reaction pathways. In these experiments, we were confronted

with the problem that the reaction products could not be detected with the mass spectrometer, either because the product does not desorb into the gas phase – as it is the case with carbon or carbonaceous species –, or because it could not be discriminated from the cracking fraction of the reactant: in our experiments, both CO and a prominent EI fragment of methanol have a mass of 28 amu. As an alternative, the CO surface coverage – which is detectable by IRAS – was applied to evaluate the kinetics in both pathways; in this way, the rate of CO-formation can be evaluated from measurements of the buildup of the CO surface coverage on a surface exposed to methanol<sup>9</sup>. The rate of carbon-formation is reflected by the velocity by which a CO steady-state coverage from methanol decomposition is displaced from the surface by accumulating carbonaceous deposits.

Unlike the previously shown experiments, the following experiments were conducted with *undeuterated* methanol (CH<sub>3</sub>OH) instead of the deuterium-labelled methanol CD<sub>3</sub>OD in order to avoid possible kinetic isotope effects on C-H-bond scission and simplify comparison with earlier experiments of our group on Pd/Al<sub>2</sub>O<sub>3</sub> [80, 138].

### Rate of C-O-Bond Scission (Carbon Formation)

First, we measured the rate of C-O-bond scission (rate of carbon-formation); for those experiments, a clean Pd/Fe<sub>3</sub>O<sub>4</sub> model catalyst was heated to the reaction temperature (445 K) and exposed to a continuous methanol beam (1.6 L/s,  $\sim 5.6 \times 10^{14}$  molecules/cm<sup>2</sup>·s); beginning with methanol exposure, 74 time-resolved IRAS spectra were recorded over a period of approx. 5000 s with a time-resolution of  $\sim 9.9$  s for the first  $\sim 179$  s, and  $\sim 84.5$  s for the rest; the spectra were referenced to a background taken right before the begin of methanol-exposure. Fig. 5.16 shows the  $\nu(\text{CO})$ -region of the IRAS spectra obtained after different exposure times; panel a) displays all spectra in a colour-coded 3-dimensional plot, and panel b) shows four representative IRAS spectra in the conventional (*Cartesian*) representation.

Under the applied conditions, an equilibrium CO-coverage from methanolic C-H-bond scission builds up rapidly within the first  $\sim 25$  seconds of the experiment; however, the spectral intensity in the  $\nu(\text{CO})$ -region decreases on the longer run, indicating that the surface loses adsorption capacity towards CO due to the buildup of carbon (and carbonaceous species) from C-O-bond scission, which displace CO from the surface. Judging from spectrum 4 in

---

<sup>9</sup>In order to perform a measurement under steady-state conditions, we have measured the rate of exchange between CO molecules when switching between the two methanol isotopomers <sup>13</sup>CH<sub>3</sub>OH and <sup>12</sup>CH<sub>3</sub>OH, which decompose into either <sup>13</sup>CO or <sup>12</sup>CO and can be discriminated by IRAS.

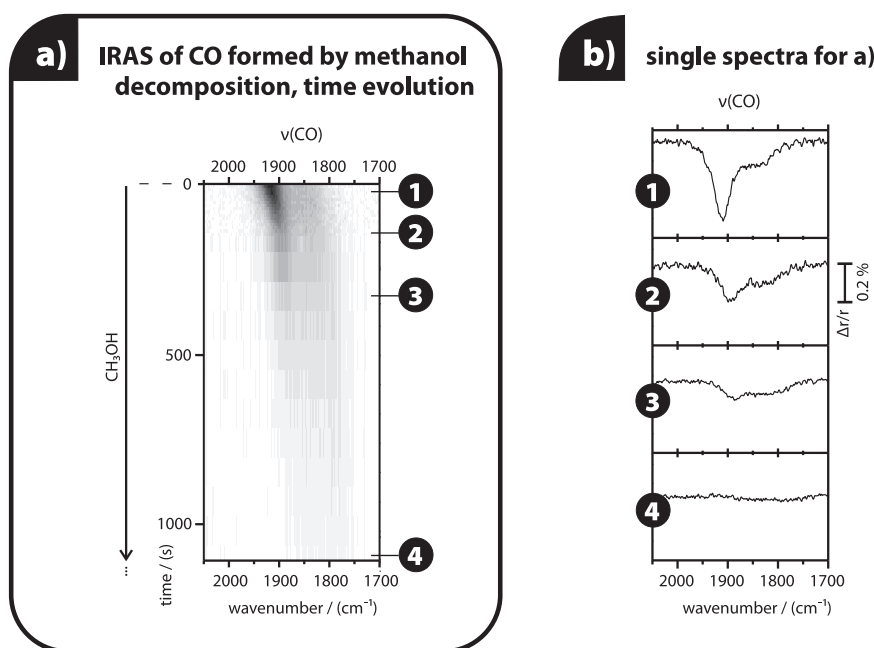


Figure 5.16: IRAS spectra in the C-O-stretching frequency region of the CO formed during an isothermal experiment of methanol  $\text{CH}_3\text{OH}$  decomposition on  $\text{Pd}/\text{Fe}_3\text{O}_4$  at 445 K; the spectra are plotted as a function of methanol exposure time for the evaluation of the carbon accumulation rate.

panel b), nearly no room for CO adsorption seems to be available at the surface after the first 1000 seconds of the experiments already<sup>10</sup>.

Such experiments allow to compare the rates of carbon-formation on different model catalysts; for this purpose, experiments of this type were conducted at identical temperature and methanol pressure on the clean  $\text{Pd}/\text{Fe}_3\text{O}_4$  and  $\text{Pd}/\text{Al}_2\text{O}_3$  model systems (the latter data originate from an earlier study carried out in our group, see [138]); both model catalysts were prepared with similar Pd metal loads, and the Pd nanoparticles on both model systems have similar diameters (6 and 7 nm, respectively) and surface densities (approx.  $1 \times 10^{12} \text{ cm}^{-2}$ ); in both model catalysts, they expose mainly (111) facets and only a minority of (100) facets. A comparison of those experiments is represented in fig. 5.17 a); for this figure, the integral intensity in the  $\nu(\text{CO})$ -region of the spectra was evaluated between 2000 and  $1700 \text{ cm}^{-1}$ , and those integrals were plotted *versus* time.

The experiments on the two model catalysts differ significantly in the poisoning half-life and rate: the  $\text{Fe}_3\text{O}_4$ -supported particles poison approx-

<sup>10</sup>Note that those spectra were recorded under continued gas exposure at 445 K, where CO is only bound in the most strongly binding sites – especially in hollow sites on the  $\text{Pd}(111)$  facets.

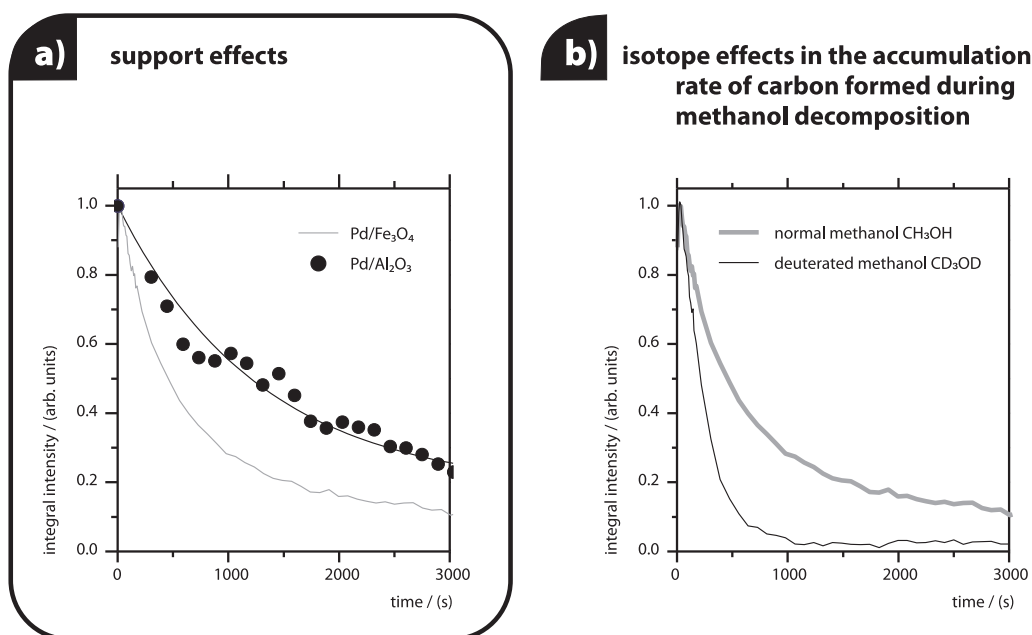


Figure 5.17: Integrated IRAS CO-intensity (see fig. 5.16) *vs.* time for the evaluation of the carbon formation rate during methanol decomposition at 445 K: a) experiments on the Pd/Al<sub>2</sub>O<sub>3</sub> and Pd/Fe<sub>3</sub>O<sub>4</sub> model catalysts, panel b) experiments with isotopically normal and deuterated methanol on Pd/Fe<sub>3</sub>O<sub>4</sub>.

imately twice as fast as the alumina-supported system. This difference in the carbon-accumulation rates may be understood based on the discussions in the previous sections in the following way: methoxy species – which are the central surface intermediate in methanol decomposition on both metal and oxide surfaces (see the literature discussion in this chapter) – may both be formed on the Pd metal surface and on the Fe<sub>3</sub>O<sub>4</sub> film, but they are known not to form on Al<sub>2</sub>O<sub>3</sub> (see [138]); since we have discussed diffusion of methoxy from the Fe<sub>3</sub>O<sub>4</sub> support to the Pd particles as the reason why methoxy species disappear from the IRAS spectra of methanol on the model catalyst between 345 and 510 K (unlike the case on the pristine Fe<sub>3</sub>O<sub>4</sub> support), it appears reasonable to assume that Fe<sub>3</sub>O<sub>4</sub> – unlike Al<sub>2</sub>O<sub>3</sub> – can act as an additional source for methoxy for the Pd nanoparticles, and that methoxy species formed at the Fe<sub>3</sub>O<sub>4</sub> support diffuse to the Pd nanoparticles at the temperature of the discussed experiment (445 K); this additional reservoir for methoxy on the Fe<sub>3</sub>O<sub>4</sub>-support – which is not available for the alumina-supported system – would result in an effectively higher methoxy flux to the Fe<sub>3</sub>O<sub>4</sub>-supported Pd nanoparticles, and if the reactant supply

limits the carbon-formation rate on the Pd particles, this might explain why the Fe<sub>3</sub>O<sub>4</sub>-supported Pd nanoparticles accumulate carbon more rapidly.

However, the Fe<sub>3</sub>O<sub>4</sub> film might not have an infinite capacity for methoxy formation<sup>11</sup>; as an additional explanation for the significantly higher carbon-formation rate on the Fe<sub>3</sub>O<sub>4</sub>-supported system, it may be that also *molecular methanol* diffuses from the Fe<sub>3</sub>O<sub>4</sub> film to the Pd nanoparticles, while the same process is significantly less efficient on the alumina support – *i.e.*, the iron oxide may form a capture zone for methanol around the Pd nanoparticles. This assumption is based on the very different desorption points of molecular methanol from the two supports (alumina: 190 K [169], Fe<sub>3</sub>O<sub>4</sub>: 300 K), which correspond to methanol desorption energies of 48.1 kJ/mole on alumina, and 77.1 kJ/mole on Fe<sub>3</sub>O<sub>4</sub> (estimated based on the Redhead-formula for first-order desorption with a typical preexponential factor  $A$  of  $10^{-13} \text{ s}^{-1}$  [149], see [32, 27]); based on those estimations, the desorption rate constants  $k_{\text{des}}$  and surface half-life times  $\tau$  of molecular methanol on the two supports at the experiment temperature of 445 K can be calculated as  $k_{\text{des}} = A \cdot \exp(-E_{\text{des}}/k_{\text{B}} \cdot T) = 2.2 \cdot 10^7 \text{ s}^{-1}$ ,  $\tau = \ln 2/k_{\text{des}} = 3.1 \cdot 10^{-8} \text{ s}$  on alumina, and  $8.8 \cdot 10^3 \text{ s}^{-1}$ ,  $7.9 \cdot 10^{-5} \text{ s}$  on Fe<sub>3</sub>O<sub>4</sub>. In order to estimate the efficiencies of the capture zones on the two supports, we compare the root mean square distances  $\bar{x}$  that molecular methanol can travel on the two oxides at 445 K during its surface half-life time; this distance is given by the diffusion coefficient as  $\bar{x} = \sqrt{2D \cdot t}$  (see chapter 2.1.1); the diffusion coefficient is described by an Arrhenius-expression as  $D = D_0 \cdot \exp(-E_{\text{diff}}/k_{\text{B}} \cdot T_s)$ ; an expression for  $D_0$  may be derived from transition state theory, and depends on the activation entropy of the process. The important quantity for surface diffusion is the activation energy; its magnitude is about a tenth of the desorption energy (see [1], vol. 3, p. 926). Assuming that the activation entropy is identical on the two supports, we can calculate the ratio of the distances that methanol can travel on the two supports:

$$\frac{\bar{x}_{\text{Al}_2\text{O}_3}}{\bar{x}_{\text{Fe}_3\text{O}_4}} = \frac{\sqrt{2 \cdot D_{\text{Al}_2\text{O}_3} \cdot \tau_{\text{Al}_2\text{O}_3}}}{\sqrt{2 \cdot D_{\text{Fe}_3\text{O}_4} \cdot \tau_{\text{Fe}_3\text{O}_4}}} = \frac{\sqrt{\exp(-E_{\text{des,Al}_2\text{O}_3}/k_{\text{B}} \cdot T \cdot 10) \cdot \tau_{\text{Al}_2\text{O}_3}}}{\sqrt{\exp(-E_{\text{des,Fe}_3\text{O}_4}/k_{\text{B}} \cdot T \cdot 10) \cdot \tau_{\text{Fe}_3\text{O}_4}}} = 0.029$$

According to this rough estimation based on its different desorption points, methanol may travel approx. 35 times further on Fe<sub>3</sub>O<sub>4</sub> than on alumina

<sup>11</sup>Note that methanol-dissociation to methoxy also forms surface hydroxyl groups, which – according to our previous discussion – desorb as water, thereby leading to surface oxygen loss and thus slowly reducing the capacity of the support for methanol dissociation. However, it might be that at 445 K surface oxygen can be replenished by oxygen diffusion from the oxide’s bulk to its surface.

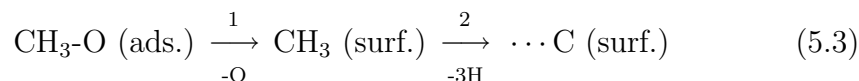


during its surface half-life time – *i.e.*,  $\text{Fe}_3\text{O}_4$  may add a significantly larger capture zone for methanol around the Pd particles than alumina; note, however, that we can not calculate an absolute size of this zone, because we do not know an absolute value for the preexponential factor  $D_0$ .

Although we believe, based on the previously discussed experiments, that a diffusion of methanol and methoxy from the support to the particles does in fact account as the major contribution for the higher carbon formation-rate on the  $\text{Fe}_3\text{O}_4$ -supported model catalyst, it must be mentioned here that the differences may in parts also be due to a second possible reason: although both model catalysts are prepared with similar Pd metal loads and under similar deposition conditions (temperature and Pd evaporator metal deposition rate), so that the equilibrium shapes and morphologies (expressed by parameters such as diameter, size distribution, or particle density on the surface) of the Pd particles are very similar, those preparation methods can not exclude slight differences in the morphologies and structure of the Pd nanoparticles in the two model catalysts; such differences might, for example, arise from the stabilization procedure of the  $\text{Fe}_3\text{O}_4$ -supported particles, which was not used in the alumina-supported system. Although STM images of the two model systems show, as discussed, that the nanoparticles have very similar morphologies with respect to the regular facets and the overall particle size, the density of *irregular* sites such as edge- and corner sites or defects on the Pd metal surfaces in the two catalysts might be different; such irregular sites, however, may account significantly for the activity of the system – in fact, the Pd-particle edge-sites were previously reported to be very active in methanolic C-O-bond scission based on experiments on the alumina-supported model system [80]. Therefore, the higher carbon-formation rates on the  $\text{Fe}_3\text{O}_4$ -supported nanoparticles might possibly be due to different densities of defect sites on the two model systems – although, as said above, we believe that this can only be an additional contribution to that of support-particle diffusion.

Fig. 5.17 b) shows two measurements of the carbon-formation rate on Pd/ $\text{Fe}_3\text{O}_4$  (at 445 K), one with isotopically normal ( $\text{CH}_3\text{OH}$ ) and the other with deuterated methanol ( $\text{CD}_3\text{OD}$ ); the beam intensity was identical to the previously discussed experiments ( $\sim 5.6 \times 10^{14}$  molecules/ $\text{cm}^2 \cdot \text{s}$ ). In those experiments, considerably higher carbon-formation rates were observed with the deuterated methanol than with isotopically normal methanol (the poisoning half-life time with deuterated methanol is only approximately half as long as with the normal isotopomer).

It seems that those differences arise from a primary kinetic isotope effect; for the discussion, let's assume that the reactions follows a reaction scheme like:



(note that, as discussed above, the sequence for carbon-formation may also be different; such different sequences, however, may also be treated similarly to the following discussion, and lead to the same interpretation). Kinetic isotope effects result from different activation barriers for the bond-scission of differently isotopically labelled bonds; such differences arise from the different zero point and transition state energies of those isotopomers, which themselves are due to the mass difference of the isotopes [175, 73]; due to the high relative mass difference of protium (normal hydrogen H) and deuterium, C-H- and C-D-bond scissions exhibit exceptionally strong kinetic isotope effects [175, 73], which results in a *faster* dehydrogenation reaction of *isotopically normal* compounds as compared to deuterated compounds, because the latter have a lower zero-point energy and therefore a higher activation barrier for dehydrogenation. However, the *opposite* seems to have been observed experimentally for the rate of carbon-formation from methanol: the deuterated compound dehydrogenates *faster* than normal methanol.

In order to suspend this seeming controversy, we need a closer inspection into the reaction mechanism: we did not yet take into account that the main reaction pathway on the surface is C-H-bond scission to CO (reaction 5.4, step 3) [159]; thus, decomposition to carbon according to the pathway 5.3 occurs only with the few species that do not undergo the rapid CO-formation or trivially desorb prior to a possible reaction. Based on this explanation, the significance of the kinetic isotope effect can now be understood as follows: During the surface residence time of methoxy, the C-O-bond scission step (1) in pathway 5.3 and the C-H-bond scission (3) in pathway 5.4 compete; however, in a deuterated compound, the dehydrogenation steps (C-D-bond scission) occur more slowly than in undeuterated compounds (C-H-bond scission steps) for the reasons discussed in the previous paragraph. As a consequence, more deuterated compounds will enter the competing pathway 5.3 than in the case of undeuterated compounds, and thus, the rate of carbon accumulation will be faster with the deuterated isotopomer, as it was experimentally observed in this work.

### Rate of CO-Exchange (CO-Formation and Desorption)

Finally, kinetic experiments aiming at a measurement of the CO-formation rate (C-H-bond scission rate) were conducted on the Pd/Fe<sub>3</sub>O<sub>4</sub> model catalyst at three different temperatures (422, 445 and 467 K); again, reference experiments exist on the Pd/Al<sub>2</sub>O<sub>3</sub> model system [138]. For those experiments, the sample was heated to the reaction temperature and then exposed to a constant flux of methanol ( $5.6 \times 10^{14}$  molecules/cm<sup>2</sup>·s), leading to the buildup of a steady-state coverage of CO by C-H-bond scission. Then, molecular beams with <sup>12</sup>CH<sub>3</sub>OH and isotopically labeled <sup>13</sup>CH<sub>3</sub>OH were repeatedly switched, so that at any time, only one of those beams hit the surface, thereby maintaining steady-state conditions throughout the experiment; those two isotopomers dehydrogenate to <sup>12</sup>CO and <sup>13</sup>CO, respectively, which replace each other at the surface after beam switching due to their formation and the desorption of the other CO-isotopomer. The adsorbed surface species were monitored *via* time-resolved IRAS spectroscopy with a temporal resolution of 0.64 s (at 467 K), 0.96 s (at 445 K) and 2.6 s (422 K). In order to improve the signal-to-noise ratio, spectra were accumulated over several beam switching cycles and averaged (14 at 467 K, ten at 445 K and four at 422 K).

The spectra obtained during such an isotope exchange experiment at 445 K are displayed in fig. 5.18; panel a) displays a colour-coded 3-dimensional plot of the obtained spectra including a description of the beam-sequence during the displayed experiment, and panel b) displays spectra at five example points labeled in panel a) in the conventional (*Cartesian*) representation. Initially, the surface was exposed to the <sup>12</sup>CH<sub>3</sub>OH-beam, producing adsorbed <sup>12</sup>CO; after switching to the <sup>13</sup>CH<sub>3</sub>OH-beam, <sup>12</sup>CO desorbs and the surface becomes progressively covered with <sup>13</sup>CO. Since the stretching frequencies of the <sup>12</sup>CO and <sup>13</sup>CO species differ by approx. 42 cm<sup>-1</sup> due to their different reduced masses – <sup>12</sup>CO exhibits a main peak at  $\sim 1902$  cm<sup>-1</sup>, and <sup>13</sup>CO exhibits this peak at  $\sim 1860$  cm<sup>-1</sup> –, IRAS allows to distinguish between those two dehydrogenation products. In order to extract the kinetics of isotope exchange from these data, we calculated the arithmetic mean absorption frequency for each spectrum in the range of 1700 and 2000 cm<sup>-1</sup>; fig. 5.19 displays a plot of those averages *vs.* time for all three experiment temperatures – both for the exchange from <sup>12</sup>C- to <sup>13</sup>C-methanol and the reverse.

Both directions of exchange occur with similar rate constants; the following values were obtained:  $0.032 \pm 0.010$  s<sup>-1</sup> (at 422 K),  $0.087 \pm 0.023$  s<sup>-1</sup> (at 445 K) and  $0.26 \pm 0.10$  s<sup>-1</sup> (at 467 K). Those data are nearly identical to the values published for the same reaction on the Pd/Al<sub>2</sub>O<sub>3</sub> model catalyst [138]; for 445 K the authors reported an exchange rate constant of

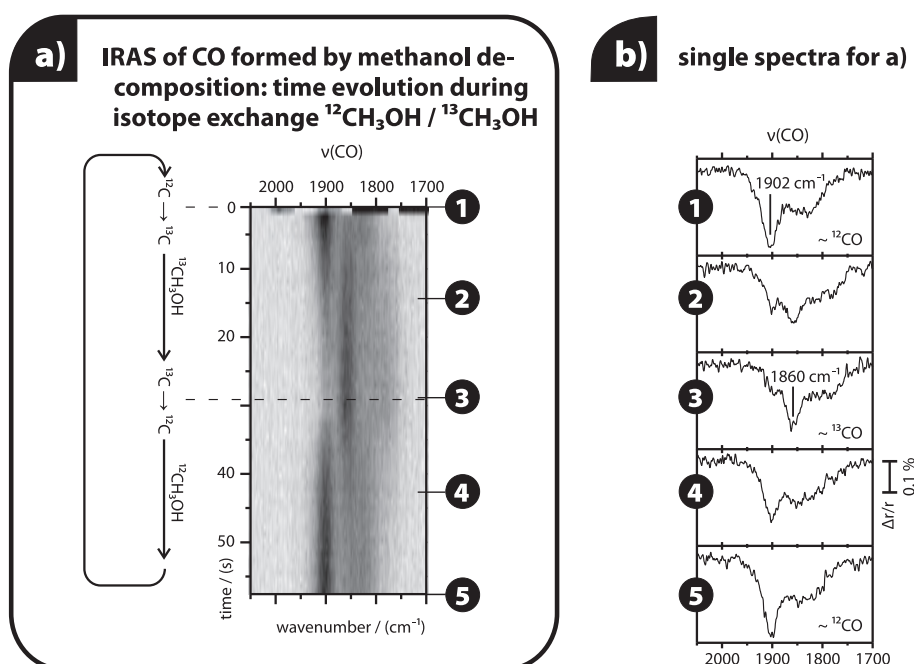


Figure 5.18: IRAS spectra in the C-O-stretching frequency region of the CO formed during an isothermal experiment of methanol decomposition on Pd/Fe<sub>3</sub>O<sub>4</sub> at 445 K in which <sup>12</sup>CH<sub>3</sub>OH was exchanged for <sup>13</sup>CH<sub>3</sub>OH; the spectra are plotted as a function of time for the evaluation of the CO exchange rate.

$0.098 \pm 0.03 \text{ s}^{-1}$  (our value:  $0.087 \pm 0.023 \text{ s}^{-1}$ ) – *i.e.*, the CO exchange rate is – within the error limit – identical on both model catalysts.

## Discussion and Conclusion

Before a discussion of this last result, we will give a short retrospect over the experiments in this section. We have discussed measurements of carbon formation- and CO-exchange rates on the Pd/Fe<sub>3</sub>O<sub>4</sub> model catalyst in the two preceding parts, and compared them to the results of identical experiments conducted on the Pd/Al<sub>2</sub>O<sub>3</sub> model system from an earlier project of our group [138]. Carbon-formation was found to proceed with twice as high rates on the iron oxide-supported model system than on Pd/Al<sub>2</sub>O<sub>3</sub>; two possible explanations were given: based on the experiments discussed in the previous sections, the observed effect is at least in parts due to support-particle-diffusion of methoxy, presumably with additional contribution by support-particle diffusion of *molecular* methanol (capture zone effect); based on the previously discussed experiments, such a diffusion is expected to occur

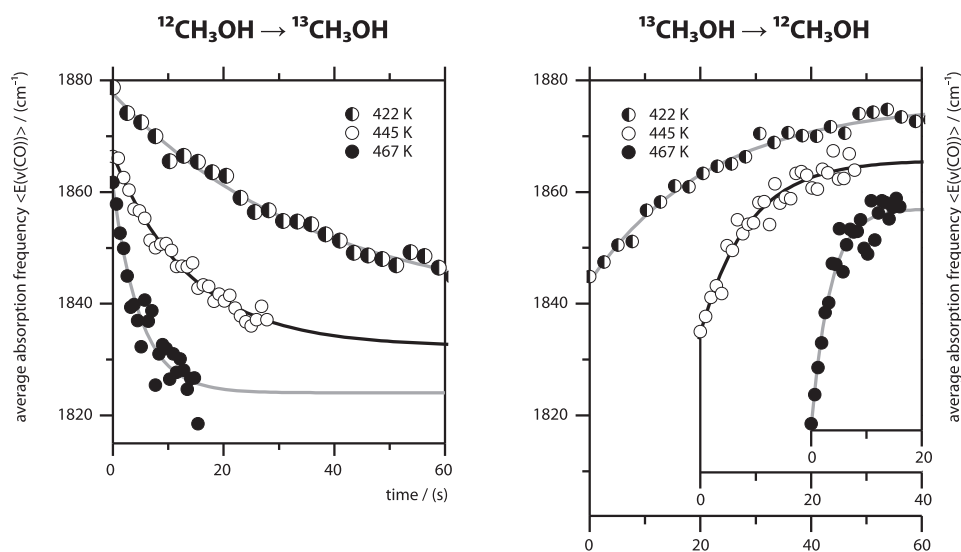


Figure 5.19: Averaged IRAS intensity in the CO stretching frequency region (see fig. 5.18) *vs.* time for the evaluation of the CO exchange (formation/desorption) rate during methanol decomposition on Pd/Fe<sub>3</sub>O<sub>4</sub> at 445 K: a) exchange of <sup>12</sup>CH<sub>3</sub>OH for <sup>13</sup>CH<sub>3</sub>OH, panel b) reverse exchange.

on the Fe<sub>3</sub>O<sub>4</sub>-supported system, but not on the Al<sub>2</sub>O<sub>3</sub>-supported model catalyst. Additionally, the different carbon-formation rates on the two differently supported model catalysts may also in parts be caused by possibly different defect-densities of the Pd nanoparticles on the two different supports, since irregular sites (such as edge-sites) were previously reported to be very active in carbon-formation from methanol. In any case, the contribution of support-particle diffusion to the different carbon-formation rates on the two model catalysts would indicate that carbon-formation from methanol was limited by the availability (*i.e.*, the surface coverage) of the central reaction intermediate methoxy under the experiment conditions.

Interestingly, the exchange of CO formed by methanol decomposition on the surface (as observed in the isotope-switching experiments discussed lastly) does *not* exhibit different rates on the two different model systems; this observation is somewhat surprising, since CO-exchange proceeds with much higher reaction rates than carbon formation (as indicated by the very different half-life times in the two experiments), and might thus be expected to depend rather more critically on the availability of the reactant than the latter reaction, and as a consequence, it should proceed rather with higher rates (and not identical rates) on the Fe<sub>3</sub>O<sub>4</sub>-supported system. Presumably, a different factor limits the rate of CO formation under the experimental

conditions. CO exchange occurs when the previously formed CO desorbs from the surface, giving room for the formation of new CO molecules from the reactant methoxy, and is thus in fact a sequence of (at least) two processes (CO-formation from methoxy, followed by CO-desorption to produce free surface sites for further reactions). This description of CO-exchange suggests the following explanation why the CO exchange rates are similar on the two model catalysts: CO-formation may be such a fast reaction, that its rates are not effectively limited by the availability of the reactant methoxy under the reaction conditions in our experiments, but by the availability of free surface sites that are needed for the reaction to occur; those free surface-sites, however, presumably are critically limited by the desorption of the product CO, which thus would be the rate-limiting step for the CO-exchange under the measurement conditions; as a consequence, the CO-formation rate would be identical to the CO desorption rate under steady-state conditions. In fact, an estimation of the surface half-life time of CO based on its desorption point of 475 K *via* the Redhead-method (frequency factor of  $10^{13} \text{ s}^{-1}$ , see before) yields a value of approx. 24 s at 445 K, which is in the range of our experimentally observed CO exchange rate.

However, it needs to be stated again that the differences between the two reaction pathways observed on the two model catalysts might also be due to possible differences in the density of defect sites on the Pd nanoparticles on the two different supports: as said above, carbon-formation was previously described to be related to irregular (presumably mainly edge- and corner-) sites on the Pd nanoparticles; CO-formation on the other hand was described to show no structural sensitivity, and thus seems to proceed mainly on regular (facet) sites [80]. If it were true that the higher rate of carbon-formation on the  $\text{Fe}_3\text{O}_4$ -supported model catalyst relates mainly to a higher density of irregular (defect) sites on the Pd nanoparticles in this model system – and not so much on the possibility of support-particle diffusion of the reactant methoxy (and presumably also molecular methanol), as it was described in this work –, then the similar rates of CO-formation could be easily explained simply with the fact that the amount of regular Pd sites – on which CO-formation mainly proceeds – is very similar on the two model catalysts; in this case, it would not be necessary to claim that the rate of CO-formation was limited by the availability of free surface reaction sites, which are limited by the desorption of CO. Nevertheless, we are lead to believe – based on the arguments given previously in this section (section 5.3.3), most importantly the observation of support-related methoxy in the experiments on an *oxidized* Pd/ $\text{Fe}_3\text{O}_4$  model system – that support-particle-diffusion of methoxy and methanol does play an important role during methanol decomposition on the Pd/ $\text{Fe}_3\text{O}_4$  model catalyst.

## 5.4 Summary

In this chapter, we have discussed experimental examinations of methanol decomposition on the  $\text{Fe}_3\text{O}_4(111)$  thin film and on the  $\text{Pd}/\text{Fe}_3\text{O}_4$  model catalyst. The decomposition of methanol is a reaction with many practical implications (*e.g.* in industrial formaldehyde synthesis, or in direct methanol fuel cells (DMFCs), where methanol is applied as a hydrogen carrier); additionally, the reverse reaction (methanol synthesis from *syngas* – a mixture of CO and hydrogen) is applied for the industrial preparation of methanol, which is an extremely important raw chemical product. In surface-science and catalysis research, methanol decomposition is a well-established model reaction that has been previously studied on many well-characterized materials; the existing reports constitute a reference for the interpretation of methanol decomposition on yet unstudied materials.

Different decomposition products of methanol have been previously reported, including formaldehyde, CO, methane, or carbonaceous species/carbon; an overview over the previously reported decomposition reactions on metals and oxides has been provided at the beginning of this chapter. In the present work, the formation of formaldehyde and water (as a side product) has been observed on the pristine oxide  $\text{Fe}_3\text{O}_4$ ; the main products on the  $\text{Pd}/\text{Fe}_3\text{O}_4$  model catalyst are carbon monoxide (CO) and hydrogen, and additionally carbonaceous species or carbon (as the minor pathway).

**Methanol Decomposition on  $\text{Fe}_3\text{O}_4$ .** At a temperature of 115 K, methanol was found by IRAS to adsorb both molecularly and dissociated into methoxy on the  $\text{Fe}_3\text{O}_4(111)$  thin oxide film; both adsorbates accumulate simultaneously at the surface. The second product of methanol dissociation into methoxy are hydrogen ions, which are accommodated on the oxide surface in the form of hydroxyl groups formed on surface oxygen ions exposed on the iron oxide. At an exposure between 1.6 and 2.3 L, the monolayer of methanol/methoxy species saturates; on further exposure at this temperature, methanol condenses into multilayers, which desorb around 155 K.

Around 260 K, water desorbs from a surface saturated with methanol due to the decomposition of unstable surface-hydroxyl groups; isotope-labeling experiments have revealed that those desorbing water molecules contain lattice oxygen from the oxide (and also a contribution of methanolic oxygen, which might indicate that methanolic C-O-bond scission might also occur on the oxide); as a consequence, the water-desorption leads to a loss of surface oxygen from the oxide. Around 300 K, a large amount of methanol desorbs; this desorption may have two conceivable sources: methanol that has been molecularly adsorbed on the oxide, and recombinative desorption of methoxy with surface-hydroxyl groups; the desorption of molecularly ad-

sorbed methanol clearly accounts for the major part of the desorption, but it was argued that recombinative desorption between some of the methoxy species and the remaining hydroxyl groups on the surface might constitute a minor contribution. However, no remainders of hydroxyl groups could be spectroscopically detected on the surface at 380 K, whereas considerable amounts of methoxy-species were still present on the surface up to a temperature between 510 and 600 K, and we believe that those methoxy species are simply forced to remain at the surface due to the previous loss of the surface hydroxyl-groups by water desorption, which otherwise could supply hydrogen for a recombinative desorption of methoxy as methanol. Thus, after water desorption, those methoxy species can only leave the surface when an alternative reaction pathway gets activated, which occurs around 555 K with the formation of molecular methanol and formaldehyde in a reaction between two methoxy species; the products desorb simultaneously at this high temperature as soon as the reaction has occurred. The hydrogen transfer between two methoxy species may either proceed under participation of surface-hydroxyl groups or directly between two methoxy species on an encounter; the lack of water desorption at this temperature might imply that hydroxyl groups presumably are not the carriers for this transfer.

Based on this description, the observed formaldehyde formation on a freshly prepared  $\text{Fe}_3\text{O}_4$  film is a consequence of the loss of some surface hydroxyl groups by water desorption at low temperatures, because it precludes the possibility for some methoxy groups to leave the surface by recombinative desorption into molecular methanol. However, less water desorbs from the surface in the later TPRS experiments, presumably because only a certain type of oxygen – which might form particularly labile hydroxyl-groups – might be responsible for water desorption from a freshly prepared  $\text{Fe}_3\text{O}_4$  film; this species seems to get nearly depleted during only one TPRS experiment on the freshly prepared film. Additional experiments from a cooperating group support the interpretation that surface-oxygen loss is responsible for the deactivation of the catalyst towards formaldehyde formation [96]; those experiments demonstrate also that the formaldehyde yield can be recovered by a simple reoxidation of the oxide. In the view of a participation of lattice-oxygen on the oxide during the formation of formaldehyde, it appears that the reaction mechanism should be classified as a *Mars-van-Krevelen* mechanism [85].

**Methanol Decomposition on the Pd/ $\text{Fe}_3\text{O}_4$  Model Catalyst.** When Pd nanoparticles are deposited on the oxide support, the selectivity of the system changes, and no formaldehyde formation can be observed anymore; instead, CO and hydrogen are found to be the main reaction products. The



following observations have been made about methanol decomposition on the Pd/Fe<sub>3</sub>O<sub>4</sub> model catalyst:

At 115 K, methanol exposure on the model catalyst leads to a simultaneous accumulation of molecularly adsorbed methanol and methoxy, as it was also observed in IRAS spectra on the pristine support; then, at slightly elevated temperatures (around ~ 245 K), CO appears as a methanol decomposition product in IRAS spectra on the Pd particles; the second decomposition product in this case is atomic hydrogen, which desorbs from the system around 330 K; CO desorption was observed around 475 K.

Unlike the case on the pristine oxide, where methoxy species could be detected up to 510 K, the IRAS-signatures of methoxy disappear from the model catalyst already at significantly lower temperatures (between 345 and 510 K); also, no desorption of formaldehyde – the methoxy decomposition product on the pristine support – has been observed. Note that the Pd nanoparticles cover only approx. 30 % of the oxide’s surface area, so that the absence of support-related methoxy species at elevated temperatures, and especially the absence of decomposition products such as formaldehyde is not immediately understood; note additionally, that the experiments on a *partially oxidized* model system discussed below indicate that the Fe<sub>3</sub>O<sub>4</sub>-support does not lose its capability to dissociate methanol into methoxy due to the deposition of Pd nanoparticles – although this might be speculated, *e.g.* because Pd might possibly nucleate at the active sites of the oxide. As an explanation for the absence of formaldehyde formation and the disappearance of methoxy species at significantly lower temperatures on the model catalyst, we believe that the support-related methoxy species diffuse onto the Pd nanoparticles between 300 and 500 K, where they rapidly decompose – mainly into CO.

Repeated TPRS experiments show a gradual decrease in the yields of CO and hydrogen on the model catalyst, indicating that carbonaceous deposits or carbon are formed at the Pd surface of the model catalyst by methanolic C-O-bond scission [159, 174]; those species accumulate slowly on the Pd surface and block its surface, leading to a decrease of the catalytic activity. IRAS surface titration experiments with CO as a probe molecule demonstrate that carbon accumulates preferentially on the edge- and other irregular sites of the Pd particles, while the regular sites on the (111) facets – which constitute the majority of sites – remain nearly free of carbon for a significantly longer time.

We have performed experiments aiming at a measurement of the carbon- and CO-formation rates on the Pd/Fe<sub>3</sub>O<sub>4</sub> model catalyst; identical experiments have been previously conducted on the Pd/Al<sub>2</sub>O<sub>3</sub> model catalyst

[80, 138] and allow to compare the reactivities of the two model systems, which resemble each other in terms of the morphology of the Pd nanoparticles; however,  $\text{Al}_2\text{O}_3$  is known to not dissociate methanol to methoxy, and also, molecularly adsorbed methanol desorbs from this oxide at a significantly lower temperature of 190 K [159] (as compared to  $\sim 300$  K on  $\text{Fe}_3\text{O}_4$ ).

The experiments show that CO formation proceeds with much higher rates than carbon-formation, indicating that it is the major pathway of methanol decomposition on the Pd particles. The rate of carbon accumulation was measured at 445 K; it is approximately twice as high on the  $\text{Fe}_3\text{O}_4$ -supported sample as compared to the  $\text{Al}_2\text{O}_3$ -supported system; the CO-formation rates on the other hand are very similar on the two model catalysts (also at 445 K). Two possible models were suggested for explanation:

1. The higher carbon formation rates on the Pd/ $\text{Fe}_3\text{O}_4$  model catalyst may be accounted for by methoxy-diffusion from the  $\text{Fe}_3\text{O}_4$  support to the Pd nanoparticles; additionally, arguments have been supplied that  $\text{Fe}_3\text{O}_4$  might also form a significantly larger capture zone for molecular methanol around the Pd particles than alumina. Those two processes may lead to an increased reactant supply to the Pd surface; because  $\text{Al}_2\text{O}_3$  does not dissociate methanol to methoxy, and additionally shows a significantly lower methanol desorption temperature, a similar supply of reactant can not occur on the Pd/ $\text{Al}_2\text{O}_3$  model catalyst. Carbon-formation is a slow reaction, and the differences observed in the carbon formation rate on the two model systems might be taken as an indication that the rate is limited by the availability of the reactant. The CO-formation rate on the other hand is more than 100 times faster than carbon formation; although it might be assumed for such a fast reaction that its rate depends sensitively on the reactant availability, no differences were observed in this case on the two model catalysts. As an explanation for this observation, it was suggested that the CO-formation rates might be limited by the availability of reaction sites, which in turn might be limited by the desorption of the product CO (note that the reaction temperature was below the CO-desorption point,  $\sim 475$  K) – thus, the CO-formation rate might be product-inhibited.
2. Alternatively, the Pd particles on the two model catalysts might simply differ in the density of Pd defect sites; in fact, a previous project of our group has indicated that certain irregular sites show an increased activity in the C-O-bond scission (carbon formation) pathway, while CO-formation was said to be structure-insensitive [80]. Thus, a higher density of defect sites might lead to an increased carbon-accumulation rate, without influencing the CO formation rates significantly. If this

possible explanation holds for the observations made in this work, the  $\text{Fe}_3\text{O}_4$ -supported Pd-particles would need to have a higher density of those defect sites.

Although both models may be good explanations for the observations, we believe that support-particle diffusion undoubtedly accounts at least in parts for the observed difference, because several other observations (named above) indicate that a support-particle diffusion of methanol/methoxy from  $\text{Fe}_3\text{O}_4$  to the Pd particles does indeed take place.

**Experiments on the Partially Oxidized Model Catalyst.** Experiments were also conducted on a model catalyst treated with oxygen at 550 K; this treatment of the catalyst leads to the formation of Pd surface oxides, which reduce the metallic part of the Pd surface by  $\sim 60\%$  and have been previously shown to deactivate the catalyst towards CO oxidation [105]. In the current project, we have observed that methoxy species have a higher thermal stability on this partially oxidized model catalyst as compared to reduced Pd/ $\text{Fe}_3\text{O}_4$ , and that they disappear from the sample only at temperatures between 510 and 600 K instead of diffusing onto the Pd surface between 300 and 510 K, as they seem to do on the unoxidized model catalyst. The high thermal stability of methoxy on the oxidized system – which is similar to the observations on the pristine support – may be due to two reasons: 1) the total metallic Pd surface area is smaller on the oxidized system due to the Pd surface oxides; this may reduce the capacity of the particles to take up and decompose methoxy as compared to the unoxidized particles; 2) certain other experimental observations might be interpreted as suggestions that the surface oxides preferentially form at the perimeter of the Pd particles; if this really was the case, it might be that those surface oxides might directly obstruct support-particle-diffusion; note that at least CO has been observed to not adsorb on the Pd surface oxides [101].

As a consequence, the support-related methoxy species could not all diffuse onto the Pd nanoparticles and decompose there as they were described to do on the unoxidized model catalyst; instead, most methoxy species on the oxidized model catalyst show a similar thermal stability as on the pristine support. Based on those observations, we believe that the  $\text{Fe}_3\text{O}_4$  support in the model catalyst is capable to dissociate methanol to methoxy – just as the pristine support (and that this ability is not decreased by the deposition of Pd nanoparticles on the support, *e.g.* due to a possible, preferential nucleation of Pd on possibly active defect sites on the oxide, or due to possible changes in the oxide surface during the oxidative stabilization procedure for the Pd nanoparticles).



# Chapter 6

## Conversion of 2-Butene

### 6.1 Introduction

This chapter concentrates on the reactions of 2-butene (see fig. 6.1) with deuterium on the Pd/Fe<sub>3</sub>O<sub>4</sub> model system as a prototype for catalytic hydrocarbon conversions. Hydrocarbon conversion is a central process in numerous industrial applications including petrochemical hydrotreating in crude oil-refining, the hardening of plant oils to edible fats, and also in some preparations of fine chemicals and pharmaceuticals [24, 25]; it is one of the oldest and most studied classes of reactions in heterogeneous catalysis, but despite its economic significance and the extensive work that has already been done, key aspects of it are still not understood – including the important question regarding the mechanisms that govern activity and chemoselectivity between the reaction pathways.

Selectivity is generally considered to depend on the catalyst's structure, and often the presence of certain coadsorbates (*modifiers*) is discussed to be the central prerequisite to obtain and tune selectivity. One modifier that has been frequently discussed to play a key role for the chemoselectivity in hydrocarbon conversion is carbon [26], which is typically present during catalytic hydrocarbon conversion under realistic conditions due to the rapid decom-

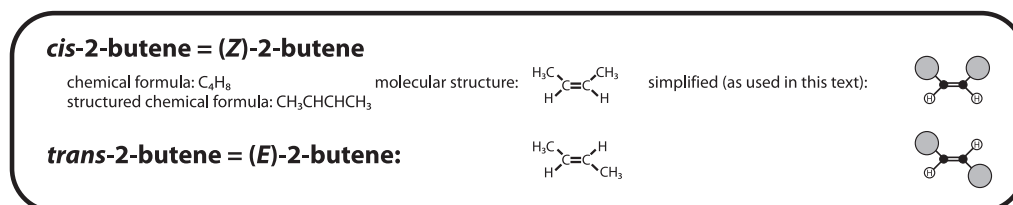


Figure 6.1: The molecules *cis*- and *trans*-2-butene.

position (dehydrogenation) of hydrocarbons on the clean metal surfaces of many catalysts; still, a general understanding of the underlying mechanism by which carbon effects chemoselectivity is not yet achieved.

With the experimental observations and interpretations presented in this work, we attempt to resume the issue. Isomerization, hydrogenation, and decomposition are the relevant reaction pathways in this work; we will not only show that sustained hydrogenation may be obtained under UHV conditions – which has so far never been reported –, but we will also show that the hydrogenation rates depend very much on the presence of previously deposited, strongly dehydrogenated carbonaceous species (*carbon*), which allows to selectively control the yield of hydrogenation products. The mechanism by which carbonaceous surface modifiers may control this chemoselectivity will be discussed; the central aspect of this discussion will be the presence and distribution between different hydrogen species in the Pd nanoparticles.

In the second part of this chapter, we will concentrate on differences in the conversion reactivity of *cis*- and *trans*-2-butene; the central intention of this project was to study the different reactivities of the two configurational isomers in the *cis-trans*-isomerization reaction – which transforms *cis*-2-butene into its *trans*-isomer, and *trans*-2-butene into the *cis*-form –, because such reactivity differences between the two isomers may result in the preferred formation of one configurational isomer (*cis-trans*-selectivity). *cis-trans*-selectivity is a long-known phenomenon and an important characteristic of hydrocarbon conversions, and it is highly desirable to understand the mechanisms that govern the configurational isomerism of the product; as an example, it is an important objective to reduce the yield of *trans*-fatty acids during partial hydrogenation of vegetable oils to edible fats, because their ingestion is considered to significantly increase the risk of cardiovascular diseases [176]. In this work, we have observed different conversion rates with both isomers, *cis*- and *trans*-2-butene, under several conditions, whereas the rates were similar under different conditions; however, always when different conversion reactivities were observed, the *cis*-isomer exhibited the higher conversion rates. Those differences in the reactivity of the two configurational isomers will be discussed in a detailed qualitative kinetic analysis, concentrating on the changes of the rate-limiting factors for the conversion reactions at the different reaction conditions; as the hypothetical central difference between the two isomers, we will use the assumption that the *cis*-isomer might be more strongly adsorbed at the surface; thus, it may reach higher surface coverages under reaction conditions, which – under certain conditions – arguably may be the rate-limiting step. Adsorption experiments are provided which may be interpreted as indications that the *cis*-isomer might indeed be more strongly adsorbed.

Our reactivity studies are based both on TPRS (*i.e.*, *non-equilibrium*) experiments and isothermal molecular beam reaction rate measurements, and the work will demonstrate that different and seemingly contradictory results may sometimes be obtained from both types of experiments under certain conditions; because real catalysis is usually performed under isothermal steady-state conditions, this observation argues for the application of isothermal experiments of the type used also in this work for the study of catalysis.

But before turning to the experimental results and their discussion, we will give a short introduction into the field of hydrocarbon conversion, concentrating first on the central reaction pathways (isomerization, hydrogenation and decomposition) and suggested reaction mechanisms, and then introducing previous experimental results obtained mainly on Pt-group metals and in reactions with small hydrocarbons (mainly ethylene and 2-butene), most of them from surface science studies. The subsequent results part will then first present experiments on the pristine  $\text{Fe}_3\text{O}_4$  support, which turned out to be inactive in all conversion pathways. The main section of the results part will thus concentrate on the experiments on the model catalyst; this section comprises two main parts, the first one concentrating on chemoselectivity between the isomerization and hydrogenation pathway, the other on selectivity in the conversion of *cis- vs. trans-2-butene*.

**The Development of Direct Hydrogenation by Catalysis.** The first hydrogenations have been made possible in the 19<sup>th</sup> century by the application of *nascent hydrogen* (hydrogen formed *in situ* in the reactor, *e.g.* by reactions of acids with base metals) on heteroorganic compounds such as esthers or aldehydes. However, nascent hydrogen was found incapable of hydrogenating unsaturated aliphatic compounds; additionally, its formation is expensive, and some of the methods applied were also very dangerous.

The successful direct application of *gaseous* hydrogen for *catalytic* hydrogenations has been quite exceptional throughout the 19<sup>th</sup> century<sup>1</sup>, and the systematic study of its application towards unsaturated organic compounds was initiated by Paul Sabatier and his disciples<sup>2</sup> at the end of that century [177]; Sabatier and Senderens achieved a breakthrough when they reported

---

<sup>1</sup>The first successful catalytic hydrogenation with gaseous hydrogen was achieved by Kuhlmann (1838: transformation of nitrogen oxide into ammonia in contact with a platinum sponge), and the first conversions of organic reactants were reported by Debus (1863: transformation of hydrocyanic acid into methylamine) and de Wilde (1874: hydrogenation of acetylene into ethylene and ethane) [177].

<sup>2</sup>The systematic study initiated by Sabatier was honoured with the Nobel price in chemistry in 1912.

on the direct catalytic hydrogenation of ethylene with hydrogen in the presence of finely divided nickel obtained by *in-situ*-reduction of nickel oxide [178, 179].

The industrial application of direct catalytic hydrogenation developed very soon after its discovery by the design of a process for the hydrogenation (*hardening*) of vegetable oils to edible fats by Wilhelm Normann in the first decade of the 20<sup>th</sup> century; this process strongly extended the availability of fat for human nutrition worldwide [180].

**Discovery of the Hydrogen Exchange Reaction and Development of a Reaction Mechanism (Horiuti-Polanyi Mechanism).** Despite this rapid transfer to application it was not before the 1930s – when deuterium as a labeling compound for kinetic experiments has become customary – that an important side reaction to hydrogenation was discovered. Farkas, Farkas and Rideal were the first to report that the side reaction



proceeds during the deuteration of ethylene [181]. Inspired by this observation, Horiuti, Ogden and Polanyi made an attempt to find the same hydrogen exchange reaction in an aromatic compound (benzene) and were able to observe its occurrence despite the very much lower reactivity of aromatic compounds as compared to aliphatic alkenes towards hydrogenation [182]; the authors suggested for the first time in this same paper that the observed exchange reactions may either occur by a dissociative-associative mechanism (see fig. 6.2, mechanism 1) or by an associative-dissociative mechanism (mechanism 2). In a subsequent paper, Horiuti and Polanyi were able to show based on kinetic experiments that both benzene and ethylene react with hydrogen by the associative-dissociative mechanism<sup>3</sup> (mechanism 2) on finely divided platinum and nickel [183].

The associative-dissociative and the dissociative-associative mechanisms differ in the surface intermediates: the former proceeds *via* an alkyl species (ethyl), and the latter *via* an alkenyl species (ethylenyl, see fig. 6.2). Horiuti and Polanyi pointed out that only the alkyl intermediate allows for a free rotation of one of the molecule's moieties around the original C=C-double

---

<sup>3</sup>It shall be mentioned that the authors also took into account a possible *concerted* association-dissociation reaction (addition of one and abstraction of the other hydrogen atom occur at the same time). Although their kinetic experiments could not discriminate between a concerted reaction and the discrete association-dissociation mechanism (mechanism 2), the authors gave convincing arguments against the concerted mechanism [183].



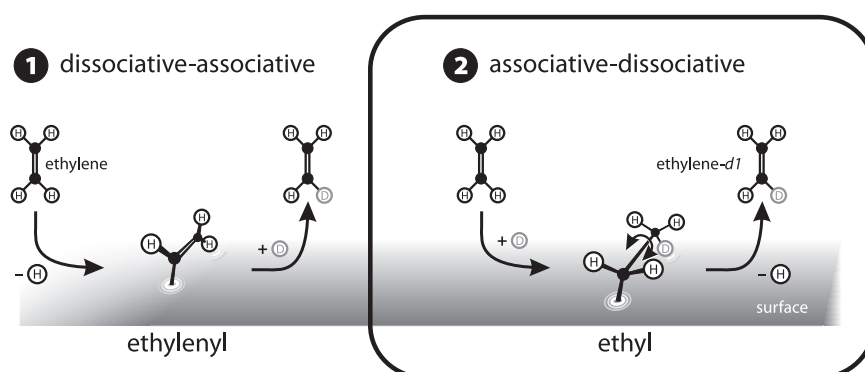


Figure 6.2: Possible reaction mechanisms for the H/D-exchange reaction in ethylene as suggested by Horiuti and Polanyi [182, 183]: 1) dissociative-associative and 2) associative-dissociative mechanism.

bond, and recognized that this rotation necessarily has to occur during the hydrogen exchange reaction if it follows the associative-dissociative mechanism; thus, hydrogen exchange according to this mechanism would always be accompanied by a *cis-trans*-isomerization (*inversion*) of the molecule<sup>4</sup>. Although Horiuti and Polanyi could not technically detect such an isomerization in their own experiments, they drew the connection to an earlier observation by Kuhn who had reported on a rapid *trans-cis*-isomerization of fumaric acid into maleic acid on a Pt-hydrogenation catalyst [184]. According to Horiuti's and Polanyi's understanding, hydrogen exchange and *cis-trans*-isomerization would always go together, because the reaction was shown to obey the associative-dissociative mechanism sequence; to clearly express this understanding, the reaction is often more specifically termed an *exchange-isomerization* reaction.

**Implications and Validity of the Horiuti-Polanyi Mechanism.** Since its original publication in 1934, the Horiuti-Polanyi mechanism has been the basis for many interpretations of hydrocarbon conversion and proved to be very adequate to understand many of the observed phenomena [185]. Two important aspects of this mechanism have constituted the basis for the interpretations of many studies on hydrocarbon conversion kinetics: 1) Isomerization and hydrogenation reactions proceed *via* the *same* surface intermediate (the half-hydrogenated alkyl species formed in the initial association step),

<sup>4</sup>Note that, as opposed to the associative-dissociative pathway, the dissociative-associative pathway (which was found to *not* be the dominant reaction route) would proceed *via* an alkenyl surface intermediate and thus would be expected to *retain* the reactant's *cis-trans* configuration.

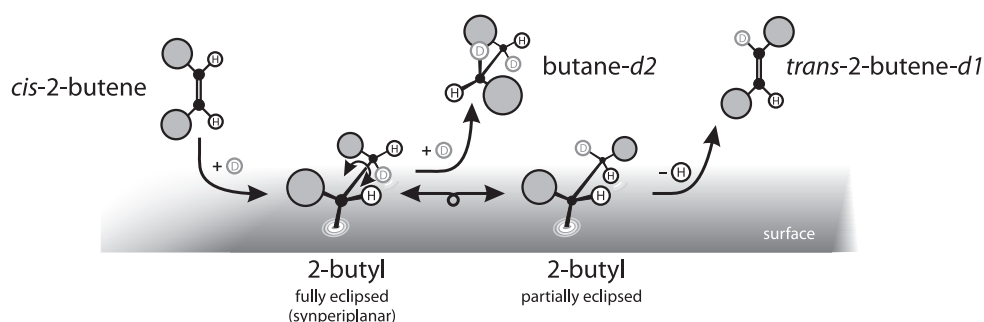


Figure 6.3: The Horiuti-Polanyi mechanism, formulated for *cis*-2-butene.

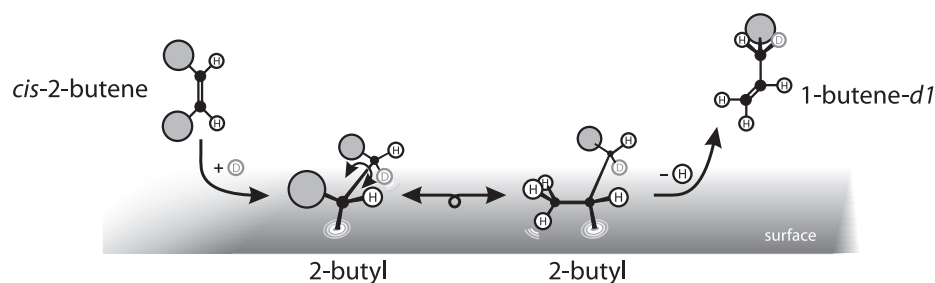


Figure 6.4: The double bond migration pathway in the Horiuti-Polanyi mechanism.

and 2) that the kinetic regio- and stereoselectivity of the isomerization – which proceeds by  $\beta$ -hydride abstraction from this intermediate – could be understood by a detailed analysis of the energetics of the transition states of all possible  $\beta$ -hydrogen abstraction steps (this assumption – which has been applied for the interpretation of many experimental observations – will be explained in detail below).

As an example for the **implications of the Horiuti-Polanyi mechanism**, we will discuss the conversion of *cis*-2-butene with deuterium theoretically; fig. 6.3 depicts the reaction according to this mechanism; note that both the exchange-isomerization and its alternative reaction (hydrogenation) proceed *via* the same intermediate, a surface-bound 2-butyl group.  $\beta$ -hydrogen abstraction from this intermediate to form an alkene can occur from two different positions; if it occurs from the secondary carbon atom on which the deuterium atom has been accommodated during the initial association step, the product will be *trans*-2-butene-*d*1 and the isomerization proceeds as a *cis*-*trans*-isomerization (as displayed in fig. 6.3); alternatively, the  $\beta$ -hydrogen abstraction could also occur from the primary carbon atom

in the terminal methyl group, leading to a different isomerization product, 1-butene-*d1* (see fig. 6.4); this event sequence is equivalent to double-bond migration. The yields of both products (the *cis-trans*-isomerized product and the double-bond migrated product) is controlled by the regioselectivity of the reaction. For the case of 2-butene, it is well known that the double-bond isomerization reaction to 1-butene is very unlikely to occur, and the main isomerization pathway is *cis-trans*-isomerization; arguments for this assumption will be discussed later in this literature review.

Likewise, when the  $\beta$ -hydrogen abstraction occurs preferentially from the secondary carbon atom of the 2-butyl intermediate, there are again two possibilities: either the previously attached deuterium atom can be abstracted (leading back to the reactant *cis*-2-butene), or the molecule's original hydrogen atom (leading to *trans*-2-butene-*d1*); the probabilities of these two reaction pathways govern the stereoselectivity of the reaction; models that help to explain the selectivity in the isomerization reaction based on the estimated energies of the transition states will be presented in the following section.

This treatment for the possible events during the conversion of *cis*-2-butene may be enough to illustrate the intricate implications that the deceptively simple Horiuti-Polanyi mechanism may have for the understanding of hydrocarbon conversions; for the example of 2-butene, it may be sufficient to understand the parameters that control the regio- and stereoselectivity of  $\beta$ -hydrogen abstraction in order to predict in which relative yields the two possible products of exchange/isomerization, 1-butene-*d1* or *trans*-2-butene-*d1*, are formed by the catalytic reaction. However, such far reaching interpretations can only yield reliable predictions if their fundamental assumption – *i.e.* the validity of the Horiuti-Polanyi mechanism – is reliable. Due to the important consequences of the **Horiuti-Polanyi mechanism**, its **validity** has been questioned and evaluated.

One of the earliest publication to do so is a joint work by Twigg, Conn and Rideal from 1939 [186, 187]; in this work, the possibility of hydrogen exchange between isotopically normal and perdeuteroethylene has been evaluated on a nickel catalyst, which could only occur by a dissociative-associative sequence; but because no exchange could be observed, the authors essentially came to the conclusion that 1) an activation of hydrocarbons by dissociation can only play an insignificant role for hydrocarbon conversion, so that 2) the associative-dissociate sequence adequately describes the dominant route of hydrocarbon conversions. The hydrogenation reaction, however, was assigned to a single reaction step between *molecular* hydrogen and ethylene by Twigg and Rideal [186].

Probably the most often cited reference for the evaluation of the Horiuti-Polanyi mechanism is a review by Horiuti and Miyahara from 1968, in which the authors inspected the ongoing discussion of ethylene hydrogenation; the authors took into account many of the mechanisms for the conversion of ethylene that had been suggested up to that time, including Twigg and Rideal's mechanism, dissociative-associative mechanisms, or a direct hydrogen transfer between hydrocarbon adsorbates. In a detailed discussion of all observations that had led to the suggestion of other mechanisms up to that time, however, the authors demonstrate that all of them could well be accounted for by theories based on the associative-dissociative mechanism and a half-hydrogenated intermediate, and conclude that it is best suited to describe those observations [188]. Finally, the authors took a step further and suggested that conversions of other hydrocarbons than ethylene may also be well described by the Horiuti-Polanyi mechanism.

More recently, however, studies have been published which in fact do conclusively suggest that partly dissociated intermediates may contribute to the reaction sequences during hydrocarbon conversions. As one example, Yoon, Yang and Somorjai have studied the conversion of 1-butene and *cis*-2-butene on the (111), (100) and (755) surfaces of Pt single crystals in a high pressure-cell, using gas chromatography as a detection technique [189]. In those studies, the rates of isomerization and hydrogenation have been measured; the hydrogenation reaction has been observed to occur with nearly identical rates on the (111) surface with both reactants, 1-butene and *cis*-2-butene, and – based also on other evidence –, the hydrogenation pathway was suggested to proceed *via* 2-butyl as the surface intermediate in both cases – *i.e.*, the reaction follows the Horiuti-Polanyi mechanism; the identical hydrogenation rates for both reactants were taken as an indication that identical steady-state coverages of this intermediate are formed during the conversion of both reactants. The other pathway, the isomerization reaction, was found to isomerize 1-butene to 2-butene (both in the *cis*- and *trans*-form), while *cis*-2-butene isomerizes only to *trans*-2-butene. Interestingly, the yield of *trans*-2-butene was observed to be significantly higher with *cis*-2-butene as a reactant than with 1-butene, and since the coverage of the 2-butyl species was found to be identical in both cases (see above), this observation was taken as an indication that the isomerization of *cis*-2-butene may follow different (additional) mechanisms than the isomerization of 1-butene, which was suggested to follow the Horiuti-Polanyi mechanism exclusively. A second argument for this interpretation was given: during the discussed study, also the structure sensitivities of both pathways with both reactants were examined by experiments on the three different crystallographic planes of Pt named above; the hydrogenation reaction was not found to exhibit any

structure sensitivity; the same is true for the isomerization reaction with 1-butene as reactant, but not with *cis*-2-butene, where the isomerization yield shows a significant structure sensitivity. This observation was also taken as a clear indication that the two reactants may isomerize *via* different mechanisms; 1-butene was described to isomerize only *via* the Horiuti-Polanyi mechanism; for *cis*-2-butene, the authors suggested that it isomerizes *via* two different mechanisms – the Horiuti-Polanyi mechanism on one hand, but additionally *via* a dissociative-associative mechanism with 2-butyne as the central intermediate. Thus, this study may be seen as an indication that a dissociative-associative sequence (non-Horiuti-Polanyi mechanism) may play a vital role during the isomerization of 2-butene – at least at high-pressure.

Lately, the possibility of dissociative-associative sequences in hydrocarbon conversions has been evaluated in UHV. One important class of possible reaction intermediates that have been discussed in this context, are the ones that follow from dissociation in the vinylic, or even more in allylic positions (see [25] chapter 7); for the latter possibility, Zaera *et al.* have come to the conclusion that no allylic dehydrogenation steps as a competitive pathway for alkene conversion are ever significant – at least under vacuum [190]; the authors base this conclusion on the following two studies:

1) Morales and Zaera have studied the conversion of methylene-cyclopentane and 1-methyl-1-cyclopentene with hydrogen and deuterium on Pt(111) by TPD and IRAS experiments [191]. This study was inspired by the fact that both reactants have very labile allylic hydrogen atoms as well as a very low propensity to be hydrogenated (or half-hydrogenated to an alkyl-intermediate) due to the high steric constraints imposed on cyclic pentanes by the *Pitzer*-tension (which is due to the envelope conformation of cyclopentane). Thus, the studied reaction system was thought to constitute a model case in which the applied hydrocarbons could be expected to show an extraordinarily low propensity to react according to the Horiuti-Polanyi mechanism, and a high propensity to get activated by dissociation in allylic positions. However, no indications for products of the speculative dissociative-associative reaction (such as 1-methyl-*d*1-1-cyclopentene) were observed experimentally; instead, the main observations were that methylene-cyclopentane rapidly isomerizes to 1-methyl-1-cyclopentene in the presence of coadsorbed hydrogen, and that H-/D-exchange in 1-methyl-1-cyclopentene occurs exclusively inside the aliphatic ring; those two observations indicate that the conversion of the two 5-membered ring molecules proceeds *via* 1-methyl-1-cyclopentyl as the central surface intermediate under the applied UHV conditions – *i.e.*, the reaction follows the Horiuti-Polanyi mechanism exclusively, even in this energetically disadvantageous case.

2) In another recent study, Chrysostomou and Zaera have studied the decomposition and conversion of propylene with deuterium on Pt(111) in UHV studies [192], focussing mainly on an identification of the different hydrogenation and self-hydrogenation products; interestingly, products in which all hydrogen atoms have been exchanged by deuterium could be detected, and also a fully exchanged and deuterated product was detected; based on this observation of fully exchanged *and* deuterated products, the authors conclude in a detailed discussion of the reaction mechanism that “any mechanism relying solely on allylic intermediates” could be ruled out.

As a **conclusion**, we see a necessity to state that the often-cited Horiuti-Polanyi mechanism, whose central assumption is that conversion reactions of alkenes with coadsorbed hydrogen (such as isomerization or hydrogenation) on metal surfaces proceed *via* an alkyl surface intermediate formed in a rapid initial half-hydrogenation of the adsorbed alkene, might not be as generally applicable for the understanding of hydrocarbon conversions as it often seems to be considered; in fact, examples for kinetic measurements of catalytic hydrocarbon conversions exist, which were explained by reaction mechanisms in which the activation step is not a half-hydrogenation step (association step), but a C-H-dissociation step (see above). On the other hand, recent studies under UHV conditions have addressed the possible participation of dissociation products in the very labile allylic position as intermediates in hydrocarbon conversions according to a hypothetical dissociative-associative mechanism; those studies, however, have come to the conclusion that such intermediates do *not* significantly contribute to the reaction events.

As a summary, studies exist arguing for both opinions – the prevalence of the Horiuti-Polanyi mechanism, and also studies which conclusively show that dissociative-associative reaction sequences may also play a vital role in hydrocarbon conversions. Unfortunately, a review about this issue – which appears to be very important for the general understanding of hydrocarbon conversions – does not exist. However, the existing reports about dissociative-associative reactions were, to the best of our knowledge, all based on experiments at elevated pressures, while no experiments in UHV has ever lead to the conclusion that a reaction sequence during hydrocarbon conversion was activated by a dissociation step; based on this notion, we believe it may be tentatively concluded here that, at least under vacuum, the Horiuti-Polanyi mechanism is the valid description for the dominant reaction mechanism of hydrocarbon conversions.

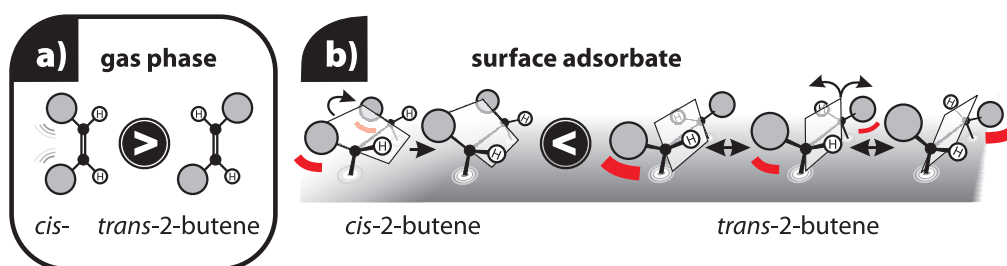


Figure 6.5: Steric repulsion as discussed origin for different stabilities of *cis*- and *trans*-2-butene a) in the gas phase (*trans* preferred) and b) adsorbed (*cis* preferred).

### Implications of the Horiuti-Polanyi Mechanism for *cis-trans*-Selectivity

It has long been known that the exchange/isomerization-reaction on metal catalysts may lead to an equilibrated mixture of the *cis*- and *trans*-products in a ratio that may strongly deviate from the distribution in the reactants – *i.e.*, those conversion reactions transform the reactants with a significant *cis-trans*-selectivity. Also other reactions – including the migration of primary to secondary double-bonds, or the dehydrohalogenation of haloalkanes – often produce alkenes with a significant *cis-trans*-selectivity (see below for references). This section will introduce explanations that have been given for this observation; the discussion will concentrate on 2-butene as a sample reactant, but the following model was suggested to be more generally applicable for alkenes [25].

*Cis*- and *trans*-2-butene have remarkably different heats of formation, with  $\Delta H_{f,298K}^{\circ}$  for (gaseous) *trans*-2-butene being approx. 4 kJ/mol below the value for *cis*-2-butene (absolute values: -11.2 vs. -7.0 kJ/mol) [193, 194]; this remarkable difference has been mainly assigned to the lower steric repulsion in the *trans* form of the product (see fig. 6.5 a). Consequently, the *trans* form would be expected to be the dominant isomer in an equilibrated gas phase mixture (*i.e.*, if the reaction that forms the secondary alkene is under thermodynamic control), and in fact, *trans*-2-butene has been observed to be the major product in high-pressure studies [195, 196, 197, 198, 199], where the gas phase may be able to reach thermal equilibrium due to the high collision numbers.

However, a selectivity towards the *trans* product was also observed in surface-science studies under low-pressure (*i.e.*, under experimental conditions with low collision numbers, so that equilibration with the gas phase products is nearly impossible, see *e.g.* in [190]); to explain the *cis-trans*-

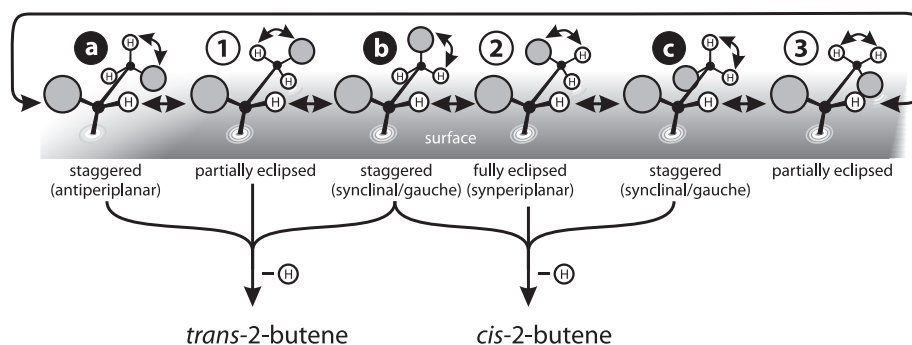


Figure 6.6: Steric repulsions and different stabilities of the eclipsed (local maxima 1, 2 and 3) and staggered (minima a, b and c) conformations (*rotamers*) in the surface intermediate 2-butyl as an explanation for *cis-trans*-selectivity [25].

selectivity observed under such conditions, the model of *kinetic* control described in the following paragraph has been suggested, which is based on the validity of the Horiuti-Polanyi mechanism [25]:

**Kinetic Control of *cis-trans*-Selectivity.** This approach qualitatively analyzes the different energetics of the different possible transition states entered by the surface intermediate – 2-butyl as an example case for this discussion – during  $\beta$ -hydrogen abstraction, when either *cis*- or *trans*-2-butene are formed [25]. In order to get abstracted from the 2-butyl-group, the  $\beta$ -hydrogen atom has to approach the metal surface; it is assumed that the possible transition states for this process each resemble one of the eclipsed *rotamers* of the 2-butyl group labelled 1 and 2 in fig. 6.6; the transition state resembling rotamer 1 exclusively forms *trans*-2-butene as a product, while rotamer 2 forms the *cis* product<sup>5</sup>. However, in order to understand *cis-trans*-selectivity based on those assumptions, further evaluations are necessary: the eclipsed conformations are the local energy *maxima* of the 2-butyl group, and thus they are only intermediately formed during  $\beta$ -hydrogen abstraction; they are also formed when the adsorbate moves between the local energy *minima*, which are the staggered conformations a, b and c in fig. 6.6. All the staggered and eclipsed conformations have different energies due to different steric repulsions between the ethyl group and the surface, with the following expected trend [25]: the staggered conformers have energies like  $a \approx b \ll c$ , and for the eclipsed conformations the trend is  $1 < 2 < 3$ . Thus,

<sup>5</sup>Note that rotamer 3 in fig. 6.6 can not resemble a transition state for  $\beta$ -hydrogen abstraction.



the staggered conformations a and b are energetically most preferable and differ only little, with conformation b being slightly favourable. Note that conformation a will exclusively distort into transition state 1 and form the *trans* product, while conformation b may form both transition states 1 and 2, thus forming both *cis*- & *trans* products; in fact, it may also prefer to distort into 1.

Based on those simple kinetic considerations, the often observed preferred formation of the *trans*-product becomes understandable; note however that a deeper understanding of the *cis-trans*-selectivity and the relative product yields in this model depends on a knowledge of the exact energetics of the stable conformers a and b and the transition states 1 and 2.

**Observation of a Reversed Selectivity: an Additional Model.** In recent publications, Lee and Zaera have reported on a reversed *cis-trans* selectivity under vacuum conditions observed in 2-butene conversion on the (111) surface of platinum by IRAS and TPRS experiments [200, 190, 201]; according to those results, *cis*-2-butene is the preferred desorption product in the conversion of both *cis*- and *trans*-2-butene on Pt(111) under vacuum. Those results are – to the best of our knowledge – in contradiction to all other observations of *cis-trans*-selectivity to date, and can not be explained based on the existing models (see the previous descriptions). In their paper, the authors suggested a new model to explain their new observation of *cis-trans*-selectivity; this model suggests that the *adsorption energies* of the reaction *products* controls whether a *cis*- or a *trans*-product is being formed – and not its gas phase energy or the different energetics of the transition states that lead to the *cis*- or *trans*-products, as in the models discussed previously. Fig. 6.5 b) depicts the central idea: the model argues that only the *cis*-form has the possibility to reduce steric repulsion by tilting the terminal methyl groups away from the surface, which makes the *cis*-form of *adsorbed* 2-butene energetically favorable over the *trans*-form and results in a lower adsorption enthalpy; note that this difference in the stability of the two *adsorbed* configurational isomers of the alkene is reversed compared to their different energetics in the gas phase (see above and in fig. 6.5 a). Lee and Zaera support this argumentation with previous experimental results: in fact, different C-C-bond lengths in adsorbed *cis*- and *trans*-2-butene have been observed by NEXAFS [202], indicating a stronger rehybridization towards the di- $\sigma$ -adsorbed state (buta-2,3-diyl) for *cis*-2-butene as compared to *trans*-2-butene; additionally, the interpretation was also justified by the adsorption geometry observed by IRAS experiments [190].

### 6.1.1 Conversion of 2-Butene on Pt-Group Metals (Group 10)

The three most typical reaction pathways discussed for hydrocarbon conversion are H-/D-exchange/isomerization, hydrogenation and decomposition<sup>6</sup> (see before). In the following paragraphs, relevant observations of those reactions on the group 10 metals Ni, Pd and Pt as discussed in literature will be presented; those include the discussion of parameters that promote the hydrogenation of alkenes on metal single-crystals, the different hydrogenation-activities of metal single-crystals as compared to metal nanoparticles, the influence of carbonaceous deposits on the activity and selectivity towards the different conversion pathways, the state of knowledge about the stepwise decomposition of 2-butene on Pt-group metals and the possible participation of double-bond isomerization (of 2-butene to 1-butene and *vice versa*) in the conversion reactions.

**Promotion of the Hydrogenation Reaction.** Hydrocarbon conversion is an intensely studied field of research, and many studies exist, especially about the conversion of ethylene. Conversion of 2-butene on the group 10 metals Pt and Pd has also been studied, both on conventional catalysts – *e.g.* on Pt/Al<sub>2</sub>O<sub>3</sub> [203] and Pd/Al<sub>2</sub>O<sub>3</sub> [204] – and on single crystal surfaces, *e.g.* Pt(111) [200, 201, 190, 205], as well as Pt(100) and (755) [189]; some of these studies were carried out at near atmospheric pressures. A good general overview over catalytic hydrocarbon conversion is given in [25], and an overview over surface-science studies can be obtained from [99, 206, 207, 208].

Generally, in most of the UHV-studies of alkene conversion published to date, H-D-exchange has been reported to dominate over the competing hydrogenation pathway, and in some cases, no hydrogenation was observed at all. Several models have been provided to understand, which factors may influence the promotion of the hydrogenation pathway. Guo and Madix [209] have studied the origins for the observation that hydrogenation of alkynes selectively leads to the formation of alkenes (and not alkanes) on the Pd(100) surface under vacuum conditions; the same selectivity is often observed on Pd hydrogenation catalysts, but it is *not* observed on many other metals including Pt and Rh. Based on their experiments, the authors suggested that this selectivity may be explained by a stronger metal-hydrogen bond on

---

<sup>6</sup>Further conversion reactions may occur with hydrocarbons, *e.g.* dehydrocyclization, hydrogenolysis or chain isomerization [26]; those reactions were not in the focus of the current work.

Pd(100) than on the other metals, and that the more strongly bonded hydrogen may not be reactive enough to hydrogenate the alkene to the corresponding alkane; as a consequence, alkynes would be selectively hydrogenated to alkenes.

The approach to understand the hydrogenation activity of a catalyst based on the metal-hydrogen bond strength of the available hydrogen species was also applied in other works: Hwu *et al.* have reported on a strongly increased hydrogenation rate towards cyclohexene as reactant on a sample that consisted of a monolayer of Ni on Pt(111), whereas pristine Pt(111) or very thick Ni overlayers on the Pt(111) substrate did not exhibit hydrogenation activity. The authors related the increased hydrogenation yield on the sample containing a Ni monolayer to a weaker metal-hydrogen bond in this sample as compared to the other two. This interpretation is in good agreement with very similar experiments conducted by Murillo *et al.* on the same Ni monolayer on Pt(111) [210]. Furthermore, Burke and Madix have observed that the hydrogenation pathway for ethylene to ethane is only available on an Fe(100) surface predosed with CO, whereas no hydrogenation occurs in the absence of CO; similar to the previously given explanations, their experiments suggest that this phenomenon is related to a considerably weakened hydrogen-metal bond strength on the metal surface in the presence of CO as compared to the pristine metal [211, 212].

More recently, the thermochemistry of alkenes on nanoparticles and metal single crystals was examined by Shaikhutdinov *et al.* in a comparative TPD study between the Pd/Al<sub>2</sub>O<sub>3</sub> model catalyst and the Pd(111) single crystal [213, 214, 215, 216, 217]; these experiments have shown that H-D-exchange occurs on both the model catalyst and the single crystal, but hydrogenation can be observed only on the model catalyst. Those results were explained with the participation of a weakly-bound subsurface hydrogen species in the hydrogenation reaction, which was described to exist only in the Pd nanoparticles. Although such a species could principally also form in single crystals, its formation was thought to be improbable in this case due to a rapid, entropy-driven diffusion of hydrogen from the subsurface sites into the bulk of the crystal.

**The Selectivity of the Isomerization Reaction.** 2-butene isomerization can proceed in two ways, either by double-bond migration as displayed in fig. 6.4 or by *cis-trans*-isomerization (see fig. 6.3); the product of double-bond migration from 2-butene would be 1-butene. The probability of double-bond migration in butene has been the subject of many studies, especially of the conversion of 1-butene, including studies under high-pressure con-

ditions on conventional Pd, Pt and also Ni powder or colloidal catalysts [203, 204, 218, 219, 220, 221, 222] as well as surface-science studies, *e.g.* by Lee and Zaera [201] and Somorjai *et al.* [189] (both on Pt(111) ). The general finding of those studies is that 1-butene isomerizes preferentially to 2-butene (and not the reverse); for the high-pressure studies, this was assigned to an equilibration between the two structural isomers according to their thermodynamic properties (the enthalpies of formation are:  $\Delta H_{f,298K}^{\circ} = -0.63 \pm 0.79$  kJ/mol for 1-butene and -11.2 kJ/mol for *trans*-2-butene [193]).

However, studies have also reported on an isomerization of 1-butene to 2-butene – but not the reverse – in UHV, where the collision numbers between reactants and surface are very low and where thus reactions may not be under thermodynamic control (*i.e.*, the equilibrium would establish very slowly). Instead, a mechanism of kinetic control for the double bond-migration has been proposed [190]: the first step in the isomerization of 1-butene to 2-butene is the half-hydrogenation to a surface-alkyl species; this process was demonstrated to occur regioselectively at the terminal carbon-atom ( $C_1$ ), so that the more stable 2-butyl species forms (as opposed to 1-butyl) [189];  $\beta$ -hydrogen abstraction from this 2-butyl group can occur from two possible places: 1-butene is formed if the hydrogen-abstraction occurs at the terminal carbon atom ( $C_1$ ), and 2-butene forms by abstraction at the other central carbon atom ( $C_3$ ). Based on experimental results obtained about the decomposition of 2-iodobutane on Pt(111) – which was found to successively decompose into surface-bonded 2-butyl, and then exclusively into *trans*-2-butene (and not 1-butene<sup>7</sup>) – it was suggested that the  $\beta$ -hydrogen abstraction proceeds with a high regioselectivity from the other central C-atom ( $C_3$ ), which makes 2-butene the preferred product. Those interpretations imply that 2-butene isomerization to 1-butene is a kinetically improbable process.

**Decomposition and Decomposition Products.** An additional pathway to H/D-exchange/isomerization and hydrogenation is the stepwise dehydrogenation (*decomposition*); this reaction sequentially forms different intermediate species (*carbonaceous deposits*) or, terminally, carbon.

The stepwise thermal decomposition of 2-butene has been studied on Pt single crystals, *e.g.* by Salmerón and Somorjai [205], by Avery and Sheppard [223, 224] and by Lee and Zaera [201, 190] (all on Pt(111) ). One general result of all of these studies is the observation of a first decomposition step around 300 K; Salmerón and Somorjai identify the decomposition product as butyldiyne ( $\equiv CCH_2CH_2CH_3$ ) based on comparison with other alkenes and

---

<sup>7</sup>Note also that *cis*-2-butene is not formed in this process either, suggesting that this reaction proceeds also with considerable *cis-trans* selectivity (stereoselectivity).

on integrations of TPD signals; the more recent papers by Lee and Zaera, and Avery and Sheppard on the other hand identify the decomposition product as 2-butyne ( $\text{H}_3\text{C}-\text{C}\equiv\text{C}-\text{CH}_3$ ) based mainly on IRAS measurements. The next decomposition step gets activated around 380 K, followed by a broad feature with three shoulders between approx. 500 (onset) and 800 K; the prominent feature around 380 K has been assigned to the formation of a strongly dehydrogenated carbonaceous species [205] with an approximate stoichiometry of  $\text{C}_4\text{H}_2$  [201].

The decomposition behaviour is of high interest for the understanding of hydrocarbon conversion, since it has been established that under realistic catalytic conditions, hydrocarbon conversion reactions do not proceed on clean metal surfaces, but rather on surfaces covered with carbonaceous deposits that quickly form, even at moderate temperatures, on the initially clean surface during its first contact with the hydrocarbons in the reaction mixture [26, 25]; thus, the presence of carbonaceous species on the metallic catalyst surface under reaction conditions may be seen to be a ubiquitous phenomenon, and a current aim of studies is to understand the role of those deposits on the activity and selectivity of the catalyst; several results indicate that carbonaceous species influence the activity and selectivity towards competing reaction pathways [26, 25], although the detailed mechanism for those effects is not yet understood.

As an example for the influence of carbon, recent studies of selectivity in the hydrogenation of acetylene on Pd black have shown that in order to obtain a selective hydrogenation to ethylene (instead of unselective ethane formation), the presence of carbon-modifiers in the near-surface region was required [225]. The observed selectivity was discussed in terms of subsurface carbon; the authors argue that this carbon helps to decouple the subsurface hydrogen from the surface, which was said to be responsible for the hydrogenation of acetylene to ethane; thus, only without the participation of subsurface hydrogen, the alkyne could be selectively hydrogenated to ethylene.

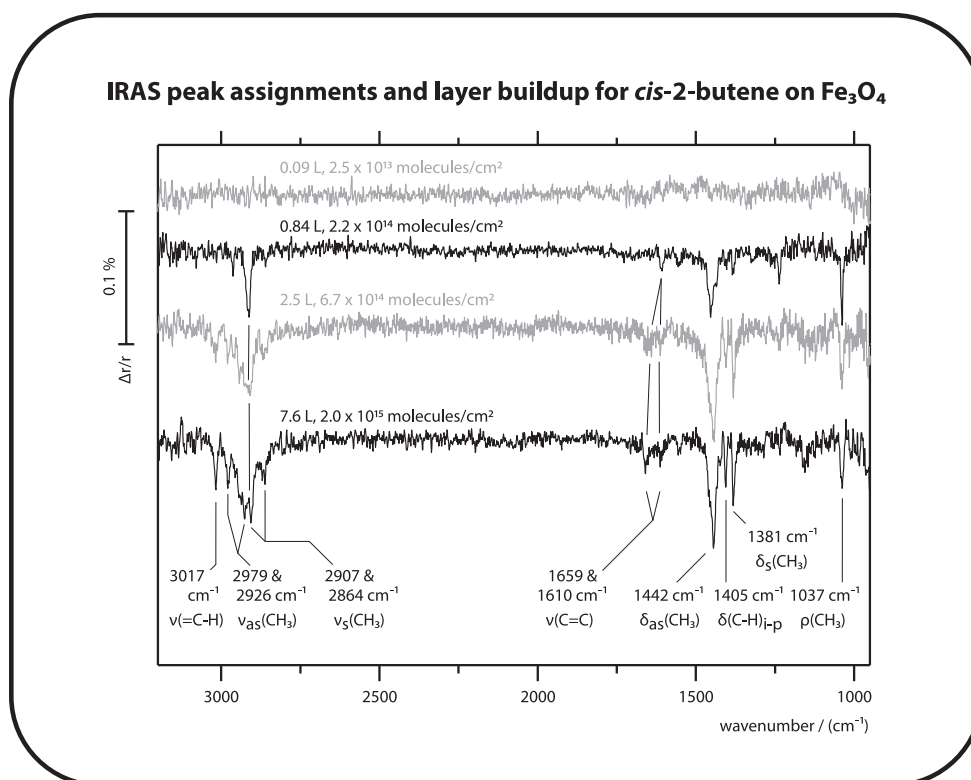


Figure 6.7: Exposure series of *cis*-2-butene on  $\text{Fe}_3\text{O}_4$  at 115 K and peak-assignment.

## 6.2 2-Butene on $\text{Fe}_3\text{O}_4$

Before concentrating on the adsorption, desorption and reaction of 2-butene on the model catalyst, we will briefly investigate its interaction with the pristine  $\text{Fe}_3\text{O}_4(111)$  (iron oxide/magnetite) film as a reference for the later sections:

### 6.2.1 Surface Infrared Spectra of 2-Butene on $\text{Fe}_3\text{O}_4$

Fig. 6.7 shows IRAS spectra of *cis*-2-butene adsorbed on the pristine  $\text{Fe}_3\text{O}_4(111)$  film at 115 K obtained as a function of exposure (from 0.09 to 7.6 L). The following observations were made, with assignments based on references [190, 226, 227, 228, 223]:

Four vibrational features dominate the spectra at low exposures (up to  $\sim 0.84$  L): the *symmetric* stretching vibration of the terminal methyl groups  $\nu_s(\text{CH}_3)$  at  $\sim 2907$   $\text{cm}^{-1}$ , the stretching mode of the C=C-double bond

$\nu(\text{C}=\text{C})$  at  $\sim 1610 \text{ cm}^{-1}$ , the *asymmetric deformation* mode of the methyl groups  $\delta_{\text{as}}(\text{CH}_3)$  at  $\sim 1450 \text{ cm}^{-1}$  and the rocking mode of the methyl groups  $\rho(\text{CH}_3)$  at  $\sim 1040 \text{ cm}^{-1}$ . With increasing exposure, additional vibrational features can be observed in the spectra, including the stretching mode of the inner C-H group  $\nu(=\text{C}-\text{H})$  around  $3016 \text{ cm}^{-1}$ , the *asymmetric* stretching modes of the methyl groups  $\nu_{\text{as}}(\text{CH}_3)$  at  $\sim 2979$  and  $2926 \text{ cm}^{-1}$ , a second<sup>8</sup> symmetric methyl stretching mode  $\nu_{\text{s}}(\text{CH}_3)$  at  $2864 \text{ cm}^{-1}$ , the *symmetric* methyl *deformation* mode (*umbrella* mode)  $\delta_{\text{s}}(\text{CH}_3)$  at  $\sim 1381 \text{ cm}^{-1}$ , the in-plane deformation mode of the solitary C-H-groups at the central C-atoms  $\delta(\text{C}-\text{H})_{\text{i-p}}$  at  $\sim 1405 \text{ cm}^{-1}$ , and, finally, a second peak for the stretching mode of the C=C-double bond  $\nu(\text{C}=\text{C})$  at  $\sim 1660 \text{ cm}^{-1}$ .

**Interpretation.** The intensity ratio between symmetric and asymmetric stretching modes in the terminal methyl groups in the spectra at low coverage allows us to determine the adsorption geometry of 2-butene on the oxide surface: according to the metal surface-selection rule (MSSR), the appearance of the symmetric stretching mode and the absence of asymmetric stretching modes in the low-coverage spectra (up to 0.84 L) together suggest that the terminal methyl groups in the adsorbed butene molecules are standing nearly perpendicular with respect to the surface, so that the asymmetric methyl stretching modes do not have a noticeable projection of dynamic dipole moment on the surface normal – which is why they cannot be observed in those spectra. Note that also the modes  $\delta_{\text{as}}(\text{CH}_3)$  (at  $\sim 1450 \text{ cm}^{-1}$ ) and  $\rho(\text{CH}_3)$  (at  $\sim 1040 \text{ cm}^{-1}$ ), which were observed at the low coverages, have components that change the dipole moment of the molecule perpendicular to the surface, and thus are IRAS-active according to the MSSR; the  $\nu(\text{C}=\text{C})$  mode will be discussed later.

When the coverage increases beyond 0.84 L, more and more vibrational modes are observed in the spectra; according to the MSSR, this indicates that the molecular orientation with respect to the surface changes – either due to the formation of 2-butene ice, which may start around 0.84 L, or due to the formation of a more condensed layer; based on the IRAS results alone, an unambiguous interpretation can not be given, but we will see from the discussion of temperature-programmed desorption experiments later that a coverage around 0.84 L is the onset-point for the formation of multilayers.

---

<sup>8</sup>Note that *cis*-2-butene possesses more than one symmetric methyl stretching mode [226]; Manzanares and coworkers have assigned vibrational modes for *cis*-2-butene in  $C_{2v}$  symmetry, and list two symmetric methyl stretching modes  $\nu_{\text{s}}(\text{CH}_3)$ , one of them belonging to the  $a_1$  irreducible representation of this point group, the other to  $b_2$ . The peak assignment in adsorbed *cis*-2-butene is based on the study by Lee and Zaera [190].

It is noteworthy that the stretching mode of the C=C-double bond  $\nu(\text{C}=\text{C})$  is observable in all spectra, even at low coverages. According to the MSSR, this observation could be interpreted as an indication that the molecule is not perfectly parallel to the surface, even at low coverages. On the other hand, some spectra and their interpretation as discussed in literature suggest that the  $\nu(\text{C}=\text{C})$  mode could also be IRAS active, even if this mode is perfectly parallel to the surface; as an example, Bandy *et al.* have observed the  $\nu(\text{CC})$  mode in ethyne (acetylene) adsorbed on Cu(111) in the dipole scattering mode of EELS spectra [229] (see also in [70]); as an explanation why this mode is observable despite the applicability of the MSSR in these experiments, it was stated that the adsorbate bond with the surface is also mediated by those  $\pi$ -electrons and that thus the oscillation of the C-C-bond (which occurs parallel to the surface) results in an oscillation in the electron transfer between the  $\pi$ -electrons and the surface; this oscillation occurs perpendicular to the surface, leading to the formation of a dynamic dipole that is oriented perpendicular to the surface – even if the carbon atoms move parallel to the surface –, and oscillates with the same frequency as the C-C-bond [70]; as a result, the  $\nu(\text{CC})$  mode gets IRAS active. A similar explanation has also been given for HR-EELS spectra of ethylene adsorbed on Pt(111) and PtSn<sub>x</sub>/Pt(111) surface alloys [230, 231]. Thus, we conclude that our observation of the  $\nu(\text{C}=\text{C})$  mode in the low-coverage spectra of 2-butene adsorbed on Fe<sub>3</sub>O<sub>4</sub> is not necessarily in conflict with our interpretation that the C=C-bond may be aligned parallel to the oxide surface.

In our spectra at low coverage (0.84 L), we have observed only one feature for the  $\nu(\text{C}=\text{C})$  mode at 1610 cm<sup>-1</sup>, but two spectral features – at  $\approx$  1660 and 1610 cm<sup>-1</sup> – occur in the multilayer spectra. The value of 1660 cm<sup>-1</sup> is nearly identical to the gas-phase value for this mode, and the shift of approx. 50 cm<sup>-1</sup> for the single mode observed in the (sub)monolayer spectra indicates that the molecules in this case interact relatively strongly with the Fe<sub>3</sub>O<sub>4</sub> surface; still, it should be noticed that the C=C-double bond is spectroscopically detected at all coverages, indicating that interaction with the oxide surface does not lead to a rehybridization of this bond.

### 6.2.2 Desorption of 2-Butene from Fe<sub>3</sub>O<sub>4</sub>

Fig. 6.8 a) shows a temperature-programmed reaction-desorption experiment (TPRS, heating rate: 3.5 K/s) of 0.84 L (to reach a near saturation of the surface) of *cis*-2-butene adsorbed at 115 K on a pristine, <sup>18</sup>O-labelled Fe<sub>3</sub><sup>18</sup>O<sub>4</sub> film. We have followed the signals of the molecular desorption as well as the possible decomposition products H<sub>2</sub> and H<sub>2</sub><sup>18</sup>O; note that the signal back-



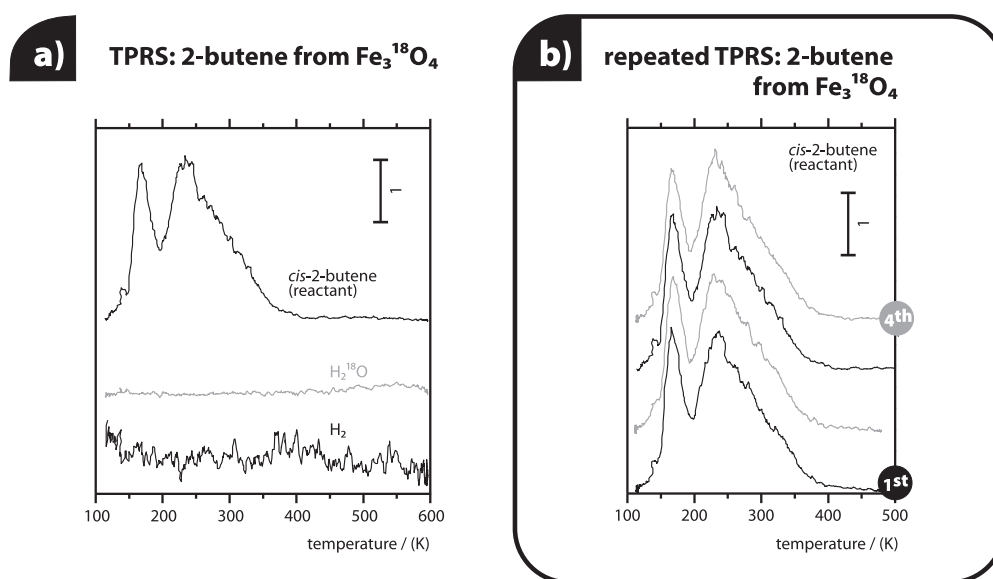


Figure 6.8: Temperature-programmed reaction-desorption (TPRS) experiments of *cis*-2-butene (0.84 L) from Fe<sub>3</sub><sup>18</sup>O<sub>4</sub> a) different species during the first TPRS from a fresh preparation, and b) evolution of molecular desorption with experiment repetition cycles.

ground on the mass of H<sub>2</sub> was relatively high (which also results in higher absolute noise), and that the signals were offset for presentation. Molecular desorption occurs in discrete features at approx. 160, 230 and a broad shoulder around 310 K; the signals for H<sub>2</sub><sup>18</sup>O and H<sub>2</sub> do not indicate any desorption of these species.

We have also followed the evolution of molecular desorption during repetitions of such TPRS experiments. For this purpose, the sample was cooled back to the exposition temperature (115 K) after the first cycle, where again 0.84 L of *cis*-2-butene were adsorbed without any intermediate treatment of the oxide such as reoxidation; finally, another TPRS experiment was conducted. Overall, four TPRS cycles were conducted (peak temperatures: 600 K in the first and also the last two cycles, 485 K in the second cycle; heating rate: always 3.5 K/s), and the results for the molecular desorption observed during those experiments are depicted in fig. 6.8 b); they clearly demonstrate that the three discrete signals of molecular desorption described above do not change with experiment repetitions, but that they are well reproducible.

Finally, we have studied the evolution of molecular desorption signals with exposure. For those experiments, *cis*-2-butene was adsorbed at 115 K on the

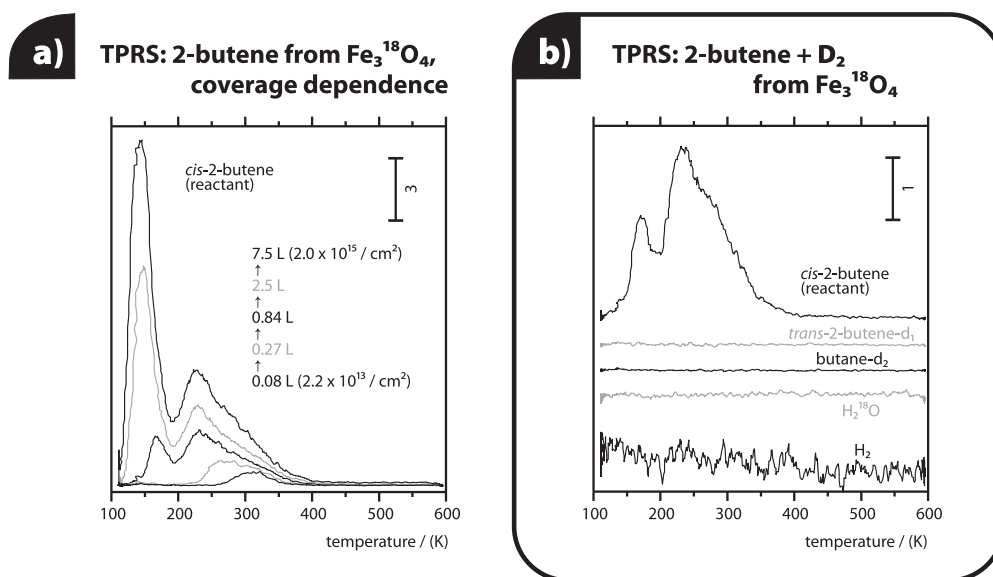


Figure 6.9: TPRS experiments of *cis*-2-butene from  $\text{Fe}_3^{18}\text{O}_4$ . a) evolution of molecular desorption with increasing exposure, b) desorption from the surface preexposed to 290 L  $\text{D}_2$ .

pristine iron oxide  $\text{Fe}_3\text{O}_4$  with exposures between 0.08 and 7.5 L; the results are displayed in fig. 6.9 a) (TPRS heating rate: 3.5 K/s). It is apparent that a high-temperature feature (around 310 K) evolves first and shifts to lower temperatures with increasing coverage; at the highest coverage, the peak is found around 230 K and shows a broad shoulder extending to higher energies ( $\sim 400$  K); at a coverage of 0.84 L, this high-temperature feature has nearly saturated. At and above 0.84 L, an additional feature at  $\sim 165$  K evolved in our experiments; this low-temperature peak gains strongly in intensity and shifts with increasing coverage, and it is found at  $\sim 145$  K at a coverage of 7.5 L; it shows a long tail extending to higher temperatures.

**Interpretation.** The absence of  $\text{H}_2^{18}\text{O}$  and  $\text{H}_2$  desorption as indicated by the results displayed in fig. 6.8 a) clearly shows that the  $\text{Fe}_3\text{O}_4$  film is inactive in butene-decomposition. This result is in good agreement with results by Weiss, Ranke and coworkers [170, 232, 83], who have studied the adsorption and reaction of another hydrocarbon (ethylbenzene) on the  $\text{Fe}_3\text{O}_4(111)$  thin film and could not observe any indication for dehydrogenation of this compound (to styrene in this case) on this material.

Instead of decomposing on the surface, all of the adsorbed alkene desorbs *molecularly* from the iron oxide in discrete desorption features at approx. 145,

and 230 K (with a long shoulder extending up to 400 K); since no reaction between the butene and the oxide occurs, this ad- and desorption is reversible and reproducible in experiment repetitions.

The strong increase of the desorption signal around 150 K with coverage in the exposure-dependant experiments (fig. 6.9 a) indicates that this feature is due to the desorption of 2-butene from multilayers; a feature due to desorption from 2-butene multilayers has already been reported on other substrates – *e.g.*, Salmerón and Somorjai have observed it during the desorption from Pt(111) at 150 K [205], which is in very good agreement with our result. Note that the onset point for the formation of multilayers of 2-butene observed in the TPRS experiments at coverages slightly below 0.84 L is in good agreement with our interpretations of the IRAS experiments described above. As soon as the formation of multilayers starts, the initially grown layer of butene molecules – the ones strongly interacting with the iron oxide film – has already built-up, and its TPRS feature does not grow with further exposure; thus, we may conclude that the monolayer of 2-butene has saturated somewhere below the exposure of 0.84 L, where the multilayer TPRS feature was first observed.

**Reaction experiments.** Finally, we have conducted TPRS experiments with deuterium and 2-butene coadsorbed on the  $\text{Fe}_3\text{O}_4$  film in order to test whether any conversion reaction can occur on the pristine oxide. For this purpose, 290 L of deuterium were dosed onto the pristine oxide at 115 K prior to deposition of 2-butene (0.84 L, *i.e.* a saturated monolayer); note that the deuterium was exposed in high excess over the alkene; it was also adsorbed first in order to prevent possible inhibition of dissociative deuterium adsorption by the hydrocarbon, which has often been reported to occur on transition metals [233] (see also below). The results are depicted in fig. 6.9 b); we have followed the mass signals for molecular desorption, for the decomposition products  $\text{H}_2$  and  $\text{H}_2^{18}\text{O}$  (see above; an  $^{18}\text{O}$ -labelled oxide was applied in this experiment as well), and the possible conversion products from hydrogenation (butane-*d2*) and exchange/isomerization (2-butene-*d1*); note that the QMS signals for those species had to be corrected for the contribution of the natural abundance of  $^{13}\text{C}$  in the reactant (see appendix A.3 for details about the signals and their correction).

However, no other signals than the one for molecular desorption could be experimentally observed; molecular desorption occurs exactly – and with very similar signal intensity – as in the previously described experiment without preexposed deuterium. Obviously, no reactions occur on the pristine iron

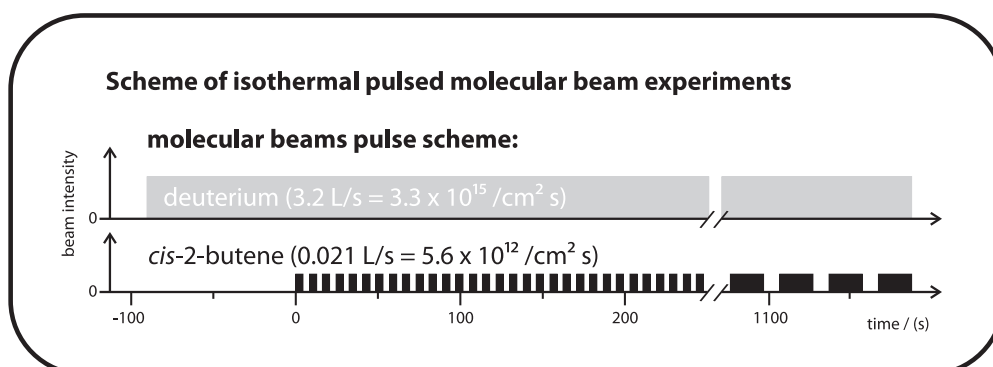


Figure 6.10: Scheme of isothermal pulsed molecular beam experiments for the measurement of ad- and desorption kinetics.

oxide. The reason for this can not be fully understood based on the simple experiment discussed here; the identical molecular desorption behaviour, the absence of any reaction products with deuterium, and the full reproducibility of all signals in repeated experiments (not shown here) indicate that all occurrences on the surface preexposed to  $\text{D}_2$  are identical to the ones observed in the experiments *without* preexposed deuterium; as an explanation for this observation, we believe that deuterium might simply not adsorb dissociatively on  $\text{Fe}_3\text{O}_4$ .

### 6.2.3 Pulsed Molecular Beam Ad- and Desorption Experiments

Finally, isothermal pulsed molecular beam adsorption/desorption experiments were conducted with 2-butene on  $\text{Fe}_3\text{O}_4$ . The scheme of these experiments is displayed in fig. 6.10; it is identical to the scheme of the isothermal molecular beam measurements conducted to study the conversion rates on  $\text{Pd}/\text{Fe}_3\text{O}_4$ , which will be the topic of the following sections. Briefly, in those experiments, the sample was first heated in vacuum to the experimental temperature (200 K in the discussed experiment), where the gas exposure was started with the initial saturation of the system with deuterium (beam intensity:  $3.2 \text{ L/s}$  ( $3.3 \times 10^{15} \text{ molecules/cm}^2 \cdot \text{s}$ )) over 90 s beam exposure to reach the same exposure as in the TPRS experiments ( $\sim 290 \text{ L}$ ). Then, under still continued deuterium beam exposure, the pulsed reactant exposure was initiated, typically starting with 50 short pulses (4 s beam on, 4 s off), followed by 30 long pulses (20 s on, 10 s off); the intensity of the butene beam was  $0.021 \text{ L/s}$  ( $5.6 \times 10^{12} \text{ molecules/cm}^2 \cdot \text{s}$ ). Note that the deuterium beam was  $\sim 590$  times more intense than the butene beam;

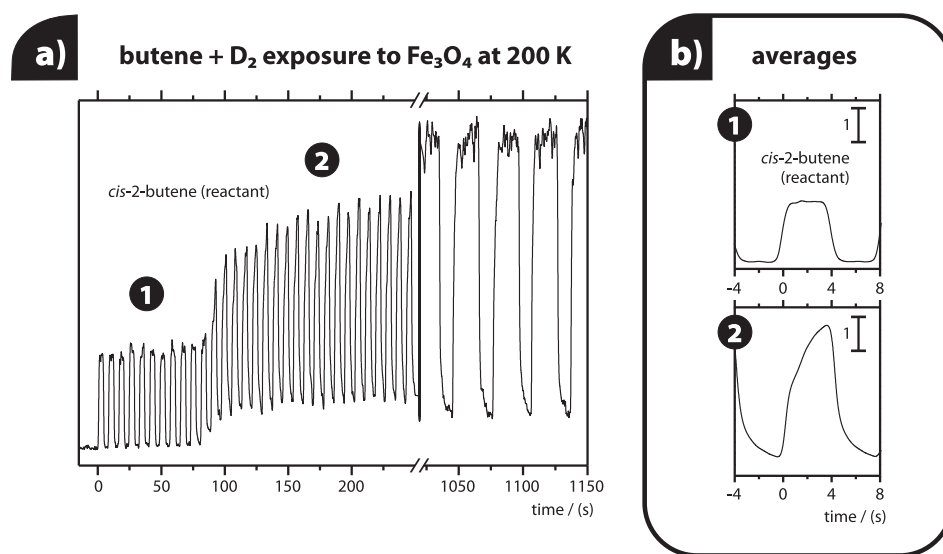


Figure 6.11: Adsorption behaviour of *cis*-2-butene on  $\text{Fe}_3\text{O}_4$  measured by isothermal molecular beam adsorption/desorption experiments at 200 K (see fig. 6.10).

this high intensity difference was chosen as a means to overcome the possible inhibition of dissociative deuterium adsorption by adsorbed hydrocarbon as much as possible.

During the whole procedure, the QMS signals of the reactant and all possible products were recorded; however, no signals for reaction products could be observed in the experiments on the pristine oxide (not shown). Fig. 6.11 shows the behaviour of the reactant signal during the beginning of the experiment (short pulses) and during the longer pulses towards the end; obviously, the signal follows the beam opening and closing processes directly, but the pulse shape exhibits an interesting evolution (this behaviour is more easily visible in the averaged pulses depicted in fig. 6.11 b): only the first ten pulses (labelled 1 in the graph) have a rectangular pulse shape, and then the pulse shape changes to a more sawtooth-like form (region 2 in the figure). The maxima reached during the first ten pulses with rectangular pulse shape is much lower (approx.  $\frac{2}{3}$  lower) than the signal reached at the end of the last (long) pulses.

**Interpretation.** The time behaviour of butene shows two distinct adsorption modes of *cis*-2-butene on the bare  $\text{Fe}_3\text{O}_4$  film, labelled 1 and 2 in the plot: during the first ten pulses, butene sticks strongly to the oxide sur-

face, and only a minor fraction of the beam intensity ( $\sim 1/3$ , referenced to the maximum during the long pulses) is scattered back into the gas phase, where it is detected; following from these data, the sticking coefficient in this regime is approximately  $2/3$ . The rectangular time behaviour of these pulses indicates that the adsorption into this mode is irreversible at the adsorption temperature (115 K). This mode saturates after an exposure of approx.  $1.6 \times 10^{14}$  molecules/cm<sup>2</sup> ( $\sim 0.6$  L), which is similar to the exposure necessary to saturate the *monolayer* as observed in the previously described TPRS and IRAS experiments.

After its saturation, the gas-phase signal of 2-butene during beam exposure changes significantly, and the maximum gas phase intensity increases, indicating a decreased sticking probability in this mode. The time-behaviour in this second adsorption mode deviates significantly from the rectangular pulse shape observed for the first mode, and is characterized by a more sawtooth-like gas phase intensity: after an initial, quick increase in the gas-phase abundance of butene, the signal increase is so slow that it does not saturate during the 4 s duration of the short pulses – but it saturates nearly during the 20 s of the longer pulses. Moreover, after beam shut-off, the gas-phase signal decreases only slowly, indicating slow desorption from this adsorption mode. This behaviour suggests that the molecules adsorb reversibly in the second adsorption mode. It might be speculated that this second adsorption mode refers to adsorption in the second layer on-top of the saturated monolayer, or probably also as weakly adsorbed species in the first layer, which could be populated only during beam exposure.

As said, no reaction products from hydrogenation, exchange/isomerization or decomposition could be detected during the isothermal molecular beam experiments (not shown – the signals are completely linear and empty). This, however, is not surprising in view of the previously discussed TPRS experiments, which also demonstrated that *no* butene conversion products could be observed on the Fe<sub>3</sub>O<sub>4</sub>(111) thin film.

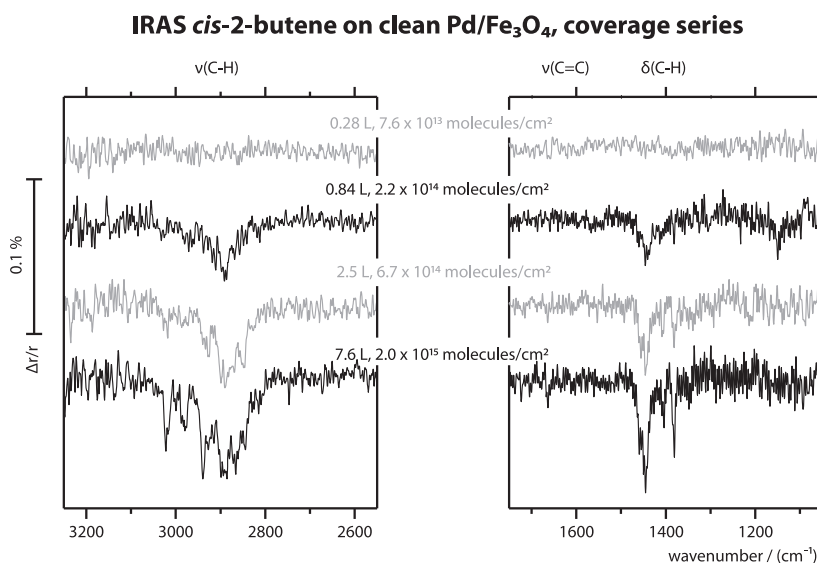


Figure 6.12: Exposure series of *cis*-2-butene on Pd/Fe<sub>3</sub>O<sub>4</sub> at 115 K in IRAS.

## 6.3 2-Butene on the Pd/Fe<sub>3</sub>O<sub>4</sub> Model Catalyst

The following part of this chapter will describe the experiments of 2-butene conversion conducted on the Pd/Fe<sub>3</sub>O<sub>4</sub> model catalyst; we will begin again with adsorption and TPRS experiments, and then turn to the systematic isothermal pulsed molecular beam reaction rate measurements to study the kinetics of butene-conversion.

### 6.3.1 Surface Infrared Spectra of 2-Butene on Pd/Fe<sub>3</sub>O<sub>4</sub>

In order to study the adsorption behaviour of *cis*-2-butene on the model catalyst, the alkene was adsorbed on the clean sample at a temperature of 115 K with exposures between 0.28 and 7.6 L, and the IRAS spectra displayed in fig. 6.12 were taken.

The peak assignment was discussed in chapter 6.2.1. At low exposures (up to 0.84 L), the peaks for the *symmetric* stretching mode  $\nu_s(\text{CH}_3)$  and the *asymmetric deformation* mode  $\delta_{\text{as}}(\text{CH}_3)$  of the terminal methyl groups dominate the spectra; they appear at  $\sim 2892 \text{ cm}^{-1}$  and  $1445 \text{ cm}^{-1}$ , respectively. With increasing exposure, additional features appear, including the *asymmetric* stretching modes  $\nu_{\text{as}}(\text{CH}_3)$  at  $\sim 2978$  and  $2939 \text{ cm}^{-1}$ , the symmetric

stretching mode  $\nu_s(\text{CH}_3)$  at  $2864\text{ cm}^{-1}$ , the *symmetric* methyl deformation mode  $\delta_s(\text{CH}_3)$  at  $\sim 1381\text{ cm}^{-1}$ , and the stretching vibration  $\nu(=\text{C-H})$  and the in-plane deformation mode  $\delta(=\text{C-H})_{i-p}$  of the solitary C-H-groups at the central C-atoms at  $\sim 3010$  and  $1405\text{ cm}^{-1}$ , respectively. Finally, the stretching mode of the C=C-double bond  $\nu(\text{C}=\text{C})$  occurs in the high-exposure spectra at  $\sim 1660\text{ cm}^{-1}$  (at very low intensity).

**Interpretation.** The intensity ratio between the symmetric and asymmetric stretching modes in the terminal methyl groups allows us to determine the adsorption geometry of *cis*-2-butene, just as discussed previously for the iron oxide: according to the MSSR, the appearance of the symmetric stretching mode and the absence of the asymmetric stretching mode in the low-coverage spectra (up to 0.84 L) suggests that the terminal methyl groups in the adsorbed *cis*-2-butene molecules are standing nearly perpendicular with respect to the surface, so that the asymmetric methyl stretching modes do not have a noticeable projection of their dynamic dipole moment on the surface normal – and thus cannot be observed in IRAS spectra. With exposures above 0.84 L, the molecular orientation with respect to the surface changes, making more and more of the vibrational modes observable in the IRAS spectra; this is presumably due to either the formation of 2-butene ice or the change of adsorption geometry due to the formation of a more condensed layer between 0.84 and 2.5 L.

However, there is one remarkable difference between the experiments on the pristine oxide and the Pd/Fe<sub>3</sub>O<sub>4</sub> model catalyst: the C=C double bond's valence mode  $\nu(\text{C}=\text{C})$  was experimentally observed on the bare oxide, but is not observable in the low-coverage spectra of 2-butene adsorbed on the model catalyst; only at very high exposures (7.6 L) does this mode get apparent by a spectral feature at  $1660\text{ cm}^{-1}$  – a frequency identical to the respective frequency in 2-butene in the gas phase, indicating that the detected 2-butene is only weakly bound; presumably, it is 2-butene adsorbed in the multilayers.

The absence of the  $\nu(\text{C}=\text{C})$ -mode in the monolayer spectra may be due to the molecule lying flat on the surface, although – as it was already said in the discussion of the spectra obtained on the bare oxide – the C=C-bond vibration may even in this case be IRAS-active<sup>9</sup>, see above; the other possible explanation why the  $\nu(\text{C}=\text{C})$ -mode was not observed in the low-coverage spectra is that 2-butene is strongly adsorbed on the Pd metal surface due

---

<sup>9</sup>The  $\pi$ -electrons in the C=C-bond would most likely participate in a  $\pi$ -bond with the surface, and could thus give rise to a dynamic dipole oriented perpendicular with respect to the surface when the C=C-bond oscillates (oscillating with the same frequency); this dipole would be IRAS-active.



to  $sp^3$ -rehybridization and the formation of two  $\sigma$  bonds between the hydrocarbon molecule and the metal; in fact, such a behaviour is typical for hydrocarbon adsorption on metals [234], and the understanding is also in good agreement with literature data on 2-butene adsorption on Pt(111) single crystals [223, 224, 190]. Furthermore, it is worth noting that spectral signatures for the  $\nu(C=C)$ -mode occur only in high-coverage spectra, and with lower intensity than in the respective spectra on the pristine support; additionally, a peak at lower frequency caused by strongly adsorbed, molecular butene – as it was observed in low-coverage spectra of 2-butene adsorbed on the pristine support (see section 6.2.1) – does not appear in the spectra on the model catalyst. According to our earlier work [55], our Pd nanoparticles cover only approx. 30 % of the oxide’s exposed surface; thus, 70 % of it is still exposed in the model catalyst, so that the significantly lower intensity at  $1660\text{ cm}^{-1}$ , and especially the complete absence of the peak at  $1610\text{ cm}^{-1}$  are not intuitively understandable. Two explanations may account for this fact. For one, the lower intensities are an indication for a lower butene coverage on the support, and it is possible that a rapid diffusion of butene from the oxide to the nanoparticles occurs – presumably, because 2-butene is more strongly adsorbed there; in this way, the nanoparticles may take up high amounts of butene, before additionally adsorbed butene molecules may begin to reside on the support. Alternatively, it is also conceivable that the adsorption properties of the support in the stabilized model catalyst is different from the one of the pristine oxide due to a possible modification during the stabilization procedure for the metal nanoparticles (see chapter 4 and appendix A.1.4); those modifications may possibly particularly account for the absence of the peak at  $1610\text{ cm}^{-1}$  (indicative of strongly-adsorbed butene on the oxide).

### 6.3.2 Desorption and Reaction of 2-Butene on Pd/Fe<sub>3</sub>O<sub>4</sub>

Our next study focussed on the desorption and reaction of 2-butene on the Pd/Fe<sub>3</sub>O<sub>4</sub> model catalyst. For a simple desorption experiment, 0.84 L of 2-butene were deposited on the clean model catalyst at 115 K, and a TPRS measurement was conducted up to a peak temperature of 485 K (heating rate: 3.5 K/s); in this experiment, we have followed the molecular desorption, the desorption of hydrogen (as a decomposition product) and the desorption of butane, which would be the product of a possible self-hydrogenation; fig. 6.13 a) displays the detected signals. Molecular desorption occurs in a broad feature peaking at 250 K with a shoulder around 180 K; additionally, a weak feature around 140 K was detected. Molecular hydrogen desorbs in

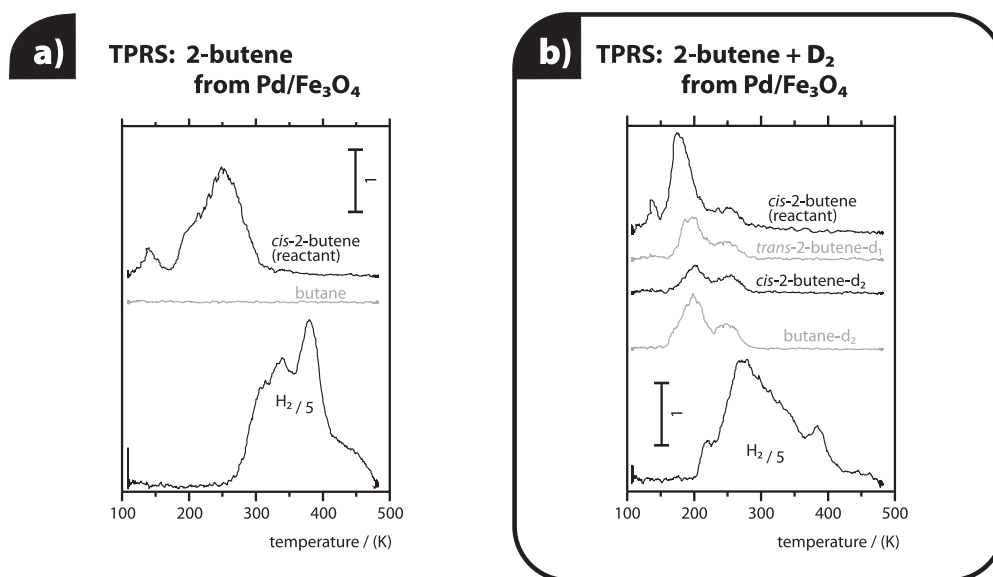


Figure 6.13: TPRS of *cis*-2-butene (0.84 L) (a) without and (b) with coadsorbed deuterium (290 L) from the Pd/Fe<sub>3</sub>O<sub>4</sub> model catalyst.

two clearly distinguishable peaks centered around 335 and 380 K; the peak at the lower temperature exhibits a shoulder around 300 K. No desorption of butane was detected.

Furthermore, we have studied the coverage-dependence of the TPRS experiments on the model catalyst with 2-butene exposures ranging from 0.08 to 7.5 L. For those experiments, the butene was always adsorbed on the clean model catalyst at 115 K; for catalyst cleaning, the same oxidation-reduction treatment was applied that is also used for stabilization (for details, see chapter 4.2.2 and appendix A.1.4). The TPRS measurements were always conducted with a heating rate of 3.5 K/s to a peak temperature of 485 K. Fig. 6.14 displays the results for the molecular desorption (panel a) and the desorption of hydrogen (panel b). At low coverages, the molecular desorption behaves as described above: it peaks around 250 K and exhibits a shoulder around 190 K; at and above a coverage of approx. 0.84 L, an additional feature at 140 K evolves, which grows considerably (and shifts slightly to 125 K at 7.5 L) with further increasing coverage, while the desorption features at higher temperatures stay essentially constant now. The desorption of hydrogen shows a single, symmetric peak around 340 K at the lowest coverage (0.08 L); this peak stays relatively constant in intensity and position with increasing coverage, but additional features develop: beginning at a coverage of approximately 0.28 L, a second, *higher* temperature-feature evolves

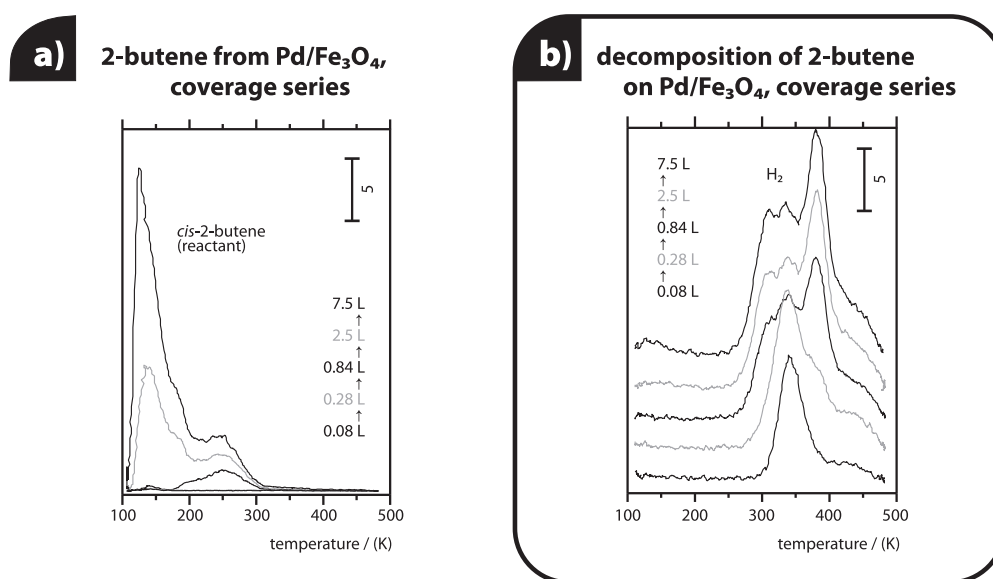


Figure 6.14: Evolution of TPRS signals from the clean model catalyst with *cis*-2-butene exposure. a) Molecular desorption, b) hydrogen from decomposition.

around 380 K and increases with coverage until it saturates around 0.84 L; from 0.84 L on and with further increasing coverage, a third feature occurs as a shoulder around 300 to 310 K.

**Interpretation.** The onset point for molecular desorption at 140 K demonstrates that the formation of multilayers commences at a coverage of  $\sim 0.84$  L; the adsorption state(s) that give(s) rise to the other molecular desorption signals have saturated at this coverage. This result complements the results of the experiments discussed above – both on the pristine iron oxide and the IRAS of the model catalyst –, which could also be interpreted as an indication for the formation of 2-butene multilayers at or slightly above an exposure of 0.84 L. Interestingly, the high-temperature molecular desorption from the model catalyst lies lower in temperature than the one observed on the pristine oxide ( $\approx 250$  vs.  $\approx 300$  K peak temperature); although this could be taken simply as an evidence for a stronger adsorption of 2-butene on the support than on the Pd metal surfaces, this is not very likely, and it appears much more convincing to us to assume that the most strongly bound butene molecules on the Pd metal do not desorb into the gas phase, but decompose; this is also in agreement with the other observations (see below). The fact that a desorption feature around 300 K – which would be indicative of

support-related butene molecules – does not occur in the experiments on the model catalyst, might be an indication that any support-related butene may diffuse rapidly to the Pd nanoparticles (on which it then decomposes) before it could desorb from the support.

Unlike the case on the bare oxide, the experiments on the model catalyst show clearly that 2-butene does not only desorb molecularly from the model catalyst, but that it also dehydrogenates there. Molecular hydrogen as a decomposition product desorbs stepwise around 300, 335 and 380 K, indicating that some hydrocarbon adsorbates dehydrogenate stepwise under formation of different decomposition products; note, that the dehydrogenation of 2-butene presumably is not complete even at the experimental peak temperature (485 K), since desorption features at higher temperatures have been observed in the very similar TPD-experiments on Pt(111), see section 6.1.1.

The desorption of H<sub>2</sub> can be understood based on reference experiments, in which the desorption of hydrogen from the surface of alumina-supported Pd nanoparticles has been studied, and which have shown that associative desorption is activated around 330 K [213]; interestingly, the authors have observed a weaker binding state that evolves when more than a monolayer of hydrogen has been exposed to the Pd metal nanoparticles; in this case, hydrogen is absorbed into the particles in the form of a subsurface species, which gives rise to a lower-temperature peak that shifts further towards lower temperature with increasing exposure. The reported desorption-points are in very good agreement with the results obtained in our work, indicating that the peak at 335 K is due to the associative desorption of surface-hydrogen, while the shoulder around 300 K might be due to desorption of hydrogen from a surface in the presence of subsurface hydrogen (see in ref. [213]). Since hydrogen desorbs at the same temperatures from a clean surface, it is impossible to unambiguously say whether the desorptions observed at 300 and 335 K of hydrogen from decomposition are desorption-limited, or if they are reaction-limited by the decomposition reaction; the fact that the desorption peaks align so very well with the literature values, however, may be considered an indication for desorption-limitation. The peak at 380 K, however, is clearly reaction-limited.

The observed peaks and intensity ratios of the hydrogen desorption are also in good agreement with the aforementioned experiments on Pt(111) conducted by Salmerón and Somorjai [205], by Avery and Sheppard [223] and by Lee and Zaera [190, 201]. Salmerón and Somorjai assigned the different hydrogen peaks to stepwise formation of different decomposition products, based on a comparative TPD-, HR-EELS- and LEED-study of the decomposition of different alkenes and alkynes; according to their assignment, the peak at 300 K is caused by the decomposition into butyldiyne

( $\equiv\text{CCH}_2\text{CH}_2\text{CH}_3$ ). On the other hand, Lee and Zaera, and Avery and Shepard explain the first decomposition point at 300 K with the formation of 2-butyne ( $\text{CH}_3\text{-C}\equiv\text{C-CH}_3$ ). The peak at 380 K was assigned by all authors to the formation of a *strongly dehydrogenated carbonaceous species* with an estimated stoichiometry of  $\text{C}_n\text{H}$  [205] or  $\text{C}_4\text{H}_2$  [201] (those values were based on an integration of the hydrogen TPD signals). Since the temperatures observed in our experiments agree so well with those literature data on decomposition on Pt(111), it appears reasonable to assume that the decomposition on the Pd nanoparticles in our model catalyst occurs under formation of the same intermediate decomposition products; unfortunately, we cannot contribute to a clarification of the decomposition product formed at 300 K, because it did not give rise to IRAS signals (not shown).

**Self-Hydrogenation.** It is known that the hydrogen released to surfaces during hydrocarbon dehydrogenation may in the following hydrogenate other hydrocarbon molecules adsorbed in the surroundings; this reaction is known as *self-hydrogenation* [25]; thus, hydrogenation products may occur on a surface during hydrocarbon conversion even without deliberate addition of hydrogen from the gas phase by the experimentalist. In order to estimate the probability of this pathway, the signal for butane was recorded during the TPRS experiments (see fig. 6.13) – but obviously, the self-hydrogenation does not occur under the conditions applied in our work. We assume that the self-hydrogenation is very unlikely to occur, presumably because the desorption rate of hydrogen at the temperatures where it is formed by decomposition may already be so high that it desorbs more quickly than it could react with butene to form butane; moreover, the hydrogen is released at a temperature where the surface coverage with 2-butene is already very low due to reactant desorption. We also assume that a principally possible, analogous *self-isomerization* reaction does not occur due to the same reasons.

### Carbon Accumulation

The strongly dehydrogenated carbonaceous species formed during the decomposition of 2-butene can not desorb into the gas phase, but are appointed to stay and accumulate at the catalyst, which would result in a considerable loss of free surface sites due to their blocking by the strongly binding carbon species. In order to study the extent and influence of carbon accumulation, we have conducted the following two experiments:

**CO-IRAS Surface Titrations.** The available Pd metal surface can be estimated by IRAS surface titration experiments with CO as probe molecule

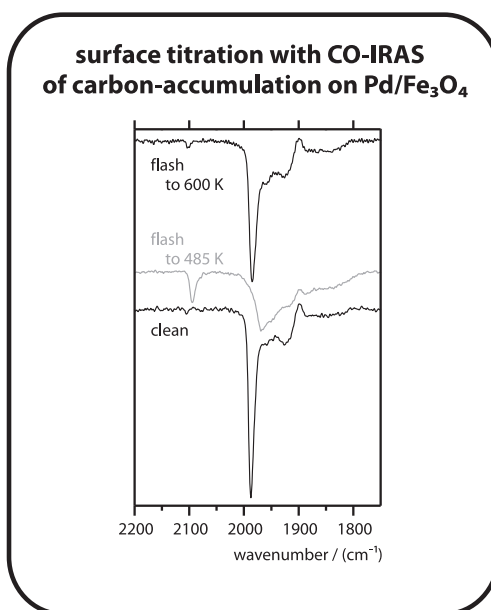


Figure 6.15: Carbon-accumulation on Pd/Fe<sub>3</sub>O<sub>4</sub> after TPRS experiments with *cis*-2-butene (0.84 L) and D<sub>2</sub> (290 L) as observed by surface IRAS-titrations with adsorbed CO (11.7 L exposed at 330 K, spectra taken at 115 K).

(see chapter 4.2.1 for more details about the experiment and the peak assignments). For those experiments, 11.7 L of CO were exposed to the model catalyst surface at approx. 330 K, and the IRAS spectrum was taken after cooling to 115 K; those CO-IRAS spectra were taken from the clean Pd/Fe<sub>3</sub>O<sub>4</sub> model catalyst, and from a system precovered with carbonaceous deposits; the carbon-deposition was effected by a TPRS experiment of the type displayed in fig. 6.13 a) (290 L of deuterium and 0.84 L 2-butene coadsorbed and then heated to 485 K). Finally, such a CO surface titration experiment was also conducted on a sample, which – after carbon-deposition according to the same method – has been flashed to the higher temperature of 600 K; all of the obtained spectra are displayed in fig. 6.15.

The spectrum of the clean sample exhibits an intense peak around 1988 cm<sup>-1</sup> ( $\nu(\text{CO})$  in edge-, corner- and defect sites, and – as minor contribution – in bridge-sites on the (100) facets), a broad peak centered around 1925 cm<sup>-1</sup> ( $\nu(\text{CO})$  on Pd(111) hollow-sites) and a broad feature between 1805 and 1895 cm<sup>-1</sup> (also  $\nu(\text{CO})$  on Pd(111) hollow-sites). After butene-adsorption and annealing at 485 K, the sample exhibits peaks at essentially identical positions, but the peak for CO in edge- and corner-sites

at  $1988\text{ cm}^{-1}$  – which is very intense in the spectrum of the clean sample –, is strongly reduced in intensity in this preexposed sample; the other features appear nearly identical as in the clean sample; additionally, a new feature appears in this spectrum at  $2094\text{ cm}^{-1}$  ( $\nu(\text{CO})$  in on-top-adsorption on Pd).

Interestingly, the spectrum obtained after butene adsorption and annealing at 600 K is nearly identical in peak intensities and positions to the spectrum obtained from the clean sample.

**Interpretation:** The prominent effect of carbon deposition by annealing predeposited 2-butene to 485 K is the disappearance of the feature at  $1988\text{ cm}^{-1}$  and the appearance of on-top adsorbed CO (*i.e.*, more weakly bound CO) at  $2095\text{ cm}^{-1}$ . These changes together indicate that the carbonaceous deposits preferentially adsorb at or near edges and corner sites (and possibly also on the (100) facets); as a result, some of the CO species switch to the less strongly binding on-top adsorption sites. Most notably, however, the spectra indicate that the regular (111) terraces remain nearly free of carbon, since the broad peak for CO on (111)-hollow-sites does not change significantly after carbon deposition. Those observations together indicate that the carbonaceous species accumulate mostly at the edge-, corner and defect sites, while the (111) facets – which in fact account for the majority of the available surface sites – remain nearly free of carbon.

Interestingly, after heating the system to 600 K, the spectrum resembles the one obtained from a clean system again, indicating that the carbon – which, of course, will also have formed on the surface during the TPRS temperature ramp – disappears from the surface at temperatures between 485 and 600 K. According to earlier investigations in our department, carbon on the Pd nanoparticles may migrate below the surface of the Pd nanoparticles in an activated process between 500 and 600 K [139]; the results discussed here are in a good agreement with this earlier observation and also indicates that the carbonaceous deposits – presumably after further dehydrogenation into carbon, as it occurs on Pt(111) above 500 K (see the literature results discussed in section 6.1.1) – migrate below the surface between 485 and 600 K. As this might lead to a slow accumulation of carbon in the bulk of the nanoparticles, we have avoided in the regular experiments to heat carbon-precovered systems beyond 500 K before they were cleaned from carbon.

**Effect of Carbon Accumulation on Surface Activity.** Finally, we have studied the effect of accumulation of carbonaceous surface species on repeated TPRS experiments on the model catalyst. For those experiments, an initially clean catalyst was exposed to 2-butene (0.84 L) at 115 K, and a TPRS measurement was conducted to a peak temperature of 485 K (heating rate:

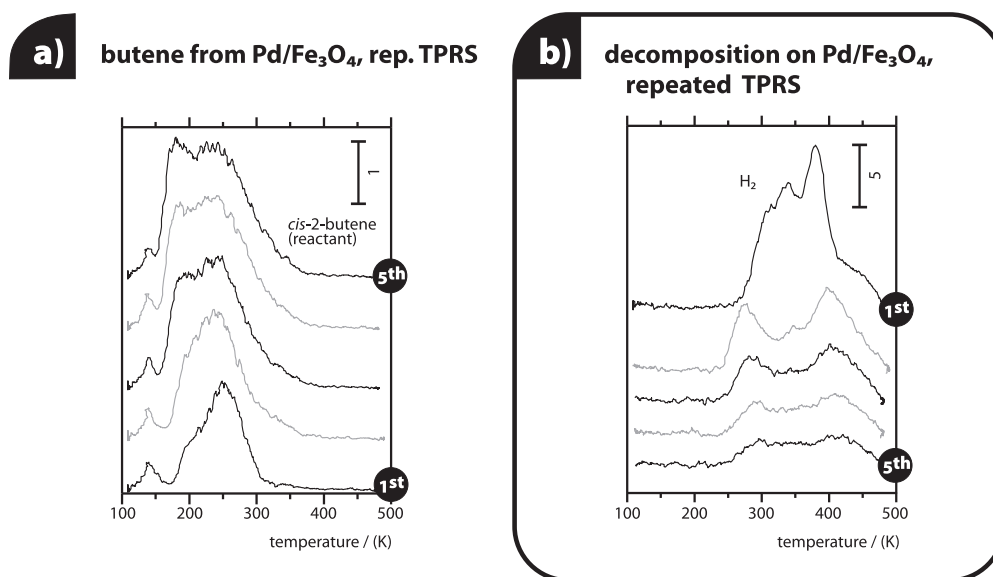


Figure 6.16: Evolution of desorption signals with TPRS repetition cycles: *cis*-2-butene (0.84 L) from Pd/Fe<sub>3</sub>O<sub>4</sub>: a) molecular 2-butene, b) H<sub>2</sub> from decomposition.

3.5 K/s). Without intermediate treatment, the sample was cooled back to the deposition temperature, and the butene deposition and TPRS measurement was repeated; overall, five identical experimental cycles were conducted; the results are depicted in fig. 6.16 for the development of the molecular desorption (panel a), and the desorption of the decomposition product H<sub>2</sub> (panel b) with repetitions.

As described above, the molecular desorption on the clean sample exhibits a peak at 250 K and a shoulder at 190 K; additionally, some multi-layer desorption was detected at 140 K. During the experiment repetitions, the shoulder around 190 K grew into a clearly distinguishable, intense peak at 180 K, and in the last cycle it was the most intense peak, while the peak at 250 K had decreased. The desorption of the decomposition product hydrogen changed even more significantly: while the clean sample exhibited the previously described peaks at 335 and 380 K and the shoulder around 300 K, hydrogen desorption from the precontaminated sample (second TPRS cycle) occurs at 275 and 400 K, and with a significantly decreased intensity compared to the clean sample. In the following three repetitions, those signals decrease further, until only very weak hydrogen desorption signals around 295 and 410 K could be detected in the last cycle.

**Interpretation:** The increase in the molecular desorption signal around 190 K and the decrease in the signal around 250 K are clearly related to the accumulation of strongly dehydrogenated carbonaceous species on the



surface, which leads to a decrease of binding energy on the surface. The progressive decrease in the dehydrogenation yield observed in the same spectra can also be attributed to the accumulation of carbonaceous species, which results in a progressive surface loss, and additionally a weakening of hydrocarbon adsorption bonds, so that more hydrocarbons may desorb instead of decomposing. The shift of the first hydrogen desorption peak towards lower temperature might also be explained by a weakening of the binding energy by the carbonaceous deposits.

The strongest changes in the dehydrogenation yield occur between the first and the second TPRS cycle (*i.e.*, during the first annealing step to 485 K); considering that the IRAS surface titration experiment after one annealing step to 485 K showed that only little amounts of the surface – mainly the very reactive edge- and defect sites – are affected by carbon accumulation (see before), it is remarkable that the decomposition activity is so strongly reduced after their blocking during the first annealing cycle; this observation may be taken as an indication that those sites are most active towards dehydrogenation – although, however, it should not be taken as an indication that decomposition occurs exclusively at those sites.

## Reactions between 2-Butene and Coadsorbed D<sub>2</sub>

Based on our acquired knowledge, the whole remainder of the chapter will concentrate on the conversion reactions of 2-butene with coadsorbed deuterium on the Pd/Fe<sub>3</sub>O<sub>4</sub> model catalyst. To begin with, a simple TPRS experiment with coadsorbed deuterium (290 L) and 2-butene (0.84 L) was conducted; the reactants were sequentially exposed at 115 K to prevent a possible inhibition of dissociative deuterium adsorption by previously adsorbed hydrocarbons, which has been previously reported to occur [233]. Fig 6.13, panel b) displays this experiment on the side of the previously discussed experiment *without* coadsorbed deuterium (panel a), which is otherwise identical in exposure and heating rate; the peak temperature in this TPRS experiment was also 485 K.

It is obvious that desorption signals in all masses (the molecular desorption, the decomposition product H<sub>2</sub>, and the products *trans*-2-butene-*d1*, *cis*-2-butene-*d2*, and butane-*d2*) were observed; note that the mass signals in this work were always corrected for the natural <sup>13</sup>C-abundance in the reactant according to the procedure described in the appendix A.3, which also includes a list of the recorded masses. The molecular desorption exhibits an intense peak at 175 K and much weaker features at 250 and 135 K; the desorption of hydrogen occurs with an intense feature around 275 K, with a shoulder around 335 K, and with another, less intense peak at 380 K; an

additional, weak shoulder was observed at 220 K. All products desorb with similar yields and peak shapes around 200 and 250 K.

**Interpretation.** Obviously, the clean model catalyst is active for 2-butene conversion with coadsorbed deuterium – both in the H-/D-exchange and the hydrogenation reaction pathway; the products form in two temperature regimes (an explanation for this behaviour can not be given yet). Additionally, decomposition (dehydrogenation) proceeds in this experiment, *i.e.* even in the presence of coadsorbed deuterium. Interestingly, the intensity distribution over the different peaks of molecular desorption and desorption of the decomposition product hydrogen differ considerably from the observations *without* coadsorbed deuterium; a similarity here is that the low-temperature peaks of H<sub>2</sub>- and molecular butene-desorption are both larger than the high-temperature features, which were the more intense features in the experiments *without* coadsorbed deuterium (note that both experiments in fig. 6.13 are displayed with the same axis scales): the feature around 175 to 190 K of the molecular desorption was found strongly increased in the presence of coadsorbed deuterium, and the desorption at 250 K is decreased; this inversion in the signal intensity distribution may be due to a weakening of the adsorbate bond by the coadsorbed deuterium that is contained in the Pd nanoparticles after the preadsorption procedure. The same reason may account for the shifts in the hydrogen desorption peaks. Furthermore, it is noteworthy that the *yield* (*i.e.*, the integrated signal) of the decomposition product hydrogen is very similar between the samples with and without coadsorbed deuterium – and it certainly is not lower on the sample with coadsorbed hydrogen (although it might have been expected, due to the weaker adsorption of butene in this case); thus, we may conclude that the decomposition activity of the sample is very similar in both experiments (with and without coadsorbed deuterium).

### Repeated TPRS series

In order to study the effect of carbon deposition on the reactivity of the sample, we have conducted *repeated* TPRS experiments with coadsorbed deuterium (290 L) and 2-butene (0.84 L), exposed sequentially at 115 K; no cleaning treatments were conducted on the sample between the TPRS cycles, but the sample was simply cooled to 115 K for a new gas exposure. Two repeated TPRS series were conducted with two different peak temperatures in the respective TPRS runs – one of them stopping at 360 K peak temperature in each cycle, the other one at 485 K; we expected, based on the decomposition behaviour of 2-butene discussed above, that different car-

**repeated TPRS (to 485 K peak temp.): desorption signals of reactants and products**

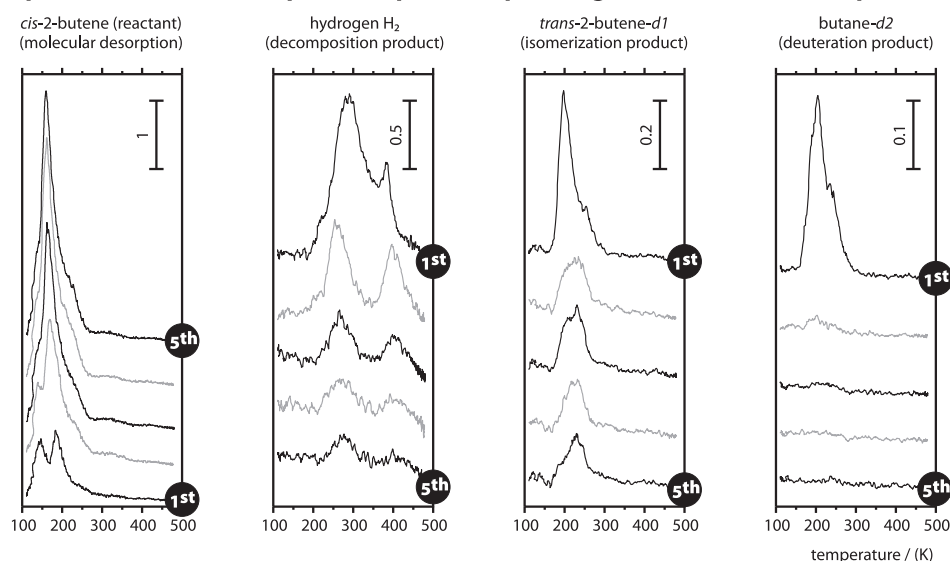


Figure 6.17: Evolution of desorption signals in repeated TPRS (peak-temperature: 485 K) of coadsorbed *cis*-2-butene (0.84 L) and  $D_2$  (290 L).

bonaceous species would remain on the sample after heating to the different peak temperatures. Fig. 6.18 shows the results obtained when the peak temperature reached during the TPRS experiments was only 360 K, and 6.17 shows the result with 485 K reached in each cycle.

The first experiment in both cases exhibits the same behaviour as discussed above for the simple desorption experiment, *i.e.*, molecular desorption at 180 K and 245 K, hydrogen desorption around 300, 330 and 380 K, and product desorption around 200 and 250 K (of course, the experiments with a peak temperature of 360 K does not exhibit the desorption peaks above this temperature). Even in the later TPRS cycles, both series show similarities in the fact that they both exhibit a strong general decrease in the product yields. However, the two experimental series exhibit remarkable differences in the later cycles: 1) The sample that is heated to 485 K in each cycle exhibits a sustained product yield from the exchange pathway (with a peak around 230 K), while no desorptions of the hydrogenation product are observed in the later cycles in this case; the yield of the isomerization product *trans*-2-butene decreases only from the first to the second cycle, then it stays nearly identical in the later cycles. 2) The sample heated to only 360 K during the TPRS cycles exhibits product formation only in the first cycle, and a rapidly collapsing product formation in the later cycles in all pathways.

**repeated TPRS (to 360 K peak temp.): desorption signals of reactants and products**

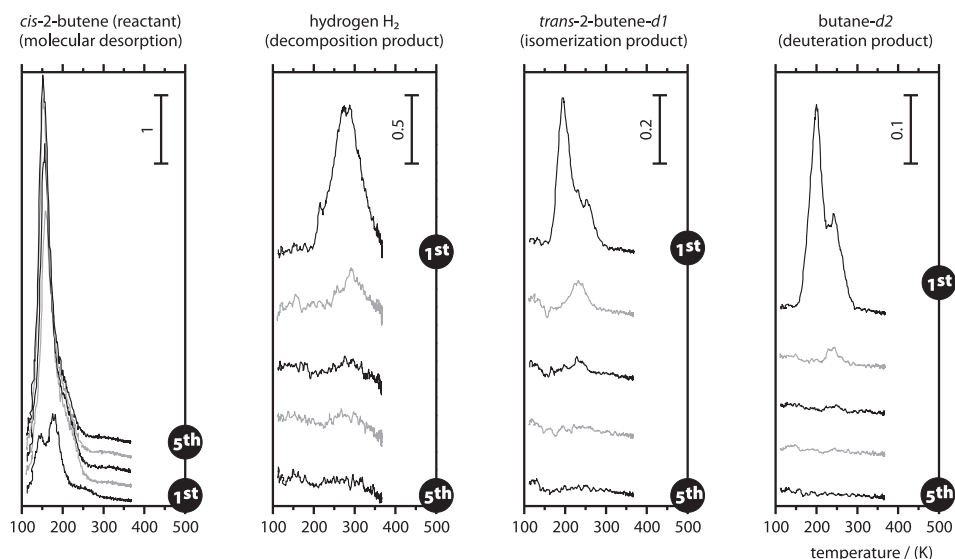


Figure 6.18: Evolution of desorption signals in repeated TPRS (peak-temperature: 360 K) of coadsorbed *cis*-2-butene (0.84 L) and D<sub>2</sub> (290 L).

The molecular desorption and the desorption of hydrogen from decomposition change similar to the above discussed experiments without coadsorbed deuterium: the low-temperature molecular desorption around 180 K increases significantly with every experimental cycle (and shifts to 160 K), while the hydrogen yield decreases significantly with each repetition; the main difference between the two series with different peak temperatures is that the molecular desorption around 160 to 190 K increases more strongly with every repetition cycle in the series heated to only 360 K.

**Interpretation.** Those experiments clearly demonstrate that the model catalyst may be capable of catalyzing hydrocarbon conversion reactions – at least towards isomerization –, even when its surface is decorated with previously deposited carbonaceous species. However, differences are observed in the conversion reactivity between the later cycles of the TPRS series with different peak temperatures: only when the sample is heated to the higher temperature of 485 K, a sustained isomerization reactivity can be obtained – whereas a sample that was only heated to 360 K after butene-adsorption on the other hand exhibits nearly no activity in the later TPRS cycles towards any of the pathways. Based on the decomposition behaviour of butene that has been discussed in the previous section, it is clear that different carbonaceous species are present on the surface after annealing at the different

temperatures (360 and 485 K), since the second butene decomposition point appears between those temperatures, at 380 K; based on our previous discussion of the decomposition behaviour on the model catalyst, the species formed during the flash to 360 K may be butylidyne or 2-butyne, and the species formed on annealing to 485 K is a strongly dehydrogenated species (stoichiometry  $\sim \text{C}_4\text{H}_2$ ).

Those experiments are a first indication that the nature of the carbonaceous deposits on the surface may have a strong impact on the activity and selectivity of the model catalyst in the conversion reactions. It is apparent that the weakly decomposed carbonaceous species formed in the heating steps to only 360 K have a strongly deactivating influence on all conversion pathways; they obviously weaken the adsorption strength of the adsorbed 2-butene and lead to strongly increased molecular desorption of unreacted 2-butene from low-temperature states with a similar desorption point (around 160 K) as the butene multilayers (see above); this might be taken as an indication that most 2-butene adsorbed at the such precovered surface are indeed adsorbed on top of a relatively dense layer of those species – *i.e.*, the weakly decomposed hydrocarbon species may have a large footprint on the surface. It might be imagined that this surface blocking may also inhibit dissociative deuterium adsorption, thereby strongly inhibiting the conversion reactivity; this interpretation is in agreement with explanations that have been provided in literature for the observation that the product yield in TPRS experiments with hydrogen and alkenes depends on the sequence in which the species are adsorbed (significant conversion can only be obtained when hydrogen is adsorbed first) [233].

The strongly dehydrogenated species formed during heating to 485 K on the other hand allow a sustained conversion activity (towards the exchange reaction). In relation with the previous discussion, this observation might be understood based on the CO-surface titrations on those surfaces discussed above, which show that the carbonaceous species formed during the heating step to 485 K decorate preferentially the edge-sites of the particles, while the main part of the surface remains nearly free of carbon at the beginning (the regular sites might get covered very slowly). Thus, it can be understood that those species leave enough open metal surface area, so that dissociative deuterium adsorption may not be as significantly inhibited on those surfaces as in the previously discussed case; additionally, they also seem to leave open metal surfaces for hydrocarbon adsorption. Note, however, that decomposition still is strongly reduced.

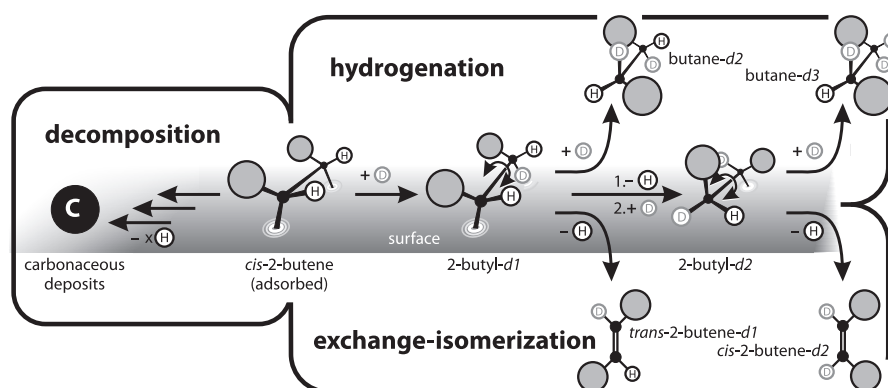


Figure 6.19: The conversion products of *cis*-2-butene as observed in this work.

**Conclusion.** The discussed experiments show that conversion reactions do proceed on the Pd/Fe<sub>3</sub>O<sub>4</sub> model catalyst; isomerization (*trans*-2-butene-*d*1 and *cis*-2-butene-*d*2), hydrogenation (butane-*d*2 and butane-*d*3), and decomposition products (hydrogen and carbonaceous deposits) have all been observed in the conversion of *cis*-2-butene with deuterium (see the summary in fig. 6.19). Additionally, they suggest that a sustained conversion reactivity may be obtained even on a carbon-precovered model catalyst.

In order to further investigate the activity and selectivity of the Pd/Fe<sub>3</sub>O<sub>4</sub> model catalyst, we have performed systematic isothermal molecular beam reaction-rate measurements in addition to the previously described TPRS measurements (*non*-equilibrium experiments); it will turn out that the isothermal experiments – in contrast to the TPRS experiments – indicate that also sustained hydrogenation can be obtained on carbon-precovered model catalysts; this shows that the different types of reactivity measurements may lead to different interpretations, and argues strongly for the conduction of isothermal rate measurements to promote the understanding of catalytic reactions.

The first section of the following part will concentrate on differences in chemoselectivity towards the reaction pathways observed in isothermal experiments on the clean and carbon-precovered samples; the second section will focus on differences in the conversion rates with *cis*- and *trans*-2-butene as reactants and its dependence on reaction conditions.

### 6.3.3 Chemoselectivity of 2-Butene-Conversion on Pd/Fe<sub>3</sub>O<sub>4</sub>

The principle of isothermal molecular beam experiments was already introduced in section 6.2.3, where it was applied to study the ad- and desorption behaviour of 2-butene on Fe<sub>3</sub>O<sub>4</sub>; briefly (see fig. 6.20), in those experiments the heated sample was first saturated with deuterium (290 L) by exposure to a continuous effusive D<sub>2</sub> beam (beam intensity:  $3.3 \times 10^{15}$  molecules/cm<sup>2</sup>·s  $\hat{=}$  3.2 L/s), and then – under still continued deuterium exposure –, the reactant *cis*-2-butene was admitted to the sample *via* the pulsed supersonic beam<sup>10</sup> (beam intensity:  $5.6 \times 10^{12}$  molecules/cm<sup>2</sup>·s  $\hat{=}$  0.021 L/s), and the reaction rates were measured by mass-spectrometric detection of the partial pressures of reactants and products in the gas phase around the catalyst. The reactant beam pulse scheme started with 50 short pulses (4 s on, 4 s off), followed by 30 longer pulses (20 s on, 10 s off).

Fig. 6.20 displays examples for the QMS signals of the reactant uptake (mass 41) and the formation rate of the first H-/D-exchange-product (mass 42) observed during a simple isothermal molecular beam reaction rate experiment on an initially clean Pd/Fe<sub>3</sub>O<sub>4</sub> sample at 200 K; the mass signals were corrected for the natural abundance of <sup>13</sup>C in the reactant (for an explanation of the detected signals and the data correction, see appendix A.3). Apparently, the reactant-signal follows the beam opening and closing processes directly, whereas the product desorbs from the sample only after the first six reactant pulses – *i.e.*, it exhibits an induction period; additionally, the reaction rate is high only over a few pulses (after the induction period) and decreases quickly.

**Ad- and Desorption Behaviour.** For a more detailed discussion, fig. 6.21 displays *all* recorded mass signals for the experiment on clean Pd/Fe<sub>3</sub>O<sub>4</sub> at 200 K: reaction rates for products of both reaction pathways – the two exchange products *trans*-2-butene-*d1* (mass 42) and *cis*-2-butene-*d2* (mass 43) as well as the hydrogenation products butane-*d2* (mass 45) and butane-*d3* (mass 46), see panel b) – together with the mass signal for the reactant uptake (mass 41) in panel a). In general, the signal of the reactant follows the beam opening and closing processes directly – *i.e.*, as soon as the butene-beam opens for the first time, a signal for the reactant can be observed in the gas phase, and when the beam is closed, the signal collapses. However, the signal's *intensity* exhibits an interesting development over the experiment,

<sup>10</sup>The supersonic beam profile was cut out to the sample size using the smallest aperture (6.3 x 7.6 mm, see chapter 3.2.1); its alignment with respect to the sample was verified daily.

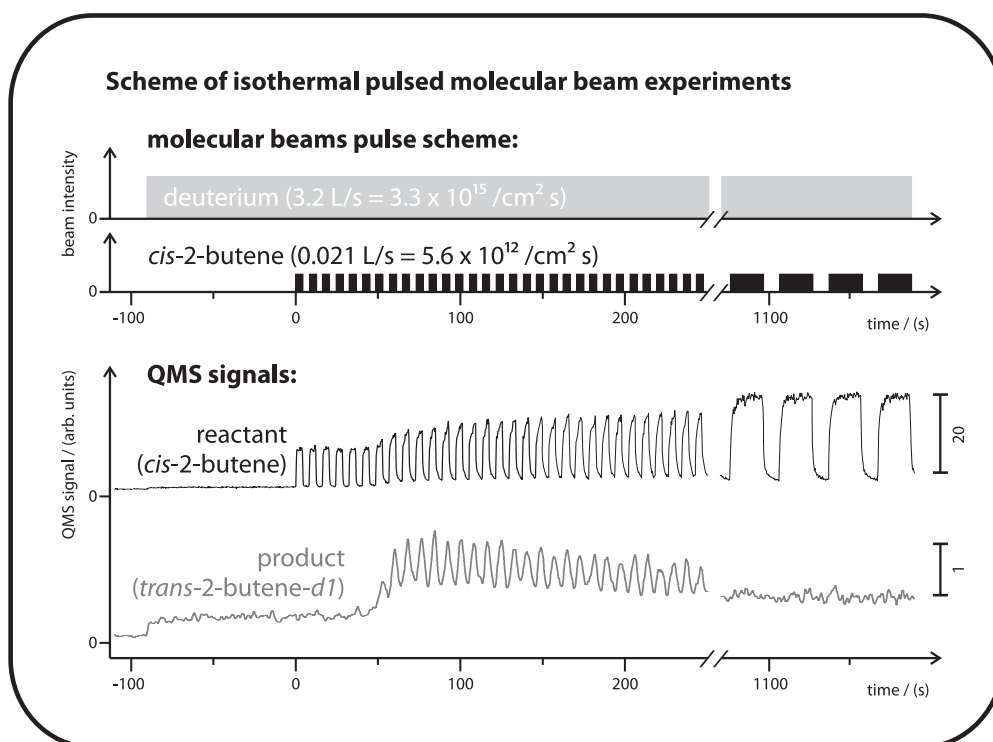


Figure 6.20: Scheme of isothermal pulsed molecular beam experiments for the measurement of transient and steady-state reaction rates; displayed are QMS signals for the reactant and the exchange-product during the conversion of *cis*-2-butene with deuterium at 200 K on the initially clean Pd/Fe<sub>3</sub>O<sub>4</sub>.

which has also been observed in a very similar way in the previously discussed experiment on the pristine support (see section 6.2.3): at the beginning, the detected signal pulses are very sharply cut out and rectangular, indicating irreversible adsorption into a strongly binding adsorption state with a sticking coefficient of approx. 60 %. After six exposure pulses (*i.e.* after an exposure of  $\sim 0.5$  L), the signal pulse shape changes and gets sawtooth-like: the intensity starts at approximately the same value as in the first pulses, but rises slowly to higher values towards the end of the pulse, and a constant signal level is only reached after long exposure times (more than 10 s, see the long exposure pulses at the end of the experiment); this indicates adsorption into a weakly binding adsorption state with low sticking probability. Also, when the beam is switched off, the signal drops only slowly, caused by significant desorption from the weakly binding state. Interestingly, the saturation of the model catalyst with the strongly bound hydrocarbon species is reached nearly twice as fast as on the pristine support; several explanations may



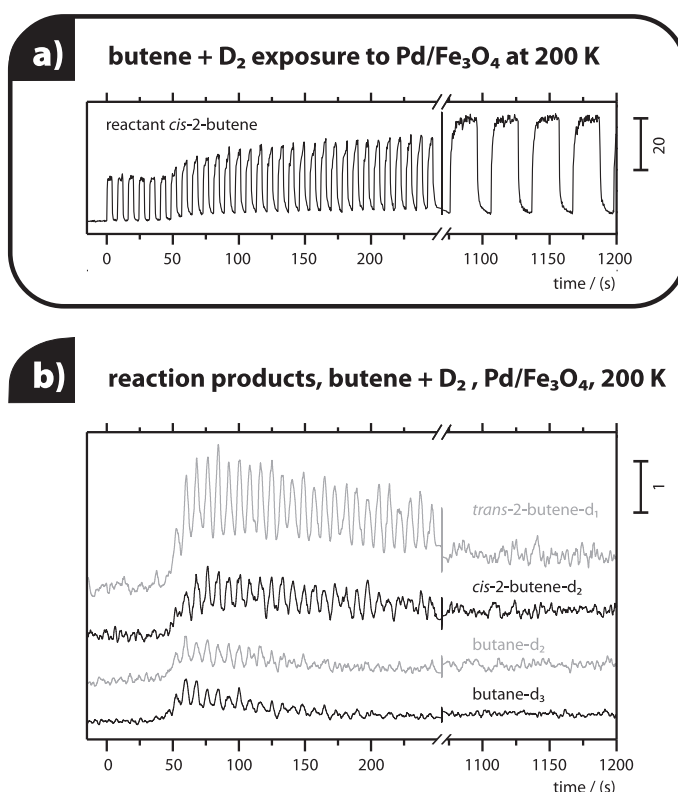


Figure 6.21: Isothermal reaction rate measurement with *cis*-2-butene and D<sub>2</sub> on Pd/Fe<sub>3</sub>O<sub>4</sub> at 200 K: overview over different products.

account for this fact: first, the adsorption properties of the iron oxide itself – which makes up a considerable fraction of the catalyst’s total surface area (only  $\approx 30\%$  of the oxide’s surface is covered with Pd nanoparticles) – may be different on the model catalyst, as a result of the Pd deposition and stabilization procedure, so that less butene might adsorb on the support in the model catalyst as compared to the pristine support. However, this effect alone can not solely account for the observed difference; in fact, we have observed that the length of the induction period *decreases* with increasing temperature (see fig. 6.22 between 210 and 250 K); this suggests that a threshold coverage of carbonaceous species builds up on the sample during the induction period, which may involve thermally activated processes such as dehydrogenation steps on the Pd metal surfaces; such partly dehydrogenated species may rapidly saturate the surface; of course, their formation can be expected to be faster at elevated temperatures.

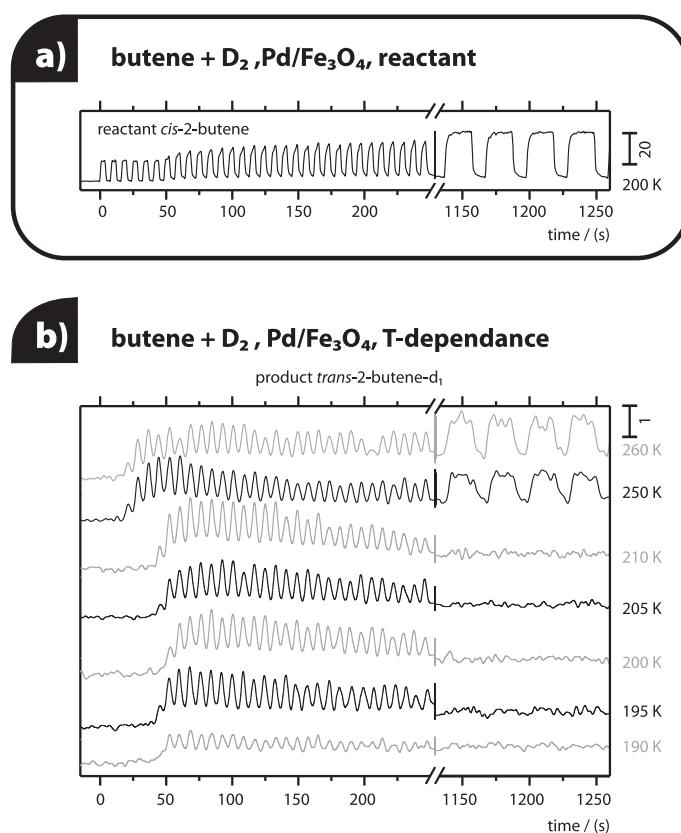


Figure 6.22: Isomerization rate during isothermal experiments with *cis*-2-butene and  $D_2$  on  $Pd/Fe_3O_4$  at *different* temperatures.

**Reactions.** In contrast to the experiments on the bare iron oxide, the experiments on the model catalyst clearly indicate the formation of isomerization and hydrogenation products, even at 200 K (see fig. 6.21). Interestingly, the desorption of all products exhibits the same induction period and starts only after the saturation of the first, strongly binding adsorption state. This fact indicates that the initial adsorption mode involves the buildup of a threshold coverage of butene and/or other hydrocarbon species on the Pd nanoparticles that do not directly participate in the reactions, but prepare the surface for the conversion reactions; only after the saturation of the metal surface with those species the catalytic conversion becomes possible.

At a temperature of 200 K all product formation rates show a maximum shortly after the induction period and then decline quickly in the longer run of the experiments, so that no product formation has been observed during the long reactant pulses towards the end of the experiment (fig. 6.21). It is noteworthy that the reaction rates in the hydrogenation pathway decline faster than in the isomerization pathway.

The next study concentrated on a detailed examination of the temperature dependence of the reactions rates; for this purpose, identical isothermal reaction rate measurements were conducted at different temperatures on a clean model catalyst; the system was cleaned immediately before each experiment and its cleanliness was verified by IRAS-surface titrations with CO as a surface-sensitive probe molecule (see section 6.3.2); fig. 6.22 displays the detected isomerization rates (product: *trans*-2-butene-*d1*) for a series of temperatures between 190 and 260 K. Here, it should be emphasized that those temperatures are well above the desorption point of the olefin, so that the observed reaction rates are not limited by hydrocarbon desorption. All signals exhibit an induction period, followed by a maximum in the reaction rate; the induction period shortens between 210 and 240 K, suggesting the onset point for the formation of a strongly adsorbed hydrocarbon species on the Pd nanoparticles at these temperatures (see above).

The most remarkable observation in those temperature-dependent experiments is the changing behaviour under steady state conditions between 210 and 250 K: at the lower temperatures, the isomerization rates drop quickly below the detection limit behind the maximum, which occurs directly after the induction period; above approx. 240 K on the other hand, the system exhibits a *sustained* reactivity, and the pulse shape indicates that the exchange rates may be sustainable over extended periods of time. The activity of the systems was actually probed for much longer times than displayed in the figures, and in fact, several turnovers (calculated with respect to the exposed Pd surface atoms in the model catalyst) and only minor decrease of the steady-state reaction rates were observed during an experiment of 2 hours duration time. This is, to the best of our knowledge, the first time that a sustained catalytic activity for hydrocarbon conversion has been observed under vacuum conditions, even in excess of hydrogen in the reaction mixtures [235, 236].

**Interpretation.** It is important to note that the abrupt change in the length of the induction period between 210 and 250 K roughly coincides with the onset of the first hydrogen desorption features observed in TPRS experiments (see fig. 6.17), which is associated with the first decomposition step of butene on the Pd nanoparticles. Remember that it could not be deduced from the TPRS experiments alone whether the onset of hydrogen-desorption (from decomposition) was kinetically limited by the alkene dissociation or by the association step of hydrogen atoms to molecular hydrogen; however, it may now be speculated based on this change in the length of the induction period in the pulsed reaction rate experiments that the first butene-dissociation step

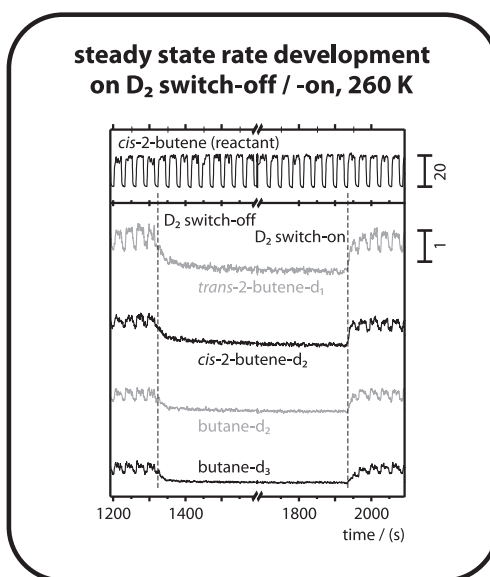


Figure 6.23: Evolution of isothermal reaction rates during modulation of deuterium supply (*cis*-2-butene + D<sub>2</sub> on Pd/Fe<sub>3</sub>O<sub>4</sub> at 260 K).

activates in the temperature window between 210 and 250 K; based on the previously discussed information from literature (see section 6.1.1), butyldiyne and/or 2-butyne are two possible decomposition products that may form at this stage.

The change towards a sustained reactivity can be understood in the following way: the lack of sustained hydrocarbon conversion in vacuum experiments is usually ascribed in the literature to the strong inhibition of dissociative deuterium adsorption on metal surfaces by strongly adsorbed hydrocarbon species [25, 237]; this understanding is also in good agreement with reported hydrogenation and isomerization rates, which follow a near first-order dependence on hydrogen pressure, but typically show a zeroth-order dependence on the hydrocarbon pressure [189]. On the basis of those considerations, it appears that the rapid drop of the conversion rates observed in the experiments at 200 K after the induction period is caused by the consumption of the preadsorbed hydrogen (from the initial deuterium exposure before the first butene pulse) and by the fast build-up of undecomposed 2-butene at the low temperatures, which quickly poisons the surface for dissociative hydrogen adsorption as the experiment proceeds, thereby eliminating the system's ability to replenish the dissociated hydrogen that is needed for and consumed by the conversion reactions; this also explains why the conversion rates are always highest directly behind the induction period.

Following this argumentation, we can understand the sustained reactivity of the sample at the higher temperature (around 250 K), where the sample seems to be able to dissociatively adsorb hydrogen in competition to 2-butene. Two possible explanations may account for the fact that the sustained (*i.e.* seemingly permanent) ability of the particles to dissociatively adsorb hydrogen does only evolve at elevated temperatures: first, the higher surface temperature leads to an increased desorption rate of 2-butene and thus results in a lower equilibrium surface-coverage of the hydrocarbon, thereby reducing its inhibiting effect towards the dissociative adsorption of deuterium; thus, the availability of deuterium atoms for the conversion reactions is increased at the higher temperature. Additionally, the dehydrogenated surface species that may form in the high-temperature experiments due to the onset of decomposition may have a smaller footprint on the catalyst's surface than the obviously undecomposed butene species that cover the surface in the lower temperature experiments, which may also facilitate dissociative deuterium adsorption, since this process needs open metal sites.

Results from further isothermal experiments, in which the deuterium beam was switched off and then on again (after a short delay, see fig. 6.23) in the steady-state reactivity regime, support the assumption that the hydrogen-supply limits the conversion rates: these experiments show a rapid collapse of the conversion rates when the hydrogen supply is cut, indicating that indeed the reactivity of the sample depends sensitively on a constant hydrogen supply – presumably because hydrogen is both rapidly consumed in reactions and also it desorbs rapidly at the reaction temperature of 260 K.

Those results show for the first time – to the best of our knowledge – that alkene conversion can be maintained over long times under vacuum conditions on a model catalyst; the sustained conversion rates critically depend on a sustained ability of the system to dissociatively adsorb hydrogen under the steady-state conditions, and it appears – based on literature reports – that similar hydrogen uptake is not possible on single-crystal surfaces covered with carbonaceous deposits [238]. Furthermore, it is worth noting that the reaction probabilities on our model system are in the range of a few percent, which is much higher than the values obtained for the same reactions on realistic catalysts at room temperature and atmospheric pressure, where reaction probabilities in the order of only  $10^{-5}$  to  $10^{-10}$  are typically observed [25, 188]; at present we do not have a fully satisfactory explanation for the unique high activity of our model catalyst.

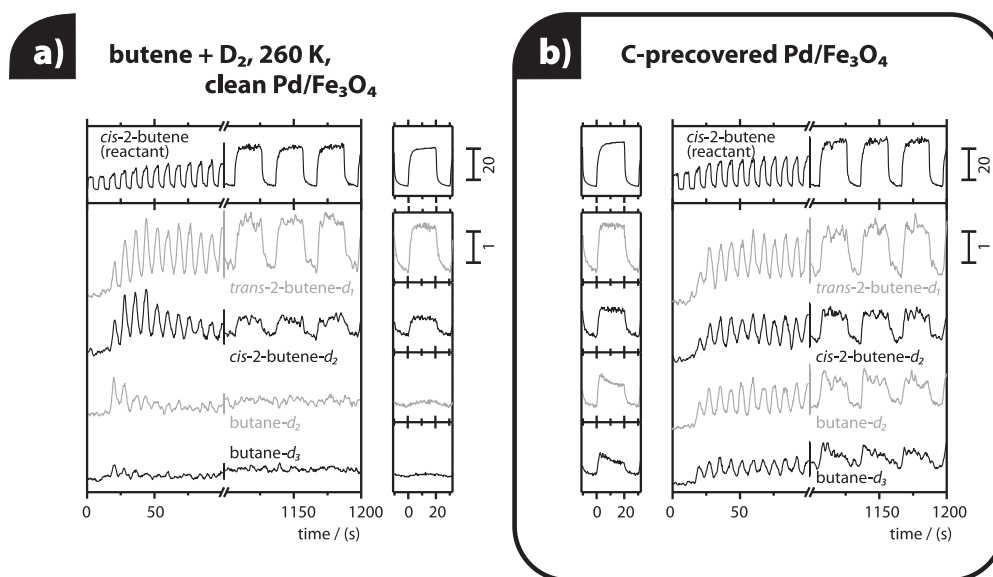


Figure 6.24: Isothermal reaction rate experiments with *cis*-2-butene and  $D_2$  on clean and carbon-precovered  $Pd/Fe_3O_4$  at 260 K; signal evolution and averaged steady-state rates are displayed.

### Chemoselectivity between Isomerization and Hydrogenation

The previously discussed repeated TPRS experiments shown in fig. 6.17 and 6.18 suggested that the presence of different carbonaceous deposits at the surface of the Pd nanoparticles may significantly affect both the activity of the catalyst, and its selectivity towards the different reaction pathways. Inspired by these two experiments, comparative isothermal pulsed molecular beam reaction rate measurements were conducted on initially clean and on carbon-precovered samples in order to probe possibly different reactivities of these samples; the carbon-precovered samples were prepared conducting one TPRS experiment under identical conditions as described for the repeated TPRS experiments (see section 6.3.2), *i.e.*, the sample was sequentially exposed to deuterium (290 L) and *cis*-2-butene (0.84 L) at 115 K, and then quickly heated in vacuum to a maximum temperature of 360 K in one case, and 485 K in the other.

Fig. 6.24 displays the time evolution of the isomerization (products *trans*-2-butene-*d1* and *cis*-2-butene-*d2*) and hydrogenation rates (products butane-*d2* and butane-*d3*) together with the uptake signals for the reactant *cis*-2-butene on an initially clean model catalyst (panel a) and on the model catalyst precovered with carbonaceous deposits by annealing at 485 K (panel b). Fig. 6.25 shows the results of the same experiment conducted on a ca-

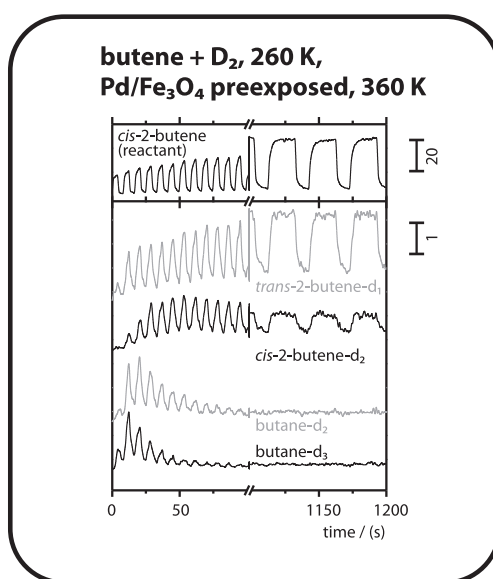


Figure 6.25: Isothermal experiments, *cis*-2-butene on Pd/Fe<sub>3</sub>O<sub>4</sub> at 260 K (exposure to butene and D<sub>2</sub>), on a model catalyst preexposed to *cis*-2-butene and D<sub>2</sub> and annealed at 360 K.

talyst precovered with the different carbonaceous deposits that are obtained by heating to only 360 K.

All reaction rates again exhibit an induction period, during which no reaction product desorbs from the sample although it is exposed to the reactant; the initially clean and the sample annealed at 485 K show nearly identical induction periods, while the sample annealed at only 360 K exhibits a much shorter one. On the initially clean sample, we find the previously discussed sustained exchange/isomerization rate, but only a short-lived hydrogenation rate after the induction period; it may also be noticed that also the isomerization-rates go through a maximum behind the induction period, while in the steady-state regime they are slightly lower. The sample *precovered with carbon* by annealing at 485 K (panel b) shows an induction period for the uptake of butene similar in length to that seen on the initially clean sample, indicating that the previously deposited, strongly dehydrogenated carbonaceous species do not significantly alter the available total surface area (note that this result is also in good agreement with the CO surface titration IRAS experiments conducted on clean and carbon-precovered model catalysts discussed in section 6.3.2). However, the most remarkable difference between the experiments on the clean and carbon-precovered sample – and possibly the most remarkable phenomenon discussed in this whole thesis –, is the fact that on the carbon-precovered sample *both* the isomer-

ization *and* hydrogenation reaction rates can be sustained throughout the whole experiment, while for the initially clean sample this is *only* true for the isomerization pathway – *i.e.*, both samples exhibit different chemoselectivities. It is noteworthy that both the carbon-precovered and the initially clean model catalyst exhibit very similar steady-state isomerization rates – moreover, the carbon-precovered sample even exhibits a slightly increased yield of the second isomerization product (*cis*-2-butene-*d*<sub>2</sub>) – *i.e.*, the *carbon* deposited in the amounts of our experiments certainly *does not deactivate* the catalyst. Another interesting fact is that very similar hydrogenation and isomerization rates are observed on the carbon-precovered catalyst.

Interestingly, the results obtained on a sample annealed at only 360 K after butene adsorption (see fig. 6.25) are qualitatively comparable to the observations on the initially clean surface (fig. 6.24 a) in the sense that only the isomerization rate can be sustained, while the hydrogenation rate declines quickly; on the other hand, they differ from the results obtained on the carbon-precovered sample that is prepared by annealing at 485 K. This indicates that the partially dehydrogenated species prepared by the pretreatment at 360 K do not lead to a different reactivity than observed on the initially clean catalyst. It is interesting to ask for the possible reason for the much shorter induction period observed on this sample pretreated at 360 K as compared to the induction periods observed on both the initially clean and on the sample pretreated at 485 K. Remember that the induction period presumably is due to saturation of a strongly binding adsorption state, from which no products can be formed; of course, on the initially clean sample, no such species are present at the beginning and their saturation needs exposure time; also the sample pretreated at 485 K has a nearly free surface, as it was demonstrated by the previously discussed IRAS surface-titration experiments with CO as a probe molecule, because the strongly dehydrogenated species present on those surfaces accumulate mostly at the edge-, corner- and defect sites, while the regular sites remain nearly free of carbon. The pretreatment at 360 K on the other hand leaves spacious carbonaceous species on the surface (see above); therefore, a much smaller surface area can be saturated in the such pretreated model system with the strongly adsorbing surface species during the induction period; it might be speculated that the species that adsorbs during the induction period (which may be a partly dehydrogenated species), and the species that is left at the surface after annealing at 360 K may be identical. In any case, those species behave very similarly, and thus we believe that the reactivity of the sample obtained by annealing at 360 K can be understood based on the same explanations that will also be given for the reactivity of the initially clean sample in the following discussions.



It is very revealing to compare the time-behaviour of the hydrogenation and isomerization rates during one butene-pulse on the clean and the carbon-precovered model catalyst (obtained by the pretreatment at 485 K) in the steady-state regime; for this purpose, the averaged signals over the individual long pulses are compiled in the two columns in the center of fig. 6.24. Those data show that the isomerization rates on both the clean as well as the carbon-precovered sample simply follow the time evolution of the reactant, suggesting that they are limited by the availability (*i.e.*, the adsorption behaviour) of the reactant *cis*-2-butene. In contrast, the hydrogenation-rate on the carbon-precovered sample follows a different time-behaviour: it is high only at the beginning of the pulse, but then drops significantly to a lower steady-state level towards the end of the pulse.

**Interpretation.** This different time behaviour of the two reaction rates is a key observation for an understanding of the observed chemoselectivity in the different samples. To explain this behaviour, it is important to note that the deuterium coverage in the sample reaches its highest value at the beginning of each butene beam exposure, because the deuterium beam is constantly running, even when the butene beam is switched off in-between the pulses, so that it may replenish the deuterium reservoir of the Pd particles; as a consequence, the catalyst is highly reactive as soon as butene becomes available at the beginning of each butene pulse. However, the situation changes during the pulse, when the deuterium availability drops to a lower steady-state level defined by the equilibrium of deuterium consumption by reaction and replenishment by dissociative adsorption, which is also partly inhibited by surface-hydrocarbon species (see above). Obviously, hydrogenation responds more strongly to this drop of hydrogen availability.

According to the Horiuti-Polanyi mechanism both isomerization and hydrogenation involve two reaction steps, the first of which is the formation of the common 2-butyl surface intermediate; the high rates in both the isomerization and hydrogenation observed at the beginning of the butene exposure pulses suggests that this intermediate is easily formed on the surface. The selectivity between isomerization and hydrogenation is controlled by the competition between the subsequent reaction steps, which either lead to isomerization (by  $\beta$ -hydrogen-abstraction) or hydrogenation (by reductive elimination of 2-butyl), respectively.  $\beta$ -hydrogen abstraction to the isomerization product does not require any additional reactants, and thus it may closely follow the kinetics of 2-butyl formation, which, in turn, depends very much on the butene-uptake. Hydrogenation on the other hand requires a second deuterium atom; the fact that the hydrogenation rates pass through a

maximum before the establishment of the steady-state indicates clearly that the hydrogenation rate is controlled by the availability of deuterium atoms at the end of the pulses.

In order to understand how carbon-deposition may change the reactivity of the system in such a way that it is possible to sustain the hydrogenation rates throughout the whole experiment, it appears that we need to understand how carbon at the surface may so significantly change the availability of hydrogen in the system; additionally, it is particularly puzzling that this change depends strongly on the *nature* of the carbonaceous species present on the surface, since both an initially clean sample and a sample annealed at only 360 K are not capable to sustain hydrogenation, while a sample annealed at 485 K may do. Obviously, hydrogenation depends strongly on the *nature* of the carbonaceous species, and the more active surface contains strongly dehydrogenated surface species.

Additionally, the deposited carbon species must also be capable to obey two other requirements in order to help preserve the catalytic activity of the surface: on one hand, it must block extensive alkene dehydrogenation as soon as a certain coverage has been reached, because otherwise the surface could eventually be poisoned by them; additionally, it must also leave open metal sites to allow for dissociative deuterium adsorption and hydrocarbon conversion throughout the whole experiment. The following three models are suggested to account for those requirements:

**Explanation Based on Different Ensemble Sizes Needed for the Pathways.** Only one possible explanation could be found that had been previously suggested in the literature, and although it turns out that it can not satisfactorily explain all of our observations, it shall be briefly discussed: dehydrogenation steps are believed to require large ensembles of metal atoms on the surface [25], so that these reactions could be expected to be easily poisoned by the deposition and accumulation of carbon or carbonaceous species, which could explain why the surface can not deactivate completely due to carbon accumulation, even after extended butene exposures. Hydrogenations may possibly need smaller ensembles of Pd-sites to proceed, and therefore might still be possible on the partially carbon-covered surfaces that are obtained by annealing at 485 K, presumably because less of the spaceous (only weakly decomposed) hydrocarbon species may accumulate on those carbon-precovered surfaces compared to the initially clean ones during butene-exposure under reaction conditions – note that carbon may slow down hydrocarbon decomposition and additionally weakens the hydrocarbon adsorption energy, which both may explain the lower coverage of spaceous

hydrocarbon species on the carbon-precovered surfaces. The isomerization reaction finally may require even smaller site ensembles, so that sustained isomerization may proceed even in the presence of the spaceous carbonaceous deposits that were discussed to inhibit hydrogenation.

Certainly, different adsorption requirements apply for alkenes and hydrogen; for example, this is manifested in the observation that the outcome of TPRS experiments between deuterium and alkene typically depends critically on the sequence in which the two reactants were dosed onto the surface (only when deuterium is adsorbed first, enough of it can accumulate on the surface, because preadsorbed hydrocarbon typically inhibits dissociative deuterium adsorption – see above) [233]. Moreover, different hydrocarbon fragments (decomposition products) may certainly require different adsorption geometries, and hydrogenation and dehydrogenation steps also involve different ensembles of surface atoms [99, 239, 208]. Indeed, many of the results from surface-science studies reported to date on hydrocarbon conversion support the idea that different sites, or different metal site ensemble sizes are required for hydrogenation and isomerization, so that the observed chemoselectivity on initially clean and carbon-precovered sample might be explained based on this idea. However, we believe that this model can not satisfactorily explain how such big differences between isomerization and hydrogenation rates can occur. For one, it is known from the IRAS surface-titrations with CO that the regular facets are even in the carbon-precovered sample nearly free of carbon, so that large amounts of spaceous carbonaceous species might also accumulate here and inhibit hydrogenation – but this one seeming contradiction might still be explained by a higher activity of the carbon-precovered sites near the particle edges. More importantly, however, both the formation of the 2-butyl surface intermediate and its reductive elimination to butane are half-hydrogenation steps, and one of them (the formation of 2-butyl from butene) is a common step of both reaction pathways, isomerization and hydrogenation. Even if it is true that hydrogenation requires larger sites ensembles than isomerization, it appears questionable how the half-hydrogenation of 2-butene to 2-butyl on one hand, and of 2-butyl to butane on the other may require so very different ensemble sizes, that one of those processes – the formation of 2-butyl – proceeds with seemingly identical rates on both the initially clean and the carbon-precovered model catalysts, while the other process – hydrogenation of 2-butyl to butane – can only occur on the carbon-precovered sample, and not on the initially clean sample, on which hydrogenation is so fully suppressed as observed experimentally. Thus, it appears that additional explanations are needed to understand the observed chemoselectivity:

**Influence of Subsurface-Carbon.** Alternatively, the different reactivities of the initially clean and carbon-precovered sample may be explained by mere electronic effects on the Pd surface atoms induced by the presence of carbon in the subsurface; in fact, Yudanov, Neyman and Rösch have suggested based on theoretical calculations that carbon may also easily migrate below the surface of Pd-nanoparticles (*i.e.*, into the subsurface region) [140]. Indeed, it was shown previously in this thesis by IRAS surface titrations that a surface precovered with carbon by annealing at 485 K is completely free of carbon after annealing at 600 K (see fig. 6.15) – which was explained by the activation of carbon subsurface-migration somewhere in the temperature range between 485 and 600 K; based on this explanation, it appears conceivable that a small fraction of the surface carbon might also migrate into the subsurface region during the flash to only 485 K.

In fact, there are several indications that the surface is relatively free of carbon after the pretreatment with butene by annealing at 485 K, and that most of the carbon accumulates mainly in defect sites; this fact might probably be taken as an indication that some carbon has migrated into the subsurface-region during the annealing step at 485 K. The indications that the surface stays nearly free of carbon during this treatment are: 1) The previously discussed IRAS surface titrations with CO have indicated that mostly defect sites are decorated with carbon deposits, while most of the regular surface-sites (esp. on the (111) facets) appear to remain nearly free of carbon. 2) The induction periods on the clean and carbon-precovered samples are nearly identical, indicating very similar available surface areas, thereby also disproving that considerable amounts of the surface might be covered with carbon. 3) The isomerization rates on the clean and carbon-precovered samples are nearly identical, indicating that the available surface area is not strongly decreased by the carbon deposits as the most simple explanation.

Subsurface carbon might modify the electronic nature of the surface palladium atoms, which might also affect the behaviour of the catalyst towards alkene hydrogenation and/or dehydrogenation – but apparently not towards H-D exchange/isomerization; if this is the case, then it is clear that the spaceous carbonaceous species that accumulate at the surface particularly of the not pretreated samples can not have a similar electronic influence on the Pd surface atoms, since hydrogenation is not induced in this case.

In fact, although subsurface carbon has been previously suggested to have an electronic influence on the Pd surface atoms and the reactions occurring on them (*e.g.* the theoretical paper by Yudanov *et al.* [140]), some very recent results of hydrocarbon conversion, however, indicate more an inhibiting effect of subsurface carbon on hydrogenation: Teschner *et al.* have studied

the dependence of 1-pentyne-conversion on hydrogen pressure (both on Pd black and foil) in a high-pressure XPS-setup and observed that the reaction leads to the formation of 1-pentene at lower hydrogen pressures (around 3.5 mbar), while the fully hydrogenated product pentane is formed at higher pressures (7.5 mbar). This change in selectivity was associated with the presence of a Pd-carbon-phase that spreads over approx. three Pd layers from the surface and that was identified by XPS; this phase is present under lower hydrogen pressures, but disaggregates at higher hydrogen pressures. Its influence on selectivity was interpreted such that it decouples the surface from subsurface-hydrogen, which was said to be necessary for the formation of the fully hydrogenated product: in its presence, 1-pentene forms selectively.

**Different Hydrogen Species.** Indeed, the third possible explanation why hydrogenation is induced on carbon-precovered samples accounts for a change in the hydrogen adsorption state in the presence of deposited carbon. Shaikhutdinov *et al.* have pointed out that hydrogenation in vacuum may easily be obtained on Pd nanoparticles, while it is only rarely observed on single crystals under the same conditions [215, 216]; the specific quality of the nanoparticles was assigned to their ability to absorb hydrogen into a weakly bound *subsurface hydrogen* state, which was described to be very active in alkene hydrogenation; note that this explanation is also in agreement with the model given later by Teschner *et al.* (see the previous paragraph). The interpretation of the weakly bound hydrogen species as being a subsurface species is further supported by recent direct measurements of hydrogen depth-profiles in supported Pd nanoparticles using non-destructive nuclear reaction analysis (NRA) by Wilde *et al.* [240] on a Pd/Al<sub>2</sub>O<sub>3</sub> model catalyst; note that the Pd nanoparticles in this Al<sub>2</sub>O<sub>3</sub>-supported model system had a similar morphology as the ones in the Pd/Fe<sub>3</sub>O<sub>4</sub> system used in this work.

It is conceivable that those two hydrogen species may also be responsible for the critical selectivity towards the hydrogenation pathway observed on a carbon-precovered sample in this work. In fact, our experimental observations indicate that two different forms of hydrogen may be involved in the competing reaction pathways, isomerization and hydrogenation: although at the beginning of an isothermal experiment on an initially clean sample (see fig. 6.24 a) – *i.e.*, after saturation of the particles with deuterium – similar isomerization and hydrogenation rates are found, the hydrogenation rate drops to zero soon afterwards, while the isomerization rate can be maintained. Both reaction pathways – hydrogenation and isomerization – proceed *via* the same reaction intermediate (2-butyl) according to the Horiuti-Polanyi mechanism, which forms readily on the surface, as indicated by the sustainability of the

isomerization pathway. Therefore all differences in the reaction kinetics of the exchange/isomerization and hydrogenation pathways are most likely related to their different requirements in deuterium atoms; it is not likely that the selective suppression of only the hydrogenation pathway on the initially clean surface can be simply explained by differences in the deuterium surface coverages, since both pathways require deuterium for the formation of their common intermediate 2-butyl, and both pathways also show similar reaction orders with respect to hydrogen pressure [189]. More likely, the vanishing hydrogenation activity may be explained with the requirement of a special type of (very reactive) hydrogen for the second half-hydrogenation step; this species might be formed during the initial deuterium exposure (before the first butene pulse), but get depleted when the reaction experiment proceeds, because it might not get replenished on an initially clean sample – whereas it might do so on the carbon-precovered sample. Based on the above cited references by Shaikhutdinov *et al.* [215, 79, 172], we assume that this species might be a weakly bound subsurface hydrogen species; as an explanation for how carbon may induce hydrogenation in this model, it could be argued that deposition of strongly bound carbonaceous species may weaken the metal-deuterium bond and make it possible to replenish this deuterium species under reaction conditions, resulting in sustained hydrogenation. Note, however, that the subsurface hydrogen species does not necessarily need to be directly involved in the reaction; its presence might simply be enough to activate surface hydrogen.

Shaikhutdinov *et al.* have suggested that the hydrogen adsorption state in the Pd nanoparticles may be probed by TPD experiments of adsorbed hydrogen [79, 172]; they have shown that hydrogen desorbs at high temperatures around 340 K at the lowest coverages, and assigned this state to strongly adsorbed hydrogen at the Pd surface. At higher coverages, additional desorption signals were also observed at lower temperatures (below 300 K); this more weakly bound species was assigned to subsurface hydrogen.

Based on this work, TPD measurements of the hydrogen adsorption state were also conducted on our clean and carbon-precovered Pd/Fe<sub>3</sub>O<sub>4</sub> model catalysts. First, we will discuss the exposure-dependent TPD experiments with deuterium on *clean* Pd/Fe<sub>3</sub>O<sub>4</sub>, which were prepared with deuterium at exposures ranging from 0.1 to 10.4 L, deposited at 115 K (see fig. 6.26 a). Those experiments exhibit a symmetrical peak around 335 K at lowest coverages, which grows with increasing coverage and develops a strong shoulder at lower temperatures that extends below 200 K at 10.4 L; the results at 3.1 and 10.4 L are nearly identical, indicating that 3.1 L are sufficient for saturation of the Pd nanoparticles. The peak around 335 K agrees well with the peak assigned to surface hydrogen atoms described by Shaikhutdinov *et al.*, and the shoulder extending towards lower temperature with the desorption from

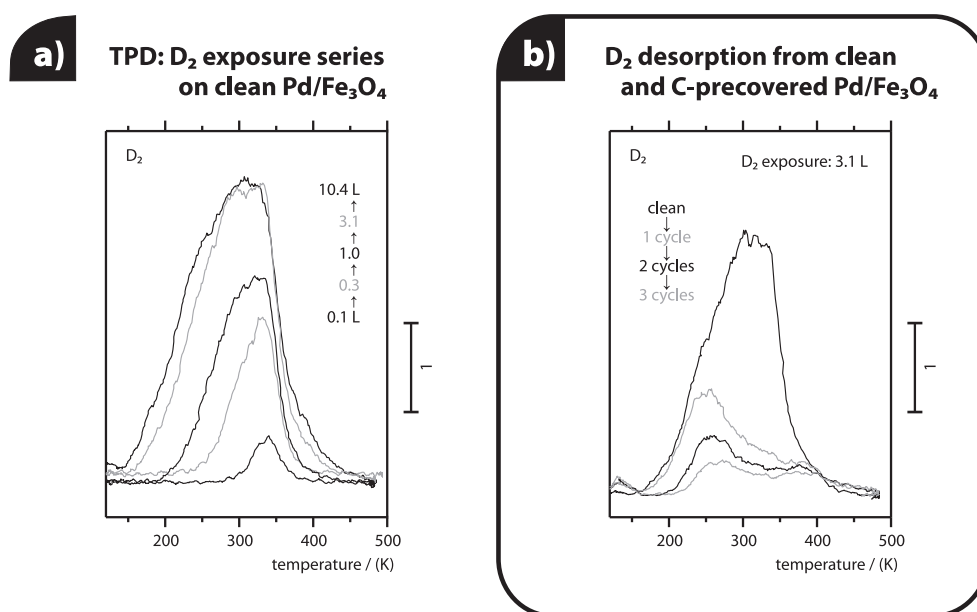


Figure 6.26: Desorption of D<sub>2</sub> from Pd/Fe<sub>3</sub>O<sub>4</sub>: a) D<sub>2</sub> exposure series (clean catalyst), b) influence of carbon-deposition (0.84 L 2-butene, annealed at 485 K).

a surface in the presence of subsurface hydrogen, as also described by the same authors; concluding from those experiments, the Pd/Fe<sub>3</sub>O<sub>4</sub> model catalyst shows a very similar hydrogen uptake behaviour as the one previously described by Shaikhutdinov *et al.* for the Pd/Al<sub>2</sub>O<sub>3</sub> model system.

In the second experiment, the saturation dose of deuterium (3.1 L) was adsorbed on the clean Pd/Fe<sub>3</sub>O<sub>4</sub> model catalyst and on systems precovered with carbon by different amounts of 2-butene adsorption and annealing cycles (0.84 L, annealed at 485 K) – see fig. 6.26 b. The maximum of the hydrogen desorption signal from the carbon-precovered samples is found around 255 K, and thus at a significantly lower temperature than the clean sample; only small desorption signals are detected on a carbon-precovered model catalyst in the region where the maximum is observed on a clean catalyst (~ 335 K). Note that – despite the near coincidence of their desorption points – it is not possible based on those data to identify the low-temperature feature in the experiments on the carbon-precovered system with the subsurface hydrogen state described by Shaikhutdinov *et al.* for the clean catalyst, because the presence of carbon may lower the desorption point  $T_{\text{des}}$  of all species; nevertheless, it is clear that the hydrogen adsorption state is significantly weakened on carbon-precovered Pd particles, suggesting that such weakly bonded species may indeed be the ones responsible for the sustained hydrogenation rates.

Nevertheless, those TPD-experiments are still not fully satisfactory, because the overall yield of hydrogen that desorbs from the carbon-precovered system is much lower than the one that desorbs from the clean system; moreover, even the amount of the weakly bonded species that desorbs from the carbon-precovered system in those experiments is still smaller than the sub-surface hydrogen-component in the experiments on the clean sample – and thus the question might arise how hydrogenation could be induced in a system that seems to contain not only less hydrogen overall, but even less of the weakly bonded, very reactive hydrogen species that has been brought in connection with hydrogenation. In order not to present a wrong model, it must be clearly stated at this point that such a direct, quantitative interpretation of the two TPD series shown in fig. 6.26 a) and b) might not validly reflect the possible distribution between the two hydrogen species *under reaction conditions*; in fact, under reaction conditions, the surface is covered – in addition to possibly present carbon – with spaceous carbonaceous species, which limit dissociative deuterium adsorption; thus, in order to understand the facilitation of hydrogenation on a carbon-precovered sample, it would rather be important to *directly probe the hydrogen distribution* in an initially clean and a carbon-precovered model catalyst under *isothermal reaction conditions*; TPD clearly can not deliver such an evaluation, and the shift in the hydrogen distribution observed in these experiments can only be regarded as a first indication for the influence of carbon. Due to this reason, direct measurements of the hydrogen depth profiles (distribution) in both the clean and carbon-precovered Pd nanoparticles have been prepared by nuclear reaction analysis (NRA, see before) under isothermal reaction conditions (*in situ*) in a joint project with a cooperating group; those measurements will be published in a forthcoming paper [241]. The main conclusion from those experiments was that hydrogenation of the butene double bond indeed requires the presence of weakly bound hydrogen species absorbed in the Pd particle volume; carbon deposition was found to strongly affect the hydrogen depth distribution in the Pd nanoparticles and thus promotes persistent hydrogenation activity; this promotion of sustained hydrogenation by carbonaceous deposits was hypothetically attributed to the facilitation of hydrogen diffusion into the bulk of the Pd nanoparticles under reaction conditions, which thus might allow a fast replenishing of the volume-absorbed hydrogen.

## Summary

In this section, we have discussed the dependence of isomerization and hydrogenation kinetics on reaction parameters such as temperature and the chemical nature of carbonaceous deposits present on the model catalysts under



reaction conditions. At the beginning of the experiments, the samples always exhibit high reaction rates in both conversion pathways – isomerization and hydrogenation – for a limited time, but the rates decline to zero quickly when the experiments are conducted at low temperature around 200 K; this is presumably due to the inhibition of dissociative hydrogen adsorption by the accumulating spaceous hydrocarbon species. Only when the experiments are conducted at elevated temperatures (around 250 K), sustained reactivity can be obtained; two cases have to be discriminated here: the initially clean catalyst exhibits sustained reactivity only in the isomerization pathway, but the hydrogenation rates still drop to zero quickly; in the presence of predeposited carbon prepared by butene adsorption and annealing at 485 K prior to experiment, the rates of both pathways can be sustained. Interestingly, the reaction rates in both pathways exhibit very different time-behaviours: at the beginning of each butene pulse, both rates rise quickly, and presumably are limited by the availability of the butene. The isomerization rate stays at a constant level in the following. The hydrogenation rate, however, drops to a lower value in the later run of the pulse, indicating that it is now limited by a different factor; according to the Horiuti-Polanyi mechanism, this can be the availability of deuterium.

In order to explain how carbon-deposition might induce hydrogenation, three possible models have been discussed: 1) One model analyzes the different ensemble sizes of reaction sites that may be required by the three reactions (hydrogenation, isomerization and dehydrogenation); hydrogenation had previously been suggested to require larger ensembles than isomerization; those large ensembles might only be available on a carbon-precovered sample, because carbon-adsorption on the surface reduces the hydrocarbon adsorption energy, thereby limiting its surface coverage; on an initially clean surface on the other hand, more spaceous hydrocarbon species may accumulate, thereby limiting the amount of available large surface sites. 2) It has been suggested that the higher reactivity in the presence of carbon might be induced by subsurface carbon-species, which may influence the Pd surface atoms electronically and change their reactivity. Those two models have been discussed, and were shown to not be fully conclusive.

Thus, a third explanation has been suggested, which also accounts for the apparently critical dependance of hydrogenation on hydrogen availability: hydrogenation may depend on the presence of a special, weakly bound and very reactive hydrogen species, which – based on previous reports in the literature – was suggested to be subsurface hydrogen. Indeed, direct measurements of hydrogen depth-profiles under reaction conditions by a cooperating group have shown that the amount of volume-absorbed hydrogen is higher in the presence of carbon at the surface – presumably because carbon facilitates

hydrogen diffusion into the Pd bulk; thus, carbon may facilitate sustained hydrogenation. This model conclusively explains all of the observed effects – including the high rates in both pathways at the beginning of the experiment, and the selective drop in the hydrogenation rate over each butene pulse due to partial subsurface-hydrogen depletion.

### 6.3.4 Selectivity in the Conversion of *cis*- and *trans*-2-Butene

To this point, we have exclusively applied *cis*-2-butene as a reactant for the study of 2-butene-conversion on the Pd/Fe<sub>3</sub>O<sub>4</sub> model catalyst. In the following section, we will inspect the possibly different behaviours of the two configurational isomers of 2-butene – *cis*- and *trans*-2-butene – in all of the reactivity experiments discussed before on the Pd/Fe<sub>3</sub>O<sub>4</sub> model catalyst. This study was originally inspired by previous reports about a *cis-trans*-selectivity during hydrocarbon conversion on metal catalysts [25]; for example, it is known that conversion of hydrocarbons on a metal catalyst under high-pressure conditions may lead to products, whose *cis-trans*-distribution may considerably deviate from the distribution in the reactants, indicating that the conversions have formed products with a significant *cis-trans*-selectivity [25]; as explanations for this selectivity, it has been suggested that the isomerization reaction might proceed with several turnovers of every reactant molecule under high-pressure conditions, thereby repeatedly isomerizing each molecule until an equilibrium distribution between the two isomer configurations has been reached in the products; this equilibrium might for example be defined by the gas phase energetics of the *cis*- and *trans*-isomers, or by their surface adsorption energies (for a more detailed explanation of those models, see the introduction at the beginning of this chapter). Additionally, a *cis-trans*-selectivity has also been observed in surface-science studies, in which – due to the short surface residence times or single-collision conditions – an equilibration with the gas phase species according to the different energetics of the gas phase isomers can be excluded; for those cases, models to explain a *cis-trans*-selectivity by kinetic control have been suggested (for a detailed illustration, see the introduction to this chapter).

In fact, an understanding of the factors that may govern *cis-trans*-selectivity during catalytic hydrocarbon conversion is strongly desired; as an example, it has been put forward in the introduction to this chapter that a control over the *cis-trans*-configuration of the products obtained by partial hydrogenation of plant oils to edible fats – an enormously important chemical process for human nutrition – is desired, because *trans*-fatty acids have been accused of significantly increasing the risk of cardiovascular diseases (see the introduction for references).

In this work, we have chosen to evaluate the reactivities of the two configurational isomers of 2-butene in both isomerization *and* hydrogenation under all reaction conditions studied before (as defined by temperature and the presence or absence of carbon deposits) in order to find the possible factors that may govern selectivity in the conversion of those two isomers from a possibly wide perspective. This section will thus be structured as follows: first, the observed conversion rates with both isomers and their dependence on the reaction conditions will be described; then, the possible reasons for the observed differences will be discussed, beginning with an analysis of the factors that may limit the rates in each of the presented reactivity experiments. Then, further experiments will be presented – including TPRS and IRAS experiments of the adsorbed 2-butenes – which suggest different surface stabilities of the two isomers on the surface. Finally, based on the observations in those experiments, the different conversion rates with the two isomers will be discussed again in order to obtain a conclusive model.

### **Isothermal Reaction Rate Measurements with *cis*- and *trans*-2-Butene**

#### Isothermal Reaction Rate Measurements with *cis*- and *trans*-2-Butene

Detailed isothermal molecular beam reaction rate measurements with both *cis*- and *trans*-2-butene were conducted at temperatures ranging from 195 to 260 K, and on the initially clean and carbon-precovered model catalyst; for those experiments, the same pulse scheme has been applied that was also used in the previously described experiments (see section 6.3.3 and fig. 6.20). Those experiments were performed using molecular *cis*- and *trans*-2-butene-beams of identical intensity, which could be ensured by monitoring the mass signals of the reactant; under application of identical pressures in the beam inlet system, also identical beam intensities with the two reactants could be obtained (measurements not shown here). Additionally, it is known from literature that both *cis*- and *trans*-2-butene have practically identical fragmentation behaviours in the EI source of the mass spectrometer [242, 243, 244], so that identical mass signals of those compounds do also indicate identical concentrations in the EI source – or, for our purpose, identical formation rates (in the pumped chamber volume).

Fig. 6.27 shows the isomerization (row 1) and hydrogenation (row 2) rates obtained on an *initially clean* Pd/Fe<sub>3</sub>O<sub>4</sub> model catalyst at *different temperatures* ranging from 195 to 260 K; the results with *cis*-2-butene as a reactant are collected in column a), and the ones with *trans*-2-butene in column b).

In addition to those experiments, fig. 6.28 compares the steady-state reaction rates in isomerization (row 1) and hydrogenation (row 2) obtained with

*cis*- (column a) and *trans*-2-butene (column b) on the initially clean *and* carbon-precovered model catalysts at a fixed temperature of 260 K (the plot displays only the averaged pulses for simplification, as previously displayed in fig. 6.24 and explained in section 6.3.3).

**Observations:** As described previously, isomerization and hydrogenation rates can not be sustained around 200 K, but exhibit only a short reactivity maximum and then decline to zero quickly (see fig. 6.27); under those conditions, *cis*-2-butene reaches significantly higher reaction rates in both pathways than *trans*-2-butene. Interestingly, this selectivity vanishes at elevated experiment temperatures, and at 250 K, both the isomerization and hydrogenation rates with the two configurational isomers of 2-butene are very similar; for the isomerization rates, this is true both for the transient component at the beginning of the experiment, and also for the steady-state reactivity regime towards the end of the experiment. If there is any difference in the selectivity with the two isomers in the two conversion pathways in those experiments, then it is that the differences between the two isomers in the hydrogenation pathway at low temperatures appear to be a bit less pronounced than in the isomerization pathway – but this is probably only due to the hydrogenation rates being generally a bit lower than the isomerization rates.

Surprisingly, a *cis-trans*-selectivity develops in the isomerization pathway at the elevated temperature of 260 K on the carbon-precovered sample (see fig. 6.28) – unlike the case on an initially clean model catalyst (as just described): on the carbon-precovered system, *trans*-2-butene isomerizes with only approx. half the rate as *cis*-2-butene; indeed, *trans*-2-butene exhibits considerable differences in the isomerization rates between an initially clean and a carbon-precovered model catalyst in the sense that the isomerization rate on the carbon-precovered model catalyst is only half the value obtained on the initially clean model catalyst, whereas *cis*-2-butene isomerizes with very similar rates on both the initially clean and carbon-precovered system.

The hydrogenation reaction on the other hand – which proceeds with sustained reactivity only on the carbon-precovered sample at elevated temperatures (as discussed in the last section) – occurs with similar rates with *cis*- and *trans*-2-butene as reactants at the end of the butene-pulse (*i.e.*, under steady-state conditions); interestingly, however, the short transient maxima at the beginning of the hydrogenation rate signal during the pulses do seem to exhibit a *cis-trans*-selectivity: they are higher for *cis*-2-butene.

reaction of 2-butene with deuterium on a clean Pd/Fe<sub>3</sub>O<sub>4</sub> model catalyst

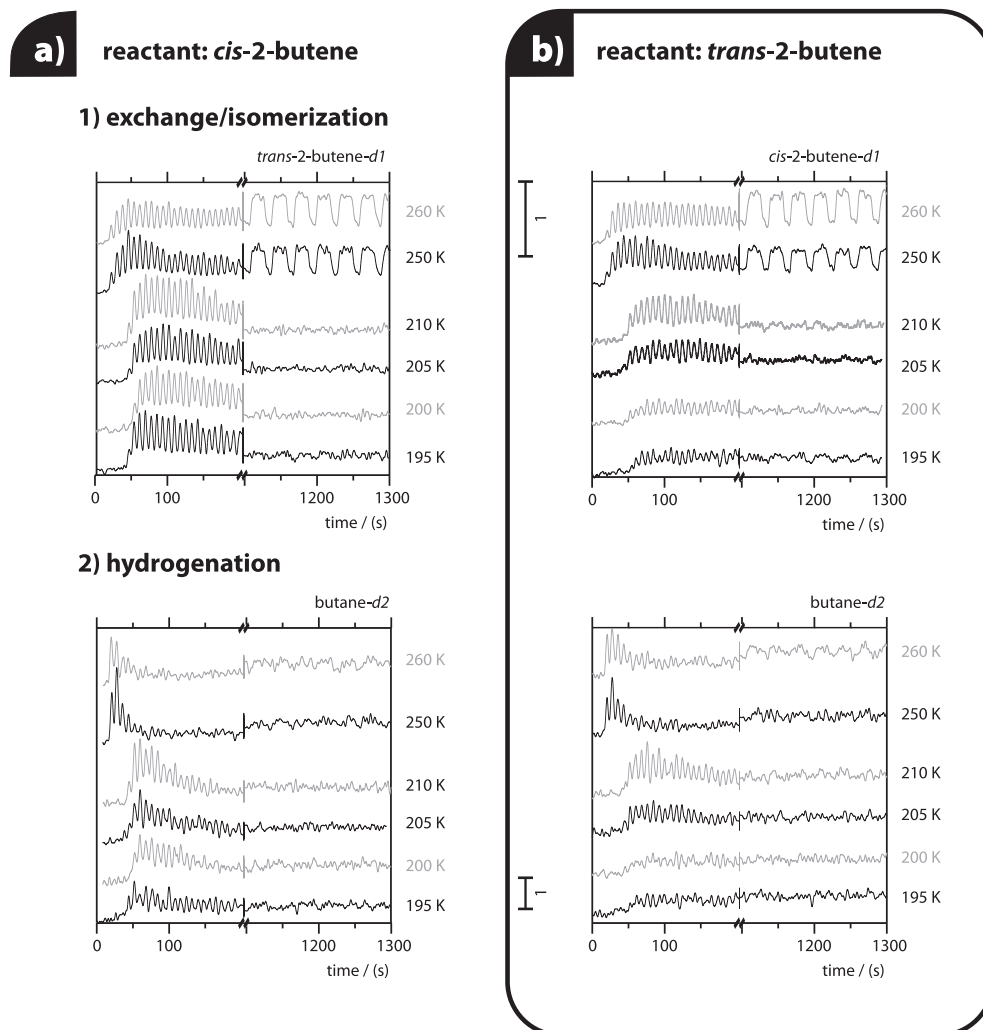


Figure 6.27: Isothermal experiments with a) *cis*- and b) *trans*-2-butene on initially clean Pd/Fe<sub>3</sub>O<sub>4</sub> at different temperatures: 1) isomerization, 2) hydrogenation.

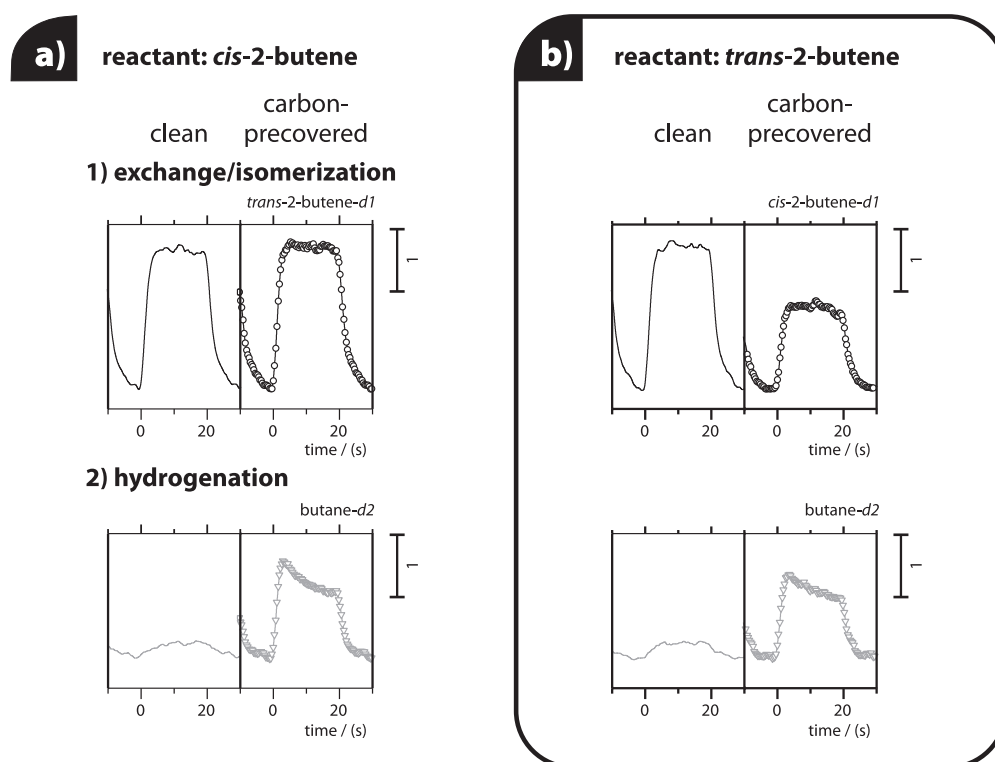


Figure 6.28: Isothermal experiments with a) *cis*- and b) *trans*-2-butene on initially clean and carbon-precovered Pd/Fe<sub>3</sub>O<sub>4</sub> at 260 K (averaged signal pulses); note that sustained hydrogenation is only obtained on a carbon-precovered model catalyst (this was extensively discussed in section 6.3.3).

**Intermittent Considerations.** The reactivity measurements with *cis*- and *trans*-2-butene indicate that different reaction rates with those isomers may in fact be observed under certain conditions, while under other conditions, no selectivity in the conversion of the two isomers is observed (*i.e.*, the two isomers are converted with nearly identical rates). However, when different conversion rates are observed between the two configurational isomers, the *cis*-isomer exhibits the higher conversion yields always; thus, the observed selectivity appears to be systematic. It shall be stated here that only some of our experimental results are shown here, and that a lot more experiments were conducted, which all indicate the described behaviour of the selectivity.

One important conclusion can already be inferred from the presented reactivity data: the higher reactivity of the *cis*-isomer is not a general property of this molecule, but it rather manifests itself only under certain reaction conditions, while it may be absent under different conditions; thus, different reactivities (*i.e.*, kinetic reaction rate constants) of the two isomers in the

elementary steps of the conversion reactions are most likely not the critical factor for the different reactivities observed under certain conditions – because under certain other reaction conditions, the reactivities of both isomers are identical<sup>11</sup>. But if the selectivity is not governed by a different reactivity between the two isomers, then the only way to explain the different rates can be found by an inspection of the rate-limiting factors under all conditions where a selectivity is observed; those rate-limiting factors may, for example, be the availabilities (*e.g.* surface coverages) of the reactants.

An indication for the rate limiting factor can be found by an inspection of the experiments on the initially clean model catalyst at low temperatures. We know from the previous section, in which those isothermal reaction rate measurements have originally been discussed –, that the reaction rates under these conditions are high only at the beginning of the experiment, when the availability of hydrogen for the reaction is high due to the long hydrogen saturation phase prior to the first butene pulse; thus, it appears valid to assume that the availability of hydrogen does not limit the initial reaction rates in both reaction pathways – isomerization and hydrogenation – at the beginning of those experiment (around the signal maximum). Additionally, it is peculiar that both conversion pathways exhibit qualitatively the same *cis-trans*-selectivity under those conditions: the *cis*-isomer shows the higher conversion rates than the *trans*-isomer in both isomerization and hydrogenation; this observation may be taken as an indication that the rates in both conversion pathways are limited by the same factor – which, based on the Horiuti-Polanyi mechanism (see fig. 6.19), may be seen in the formation rate of the common reaction intermediate (the 2-butyl species). If, however, the availability of the coreactant hydrogen is not rate limiting for the conversion reactions under those conditions, as described before, it must be the availability (*i.e.*, surface coverage) of the alkene 2-butene that limits the reaction rates under those conditions.

Consequently, it appears reasonable to look for possible reasons why the surface coverages of the two isomers might be different; for this purpose, IRAS and TPD/TPRS studies with the two isomers have been conducted to study their adsorption behaviour:

### IRAS Spectra of Adsorbed *cis*- and *trans*-2-Butene

As a first step, we investigated the IRAS spectra of *cis*- and *trans*-2-butene on the Pd/Fe<sub>3</sub>O<sub>4</sub> model catalyst; for those experiments, 290 L of deuterium and 0.84 L of the respective configurational isomer of 2-butene were coadsorbed

---

<sup>11</sup>Of course, the identical rates might also arise from an incidental compensation of different reactivities (reaction rates) and surface coverages of the reactants; such an incidental compensation under different conditions, however, appears very unlikely.

IRAS: *cis*- and *trans*-2-butene + D<sub>2</sub> on clean Pd/Fe<sub>3</sub>O<sub>4</sub>

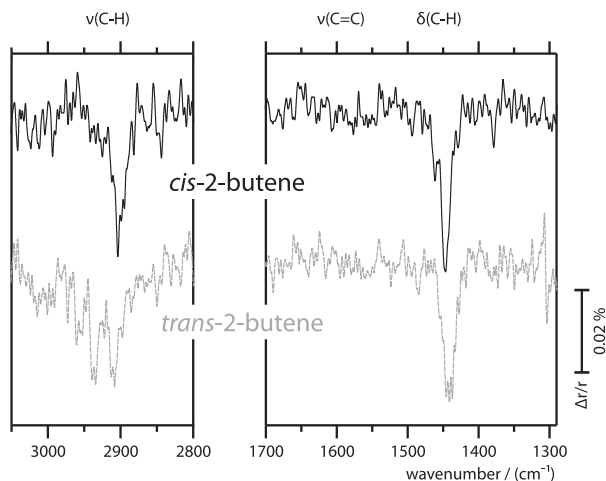


Figure 6.29: Comparison: IRAS spectra of *cis*- and *trans*-2-butene (0.84 L) coadsorbed with D<sub>2</sub> (290 L) on clean Pd/Fe<sub>3</sub>O<sub>4</sub> at 115 K.

at 115 K to obtain near saturation of the surface with butene (see before); the spectra displayed in fig. 6.29 were obtained. Two groups of absorption features dominate those spectra (see also section 6.3.1): the asymmetric deformations  $\delta_{as}(\text{CH}_3)$  (around 1445  $\text{cm}^{-1}$ ) and the C-H stretching vibrations  $\nu(\text{CH}_3)$  of the terminal methyl groups (between 2850 and 2970  $\text{cm}^{-1}$ ). *cis*- and *trans*-2-butene show significant differences in the latter region: while the adsorbed *trans*-2-butene shows three distinct absorptions in this region (the symmetric C-H stretching vibration  $\nu_s(\text{CH}_3)$  at 2907  $\text{cm}^{-1}$ , and two asymmetric C-H stretching vibrations  $\nu_{as}(\text{CH}_3)$  at 2937 and 2956  $\text{cm}^{-1}$ ), the spectrum of adsorbed *cis*-2-butene exhibits only one feature: the one for the *symmetric* C-H stretching vibration  $\nu_s(\text{CH}_3)$  at 2902  $\text{cm}^{-1}$ . Additionally, *trans*-2-butene shows a broad feature for the C-H stretching mode  $\nu(=\text{C-H})$  of the inner hydrogen atoms (around 3010  $\text{cm}^{-1}$ ).

The pronounced differences in the intensities of the CH<sub>3</sub> stretching modes indicate different orientations of the terminal methyl groups in *cis*- and *trans*-2-butene with respect to the surface: the more upright these terminal methyl groups stand on the surface, the larger will be the perpendicular component of the dynamic dipole moment for the *symmetric* stretching mode, and the smaller will be the component for the *asymmetric* mode. Thus, based on the MSSR, the intense feature for the symmetric stretching mode and the minimal intensity of the asymmetric modes in the spectrum of *cis*-2-butene may be understood with a nearly upright orientation of the terminal methyl groups in adsorbed *cis*-2-butene; in contrast, the similar intensities of sym-



metric and asymmetric modes in the spectrum of *trans*-2-butene indicate that the methyl groups in this adsorbed molecule have an intermediate inclination angle (are tilted with respect to the surface normal).

### Desorption Spectra of *cis*- and *trans*-2-Butene

Next, we investigated the adsorption, desorption and decomposition of *cis*- and *trans*-2-butene in TPRS experiments; for those experiments, the configurational isomers were adsorbed individually on the clean model catalyst (0.84 L at 115 K to ensure near saturation of the surface with butene, see before) before the TPRS experiment (heating rate  $\sim 3.5$  K/s); the results are displayed in fig. 6.30. *cis*- and *trans*-2-butene show significantly different peak shapes and temperatures for the molecular desorption: *trans*-2-butene desorption peaks at a temperature of approx. 220 K, and shows a broad shoulder towards higher energies, while *cis*-2-butene desorbs with a nearly symmetric peak around 265 K; note that the sharp signal around 145 to 150 K is due to the desorption from multilayers, and that differences in this peak are most probably simply due to slightly different exposures, which, however, are irrelevant for our purpose (because we are only interested in the desorption of butene that had been adsorbed directly on the catalyst surface). Interestingly, despite the difference in the molecular desorption, the two configurational isomers exhibit no difference in the yield and peak positions of the hydrogen signal (which originates from hydrocarbon decomposition).

**Interpretation.** The different peak positions of the molecular desorption of butene indicate that *cis*-2-butene is more strongly adsorbed on the clean Pd particles than the *trans*-isomer. The identical decomposition yields from the two isomers on the other hand indicate that decomposition proceeds through identical surface intermediates with both isomers, which seem to reach similar coverages at the surface with both configurational isomers – presumably because the surface is saturated with it; we may speculate at this stage, that decomposition might proceed only with strongly adsorbed hydrocarbon species, possibly adsorbed in certain, highly reactive sites.

The higher adsorption stability of *cis*-2-butene is in a good agreement with previous reports, *e.g.* with reports of *cis*- and *trans*-2-butene adsorbed on a Pt(111) single crystal [202, 200, 201, 190]; it was explained with the ability of the *cis*-isomer to reduce steric repulsion of the spaceous methyl groups from the surface by tilting the molecule plane away from a flat configuration – a possibility that the *trans*-isomer does not have, as it is graphically represented in fig. 6.5 b); this sketch illustrates that *cis*-2-butene may

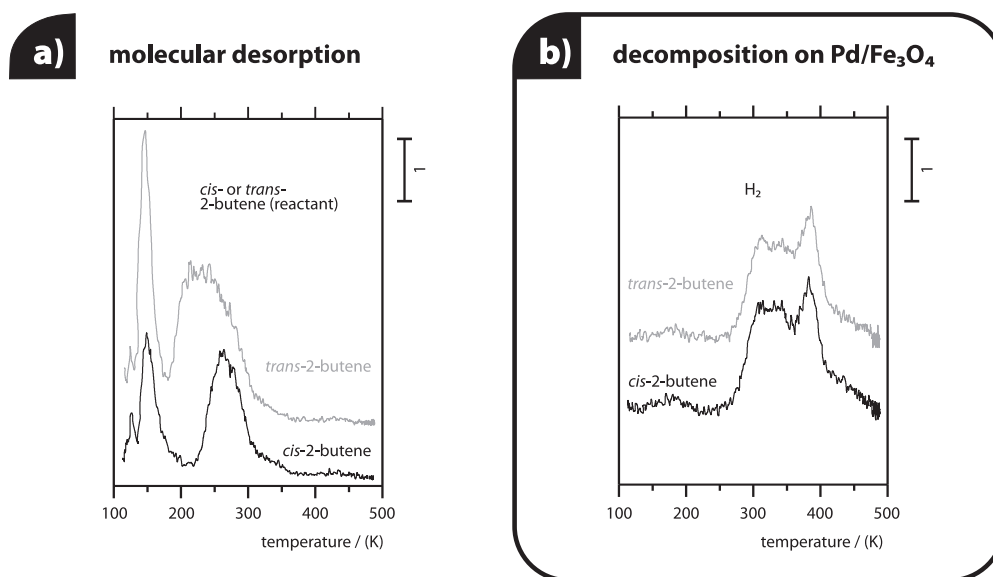


Figure 6.30: Comparison: individual TPRS experiments with *cis*- and *trans*-2-butene (0.84 L adsorbed at 115 K) from clean Pd/Fe<sub>3</sub>O<sub>4</sub>.

tilt away from the surface to adopt a more upright geometry, in which the methyl groups are standing relatively upright on the surface. It is worth noting that this difference in the adsorption geometry would also be in a very good agreement with our interpretations of the IRAS spectra of the adsorbed butene-isomers. Therefore, based on those two discussed experiments, we believe that the previously proposed model for the adsorption geometry is a valid description, and that *cis*-2-butene may stabilize on the surface by a reduction of steric repulsion between the terminal methyl-groups and the surface by tilting those groups away from the surface; those different abilities between the two isomers might explain why *cis*-2-butene could be considerably more strongly adsorbed on the surface of our model catalyst; as a consequence, it might also reach higher surface coverages under reaction conditions in adsorption-desorption(-reaction)-equilibrium.

### Thermal Desorption Spectra with Coadsorbed 2-Butene and Deuterium

As a next step, we investigated the conversion of *cis*- and *trans*-2-butene with coadsorbed deuterium in TPRS experiments; for those experiments, 290 L of deuterium and 0.84 L (to reach near saturation) of the respective isomer were adsorbed at 115 K on the clean model catalyst prior to the TPRS experiment; fig. 6.31 shows the results with the two isomers. As described

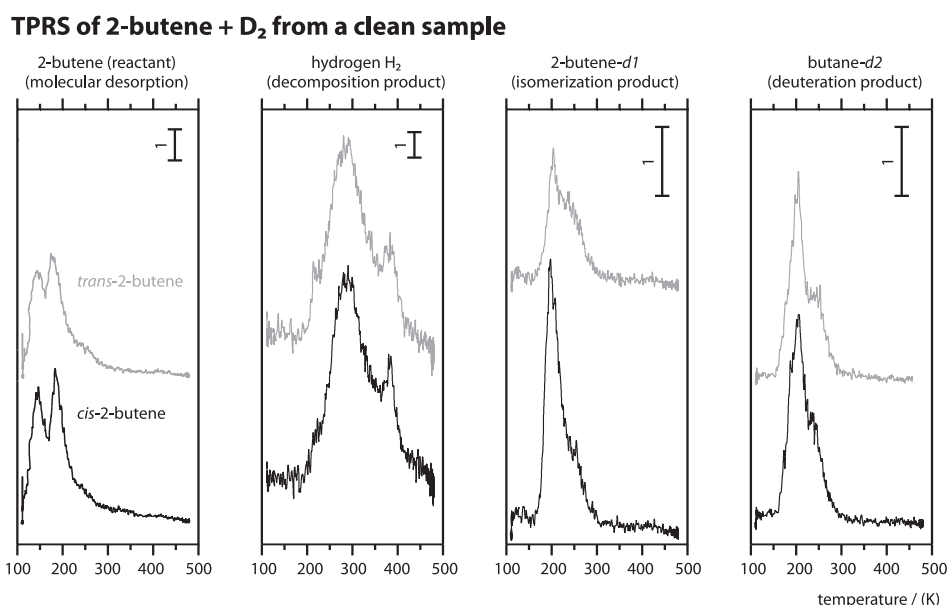


Figure 6.31: Comparison: TPRS experiments with *cis*- and *trans*-2-butene (0.84 L at 115 K) coadsorbed with D<sub>2</sub> (290 L) from clean Pd/Fe<sub>3</sub>O<sub>4</sub>.

in section 6.3.2, products from both the exchange/isomerization as well as the hydrogenation pathway can be obtained when the butene is coadsorbed with deuterium, together with dehydrogenation and molecular desorption. In comparison with the experiments on a sample without coadsorbed deuterium, it is apparent that the molecular desorption signals of 2-butene and hydrogen (from decomposition) are shifted significantly towards lower temperature due to the presence of coadsorbed hydrogen in the particles; still, however, *cis*-2-butene exhibits a higher desorption point than *trans*-2-butene (185 *vs.* 175 K), again indicating that it is more strongly adsorbed – but the differences between the two isomers are significantly smaller in the presence of coadsorbed deuterium.

Interestingly, *cis*-2-butene also yields significantly higher amounts of the isomerization product than *trans*-2-butene, whereas no different yields could be observed in hydrogenation and also dehydrogenation; additionally, the isomerization product of the *cis*-reactant desorbs at lower temperature (peak ~ 195 K) than of the *trans*-reactant (~ 205 K).

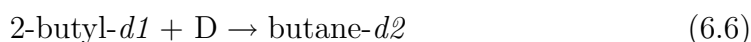
**Interpretation.** Those TPRS experiments clearly demonstrate the different activities of the Pd nanoparticles in *cis-trans*-isomerization towards the two butene-configurational isomers, whereas the hydrogenation reaction proceeds with identical rates under TPRS conditions. It should be pointed out that the *cis*-isomer yields larger isomerization rates, although the TPRS ex-

periments suggest that it has the higher stability at the surface; thus, those experiments might indicate that a higher stability of the adsorbed species does not necessarily result in a lower reactivity, although it might be expected that the isomerization reaction would form the more stable product (see in the introduction for a description of the previous experiments by Zaera *et al.*); based on our experiments, it rather appears that other factors might critically control the *cis-trans*-isomerization selectivity, which are difficult to unravel in *non*-isothermal experiments.

### A Model for *cis-trans*-Selectivity

Based on the experiments described in the previous paragraphs, it appears that the two configurational isomers of 2-butene, *cis*- and *trans*-2-butene, might have different adsorption energies on the catalyst surface – and although the coadsorption of hydrogen reduces the difference in this property, we will now try to use it as the key hypothesis to understand the different reaction rates observed with the two isomers under certain conditions. Specifically, we have shown that *cis*-2-butene yields higher rates compared to *trans*-2-butene in both the *cis-trans*-isomerization and hydrogenation pathway in the low-temperature experiments (195 - 210 K). Those differences vanish, however, when the reaction temperature increases above  $\sim 240$  K, which leads to very similar *cis-trans*-isomerization rates for both configurational isomers under steady-state conditions. The presence of small amounts of carbon can in turn switch this catalytic regime back to a situation in which the *cis*-isomer exhibits higher yields than the *trans*-isomer (more specifically, the *cis*-isomer exhibits similar isomerization rates on the clean and carbon-precovered catalyst, while the isomerization rate of the *trans*-isomer on the carbon-precovered catalyst drops to only approx. half the value that it reaches on the initially clean catalyst). Interestingly, only the *cis-trans*-isomerization pathway is affected by the co-adsorbed carbonaceous deposits, whereas the hydrogenation reaction produces similar amounts of butane-*d*2 from both isomers under steady-state conditions.

In order to understand *cis-trans*-selectivity in all those cases, it may help to inspect all of the reaction steps in the Horiuti-Polanyi mechanism again (see also fig. 6.19):



It is important to emphasize that – unlike described by reaction 6.2 – in fact two different types of hydrogen (deuterium) species seem to be involved in the two reaction pathways, according to the previous discussions (see section 6.3.3): surface and subsurface hydrogen; the latter is critically important for the hydrogenation reaction (although this should not be understood in the sense that subsurface hydrogen would be *directly* involved). Additionally, it should be noted that the desorption of the two products is not included in the reaction mechanism, because it is fast at the reaction temperatures as compared to reaction, since the reaction is conducted above the desorption point of the reactant from a hydrogen-containing system (according to the TPRS experiments).

**Discussion of the Elementary Steps.** We will first discuss the elementary steps according to the Horiuti-Polanyi mechanism and their possible involvement in the *cis-trans*-selectivity, and then try to apply this knowledge to explain the observed selectivities:

1. **Hydrogen-Adsorption (reaction 6.2).** It has been pointed out in the previous section, that the dissociative adsorption of hydrogen may play a critical role and be a rate-limiting factor for both conversion pathways under certain conditions: at low temperature (around 200 K), the conversion rates drop quickly after the first butene exposure pulses, due to the quickly evolving inhibition of dissociative deuterium adsorption by the accumulation of spaceous hydrocarbon species at the surface; at elevated temperature (around 250 K), this inhibition is reduced due to the onset of hydrocarbon desorption and also decomposition, which leads to a lower coverage (or footprint) of hydrocarbon species on the metal surface, which allows for some dissociative hydrogen-adsorption on the surface and thus critically increases hydrogen availability at the surface (despite the onset point of hydrogen desorption at around the same temperature). Additionally, hydrogenation seems to depend on a certain hydrogen *species* (subsurface hydrogen), which can only be replenished in the presence of carbon at the surface (see above).
2. **Butene-Adsorption (reaction 6.3).** The adsorption-desorption equilibrium of the two configurational isomers may, of course, critically control the reaction rates at the surface; the experiments discussed in the previous paragraphs suggest that *cis*-2-butene might be more strongly adsorbed at the Pd-surface than *trans*-2-butene; we will use this property as our key hypothesis in the following discussion. As a

result of this lower adsorption energy, the desorption rate of *trans*-2-butene is expected to be noticeably faster as compared to *cis*-2-butene at any given temperature, so that *cis*-2-butene might reach higher surface-coverages in adsorption-desorption-reaction equilibrium.

- 3. Formation of the 2-Butyl-Intermediate (reaction 6.4).** The rate of this step depends on both the surface concentration of the molecular butene and the atomic deuterium species, and on the reaction probability between them. It is not known to the best of our knowledge whether this reaction probability is different for *cis*- and *trans*-2-butene; based on the observed identical conversion rates in both reaction pathways under certain conditions (*e.g.*, on a clean surface at elevated temperature, where reaction rates are presumably limited by 2-butyl formation due to a low deuterium-availability), however, we tentatively assume that the reaction rate constant for the formation of this intermediate is not different for the two isomers. Note, however, that the identical conversion rates observed under some conditions might also be due to an incidental compensation of different, complex effects (although this appears unlikely) – but the idea of identical formation rate constants of 2-butyl for the two 2-butene isomers is merely an assumption.
- 4.  $\beta$ -Hydrogen Abstraction (Formation of the Isomerization Product), reaction 6.5.** The effective reaction probability of this process may depend sensitively on the barriers that the rotating ethyl-group in the 2-butyl surface intermediate has to overcome before it can form the transition state for  $\beta$ -hydrogen abstraction (see the illustration in the introduction to this chapter for details); those barriers might be very different for the two isomers, and as a consequence, the isomerization rates of the two isomers may be different. Due to the large variety of possible adsorption geometries during the rotation and  $\beta$ -hydrogen-abstraction, however, the possible influence of such differences between the two isomers on the reaction rates appears to be very difficult to predict.
- 5. Half-Hydrogenation (Formation of the Hydrogenation Product), reaction 6.6.** This reaction depends very much on the availability of subsurface-deuterium, as previously described. Just as for  $\beta$ -hydrogen abstraction, it is not known if different reaction rate constants apply for the half-hydrogenation of the 2-butyl intermediates formed from the *cis*- or *trans*-isomer; we will leave those questions open for the moment and see later, whether this knowledge is needed.

**Evaluation of the Observed Selectivities.** Based on this discussion of the elementary steps of both reaction pathways, we will now try to examine which of those steps might be responsible for the different activity of *cis*- and *trans*-2-butene observed at the low temperature, the quenching of this selectivity at elevated temperature, and the new occurrence of this selectivity in the isomerization pathway at elevated temperature, when the reaction is conducted on a carbon-precovered model catalyst:

- **Reactivity at Low Temperatures.** At the low temperatures (195 to 210 K), both isomerization and hydrogenation proceed with higher rates with *cis*-2-butene as a reactant than with *trans*-2-butene; the possible reason for this observation has already been discussed in the intermittent consideration above, where it was said that under those conditions of short-lived reactivity, the reaction rates are not limited by the availability of deuterium at the very beginning of the experiment, because a lot of it is available after the deuterium-preadsorption before the first butene pulse. The fact that both reaction pathways exhibit similar selectivities (higher rates are observed with *cis*-2-butene in both pathways) may be understood as a good indication that the rate-limiting factor is the formation of the common 2-butyl surface intermediate; and because the availability of deuterium is high under those conditions, it appears very probable that the reaction rates are limited by the surface-coverages of the alkene, which seems to be higher for *cis*-2-butene – presumably because it has a higher stability on the surface, in agreement with the described adsorption experiments and discussions in literature.
- **Reactivity at Elevated Temperatures.** The experiments above approx. 240 K show high and sustained activity for the isomerization pathway on the clean catalyst; interestingly, both *cis*- and *trans*-2-butene isomerize with very similar rates under those conditions. Here, we do not have an ultimate explanation, but it can be quite safely concluded that the switch to an identical selectivity with both isomers must be due to a temperature-induced change in the rate-determining step; this rate-determining step seems to proceed with an equal probability for both starting reactants (the butenes). We assume that the higher stability of adsorbed *cis*-2-butene as compared to *trans*-2-butene is a general property that does not change with temperature, so that the equilibrium surface-coverage of *cis*-2-butene would always be higher than with *trans*-2-butene under identical temperatures and pressures. Based on this assumption, we conclude that the rate-determining step

in the experiments at elevated temperatures might exhibit a nearly zeroth formal order with respect to the olefin coverage. This situation might be achieved, for example, if the slowest step in the isomerization pathway was reaction 6.4, the first half-hydrogenation of the molecularly adsorbed species to the 2-butyl surface intermediate, when it proceeds – unlike the case at the low temperatures – under hydrogen-deficient conditions (as it is known to do at the elevated temperatures); as a consequence, its rate depends strongly on the availability of hydrogen now, and to a much lesser extent on the availability of molecularly adsorbed olefin, making the reaction rate nearly independent from the different adsorption-desorption equilibria of the two butene-isomers. Alternatively, the rate-determining step might also be the  $\beta$ -hydrogen abstraction step (reaction 6.5); however, it appears to be less probable that this reaction would exhibit a nearly zeroth-order dependence on the coverage of molecularly adsorbed olefin, although this possibility can not be ruled out based on the presented experiments.

- **Hydrogenation on Carbon-Precovered Samples at Elevated Temperature.** It was shown in the previous section that the hydrogenation reaction depends very critically on the presence of subsurface hydrogen; indeed, it does this so sensitively, that the reaction proceeds only on a carbon-precovered surface with sustained reactivity, which seems to be able to replenish this species much faster than the initially clean system (see section 6.3.3); thus, it appears reasonable to assume that the rate-limiting step in the hydrogenation reaction is reaction 6.6. It was discussed in the previous item that also the isomerization rates at elevated temperature on a clean catalyst are probably limited by the availability of hydrogen (which limits the formation rate of the alkyl-intermediate), so that it exhibits identical rates with both butene-isomers; in view of this interpretation, it appears understandable that the hydrogenation rate may also show identical rates with both *cis*- and *trans*-2-butene: for one, the reaction intermediate 2-butyl might form with nearly identical rates from both isomers (for the same reasons discussed in the previous item about the isomerization), and additionally, the hydrogenation rates for this intermediate are limited by the availability of subsurface-hydrogen. It is interesting to note that this dependence is different at the low temperatures on the initially clean sample (as discussed before), where the availability of the alkene limits all conversion rates; in view of this interpretation, it might be that the same explanation may also account for the different hydrogenation rates observed at the beginning of the butene pulses



at elevated temperature (in the maximum), because the availability of subsurface hydrogen is still high at this stage due to the hydrogen uptake in between the butene pulses, so that enough subsurface hydrogen seems to be available for a short time; the hydrogenation rates might then – again – be limited by the different surface-availabilities of the two butene isomers due to their different stabilities for a short time.

- **Different Isomerization Rates on the Carbon-Precovered Catalyst.** On a carbon-precovered model catalyst at elevated temperature, the isomerization rate with *trans*-2-butene drops significantly below its value on an initially clean catalyst - unlike the case with *cis*-2-butene (which exhibits similar rates on both clean and carbon-precovered systems). We do not have a satisfactory explanation for this observation; obviously, the presence of carbon shifts the reaction behaviour back to a situation where the reaction rates are controlled by an elementary step that exhibits different probabilities for the two isomers; one of the possible reasons is that the *trans*-isomer might be more strongly destabilized on a carbon-precovered system, whereby the adsorption-desorption equilibria would be shifted considerably more strongly for the *trans*-isomer than for the *cis*-isomer, so that the isomerization rate of the *trans*-isomer now critically depends on the alkene availability again (which it does not on an initially clean system). However, this explanation is not supported by any other experiment, and it is merely based on the previously discussed factors.

### Summary: *cis-trans*-Selectivity

Concluding, in this section we have discussed the possible origins of different conversion rates with *cis*- and *trans*-2-butene on the Pd/Fe<sub>3</sub>O<sub>4</sub> model catalyst, which were experimentally observed under certain reaction conditions (while under several other conditions the rates were similar). In all cases when such a selectivity was observed, *cis*-2-butene reaches higher reaction rates than *trans*-2-butene. The molecular origin of this selectivity were discussed based on a qualitative kinetic analysis of the isothermal experiments with the aim to possibly acquire a conclusive model. As a key hypothesis to explain the systematically higher reaction rates of the *cis*-isomer under certain conditions, we have suggested – based on a (somewhat tentative) evaluation of TPRS and IRAS experiments – that the *cis*-isomer might be more strongly adsorbed at the surface than the *trans*-isomer, so that it might reach higher surface-coverages under reaction conditions than the latter.

Specifically, we have observed higher conversion rates with the *cis*-isomer in the isothermal reaction rate measurements in all cases where the reaction

rates seem to be limited essentially by the availability of the reactant 2-butene, according to the kinetic analysis; in particular, this is the case at the low temperatures around 200 K in both conversion pathways, where hydrogen is easily available at the beginning of the experiment, so that the reaction rates are limited by the alkene coverage. At elevated temperatures around 250 K, isomerization and hydrogenation are more critically controlled by the availability of hydrogen (hydrogenation depends on the presence of a special hydrogen species), so that both isomers exhibit similar hydrogenation or isomerization rates under these conditions; however, this is not the case for the isomerization pathway on a *carbon-precovered* catalyst with *trans*-2-butene as a reactant, which shows significantly lower isomerization rates than on a clean catalyst (and than the *cis*-isomer); this is possibly due to a particularly strong destabilization of the adsorbed *trans*-isomer (presumably much stronger than with the *cis*-isomer) in the presence of carbon.

## 6.4 Summary

In this chapter, we have investigated the origin of selectivity during the conversion of 2-butene with deuterium on the Pd/Fe<sub>3</sub>O<sub>4</sub> model catalyst as a model reaction for catalytic hydrocarbon conversion. Generally, hydrocarbon conversion denotes the reaction of hydrocarbons with hydrogen; it is a central process in many industrial applications such as petrochemical hydrotreating in crude oil-refining, the partial hydrogenation of plant oils to edible fats, and also in some preparations of fine chemicals and pharmaceuticals. Many different possible reaction pathways exist in hydrocarbon conversion, including hydrogenation, isomerization, or hydrogenolysis; additionally, dehydrogenation reactions may also occur – even in the presence of hydrogen –, including dehydrocyclizations, aromatisations, or the decomposition to carbonaceous species (or, ultimately, to carbon). Selectivity in hydrocarbon conversion has been often ascribed to the presence of carbon as a modifier, which is typically present under realistic reaction conditions due to the rapid decomposition of hydrocarbons on many clean metal surfaces; however, a general understanding of the underlying mechanisms has not yet been achieved.

Three processes occur in the conversion of 2-butene with deuterium under the vacuum conditions used in this work: hydrogenation (*viz.*, deuteration) of the double-bond, isomerization<sup>12</sup> (which occurs as a consequence of an H/D-

---

<sup>12</sup>Isomerization might proceed both under migration of the double-bond (to form 1-butene) or under inversion of the *cis-trans*-configuration; arguments have been given in this text that the double-bond isomerization of 2-butene to 1-butene can be neglected

exchange of hydrogen atoms in the molecule) and stepwise dehydrogenation (decomposition) into carbonaceous species. Specifically, we have studied the origin of two types of selectivities in this work; the first part concentrates on the factors that are necessary to induce sustained hydrogenation rates (as an example for *chemoselectivity*) besides isomerization; the second part searches for the origins of the different reaction rates observed under certain reaction conditions in the conversion of *cis*- and *trans*-2-butene as reactants.

**Experiments on the Fe<sub>3</sub>O<sub>4</sub> film.** The bare Fe<sub>3</sub>O<sub>4</sub> iron oxide support was found to adsorb 2-butene molecularly, but it is chemically inert towards the hydrocarbon, and neither conversion reactions of butene (after additional dosage of deuterium) nor decompositions occur on the oxide. 2-butene desorption from the oxide takes place in two temperature-regimes after butene-exposure at 115 K: a strong adsorption mode gives rise to desorption signals at high temperature ( $\sim 300$  K at the lowest exposure that shifts to  $\sim 230$  K after multilayer exposure; it has a tail extending to  $\sim 400$  K), and a weak adsorption state due to adsorption in multilayers (desorption around 150 K).

Two adsorption modes for 2-butene could also be identified on the oxide in isothermal pulsed molecular beam experiments (at 200 K): a strong and – at the measurement temperature – irreversible state that populates first, at the beginning of the olefin uptake, and is characterized by a high sticking coefficient ( $2/3$ ); and, secondly, a weaker and reversible adsorption state that populates only under beam exposure and is characterized by a low sticking coefficient (butene adsorbs into this mode during beam exposure and desorbs again when the beam is switched off).

**Adsorption, Decomposition and Reactions on the Pd/Fe<sub>3</sub>O<sub>4</sub> Model Catalyst.** The Pd/Fe<sub>3</sub>O<sub>4</sub> model catalyst also adsorbs 2-butene; the desorption of 2-butene (adsorbed at 115 K) occurs in different temperature regimes: similar to the case on the pristine support, a feature for the desorption from multilayers appears around 150 K; a second butene desorption peak was found around 250 K (with a shoulder around 180 K). Unlike the experiments on the pristine support, we have found no molecular desorption at higher temperatures; instead, hydrogen from butene-decomposition desorbs with several peaks at higher temperatures than the last molecular desorption-peak – one peak around 330 (with a shoulder around 300 K), and a second peak around 380 K –, indicating a stepwise decomposition of the alkene; the first hydrogen-desorption feature (at 300 to 330 K) may be desorption-limited, because hydrogen adsorbed on a pristine Pd model catalyst desorbs

---

under the applied conditions.

also around 330 K; the peak at 380 K, however, is clearly reaction-limited. The observed decomposition behaviour of 2-butene on the model catalyst agrees well with reports in literature of the decomposition on Pt(111); those reports suggest that the first decomposition step dehydrogenates the adsorbate either to 2-butyne ( $\text{H}_3\text{C}-\text{C}\equiv\text{C}-\text{CH}_3$ ) [223, 224, 201, 190] or butylidyne ( $\equiv\text{CCH}_2\text{CH}_2\text{CH}_3$ ) [205]; the decomposition step around 380 K was described as the formation of a strongly dehydrogenated carbonaceous species with an estimate stoichiometry of  $\text{C}_4\text{H}_2$  [201] (based on integrated TPD signals).

In the presence of coadsorbed deuterium, the formation of conversion products could be observed on the Pd/Fe<sub>3</sub>O<sub>4</sub> model catalyst, including the hydrogenation products (butane-*d*2 and butane-*d*3), and isomerization products (for *cis*-2-butene as a reactant, those are *trans*-2-butene-*d*1 and *cis*-2-butene-*d*2); they desorb in two temperature regimes – the first around 200 K, the second around 250 K. Additionally, also dehydrogenation occurs, even in the presence of coadsorbed deuterium; hydrogen from decomposition desorbs at around the same temperatures as in the experiment without coadsorbed deuterium described above. Coadsorption of deuterium weakens the adsorption strength of butene; the main molecular desorption feature occurs around 180 K, whereas the peak around 250 K is strongly decreased.

Repeated TPRS experiments with coadsorbed 2-butene and deuterium on an initially clean model catalyst exhibit strong changes over the repetition cycles, which are due to the accumulation of carbon from decomposition (the TPRS peak temperature was 485 K); the deposited carbon limits the dehydrogenation rates in the later cycles, and increases molecular desorption of the reactant; additionally, it also changes to activity of the sample in the other conversion pathways, but unlike decomposition it does not lead to a strong deactivation, and sustained isomerization activity could be observed in the later TPRS cycles. Interestingly, IRAS surface titrations with CO as a surface-sensitive probe molecule indicate that this deposition of carbon affects preferentially the edge- and other irregular sites of the particles first, while the majority of the regular sites on the (111) facets stay nearly free of carbon for much longer.

In order to understand the reactivity of the system in more detail, isothermal pulsed molecular beam reaction rate measurements were conducted in addition to the TPRS experiments; those experiments show, unlike the TPRS experiments, that sustained hydrogenation may also be obtained on the model catalyst – and thus argue for the power of such isothermal experiments in the study of steady-state reactivity:

**Isothermal Experiments on the Pd/Fe<sub>3</sub>O<sub>4</sub> Model Catalyst.** The uptake of 2-butene on the Pd/Fe<sub>3</sub>O<sub>4</sub> model catalyst around 200 K exhibits two adsorption regimes, similar to the experiments on the pristine support: a strong, irreversible adsorption mode with a sticking coefficient of  $\sim 2/3$  that saturates first, and a weaker and reversible adsorption regime, onto which butene adsorbs during beam exposure, and from which it desorbs again when the beam is switched off. The strongly binding adsorption mode can be saturated faster at elevated temperature (around 250 K), which might be taken as an indication that also partly dehydrogenated butene derivatives may saturate the surface under those conditions, whose formation is due to a thermally activated step.

Conversion products can be detected only after the saturation of the strongly binding adsorption state; directly behind this induction period, the sample exhibits a high reactivity towards both *cis-trans*-isomerization and hydrogenation, because hydrogen is easily available in the system due to the saturation of the system with hydrogen prior to the first butene pulse in those experiments; at low temperatures (195 to 210 K), however, the rates decrease to zero quickly; this behaviour is likely a consequence of the strong inhibition of dissociative deuterium adsorption by the presence of bulky hydrocarbon species, which accumulate at the surface at such low temperatures.

When isothermal experiments are conducted at elevated temperatures (around 250 K), sustained catalytic activity towards *cis-trans*-isomerization is possible; this is, to the best of our knowledge, the first time that such a sustained catalytic behaviour in hydrocarbon conversion has been observed under vacuum conditions. This behaviour is most likely due to the increased rate of hydrocarbon desorption at the higher temperature, which reduces the surface coverage of butene under reaction conditions and thus allows for dissociative deuterium adsorption (in competition with butene adsorption) to occur again throughout the reaction, thereby supplying this critical coreactant; additionally, it was discussed that parts of the surface hydrocarbon species at the elevated temperature are partly dehydrogenated species, which might have a smaller footprint on the Pd surface, so that they might also leave more open surface area for deuterium dissociation.

However, the hydrogenation reaction – unlike isomerization – can not be sustained on the initially clean model catalyst, even at elevated temperatures. Remarkably, this changes when strongly dehydrogenated carbonaceous species are deposited on the model catalyst prior to the reaction experiments by a procedure identical to the TPRS experiments described above (2-butene and deuterium coadsorbed, and then annealed at 485 K). In the presence of such species, sustained hydrogenation *and* isomerization rates can be obtained on the model catalyst, and the isomerization and hydrogenation

rates are very similar; moreover, the isomerization rates on the initially clean model catalyst (as described in the previous paragraph) and on the carbon-precovered model system are also very similar, which may be taken as a further indication (in addition to the above described IRAS-surface titration experiments with CO) that the carbon-deposition does not significantly diminish the active Pd metal surface.

Possible origins for the sustainability of hydrogenation in the presence of such small amounts of carbon have been discussed, and it might be ascribed to one or a combination of the following factors: (*i*) different space requirements for the H-/D-exchange/isomerization and the hydrogenation competing reaction pathways, (*ii*) an electronic modification of the surface by the presence of subsurface carbon, and/or (*iii*) changes in the distribution of deuterium between weakly and strongly bound adsorption states, which may exhibit different activities in the hydrogenation pathway. In our discussion, we have indicated that the first two models do not appear to fully satisfactorily explain the observations. Additionally, it was discussed that later measurements by a cooperating group of hydrogen depth profiles during 2-butene-conversion under identical reaction conditions – which are not described in this work, but in a recent publication [241] – indicate that the facilitation of hydrogenation may indeed be ascribed to the presence of subsurface hydrogen, which seems to be more easily replenished in the presence of carbon; carbon might possibly simply facilitate subsurface migration of hydrogen.

**Selectivity in the Conversion of *cis*- and *trans*-2-Butene.** Finally, isothermal reaction rate measurements were conducted on the Pd/Fe<sub>3</sub>O<sub>4</sub> model catalyst both with *cis*- and *trans*-2-butene as reactants under all conditions described before; under certain reaction conditions, different reaction rates were observed with the two configurational isomers, while under other conditions, the rates were very similar (see the detailed discussion below) – but in all cases where a selectivity was observed, *cis*-2-butene reaches higher reaction rates than *trans*-2-butene. The molecular origins of this selectivity were discussed based on a qualitative kinetic analysis of the isothermal experiments. As a key hypothesis to explain the systematically higher reaction rates of the *cis*-isomer under certain conditions, we have suggested – based on an evaluation of TPRS experiments with the two adsorbed butene isomers (which exhibit different molecular desorption points of the two isomers) – that the *cis*-isomer might be more strongly adsorbed at the surface than the *trans*-isomer, so that it might reach higher surface-coverages under reaction conditions than the latter. This interpretation would be also in agreement

with the interpretation of IRAS experiments with the two 2-butene isomers, which show that the terminal methyl groups in *cis*-2-butene stand nearly upright on the surface, while they take up an intermediate inclination angle with *trans*-2-butene; this could be explained with the possibility of *cis*-2-butene to tilt the methyl groups away from the surface to reduce steric repulsion and stabilize – a possibility that the *trans*-isomer does not have.

Specifically, we have observed higher conversion rates with the *cis*-isomer in the isothermal reaction rate measurements in all cases where the reaction rates seem to be limited essentially by the availability of the reactant 2-butene; in particular, this is the case at the low temperatures around 200 K in both conversion pathways, where hydrogen is easily available at the beginning of the experiment, so that the reaction rates are limited by the alkene coverage. At elevated temperatures around 250 K, isomerization and hydrogenation are more critically controlled by the availability of hydrogen (hydrogenation depends on the presence of a special hydrogen species), so that it may be understood that both isomers exhibit similar hydrogenation or isomerization rates under those conditions; however, this is not the case for the isomerization on a *carbon-precovered* catalyst with *trans*-2-butene as a reactant, which shows much lower isomerization rates than on a clean catalyst (and than the *cis*-isomer); this is possibly due to a particularly strong destabilization of the adsorbed *trans*-isomer in the presence of carbon.





# Chapter 7

## Summary

One of the central objectives in catalysis – and in chemistry in general – is the ability to guide reactants through the network of possible reaction pathways, and selectively promote the formation of a target product while limiting the yield of undesired products; this ability is commonly termed *selectivity*. A prerequisite for the deliberate achievement of selectivity is to obtain a detailed knowledge about the mechanism of the reactions that can occur. In catalysis, selectivity is thought to be governed by the catalyst's structure, *i.e.*, by the correlation between the geometric and electronic structure of the catalyst and the surface processes that occur on this template between the adsorbed reactants, products and side products; those structural parameters may include the chemical identities of the catalyst components (typically metal nanoparticles supported on an oxide support), their oxidation state, the size distribution and morphology of the metal particles, and the characters and densities of defect sites, modifiers and promoters.

However, despite its enormous significance for economic wealth, such a detailed, maybe even general understanding of catalysis that would allow to design new catalysts based on theoretical insight, has not yet been reached; this is mainly due to the structural complexity of practical catalyst materials. In order to overcome this experimental challenge, a combined approach between reactivity and structural elucidations on the highly complex real catalysts, and detailed structure-reactivity studies on simplified systems – often simply single crystals – at *microscopic* level (known as the *surface science approach*) is taken today; in order to understand catalysis based on this combined approach, it is necessary to bridge the *complexity-gap* between the two sides of the approach.

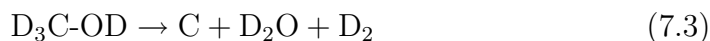
As one approach to bridge this *complexity-gap*, the *model catalyst approach* has recently been put forward; model catalysts typically consist of thin, epitaxially grown oxide films on single crystal surfaces, which then

act as the support for the deposition of metal (or sometimes metal oxide) nanoparticles. Model catalysts mimic considerably more of the structural complexity of real catalysts than single-crystals, but they are structurally well-defined and – unlike many practical catalysts – can be characterized by the surface-science standard techniques, including scanning-probe methods (STM and AFM), electron diffraction (LEED) and photoelectron spectroscopies (XPS and UPS).

For the current work, we have chosen to study the origin of selectivity in two model reactions – the decomposition of methanol and the conversion of 2-butene with deuterium – on a Pd/Fe<sub>3</sub>O<sub>4</sub>(111)/Pt(111) *model catalyst*. This model catalyst has been previously characterized in detail with respect to its structure, stability and oxidation behaviour; in this work, we have shown that an oxidation of this catalyst is able to remove carbonaceous decomposition products of the reactants methanol and 2-butene from the surface. The reactions were studied in *molecular beam* experiments by a combination of mass spectrometric rate measurements and infrared-spectroscopic detection of adsorbates.

## 7.1 Methanol Decomposition

The decomposition of methanol is one of the most-studied surface reactions in catalysis. It has practical significance for the industrial production of formaldehyde, or the reactions in direct methanol fuel cells (DMFCs); additionally, it is related (as the reverse reaction) to methanol formation from *synthesis gas* (CO + hydrogen). Methanol decomposition may yield many different products on oxides and metals (a literature overview has been provided in this work as an introduction to chapter 5); the main products observed in this work are formaldehyde, CO and carbon:



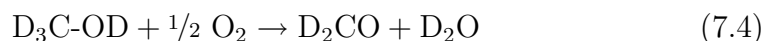
(deuterated methanol was applied in this work). Reaction 7.1 describes the formation of formaldehyde, reaction 7.2 of CO, and reaction 7.3 of carbon (plus side products).

**Methanol Decomposition on Fe<sub>3</sub>O<sub>4</sub>.** We have found that methanol and its dissociation product methoxy accumulate simultaneously on the pristine

Fe<sub>3</sub>O<sub>4</sub>(111) oxide film during exposure at 115 K; the second dissociation product, hydrogen, is accommodated on the lattice-oxygen in the form of surface-hydroxyl groups. After thermal activation during TPRS experiments, some of those hydroxyl-groups disproportionate into surface-oxygen and water, which desorbs from the surface at around 260 K, leading to a depletion of surface-oxygen from the oxide. We argue that – as a consequence of this desorption of hydroxyl-groups –, some of the surface-methoxy groups do not find a hydroxyl-group to recombine into molecular methanol, and thus are forced to remain at the surface until an alternative decomposition pathway gets activated; this occurs only at very high temperatures (around 555 K), where the remaining surface-methoxy species disproportionate into formaldehyde and methanol, which desorb immediately from the surface after their formation and give rise to a simultaneous methanol- and formaldehyde desorption signal.

It was shown by isotope labeling-experiments that the reaction proceeds under participation of surface-oxygen, which is being consumed by the formation of water and was not reestablished during our experiments; thus, the formaldehyde yield was observed to decrease in the later TPRS cycles; it was speculated, based on several experimental observations, that the reaction might be due to a certain oxygen species, which might form certain, very labile surface hydroxyl groups. Further results from a cooperating group on methanol decomposition on the same oxide indicate that the reactivity towards formaldehyde formation can be sustained when the sample is reoxidized in between the reaction cycles; based on this discussion, it might be possible that sustained, steady-state formaldehyde yield could be achieved with a reactant-mixture of methanol and oxygen.

In summary, the formation of formaldehyde may be described as a reaction of adsorbed methanol with lattice- (surface)-oxygen from the oxide (*Mars-van-Krevelen* mechanism), and the overall reaction may best be expressed as an oxidative dehydrogenation:



**Methanol Decomposition on Pd/Fe<sub>3</sub>O<sub>4</sub>.** In the presence of Pd nanoparticles on the oxide, the final product of methanol decomposition changes, and no formaldehyde formation is observed anymore; instead, CO and carbon are the main products:

We have observed that the adsorption behaviour of methanol on the model catalyst at 115 K is similar to the one on the pristine support, and that molecularly adsorbed methanol and methoxy both accumulate simultaneously; however, all of the methoxy species disappear from IRAS spectra at

much lower temperatures (between 300 and 510 K) than on the pristine support, where those species exhibit a high thermal stability up to the point where formaldehyde is formed (around 555 K). On the model catalyst, Pd-bound CO appears instead as a decomposition product in the IRAS spectra (at and above  $\sim 200$  K) and desorbs around 475 K. The difference between the experiments on the pristine support and the model catalyst might appear to be remarkable, since a fraction of 70 % of the oxide's surface area is also exposed in the Pd/Fe<sub>3</sub>O<sub>4</sub> model system, so that formaldehyde-formation from methanol adsorbed on the oxide might also be expected on this system; this lack of high-temperature methoxy species and formaldehyde as a decomposition product was explained by a rapid support-particle diffusion of all support-related methanol and methoxy species before formaldehyde could be formed on the oxide; instead, those species decompose on the Pd surfaces. Arguments have been given which indicate that the oxide might still be capable to form formaldehyde, even in the presence of the deposited Pd nanoparticles (and that the lack of formaldehyde formation is not simply due to a possible preferential nucleation of the Pd particles on certain surface sites on the Fe<sub>3</sub>O<sub>4</sub> that might be particularly reactive towards formaldehyde formation): on a *partially oxidized* model catalyst, where the metallic Pd surface area is reduced by more than 50 % due to Pd surface oxidation, the support-related high-temperature methoxy species (which were brought in connection with the formation of formaldehyde) could also be spectroscopically observed up to a temperature between 510 and 600 K, presumably because support-particles diffusion of methoxy is inhibited due to the partial surface-oxidation of the Pd particles. This might be taken as an indication that formaldehyde formation on the support in the model catalyst might also be possible, if the support-related methoxy species did not preferentially diffuse onto the Pd particles before formaldehyde formation on the oxide could get activated.

Repeated TPRS experiments with methanol on the model catalyst indicate that the reactivity of the system towards CO formation decreases with every repetition cycle (peak temperature: 600 K); based on earlier experiments on methanol decomposition on Pd/Al<sub>2</sub>O<sub>3</sub>, this could be ascribed to the slow accumulation of carbonaceous species or carbon at the Pd surfaces of the model catalyst, which are formed by methanolic C-O-bond scission [159].

Kinetic measurements of the CO- and carbon formation rates have been conducted on the model catalyst; reference values (obtained in the same setup under identical conditions) exist for the Pd/Al<sub>2</sub>O<sub>3</sub> model catalyst [159]; the Pd particles in both supported model catalysts show a very similar morphology in STM, but unlike the iron oxide, the alumina support is not capable to

dissociate methanol to methoxy, and also molecularly adsorbed methanol is known to desorb at significantly lower temperatures from alumina than  $\text{Fe}_3\text{O}_4$  (190 K *vs.* 300 K). In our experiments, we have observed that the accumulation of carbon proceeds with significantly higher rates (approx. twice as fast) on the  $\text{Fe}_3\text{O}_4$ -supported Pd particles than the ones on alumina, whereas CO-formation (which exhibits more than 100 times higher rates than carbon formation) proceeds with similar rates on the two model catalysts. This observation was discussed in terms of two possible models: 1) it was argued that support-particle diffusion of methanol and methoxy – which may proceed on the  $\text{Fe}_3\text{O}_4$ -supported system, but not from alumina – may lead to an increased reactant flux to the  $\text{Fe}_3\text{O}_4$ -supported particles; the rates in the slow carbon formation pathway might be limited by the availability of the reactant, while the rates in CO formation might be so high, that they are effectively limited by the availability of free surface sites (which, in turn, is presumably limited by CO-desorption). 2) Alternatively, the different carbon-formation rates on the two model catalysts might be due to different densities of irregular sites on the two Pd particles, which have previously been described to be particularly active in C-O-bond scission [138]; the CO-formation reaction on the other hand was described to not exhibit such a structure sensitivity.

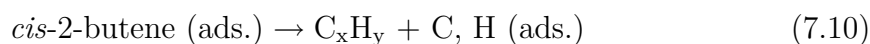
Both models may satisfactorily explain the observations; based on the experiments discussed above, which indicate that support-particle diffusion may indeed occur on the  $\text{Fe}_3\text{O}_4$ -supported system, we believe that this effect certainly contributes at least in parts to the observed differences; the possibility of different defect densities on the Pd particles in the two model catalysts is more complicated to estimate, and a further clarification can not be supplied here.

## 7.2 Conversion of 2-Butene with Deuterium

In our second project, we have concentrated on 2-butene conversion with deuterium as a model reaction for hydrocarbon conversions. Hydrocarbon conversions are an important element in many industrial processes, including petrochemical hydrotreating in crude oil-refining, or the partial hydrogenation of vegetable oils to storeable, edible fats. Many possible conversion pathways can contribute to hydrocarbon conversion (see the introduction in chapter 6), and it is highly desirable for applications to understand which factors may control the selectivities between those possible pathways. One modifier that has been frequently discussed to play a key role for the chemoselectivity in hydrocarbon conversion is carbon [26], which is typically present during catalytic hydrocarbon conversion due to the rapid decomposition of

hydrocarbons on many metal surfaces in catalysts; still, an understanding of the underlying mechanisms has not yet been achieved.

The following reactions and steps have to be considered under vacuum conditions for the model reaction discussed in this work, the conversion of 2-butene with deuterium:



Reaction 7.5 represents dissociative deuterium-adsorption, and 7.6 the adsorption-desorption equilibrium of 2-butene. The following surface-reactions are accounted for by the Horiuti-Polanyi mechanism, which assumes that both reaction pathways – hydrogenation and H-/D-exchange (which is accompanied by *cis-trans*-isomerization) – proceed *via* the same surface intermediate 2-butyl-*d1*, which is formed by the initial half-hydrogenation 7.7. Isomerization occurs from this intermediate by  $\beta$ -H-abstraction (reaction 7.8), and hydrogenation by insertion of a second deuterium atom into the butyl-surface bond (reaction 7.9). Additionally, 2-butene may also decompose on Pd metal, forming sequentially different hydrocarbon species (reaction 7.10). In this work, we have studied the influence of carbonaceous deposits on the conversion selectivity; additionally, we compare the conversion rates with *cis*- and *trans*-2-butene as reactants:

**Experiments on the Fe<sub>3</sub>O<sub>4</sub> film.** The pristine Fe<sub>3</sub>O<sub>4</sub> support was found to be chemically inert towards 2-butene, and although the molecule adsorbs on this material, it desorbs molecularly (around 300 K at the lowest exposures), without any indication of decomposition steps; no conversion reactions occur after additional dosage of deuterium as a coreactant (prior to alkene adsorption), even in large excess. Nevertheless, the adsorption bond on the support is relatively strong (as indicated by the high desorption point), so that the support might contribute to the reactant flux to the Pd particles.

**Experiments on the Pd/Fe<sub>3</sub>O<sub>4</sub> Model Catalyst.** The Pd/Fe<sub>3</sub>O<sub>4</sub> model catalyst, however, was found to be active in all three reaction pathways – isomerization, hydrogenation and decomposition –, as evidenced *e.g.* by

TPRS experiments between coadsorbed deuterium and 2-butene. The hydrogen desorption from 2-butene decomposition occurs stepwise; the first peak was observed around 330 K (with a shoulder around 300 K and an onset at  $\sim 250$  K), and a second around at 380 K, but no higher decomposition steps could be observed during the usual annealing step (485 K). Based on references on butene-decomposition on Pt(111), the first decomposition step might be associated with the formation of butylidyne ( $\equiv\text{C}-\text{CH}_2-\text{CH}_2-\text{CH}_3$ ) [205] or 2-butyne ( $\text{H}_3\text{C}-\text{C}\equiv\text{C}-\text{CH}_3$ ) [223, 224, 201, 190], and the second step ( $\sim 380$  K) with formation of a strongly dehydrogenated species (*carbon*) with an estimate stoichiometry of  $\text{C}_4\text{H}_2$  [201].

Repeated TPRS experiments (peak temperature: 485 K) with coadsorbed deuterium and 2-butene without any intermediate cleaning treatment between the cycles show that the hydrogenation and decomposition activity of the system collapses rapidly in only a few cycles, whereas the activity in the isomerization reaction was reduced in the second cycle, but then stays essentially unchanged at this lower level throughout the later cycles. IRAS surface titration experiments with CO as a probe molecule indicate that the carbon deposited in one such TPRS cycle accumulates preferentially on irregular sites (such as edges), while the regular (111) facets with the majority of sites stay nearly clean of carbon. Thus, the experiments suggest that even the presence of little amounts of carbon might strongly influence the activity and selectivity of the system.

In order to further study the reactivity of the system under different conditions, the following isothermal molecular beam reaction rate measurements were conducted:

**Chemoselectivity.** Under all studied reaction conditions, products from the conversion pathways desorb only after an induction period, during which strongly adsorbed hydrocarbon species seem to accumulate at the surface that do not participate in conversions.

On an initially clean model catalyst at low temperatures (around 200 K), high reaction rates in both conversion pathways (hydrogenation and isomerization) can be observed for a limited time directly after the induction period, but the rates decrease to zero rapidly; since the first butene exposure pulse in those experiments was only admitted after an initial deuterium-saturation phase, the availability of deuterium is high at the beginning, and may account for the initially high rates; however, the fast accumulation of spaceous hydrocarbon species at the surface at this low temperature is believed to strongly inhibit dissociative deuterium adsorption, thereby rapidly eliminating the conversion rates.

Interestingly, this situation changes at elevated temperatures (250 K), where sustained isomerization can be observed; this possibility was explained by two factors: for one, the increased temperature leads to an increased hydrocarbon-desorption rate, thereby reducing its surface coverage and its inhibiting effect towards dissociative deuterium adsorption, resulting in increased hydrogen supply. Additionally, the hydrocarbon species might have an overall smaller footprint on the surface at elevated temperature due to the onset of decomposition, thereby leaving a larger surface area for D<sub>2</sub>-dissociation.

However, hydrogenation does not proceed with sustained rates on an initially clean model catalyst, not even at 250 K. Interestingly, however, this changes when carbon has been deposited on the surface prior to the experiment; under those conditions, not only sustained isomerization, but also sustained hydrogenation can be obtained (both with similar rates as isomerization on the initially clean system). This important observation was discussed based on three possible models; we have indicated that both the possibly different sizes of the metal site ensembles required by the different pathways, and also a possible influence of subsurface carbon may not satisfactorily explain all our observations; instead, we suggest that the induction of hydrogenation may best be explained by the influence of subsurface hydrogen, whose formation under reaction conditions seems to be facilitated in the presence of carbon. Direct measurements of hydrogen depth profiles under reaction conditions by a second group indeed show that significantly more subsurface hydrogen may be present on carbon-covered surfaces [241].

**Selectivities in Conversion of *cis*- and *trans*-2-Butene.** Finally, we have discussed experiments with both *cis*- and *trans*-2-butene on the model catalyst under all of the above discussed reaction conditions; under certain conditions, *cis*-2-butene exhibited higher conversion rates than *trans*-2-butene, whereas under all other conditions, the rates were very similar. The molecular origin of this selectivity was discussed based on a qualitative kinetic analysis of the rate-determining steps; as a key hypothesis to explain the systematically higher reaction rates of the *cis*-isomer under certain conditions, we have suggested – based on a tentative evaluation of adsorption experiments – that the *cis*-isomer might be more strongly adsorbed at the surface, so that it might reach higher surface-coverages under reaction conditions; we argue that, whenever the alkene-coverage is rate-limiting, *cis*-2-butene might then reach higher conversion rates.



## 7.3 Conclusions

In this work, the origin of selectivity in two catalytic model reactions – the decomposition of methanol and the conversion of 2-butene with deuterium – was studied under many different reaction conditions, using a combination of surface-sensitive detection techniques and molecular beam methods for controlled gas exposure under ultra-high vacuum; in both cases, the well-defined Pd/Fe<sub>3</sub>O<sub>4</sub>(111)/Pt(111) system was applied as a supported model catalyst.

Both model reactions may proceed *via* different pathways and under formation of different products. For the case of methanol decomposition, which proceeds both on the pristine support Fe<sub>3</sub>O<sub>4</sub> as well as the Pd nanoparticles, it was demonstrated that different decomposition products are formed on the two components: formaldehyde is formed with high selectivity on the pristine support, and carbon monoxide is the main product on the Pd nanoparticles. In the case of the model catalyst, the support-related methoxy species – which are the central reaction intermediate of methanol decomposition – diffuse from the support onto the Pd nanoparticles, where they are rapidly decomposed into CO; as a consequence, no formaldehyde formation could be observed on the model catalyst. Based on additional kinetic experiments, it was demonstrated that this support-particle diffusion of methoxy (and also of molecular methanol) may significantly increase the reactant flux to the Pd nanoparticles in addition to direct reactant adsorption from the gas phase, and thereby it may have an influence on the overall reaction rates on the catalyst. In this sense, the experiments described in this work constitute one example of the chemical function that a catalyst support may have in addition to its original purpose (to prevent the metal nanoparticles (the active phase) from sintering).

Conversion of 2-butene with deuterium proceeds only on the Pd surfaces of the model catalyst. In this work, it was demonstrated for the first time that sustained hydrocarbon conversion rates can be obtained under vacuum conditions. Moreover, it was possible to show based on isothermal molecular beam reaction rate measurements, that the presence of previously deposited, strongly dehydrogenated carbonaceous species is the critical factor to obtain sustained hydrogenation at the model catalyst under vacuum conditions – whereas the alternative reaction pathway, hydrogen-exchange, proceeds with sustained rates even on an initially clean catalyst surface. Interestingly, very little amounts of those strongly dehydrogenated carbonaceous species on the metal surface are sufficient to selectively induce hydrogenation; possible explanations for this selective induction of hydrogenation in the presence of carbon at the surface have been discussed. Additionally, the kinetic evaluation of the experiments yielded a detailed model of the possible rate-limiting

factors under the different reaction conditions; this model could then be applied to suggest a conclusive explanation why higher conversion rates have been observed with *cis*-2-butene as reactant as compared to *trans*-2-butene under certain reaction conditions, and why the rates under different conditions were sometimes identical.

# Appendix A

## Experimental Procedures

### A.1 Preparation of the Model Catalyst

This section describes the sample preparation in a level of detail sufficient to allow a repetition of the experiments. All metal depositions by PVD were effected using conventional electron beam metal evaporators (Omicron Focus EFM3) as described in chapter 3.1. The Pd evaporator was routinely calibrated using a quartz microbalance (Caburn MDC); the Fe evaporator was calibrated directly following the completion of the FeO-monolayer by IRAS of adsorbed carbon monoxide, which adsorbs on the preparation substrate Pt(111), but not on FeO. Gas exposures during preparation were performed by chamber backfilling, and the pressure measured by a Bayard-Alpert type ionization gauge (Arun Microelectronics Ltd., AML). Gas exposures during stabilization or cleaning procedures were effected using the effusive beams.

#### A.1.1 Preparation of the Pt(111) Single Crystal

All preparation steps of the single crystal described in this section were conducted by specialized service personnel in the crystal lab at the Fritz-Haber institute:

The standard substrate used in these experiments is a Pt(111) single crystal of 10 x 11 x 2 mm dimensions cut by sparc erosion from a bigger rod (MaTecK GmbH, Jülich, Pt, > 99.99 % purity), which was carefully aligned to the (111) direction using *Laue* back reflection. The raw cut crystal was treated by grinding and etching in *aqua regia*, and then further flattened by repeated grinding and polishing with SiC discs and diamond pastes of decreasing grain sizes until the crystallographic orientation was fine-corrected and the Laue X-ray diffraction from the obtained crystal plate showed clear spots.

### A.1.2 Cleaning of the Pt(111) Single Crystal

The Pt(111) single crystal mounted on the sample holder was cleaned by the following standard procedure [245]: First, the crystal was annealed for 15 minutes in UHV at  $\sim 1300$  K to vaporize oxide films that had been deposited on the crystal in earlier preparation cycles. The crystal was then slowly cooled to room temperature and sputtered twice under bombardment with fast Ar ions (typically: 1.5 keV,  $\sim 5 \mu\text{A}$  ion current) for 30 min. with one annealing (3 min. at  $\sim 1300$  K) and cooling step between the two sputtering cycles. Carbon deposits that might have segregated onto the surface during this treatment were removed by an oxidation treatment in oxygen atmosphere (720 K,  $1 \times 10^{-6}$  mbar  $\text{O}_2$ ). Finally, the sample was annealed again (3 min.,  $\sim 1300$  K). New crystals prepared by the method described in section A.1.1 were repeatedly subjected to this procedure ( $\sim 5 - 10$  cycles), until the IRAS of adsorbed CO resembled reference spectra.

### A.1.3 Preparation of the Iron Oxides FeO and $\text{Fe}_3\text{O}_4$

The preparation of iron oxides on the clean Pt(111) single crystal follows a procedure studied in detail by Weiss and coworkers [90] and described succinctly by Lemire *et al.* in [92]. According to this procedure, first the iron oxide FeO (*wüstite*) is grown on the clean Pt single crystal. The higher-oxidized iron oxide  $\text{Fe}_3\text{O}_4$  (*magnetite*) starts to grow on the FeO film when additional iron is deposited on this first layer and oxidized (*Stranski-Krastanov growth mode*):

1. FeO preparation: deposit 1 ML of Fe by PVD at room temperature (sample biased to the potential of the evaporator rod, 800 V; deposition rate  $\sim 1$  ML/min.); heat up and oxidation in oxygen atmosphere ( $p_{\text{O}_2} = 1.0 \times 10^{-6}$  mbar) at 1000 K (2 min.). Oxygen pumped off at  $\sim 500$  K during cooling.
2. After FeO characterization: quick annealing in UHV at 600 K.
3.  $\text{Fe}_3\text{O}_4$  preparation. 6 cycles of:
  - Deposit  $\sim 4$  ML of Fe by PVD at temperature below 125 K (sample biased to the potential of the evaporator rod, 800 V; deposition rate  $\sim 1$  ML/min.).
  - Heat up and oxidation in oxygen atmosphere ( $p_{\text{O}_2} = 1.0 \times 10^{-6}$  mbar) at 875 K (5 min.). Oxygen pumped off at  $\sim 500$  K.
4. Quick annealing in UHV at 800 K.

The  $\text{Fe}_3\text{O}_4$  film can be annealed in UHV at temperatures of 800 K.

### A.1.4 Preparation of Pd Nanoparticles

The preparation of Pd nanoparticles of different sizes has been studied in detail in our group in an earlier work [103]. Nanoparticles of approximately 7 nm diameter have been exclusively applied for this thesis. Our group has previously shown that Pd deposited on the Fe<sub>3</sub>O<sub>4</sub> thin film aggregates in nanoparticles on deposition and subsequent annealing at 600 K [59]. We have shown in the same paper, that the particles restructure under a certain treatment with oxygen and carbon monoxide at 500 K, until they have reached an equilibrium shape; this treatment is referred-to as *stabilization*. The same treatment can be used to burn carbon deposits that have accumulated on the surface during experiments with organic reactants (*e.g.* 2-butene or methanol); such a treatment will not alter the equilibrium structure after stabilization. The following lines summarize the procedure:

Before Pd deposition, the Fe<sub>3</sub>O<sub>4</sub> thin film was briefly annealed at 800 K in UHV to evaporize adsorbates (mainly water). Then  $\sim 4$  Å Pd was deposited by PVD at 115 K from a calibrated evaporator (sample biased to the potential of the evaporator rod, 800 V; deposition rate  $\sim 0.4$  Å/min.). The sample was annealed at 600 K for 1 min.

The stabilization was effected by at least five cycles of:

- 1000 s oxidation in oxygen atmosphere ( $p_{\text{O}_2} = 8 \times 10^{-7}$  mbar) at 500 K.
- 3000 s reduction in carbon monoxide atmosphere ( $p_{\text{CO}} = 8 \times 10^{-7}$  mbar) at 500 K.

Typically, one cycle of this treatment is enough to remove carbon deposits from the surface.

### A.1.5 Oxidation of the Model Catalyst for Experiments

For experiments on the oxidized model system, it was oxidized directly before the experiments according to the following procedure: first, the model catalyst was oxidized by an exposure to oxygen ( $p_{\text{O}_2} = 8 \times 10^{-7}$  mbar) at 550 K for 1000 s (650 L); subsequently, it was quickly cooled down in oxygen to  $\sim 505$  K and shortly exposed to CO ( $p_{\text{CO}} = 4 \times 10^{-6}$  mbar) for approx. 8 s (5.2 L) at  $\sim 500$  K to remove chemisorbed surface-oxygen. The system was then cooled down to the adsorption temperature (115 K) in UHV. Such a system was found by IRAS Pd-surface titration experiments using CO as probe molecule to have lost approx. 60 % of its integrated spectral CO intensity [101]; this value can be taken as a measure for the surface loss due to surface oxidation [105, 104].

## A.2 Chemicals: Handling and Beam Formation.

### A.2.1 Purities and Suppliers of Chemicals

The tables A.1, A.2 and A.3 summarize the applied batches of metals, liquids and gases.

Table A.1: Metals used for physical vapour deposition (PVD).

metal	form	supplier	purity (as stated by supplier)
Iron (Fe)	wire	Goodfellow	> 99.99 %
Palladium (Pd)	wire	Goodfellow	> 99.99 %

Table A.2: Liquid chemicals applied in the experiments.

substance	supplier (manufacturer)	purity (as stated by supplier)
isotopically normal methanol (CH <sub>3</sub> OH)	Merck KGaA	> 99.9 % ( <i>Uvasol</i> ), < 0.02 % water
fully deuterated methanol CD <sub>3</sub> OD	Merck KGaA	<i>Uvasol</i> , min. 99.8 % deuterium, < 0.002 % water
methanol-13C ( <sup>13</sup> CH <sub>3</sub> OH)	EURISO-TOP (Cambridge Isotope Laboratories)	min. 99 % C-13, < 0.02 % water

### A.2.2 Handling and Storage of Chemicals

The metals were used as supplied in the metal rod electron beam evaporators. Gases were used as supplied and fed into the measurement setup either *via* the molecular beams or into the preparation chamber using the sputter gun valve (*backfilling*). To ensure the purity of the gases, the gas lines of the gas inlet system were in all cases pumped below a pressure of  $2.0 \times 10^{-2}$  mbar before admitting the gas. The gas inlet system was checked to be leak-tight, and the measurement gas pressures in the gas inlet system were set

Table A.3: Gaseous chemicals applied in the experiments.

gas	supplier (manufacturer)	purity (as stated by supplier)
hydrogen (H <sub>2</sub> )	Linde	6.0 (99.9999 %)
deuterium (D <sub>2</sub> )	Campro (Isotec)	4.5 (99.995 %), min. 99.8 % deuterium, below 14 ppm water and 4 ppm hydrocarbons
carbon monoxide (CO)	Linde	4.7 (99.997 %)
oxygen (O <sub>2</sub> )	Linde	5.0 (99.999 %)
<i>cis</i> -2-butene	Aldrich	> 99 %
<i>trans</i> -2-butene	Aldrich	> 99 %

above atmospheric pressure to minimize gas leakage into the gas inlet system, except for the methanol experiments (*vide infra*). Carbon monoxide (CO) was purified from volatile carbonyl complexes (mainly Ni(CO)<sub>4</sub>) by means of a gas filter behind the reduction valve (Mykrolis).

Liquids were stored in glass flasks attached to the gas inlet system, and had to be freed from the gases over the liquids (mainly air from the filling procedure or leakages). The typical cleaning procedure for all methanol isotopomers was a threefold repetition of the following cool-pump-warm-cycle: the liquid methanol was cooled to approximately -100 °C, *i.e.* slightly above its melting point (to avoid freezing). The gas over the cold methanol was pumped-off to a pressure below  $2.5 \times 10^{-2}$  mbar. Then the gas was warmed again to allow equilibration between gases solved in the liquid and the gas phase over the liquid.

### A.2.3 Beam Formation with Organic Reactants

The purified methanol was directly applied for the formation of effusive beams. The vapor pressure over methanol at room temperature (295 K) is  $\sim 140$  mbar [246]. Methanol was fed at this pressure into the pressure regulation system of the effusive beams; the beam intensity was regulated setting the pressure behind the expansion stage. For application in the supersonic beam, the total pressure behind the nozzle had to be set to  $\sim 1.1$  bar.

To ensure this value, a stream of argon as a carrier gas was saturated with methanol in a closed, temperate saturation setup, and a stable supersonic beam was produced from this mixture by fine-adjustment of the pressure ( $\sim 1.1$  bar). This results in a fraction of  $\sim 13$  % (pressure-ratio) of methanol in the mixture. The supersonic beam with methanol was applied without the chopper. Intensities calculated for the supersonic beam were directly calculated from the beam intensities of an argon supersonic beam and the partial-pressure-ratio of methanol of 13 %.

*cis*- and *trans*-2-butene both are liquefied gases with boiling points below room temperature. Thus, they could be directly fed into the supersonic beam using a special reduction valve for the application of liquefied gases (Linde). The supersonic beam with the 2-butenes was operated with the chopper set to 3.3 % duty cycle. The beam intensity was measured using the reference method described in chapter 3.2.1. It was established that for the precise calculation of the beam intensity, the sensitivity of the ionization gauge for 2-butene had to be taken into account; ionization gauges of the Bayard-Alpert type were found by Nakao [247] to be 3.60 times more sensitive to 2-butene than to the reference gas  $N_2$ ; this critical value was later confirmed by Dannetun *et al.* [248], and formula for the calculation of the ionization cross section from the number of electrons in organic molecules [249] [250] come to comparable results. The value of 3.6 was applied for this thesis to calculate the beam intensity with 2-butene.

The following tables state the intensities of molecular beams used in this thesis in different units.

### A.3 Data Correction

The QMS-data in the kinetic experiments had to be corrected for the contribution of molecule cracking on electron impact and decomposition of molecules on the hot filament in the QMS ion source, and additionally for the contribution of natural isotopomers (esp. C-13 isotopomers of 2-butene). The contribution of cracking depends mainly on the ionization energy; values can be estimated from signal intensities on different masses in reference mass spectra taken at 70 eV (the same ionization energy was used for all QMS spectra in this work). Some masses, however, have to be corrected further, due to the cracking on the hot filament of the QMS ionizer (the specific construction of the ion source has big impact on this contribution and complicates

---

<sup>1</sup>Exposure before IRAS flash series. The exposures in the coverage series were done with only a tenth of this intensity to allow for a better control over the coverage.

<sup>2</sup>Not calibrated; assuming identical intensity as with oxygen (diatomic gas).



Table A.4: Effusive beam intensities.

gas	application	intensity /		
		(molecules/ cm <sup>2</sup> ·s)	(10 <sup>-6</sup> mbar)	(L/s)
argon	calibration	2.1 x 10 <sup>14</sup>	0.86	0.65
CO	stabilization & cleaning	2.5 x 10 <sup>14</sup>		
oxygen		2.3 x 10 <sup>14</sup>		
methanol- <i>d</i> <sub>4</sub>	exposure <sup>1</sup>	2.2 x 10 <sup>14</sup>		
methanol	kinetic experiments	5.6 x 10 <sup>14</sup>	2.1	1.5
methanol- <i>d</i> <sub>4</sub>			2.2	1.6
methanol-C13			2.2	1.6
deuterium	kinetic experiments	3.3 x 10 <sup>15</sup>	4.3	3.2
hydrogen			3.0	2.3

Table A.5: Supersonic beam intensities.

gas	application	intensity /		
		(molecules/ cm <sup>2</sup> ·s)	(10 <sup>-6</sup> mbar)	(L/s)
argon	calibration	1.1 x 10 <sup>15</sup>	4.5	3.4
hydrogen	exposure for TPRS <sup>2</sup>	≈ 4.6 x 10 <sup>14</sup>	≈ 0.42	≈ 0.32
methanol- <i>d</i> <sub>4</sub>	exposure for TPRS	1.4 x 10 <sup>14</sup>	0.55	0.41
2-butene ( <i>cis</i> & <i>trans</i> )	kinetic experiments	5.6 x 10 <sup>12</sup>	0.027	0.021

obtaining correction parameters from reference spectra). The contributions from the hot filament have to be taken directly from QMS measurements of the pure molecule in the measurement setup. The hot filament produces only stable molecules, and for this work, only the mass signals of  $D_2$ , CO and formaldehyde ( $D_2CO$ ) had to be corrected for significant contributions of methanol-*d*4 cracking on the hot filament.

For the experiments with methanol, this means that the signals of formaldehyde ( $D_2CO$ , mass 32 amu), carbon monoxide (CO, mass 28 amu) and deuterium ( $D_2$ , mass 4 amu) had to be corrected for the cracking contributions of the molecule ( $CD_3OD$ , mass 36 amu) to discriminate cracking signals from true desorptions of these molecular products. The respective cracking fractions (from the intensity of the most intense mass peak of methanol: mass 34 amu, *not* the mother molecule on mass 36) that had to be subtracted from the signals are listed in table A.6.

Table A.6: Cracking fractions of  $CD_3OD$  (100 % on mass 34 amu; *not* the mother ion!) in masses of other products.

product	mass / (amu)	cracking fraction from mass 34 / (%)
formaldehyde $CD_2O$	32	9.0
carbon monoxide (CO)	28	7.2
deuterium ( $D_2$ )	4	0.3

The QMS measurements with 2-butene were conducted using fragment masses, because the molecular masses of all reactants and products (2-butene, mass 56 amu; butane-*d*2, mass 60 amu) exceeded the mass range of the high sensitivity QMS. Instead, all measurements were done with the fragment formed by molecular cracking by abstraction of the methyl group (molecular mass minus 15 amu). The signals of the *d*1 and *d*2 products were corrected for significant influences of carbon-13 contribution (natural C-13 abundance in carbon:  $\sim 1.1$  % [69]). The fragment ions followed to observe formation of the different products together with their correction factors are given in table A.7.

Table A.7: Observed fragments and C-13 contributions of  $\text{H}_3\text{C}-\text{CH}=\text{CH}-\text{CH}_3$  (2-butene, 56 amu, 100 %) in masses of products.

molecule	mass / (amu)	detected fragment	mass / (amu)	C-13 contribution, ratio to mass 41 / (%)
2-butene $\text{C}_4\text{H}_8$	56	$\text{C}_3\text{H}_5^\oplus$	41	–
2-butene- <i>d1</i> $\text{C}_4\text{H}_7\text{D}$	57	$\text{C}_3\text{H}_4\text{D}^\oplus$	42	3.9
2-butene- <i>d2</i> $\text{C}_4\text{H}_6\text{D}_2$	58	$\text{C}_3\text{H}_3\text{D}_2^\oplus$	43	0.12
<i>n</i> -butane- <i>d2</i> $\text{C}_4\text{H}_8\text{D}_2$	60	$\text{C}_3\text{H}_5\text{D}_2^\oplus$	45	–
<i>n</i> -butane- <i>d3</i> $\text{C}_4\text{H}_7\text{D}_3$	61	$\text{C}_3\text{H}_4\text{D}_3^\oplus$	46	–



# Abbreviations

<b>AC</b>	Alternating Current
<b>AES</b>	Auger-Electron-Spectroscopy
<b>AFM</b>	Atomic Force Microscopy
<b>Ag</b>	Silver ( <i>argentum</i> , chemical element symbol, IUPAC)
<b>AQP</b>	Acquisition Processor
<b>Ar</b>	Argon (chemical element symbol, IUPAC)
<b>Au</b>	Gold ( <i>aurum</i> , chemical element symbol, IUPAC)
<b>BASF</b>	Badische Anilin- und Sodafabrik
<b>bcc</b>	body-centered cubic
<b>CO</b>	Carbon monoxide
<b>Cu</b>	Copper ( <i>cuprum</i> , chemical element symbol, IUPAC)
<b>DC</b>	Direct Current
<b>DFT</b>	Density Functional Theory
<b>DMFC</b>	Direct Methanol Fuel Cell
<b>EB</b>	Effusive Beam
<b>EELS</b>	Electron-Energy-Loss-Spectroscopy (variant: HR-EELS)
<b>EI</b>	Electron Impact-Ionization
<b>EPN</b>	Electropneumatic Valve
<b>fcc</b>	face-centered cubic
<b>Fe</b>	Iron ( <i>ferrum</i> , chemical element symbol, IUPAC)
<b>FIR</b>	Far Infrared range (50000 - 500000 nm)
<b>FT</b>	Fourier-Transform
<b>FWHM</b>	Full Width at Half Maximum (of a spectral peak)
<b>GC</b>	Gas Chromatography
<b>GCA</b>	Glass Capillary Array
<b>hcp</b>	hexagonal close-packed
<b>HOMO</b>	Highest Occupied Molecular Orbital
<b>HR-EELS</b>	High-Resolution-Electron-Energy-Loss-Spectroscopy
<b>HV</b>	High Vacuum – sometimes also: High Voltage
<b>ICI</b>	Imperial Chemical Industries
<b>IR</b>	Infrared

<b>IRAS</b>	Infrared Reflection-Absorption-Spectroscopy
<b>IUPAC</b>	International Union for Pure and Applied Chemistry
<b>I-V</b>	Intensity-Voltage-LEED
<b>KBr</b>	Potassium bromide
<b>L</b>	Langmuir – measure for exposure; 1 L = $1.0 \times 10^{-6}$ Torr · s.
<b>LEED</b>	Low-Energy Electron-Diffraction)
<b>LUMO</b>	Lowest Unoccupied Molecular Orbital
<b>MB</b>	Molecular Beam
<b>ML</b>	Monolayer
<b>MCT</b>	Mercury Cadmium Telluride (IR-detector material)
<b>MIR</b>	Mid Infrared range (2500 - 50000 nm; 4000 - 200 $\text{cm}^{-1}$ )
<b>MTBE</b>	<i>tert</i> -butyl-methyl-ether
<b>MSSR</b>	Metal Surface-Selection Rule
<b>NEXAFS</b>	Near-Edge X-ray Absorption Fine Structure
<b>Ni</b>	Nickel (chemical element symbol, IUPAC)
<b>NIR</b>	Near Infrared range (800 - 2500 nm)
<b>NO</b>	Nitrogen Monoxide
<b>NO<sub>x</sub></b>	Nitrogen Oxides (all possible stoichiometries)
<b>O</b>	Oxygen ( <i>oxygenium</i> , chemical element symbol, IUPAC)
<b>PC</b>	Personal Computer
<b>Pd</b>	Palladium (chemical element symbol, IUPAC)
<b>PES</b>	Photoelectron Spectroscopy
<b>PM-IRAS</b>	Polarization-Modulation Infrared- Reflection Absorption-Spectroscopy
<b>PSMB</b>	Pulse-Sequence Molecular Beam experiments
<b>Pt</b>	Platinum (chemical element symbol, IUPAC)
<b>PVD</b>	Physical Vapor-Deposition
<b>QMS</b>	Quadrupole Mass Spectrometry
<b>RAIRS</b>	Reflection-Absorption Infrared-Spectroscopy
<b>Rh</b>	Rhodium (chemical element symbol, IUPAC)
<b>Ru</b>	Ruthenium (chemical element symbol, IUPAC)
<b>SFG</b>	Sum Frequency Generation spectroscopy
<b>SiC</b>	Silicon Carbide
<b>SIMS</b>	Secondary Ion-Mass Spectrometry
<b>SMSI</b>	Strong Metal-Support-Interaction
<b>SSB</b>	Supersonic Beam
<b>STM</b>	Scanning-Tunneling Microscopy
<b>Ti</b>	Titanium (chemical element symbol, IUPAC)
<b>TMP</b>	Turbo-Molecular Pump
<b>TDS</b>	Temperature programmed Desorption Spectroscopy

<b>TPD</b>	Temperature Programmed Desorption spectroscopy
<b>TPRS</b>	Temperature Programmed Reaction Spectroscopy
<b>TRS</b>	Time-Resolved Scan
<b>TTL</b>	Transistor-Transistor-Logic
<b>UHV</b>	Ultrahigh Vacuum
<b>UPS</b>	Ultraviolet Photoelectron-Spectroscopy
<b>XPS</b>	X-ray Photoelectron-Spectroscopy
<b>XPD</b>	X-ray Photoelectron diffraction





# Acknowledgements

This dissertation represents the work of three experimental years at the Fritz-Haber-Institute in Berlin, and it would not have been possible without support. Besides a large number of technicians or administrative workers, who all contribute to our work by keeping the necessary technical facilities running, a large number of persons were involved directly in the scientific projects that are discussed in this work:

At the first place, I would like to thank Prof. Dr. Hans-Joachim Freund for his support, for his continuous interest in the projects described here and for giving me the opportunity to conduct this work in this excellent and stimulating scientific environment in the Department for Chemical Physics at the Fritz Haber-Institute in Berlin.

Next, I would like to acknowledge Prof. Dr. Klaus Rademann from the Humboldt University in Berlin for the good cooperation and the discussions we had about this work.

I would like to express my gratitude to my group leaders Dr. Svetlana Schauermaun and Prof. Dr. Jörg Libuda for their guidance during the course of this research, for the many discussions we had about the experiments, for encouragement and suggestions.

The butene project was originally suggested by Prof. Francisco Zaera during his stay in our department as a Humboldt awardee. I am cordially thankful for his encouraging support, his confidence in the feasibility of these experiments, many discussions and his guidance while setting up the experimental conditions; I have strongly benefited from his experience with hydrocarbon reactions under UHV conditions.

Many thanks go to my fellow group members. I have profited very much learning from my senior colleagues Dr. Svetlana Schauermaun and Dr. Mathias Laurin, and – most of all – I have gained the necessary degree of understanding and creativity for molecular beam experiments in the many discussions with Dr. Tobias Schalow during the course of our earlier project. I want to express my gratitude to my junior colleagues Wiebke Ludwig and Jan-Henrik Fischer who have contributed a lot of encouragement to the experiments shown in this thesis, while I tried to introduce them to our exper-

imental routine; also Tobias Schalow was involved in our first experiments with methanol. I also thank Jens Hartmann for his help in maintenance and routine procedures.

I want to thank Dr. Dario Stacchiola, with whom I could discuss some of the issues in the butene-project, especially the interpretation of IR-spectra; although we did not further concentrate on that particular question, I want to express my gratitude for the help he offered and the commitment that he showed to help clarify my questions. Also, I want to thank the members of the methanol-club, Dr. Marta Borasio, Dr. Sarp Kaya, Dr. Alexander Uhl and Yuriy Romanyshein, for the discussions we had about methanol decomposition on our different metals and metal oxides. And additionally, I am very grateful for the additional TPD experiments that Ying-Na Sun, Dr. Sarp Kaya and Dr. Shamil Shaikhutdinov have conducted with methanol on the  $\text{Fe}_3\text{O}_4$  film and the Pd/ $\text{Fe}_3\text{O}_4$  model catalyst; they are also cited in this work.

I also need to express my gratitude to Klaus-Peter Vogelgesang and Matthias Naschitzki for their readily offered help and technical assistance with numerous bugs, constructions and improvisations, and to our secretaries Gabriele Mehnert and Manuela Misch for their help with administrative tasks.

There is a number of people who may not have directly contributed to this work, but who have helped to also make this work a pleasure. This includes my office mates Alex Bondarchuk, Sarp Kaya, Mikolaj Lewandowski, and Stefan Ulrich. Stefan was also the guy at the machine next to ours in the lab hall, and I want to thank him and all the other people in the lab and our department for sharing this nice part of our lives together.

Finally, I want to extend my expression of gratitude to people outside the Fritz-Haber institute. I want to thank the people at the university of Kiel who have influenced my initial scientific education: Prof. Dr. Friedrich Temps, Dr. Gernot Friedrichs, Dr. Falk Renth, Dr. Jens Riedel, Prof. Dr. Heiner Homborg, Prof. Dr. Dieter Heber, Prof. Dr. Willy Friedrichsen, Dr. Yvonne Klawitter and Assistant-Prof. Dr. Jan-Uwe Rohde. My special thank goes to Prof. Dr. Dr. h.c. Gerhard Lagaly; legendary for routinely snuffling in front a chemistry course, he has taught me to see the poetry in the prosaic world of natural sciences. Of course, I also have to thank my colleagues during many, many lab courses, seminars and lecture courses, Jan Bornhöft, Jan Clausen, Florian Paulat and all the others – it was a pleasure to learn chemistry together with them.

And then, I have to express my deepest gratitude to my family and friends and all the other people who have touched my life in the past; although they may not have directly influenced this work, they still have contributed a lot to it.

# Publications

1. R. Meyer, D. Lahav, T. Schalow, M. Laurin, **B. Brandt**, S. Schauer-  
mann, S. Guimond, T. Klüner, H. Kuhlenbeck, J. Libuda, Sh.K. Shaikh-  
hutdinov, H.-J. Freund: CO adsorption and thermal stability of Pd  
deposited on a thin FeO(111) film.  
*Surf. Sci.*, 586(1-3), 174-182 (2005).
2. T. Schalow, M. Laurin, **B. Brandt**, S. Schauer-  
mann, S. Guimond, H. Kuhlenbeck, D.E. Starr, Sh.K. Shaikhutdinov, J. Libuda, H.-J.  
Freund: Oxygen Storage at the Metal/Oxide Interface of Catalyst  
Nanoparticles.  
*Angew. Chem. Int. Ed.*, 44(46), 7601-7605 (2005).  
T. Schalow, M. Laurin, **B. Brandt**, S. Schauer-  
mann, S. Guimond, H. Kuhlenbeck, D.E. Starr, Sh.K. Shaikhutdinov, J. Libuda, H.-J.  
Freund: Sauerstoffspeicherung an der Metall-Oxid-Grenzfläche von  
Katalysatornanopartikeln.  
*Angew. Chem.*, 117(46), 7773-7777 (2005).
3. T. Schalow, **B. Brandt**, D.E. Starr, M. Laurin, S. Schauer-  
mann, Sh.K. Shaikhutdinov, J. Libuda, H.-J. Freund: Oxygen-induced re-  
structuring of a Pd/Fe<sub>3</sub>O<sub>4</sub> model catalyst.  
*Catal. Lett.*, 107(3-4), 189-196 (2006).
4. W. Ludwig, **B. Brandt**, G. Friedrichs, F. Temps: Kinetics of the  
Reaction C<sub>2</sub>H<sub>5</sub> + HO<sub>2</sub> by Time-Resolved Mass Spectrometry.  
*J. Phys. Chem. A*, 110(9), 3330-3337 (2006).
5. T. Schalow, **B. Brandt**, D.E. Starr, M. Laurin, Sh.K. Shaikhutdinov,  
S. Schauer-  
mann, J. Libuda, H.-J. Freund: Size-dependent oxidation  
mechanism of supported Pd nanoparticles.  
*Angew. Chem. Int. Ed.*, 45, 3693-3697 (2006).  
T. Schalow, **B. Brandt**, D.E. Starr, M. Laurin, Sh.K. Shaikhutdinov,  
S. Schauer-  
mann, J. Libuda, H.-J. Freund: Größenabhängiger Oxi-

- tionsmechanismus trägerfixierter Pd-Nanopartikel.  
*Angew. Chem.*, 118(22), 3775-3780 (2006).
6. T. Schalow, **B. Brandt**, M. Laurin, S. Schauermann, S. Guimond, H. Kuhlenbeck, J. Libuda, H.-J. Freund: Formation of interface and surface oxides on supported Pd nanoparticles.  
*Surf. Sci.*, 600(12), 2528-2542 (2006).
  7. T. Schalow, **B. Brandt**, M. Laurin, S. Schauermann, J. Libuda, H.-J. Freund: CO oxidation on partially oxidized Pd nanoparticles.  
*J. Catal.*, 242(1), 58-70 (2006).
  8. J. Libuda, T. Schalow, **B. Brandt**, M. Laurin, S. Schauermann: Model Studies in Heterogeneous Catalysis at the Microscopic Level: From the Structure and Composition of Surfaces to Reaction Kinetics.  
*Microchim. Acta*, 156(1-2), 9-20 (2007).
  9. **B. Brandt**, T. Schalow, M. Laurin, S. Schauermann, J. Libuda, H.-J. Freund: Oxidation, Reduction, and Reactivity of Supported Pd Nanoparticles: Mechanism and Microkinetics.  
*J. Phys. Chem. C*, 111(2), 938-949 (2007).
  10. T. Schalow, **B. Brandt**, D.E. Starr, M. Laurin, Sh.K. Shaikhutdinov, S. Schauermann, J. Libuda, H.-J. Freund: Particle Size Dependent Adsorption and Reaction Kinetics on Reduced and Partially Oxidized Pd Nanoparticles.  
*Phys. Chem. Chem. Phys.*, 9(11), 1347-1361 (2007).
  11. T. Schalow, **B. Brandt**, M. Laurin, S. Guimond, D.E. Starr, Sh.K. Shaikhutdinov, S. Schauermann, J. Libuda, H.-J. Freund: Formation and Catalytic Activity of Partially Oxidized Pd Nanoparticles.  
*Top. Catal.*, 42-43(1-4), 387-391 (2007).
  12. **B. Brandt**, J.-H. Fischer, W. Ludwig, J. Libuda, F. Zaera, S. Schauermann, H.-J. Freund: Isomerization and Hydrogenation of *cis*-2-Butene on Pd Model Catalyst.  
*J. Phys. Chem. C*, 112(30), 11408-11420 (2008).
  13. M. Wilde, K. Fukutani, W. Ludwig, **B. Brandt**, J.-H. Fischer, S. Schauermann, H.-J. Freund: Influence of carbon deposition on the hydrogen distribution in Pd nanoparticles and their reactivity in olefin hydrogenation.  
*Angew. Chem. Int. Ed.* (2008), in press.

M. Wilde, K. Fukutani, W. Ludwig, **B. Brandt**, J.-H. Fischer, S. Schauer mann, H.-J. Freund: Einfluss von Kohlenstoffablagerungen auf die Wasserstoffverteilung in Pd-Nanopartikeln und deren Reaktivität in der Olefinhydrierung.

*Angew. Chem.* (2008), in press.

14. **B. Brandt**, W. Ludwig, J.-H. Fischer, J. Libuda, F. Zaera, S. Schauer mann: Activity of *cis*- and *trans*-2-Butene in Conversions with Hydrogen on Pd/Fe<sub>3</sub>O<sub>4</sub> Model Catalyst.  
in preparation



# Bibliography

- [1] G. Ertl, H. Knözinger, F. Schüth, and J. Weitkamp, editors. *Handbook of Heterogeneous Catalysis (8 volumes)*. Wiley VCH, Weinheim, 2008.
- [2] G. Ertl, H. Knözinger, and J. Weitkamp, editors. *Environmental Catalysis*. Wiley VCH, Weinheim, 1999.
- [3] J.M. Thomas and W.J. Thomas, editors. *Principle and Practice of Heterogeneous Catalysis*. Wiley VCH, Weinheim, 1997.
- [4] W.C. Conner and J.L. Falconer. Spillover in Heterogeneous Catalysis. *Chem. Rev.*, 95(3):759–788, 1995.
- [5] M. Boudart. Catalysis by Supported Metals. *Adv. Catal.*, 20:153–166, 1969.
- [6] M. Che and C.O. Bennett. The Influence of Particle Size on the Catalytic Properties of Supported Metals. *Adv. Catal.*, 36:55–172, 1989.
- [7] G.C. Bond. The Origins of Particle Size Effects in Heterogeneous Catalysis. *Surf. Sci.*, 156(2, 3):966–981, 1985.
- [8] G. Ertl. Elementary Steps in Heterogeneous Catalysis. *Angew. Chem. Int. Ed.*, 29(11):1219–1227, 1990.
- [9] A. Mittasch. *Geschichte der Ammoniaksynthese*. Verlag Chemie, Weinheim, 1951.
- [10] I. Langmuir. The Constitution and fundamental properties of solids and liquids. Part I: Solids. *J. Am. Chem. Soc.*, 38(11):2221–2295, 1916.
- [11] I. Langmuir. Chemical Reactions on Surfaces. *Trans. Farad. Soc.*, 17: 607–620, 1922.
- [12] M. Polanyi. Über Adsorptionskatalyse. *Z. f. Elektrochemie*, 27(7/8): 142–150, 1921.

- [13] M. Polanyi. Betrachtungen über den Aktivierungsvorgang an Grenzflächen. *Z. f. Elektrochemie*, 35(9):561–567, 1929.
- [14] I. Langmuir. Surface Chemistry (Nobel lecture, given dec. 14th.), 1932.
- [15] G. Ertl and T. Gloyna. Katalyse: Vom Stein der Weisen zu Wilhelm Ostwald. *Z. Phys. Chem.*, 217:1207–1219, 2003.
- [16] J.W. Niemantsverdriet. *Spectroscopy in Catalysis: an Introduction (3rd edition)*. Wiley VCH, Weinheim, 2007.
- [17] H. Lüth. *Surfaces and Interfaces of Solids*. Number 15 in Springer Series in Surface Sciences. Springer, Berlin, Heidelberg, New York, 1993.
- [18] A. Zangwill. *Physics at Surfaces*. Cambridge University Press, Cambridge, 1988.
- [19] J. Libuda and H.-J. Freund. Molecular beam experiments on model catalysts. *Surf. Sci. Rep.*, 57(7-8):157–298, 2005.
- [20] C.R. Henry. Surface studies of supported model catalysts. *Surf. Sci. Rep.*, 31(7-8):231–325, 1998.
- [21] M. Bäumer and H.-J. Freund. Metal deposits on well-ordered oxide films. *Prog. Surf. Sci.*, 61(7-8):127–198, 1999.
- [22] M. Mavrikakis and M.A. Barteau. Oxygenate reaction pathways on transition metal surfaces. *J. Molec. Catal. A: Chemical*, 131:135–147, 1998.
- [23] M.A. Barteau. Organic Reactions at Well-Defined Oxide Surfaces. *Chem. Rev.*, 96(4):1413–1430, 1996.
- [24] V. Ponc and G.C. Bond. *Catalysis by Metals and Alloys*. Elsevier, Amsterdam, 1995.
- [25] G.C. Bond. *Metal-Catalysed Reactions of Hydrocarbons*. Springer Science, New York, 2005.
- [26] G. Somorjai. *Introduction to Surface Chemistry and Catalysis*. John Wiley & Sons Inc., New York, 1994.
- [27] K.W. Kolasinski. *Surface Science. Foundations of Catalysis and Nanoscience*. John Wiley & Sons Ltd., West Sussex (England), 2002.



- [28] A.W. Kleyn. Molecular beams and chemical dynamics at surfaces. *Chem. Soc. Rev.*, 32(2):87–95, 2003.
- [29] C.T. Rettner, D.J. Auerbach, J.C. Tully, and A.W. Kleyn. Chemical Dynamics at the Gas-Surface Interface. *J. Phys. Chem.*, 100(31):13021–13033, 1996.
- [30] D.A. King and M.G. Wells. Molecular Beam Investigation of Adsorption Kinetics on Bulk Metal Targets: Nitrogen on Tungsten. *Surf. Sci.*, 29:454–482, 1972.
- [31] D.A. King and M.G. Wells. Reaction mechanism in chemisorption kinetics: nitrogen on the {100} plane of tungsten. *Proc. Roy. Soc. London A.*, 339(1617):245–269, 1974.
- [32] P.A. Redhead. Thermal Desorption of Gases. *Vacuum*, 12(4):203–211, 1962.
- [33] W.L. Jorgensen and L. Salem. *The Organic Chemist's Book of Orbitals*. Academic Press, New York, 1973.
- [34] G. Blyholder. Molecular Orbital View of Chemisorbed Carbon Monoxide. *J. Phys. Chem.*, 68(10):2772–2778, 1964.
- [35] G. Blyholder. CNDO Model of Carbon Monoxide Chemisorbed on Nickel. *J. Phys. Chem.*, 79(7):756–761, 1975.
- [36] F. M. Hoffmann. Infrared reflection-absorption spectroscopy of adsorbed molecules. *Surf. Sci. Rep.*, 3:107–192, 1983.
- [37] A.M. Bradshaw and F.M. Hoffmann. The chemisorption of carbon monoxide on palladium single crystal surfaces: IR spectroscopic evidence for localised site adsorption. *Surf. Sci.*, 72:513–535, 1978.
- [38] A. Ortega, F.M. Hoffmann, and A.M. Bradshaw. The adsorption of CO on Pd(100) studied by IR reflection absorption spectroscopy. *Surf. Sci.*, 119:79–94, 1982.
- [39] H. Ohtani, M.A. van Hove, and G. Somorjai. LEED intensity analysis of the surface structures of Pd(111) and of CO adsorbed on Pd(111) in a  $(\sqrt{3}\times\sqrt{3})R30^\circ$  arrangement. *Surf. Sci.*, 187:372–386, 1987.
- [40] M. Tüshaus, W. Berndt, H. Conrad, A.M. Bradshaw, and B. Persson. Understanding the Structure of High Coverage CO Adlayers. *Appl. Phys. A – Solids and Surfaces*, 51:91–98, 1990.

- [41] T. Gießel, O. Schaff, C.J. Hirschmugl, V. Fernandez, K.-M. Schindler, A. Theobald, S. Bao, R. Lindsay, W. Berndt, A.M. Bradshaw, C. Baddeley, A.F. Lee, R.M. Lambert, and D.P. Woodruff. A photoelectron diffraction study of ordered structures in the chemisorption system Pd{111}-CO. *Surf. Sci.*, 406:90–102, 1998.
- [42] D. Loffreda, D. Simon, and P. Sautet. Dependence of stretching frequency on surface coverage and adsorbate-adsorbate interactions: a density-functional theory approach of CO on Pd(111). *Surf. Sci.*, 425:68–80, 1999.
- [43] S. Surnev, M. Sock, M.G. Ramsey, F.P. Netzer, M. Wiklund, M. Borg, and J.N. Andersen. CO adsorption on Pd(111): a high-resolution core level photoemission and electron energy loss spectroscopy study. *Surf. Sci.*, 470:171–185, 2000.
- [44] M.K. Rose, T. Mitsui, J. Dunphy, A. Borg, D.F. Ogletree, M. Salmerón, and P. Sautet. Ordered structures of CO on Pd(111) studied by STM. *Surf. Sci.*, 512:48–60, 2002.
- [45] H. Unterhalt, G. Rupprechter, and H.-J. Freund. Vibrational Sum Frequency Spectroscopy on Pd(111) and Supported Pd Nanoparticles: CO Adsorption from Ultrahigh Vacuum to Atmospheric Pressure. *J. Phys. Chem. B*, 106(2):356–367, 2002.
- [46] W.K. Kuhn, J. Szanyi, and D.W. Goodman. CO adsorption on Pd(111): the effects of temperature and pressure. *Surf. Sci. Lett.*, 274:L611–L618, 1992.
- [47] C.N. Hinshelwood. *The Kinetics of Chemical Change*. Clarendon Press, Oxford, 1940.
- [48] D.D. Eley and E.K. Rideal. Parahydrogen Conversion on Tungsten. *Nature*, 146(3699):401–402, 1940.
- [49] C.T. Rettner. Reaction of an H-atom beam with Cl/Au(111): Dynamics of concurrent Eley-Rideal and Langmuir-Hinshelwood mechanisms. *J. Chem. Phys.*, 101(2):1529–1546, 1994.
- [50] E. Gillet, S. Channakhone, V. Matolin, and M. Gillet. Chemisorptional behaviour of Pd small supported particles depending on size and structure: TDS, SSIMS and TEM investigations. *Surf. Sci.*, 152/153:603–614, 1985.

- [51] V. Matolin and E. Gillet. The surface diffusion in CO oxidation on small supported Pd particles: Experimental evidence. *Surf. Sci.*, 166: L115–L118, 1986.
- [52] S. Khoobiar. Particle to Particle Migration of Hydrogen Atoms on Platinum-Alumina Catalysts from Particle to Neighboring Particles. *J. Phys. Chem.*, 68(2):411–412, 1964.
- [53] M. Boudart, M.A. Vannice, and J.E. Benson. Adlineation, Portholes and Spillover. *Z. Phys. Chem. NF*, 64:171–177, 1969.
- [54] N. Takahashi, H. Shinjoh, T. Iijima, T. Suzuki, K. Yamazaki, K. Yokota, H. Suzuki, N. Miyoshi, S. Matsumoto, T. Tanizawa, T. Tanaka, S. Tateishi, and K. Kasahara. The new-concept 3-way catalyst for automotive lean-burn engine: NO<sub>x</sub> storage and reduction catalyst. *Catalysis Today*, 27(1-2):63–69, 1996.
- [55] T. Schalow. *Bildung und katalytische Aktivität partiell oxidierter Pd-Nanopartikel*. PhD thesis, Fakultät II (Mathematik und Naturwissenschaften), Technische Universität Berlin, Berlin, 2006.
- [56] H.S. Taylor. A Theory of the Catalytic Surface. *Proc. Roy. Soc. London A*, 108(745):105–111, 1925.
- [57] H.S. Taylor. Über aktive Stellen an Katalysatoren. *Z. f. Elektrochemie*, 35(9):542–549, 1929.
- [58] A. Smekal. Kristallbaufehler und Aktivzentren heterogener Katalyse. *Z. f. Elektrochemie*, 35(9):567–573, 1929.
- [59] T. Schalow, B. Brandt, D.E. Starr, M. Laurin, S. Schauermann, Sh.K. Shaikhutdinov, J. Libuda, and H.-J. Freund. Oxygen-induced restructuring of a Pd/Fe<sub>3</sub>O<sub>4</sub> model catalyst. *Catal. Lett.*, 107(3-4):189–196, 2006.
- [60] J. Libuda, I. Meusel, J. Hartmann, and H.-J. Freund. A molecular beam/surface spectroscopy apparatus for the study of reactions on complex model catalysts. *Rev. Sci. Inst.*, 71(12):4395–4408, 2000.
- [61] I. Meusel. *Aufbau einer Molekularstrahlapparatur für oberflächenkinetische Untersuchungen*. PhD thesis, Fakultät II (Mathematik und Naturwissenschaften), Technische Universität Berlin, Berlin, 2002.
- [62] G. Scoles, editor. *Atomic and Molecular Beam Methods*. Oxford University Press, Oxford, 1988.

- [63] H. Pauly. *Atom, Molecule, and Cluster Beams I*. Springer-Verlag, Berlin, Heidelberg, 2000.
- [64] W. Paul and H. Steinwedel. Ein neues Massenspektrometer ohne Magnetfeld. *Z. Naturforschung*, 8a:448–450, 1953.
- [65] W. Paul and M. Raether. Das elektrische Massenfilter. *Z. Phys.*, 140: 262–273, 1955.
- [66] W. Paul, H. P. Reinhard, and U. von Zahn. Das elektrische Massenfilter als Massenspektrometer und Isotopentrenner. *Z. Phys.*, 152:143–182, 1958.
- [67] P. H. Dawson. *Quadrupole Mass Spectrometry and its Applications*. American Institute of Physics Press, Woodbury, NY, 1995. originally published 1979 by Elsevier Publishing Co., Amsterdam.
- [68] J.D. Graybeal. *Molecular Spectroscopy*. McGraw-Hill, New York, 1988.
- [69] M. Hesse, H. Meier, and B. Zeeh. *Spektroskopische Methoden in der organischen Chemie (5. überarbeitete Neuauflage)*. Georg Thieme Verlag, Stuttgart, New York, 1995.
- [70] C.N. Banwell and E.M. McCash. *Molekülspektroskopie*. Oldenbourg Verlag, München Wien, 1999.
- [71] P. Hollins. The influence of surface defects on the infrared spectra of adsorbed species. *Surf. Sci. Rep.*, 16:51–94, 1992.
- [72] P.W. Atkins and R.S. Friedman. *Molecular Quantum Mechanics*. Oxford University Press, Oxford, third edition, 1996.
- [73] P.W. Atkins. *Physical Chemistry*. Oxford University Press, Oxford, sixth edition, 1998.
- [74] F. Engelke. *Aufbau der Moleküle*. B.G. Teubner, Stuttgart, third edition, 1996.
- [75] J.M. Hollas. *High Resolution Spectroscopy*. Butterworth & Co., London, 1982.
- [76] E.B. Wilson Jr., J.C. Decius, and P.C. Cross. *Molecular Vibrations*. McGraw-Hill Book Company, Inc., New York, 1955.
- [77] S.A. Francis and A.H. Ellison. Infrared Spectra of Monolayers on Metal Mirrors. *J. Opt. Soc. Am.*, 49(2):131–138, 1959.

- [78] T. Dellwig, J. Hartmann, J. Libuda, I. Meusel, G. Rupprechter, H. Unterhalt, and H.-J. Freund. Complex model catalysts under UHV and high pressure conditions: CO adsorption and oxidation on alumina-supported Pd particles. *J. Molec. Catal. A*, 162(1-2):51–66, 2000.
- [79] Sh.K. Shaikhutdinov, M. Heemeier, M. Bäumer, T. Lear, D. Lennon, R.J. Oldman, S.D. Jackson, and H.-J. Freund. Structure-Reactivity Relationships on Supported Metal Catalysts: Adsorption and Reaction of Ethene and Hydrogen on Pd/Al<sub>2</sub>O<sub>3</sub>/NiAl(110). *J. Catal.*, 200:330–339, 2001.
- [80] S. Schauer mann, J. Hoffmann, V. Johánek, J. Hartmann, J. Libuda, and H.-J. Freund. Catalytic Activity and Poisoning of Specific Sites on Supported Metal Nanoparticles. *Angew. Chemie Int. Ed.*, 41(14):2532–2535, 2002.
- [81] R. Meyer, Sh.K. Shaikhutdinov, and H.-J. Freund. CO Oxidation on a Pd/Fe<sub>3</sub>O<sub>4</sub>(111) Model Catalyst. *Z. Phys. Chem.*, 218(8):905–914, 2004.
- [82] A. Barbieri, W. Weiss, M.A. Van Hove, and G.A. Somorjai. Magnetite Fe<sub>3</sub>O<sub>4</sub>(111): surface structure by LEED crystallography and energetics. *Surf. Sci.*, 302:259–279, 1994.
- [83] W. Weiss and W. Ranke. Surface chemistry and catalysis on well-defined epitaxial iron-oxide layers. *Prog. Surf. Sci.*, 70(1-3):1–151, 2002.
- [84] P. Mars and D.W. van Krevelen. Oxidations carried out by means of vanadium oxide catalysts. *Chem. Eng. Sci. (Special Suppl.)*, 3:41–59, 1954.
- [85] C. Doornkamp and V. Ponec. The universal character of the Mars and Van Krevelen mechanism. *J. Molec. Catal. A*, 162(1-2):19–32, 2000.
- [86] G.H. Vurens, M. Salmerón, and G.A. Somorjai. Structure, composition and chemisorption studies of thin iron oxide films on platinum (111). *Surf. Sci.*, 201:129–144, 1988.
- [87] G.H. Vurens, V. Maurice, M. Salmerón, and G.A. Somorjai. Growth, structure and chemical properties of FeO overlayers on Pt(100) and Pt(111). *Surf. Sci.*, 268:170–178, 1992.

- [88] H.C. Galloway, J.J. Benítez, and M. Salmerón. The structure of monolayer films of FeO on Pt(111). *Surf. Sci.*, 298:127–133, 1993.
- [89] Y.J. Kim, C. Westphal, R.X. Ynzunza, Z. Wang, H.C. Galloway, M. Salmerón, M.A. Van Hove, and C.S. Fadley. The growth of iron oxide films on Pt(111): a combined XPD, STM, and LEED study. *Surf. Sci.*, 416:68–111, 1998.
- [90] W. Weiss and M. Ritter. Metal oxide heteroepitaxy: Stranski-Krastanov growth for iron oxides on Pt(111). *Phys. Rev. B*, 59(7):5201–5213, 1999.
- [91] Sh.K. Shaikhutdinov, M. Ritter, X.-G. Wang, H. Over, and W. Weiss. Defect structures on epitaxial Fe<sub>3</sub>O<sub>4</sub>(111) films. *Phys. Rev. B*, 60(15):11062–11069, 1999.
- [92] C. Lemire, R. Meyer, V.E. Henrich, Sh. Shaikhutdinov, and H.-J. Freund. The surface structure of Fe<sub>3</sub>O<sub>4</sub>(111) films as studied by CO adsorption. *Surf. Sci.*, 572:103–114, 2004.
- [93] W. Weiss, A. Barbieri, M.A. Van Hove, and G.A. Somorjai. Surface Structure Determination of an Oxide Film Grown on a Foreign Substrate: Fe<sub>3</sub>O<sub>4</sub> Multilayer on Pt(111) Identified by Low Energy Electron Diffraction. *Phys. Rev. Lett.*, 71(12):1848–1851, 1993.
- [94] W.H. Bragg and F.R.S. Cavendish. The Structure of the Spinel Group of Crystals. *Phil. Mag.*, 30(176):305–315, 1915.
- [95] M Ritter and W. Weiss. Fe<sub>3</sub>O<sub>4</sub>(111) surface structure determined by LEED crystallography. *Surf. Sci.*, 432:81–94, 1999.
- [96] Y.N. Sun, S. Kaya, Sh.K. Shaikhutdinov, and H.-J. Freund. Personal Information (to be published), 2007.
- [97] K. Wolter, O. Seiferth, H. Kuhlenbeck, M. Bäumer, and H.-J. Freund. Infrared spectroscopic investigation of CO adsorbed on Pd aggregates deposited on an alumina model support. *Surf. Sci.*, 399:190–198, 1998.
- [98] S. Bertarione, D. Scarano, A. Zecchina, V. Johánek, J. Hoffmann, S. Schauer mann, M.M. Frank, J. Libuda, G. Rupprechter, and H.-J. Freund. Surface Reactivity of Pd Nanoparticles Supported on Polycrystalline Substrates As Compared to Thin Film Model Catalysts: Infrared Study of CO Adsorption. *J. Phys. Chem. B*, 108(11):3603–3616, 2004.

- [99] F. Zaera. An Organometallic Guide to the Chemistry of Hydrocarbon Moieties on Transition Metal Surfaces. *Chem. Rev.*, 95(8):2651–2693, 1995.
- [100] T. Schalow, M. Laurin, B. Brandt, S. Schauermann, S. Guimond, H. Kuhlenbeck, D.E. Starr, Sh.K. Shaikhutdinov, J. Libuda, and H.-J. Freund. Oxygen Storage at the Metal/Oxide Interface of Catalyst Nanoparticles. *Angew. Chem. Int. Ed.*, 44(46):7601–7605, 2005.
- [101] T. Schalow, B. Brandt, M. Laurin, S. Schauermann, S. Guimond, H. Kuhlenbeck, J. Libuda, and H.-J. Freund. Formation of interface and surface oxides on supported Pd nanoparticles. *Surf. Sci.*, 600: 2528–2542, 2006.
- [102] T. Schalow, B. Brandt, D.E. Starr, M. Laurin, Sh.K. Shaikhutdinov, S. Schauermann, J. Libuda, and H.-J. Freund. Size-Dependant Oxidation Mechanism of Supported Pd Nanoparticles. *Angew. Chem. Int. Ed.*, 45(22):3693–3697, 2006.
- [103] T. Schalow, B. Brandt, D.E. Starr, M. Laurin, Sh.K. Shaikhutdinov, S. Schauermann, J. Libuda, and H.-J. Freund. Particle size dependent adsorption and reaction kinetics on reduced and partially oxidized Pd nanoparticles. *Phys. Chem. Chem. Phys.*, 9:1347–1361, 2007.
- [104] B. Brandt, T. Schalow, M. Laurin, S. Schauermann, J. Libuda, and H.-J. Freund. Oxidation, Reduction, and Reactivity of Supported Pd Nanoparticles: Mechanism and Microkinetics. *J. Phys. Chem. C*, 111(2):938–949, 2007.
- [105] T. Schalow, B. Brandt, M. Laurin, S. Schauermann, J. Libuda, and H.-J. Freund. CO oxidation on partially oxidized Pd nanoparticles. *J. Catal.*, 242(1):58–70, 2006.
- [106] The Methanol Institute (MI), 2007. URL <http://www.methanol.org/pdf/faqs.pdf>.
- [107] H.F. Kung. Methanol synthesis. *Catal.Rev.-Sci.Eng.*, 22(2):235–259, 1980.
- [108] G.A. Olah, A. Goepfert, and G.K. Surya Prakash. *Beyond Oil and Gas: The Methanol Economy*. Wiley-VCH, New York, 2006.
- [109] M.D. Thomas. Preparation of formaldehyde. *J. Am. Chem. Soc.*, 42(5):867–882, 1920.

- [110] J.F. Walker. *Formaldehyde*. Reinhold, New York, 1964.
- [111] C.L. Thomas. *Catalytic Processes and Proven Catalysts*. Academic Press, New York, 1970.
- [112] H. Sperber. Herstellung von Formaldehyd aus Methanol in der BASF. *Chem. Ing. Tech. – CIT*, 41(17):962–966, 1969.
- [113] J.K. Dixon and J.E. Longfield. Oxidation, hydration, dehydration and cracking catalysts. In P.H. Emmet, editor, *Catalysis, Vol. 7*, pages 231 – 236. Reinhold, New York, 1960.
- [114] J.J. Chen, Z.-C. Jiang, Y. Zhou, B.R. Chakraborty, and N. Winograd. Spectroscopic studies of methanol decomposition on Pd(111). *Surf. Sci.*, 328:248–262, 1995.
- [115] O. Rodríguez de la Fuente, M. Borasio, P. Galletto, G. Rupprechter, and H.-J. Freund. The influence of surface defects on methanol decomposition on Pd(111) studied by XPS and PM-IRAS. *Surf. Sci.*, 566-568:740–745, 2004.
- [116] K. Christmann and J.E. Demuth. The adsorption and reaction of methanol on Pd(100). II. Thermal desorption and decomposition. *J. Chem. Phys.*, 76(12):6318–6327, 1982.
- [117] S.M. Gates, J.N. Russell Jr., and J.T. Yates Jr. Scanning Kinetic Spectroscopy (SKS): A new method for investigation of surface reaction processes. *Surf. Sci.*, 159:233–255, 1985.
- [118] J.S. Huberty and R.J. Madix. An FTIR study of the bonding of methoxy on Ni(100): effects of coadsorbed sulfur, carbon monoxide and hydrogen. *Surf. Sci.*, 360:144–156, 1996.
- [119] F. Solymosi, A. Berkó, and T.I. Tarnóczy. Adsorption and decomposition of methanol on Rh(111) studied by Electron Energy Loss and Thermal Desorption Spectroscopy. *Surf. Sci.*, 141:533–548, 1984.
- [120] J.E. Parmeter, X. Jiang, and D.W. Goodman. The adsorption and decomposition of methanol on the Rh(100) surface. *Surf. Sci.*, 240: 85–100, 1990.
- [121] J.P. Lu, M.R. Albert, and S.L. Bernasek. The decomposition of surface methoxy on clean and oxygen post dosed Fe(100); Control of reaction selectivity. *Catal. Lett.*, 6(2):245–254, 1990.



- [122] R.B. Barros, A.R. Garcia, and L.M. Ilharco. The effect of pre-adsorbed atoms on the reactivity of methanol- $d_4$  on Ru(001): Comparison between hydrogen and oxygen. *Surf. Sci.*, 600:2425–2433, 2006.
- [123] I.E. Wachs and R.J. Madix. The oxidation of methanol on a silver (110) catalyst. *Surf. Sci.*, 76:531–558, 1978.
- [124] J.N. Russell Jr., S.M. Gates, and J.T. Yates Jr. Reaction of methanol with Cu(111) and Cu(111)+O(ads). *Surf. Sci.*, 163:516–540, 1985.
- [125] M. Bowker and R.J. Madix. XPS, UPS and thermal desorption studies of alcohol adsorption on Cu(110). I. Methanol. *Surf. Sci.*, 95:190–206, 1980.
- [126] W.S. Sim, P. Gardner, and D.A. King. Structure and Reactivity of the Surface Methoxy Species on Ag{111}. *J. Phys. Chem.*, 99(43):16002–16010, 1995.
- [127] V. Efstathiou and D.P. Woodruff. An infrared vibrational spectroscopic study of the interaction of methanol with oxygen-covered Cu(111). *Surf. Sci.*, 526:19–32, 2003.
- [128] J.L. Davis and M.A. Barteau. The influence of oxygen on the selectivity of alcohol conversion on the Pd(111) surface. *Surf. Sci.*, 197:123–152, 1988.
- [129] S.W. Jørgensen and R.J. Madix. Hydrogen transfer pathways in the oxidation of methanol on Pd(100). *Surf. Sci.*, 183:27–43, 1987.
- [130] F. Solymosi, J. Cserényi, and L. Ovári. A comparative study of the complete oxidation of dimethylether on supported group VIII metals. *Catal. Lett.*, 44:89–93, 1997.
- [131] J.L. Davis and M.A. Barteau. Spectroscopic identification of alkoxide, aldehyde, and acyl intermediates in alcohol decomposition on Pd(111). *Surf. Sci.*, 235:235–248, 1990.
- [132] J. Hrbek, R.A. dePaola, and F.M. Hoffmann. The interaction of methanol with Ru(001). *J. Chem. Phys.*, 81(6):2818–2827, 1984.
- [133] R.J. Levis, J. Zhicheng, and N. Winograd. Evidence for activation of the C-O-bond of methanol on the Pd(111) surface after low-temperature adsorption. *J. Am. Chem. Soc.*, 110:4431–4432, 1988.

- [134] N. Kruse, M. Rebholz, and V. Matolin. Methanol decomposition on Pd(111) single crystal surfaces. *Surf. Sci. Lett.*, 238(1-3):L457–L462, 1990.
- [135] J.L. Davis and M.A. Barteau. Decarbonylation and decomposition pathways of alcohols on Pd(111). *Surf. Sci.*, 187:387–406, 1987.
- [136] M. Rebholz and N. Kruse. Mechanisms of methanol decomposition on Pd(111). *J. Chem. Phys.*, 95:7745–7759, 1991.
- [137] I.V. Yudanov, K.M. Neyman, and N. Rösch. C-O bond scission of methoxide on Pd nanoparticles: A density functional study. *Phys. Chem. Chem. Phys.*, 8:2396–2401, 2006.
- [138] S. Schauermann, J. Hoffmann, V. Johánek, J. Hartmann, J. Libuda, and H.-J. Freund. The Molecular Origins of Selectivity in Methanol Decomposition on Pd Nanoparticles. *Catal. Lett.*, 84(3-4):209–217, 2002.
- [139] M. Morkel. *SFG-Schwingungsspektroskopie an Pd-Modellkatalysatoren unter Hochdruckbedingungen*. PhD thesis, Fachbereich Physik, Freie Universität Berlin, Berlin, 2004.
- [140] I.V. Yudanov, K.M. Neyman, and N. Rösch. Density functional study of Pd nanoparticles with subsurface impurities of light element atoms. *Phys. Chem. Chem. Phys.*, 6(1):116–123, 2004.
- [141] J. Wang and R.I. Masel. Methanol adsorption and decomposition on (1×1)Pt(110) and (2×1)Pt(110): Identification of the active site for carbon-oxygen bond scission during alcohol decomposition on platinum. *J. Catal.*, 126(2):519–531, 1990.
- [142] J. Wang and R.I. Masel. C-O Bond Scission during Methanol Decomposition on (1×1)Pt(110). *J. Am. Chem. Soc.*, 113(15):5850–5856, 1991.
- [143] N. Wiberg, E. Wiberg, and A.F. Holleman. *Lehrbuch der Anorganischen Chemie (101. Auflage)*. Gruyter, Berlin, New York, 1995.
- [144] Y.J. Kim, C. Westphal, R.X. Ynzunza, H.C. Galloway, M. Salmerón, M.A. Van Hove, and C.S. Fadley. Interlayer interactions in epitaxial oxide growth: FeO on Pt(111). *Phys. Rev. B*, 55(20):R13448–R13451, 1997.
- [145] K.S. Kim and M.A. Barteau. Reactions of methanol on TiO<sub>2</sub>(001) single crystal surfaces. *Surf. Sci.*, 223:13–32, 1989.

- [146] J.M. Vohs and M.A. Barteau. Conversion of methanol, formaldehyde and formic acid on the polar faces of zinc oxide. *Surf. Sci.*, 176:91–114, 1986.
- [147] X.D. Peng and M.A. Barteau. Acid-Base Properties of Model MgO Surfaces. *Langmuir*, 7(7):1426–1431, 1991.
- [148] P.A. Dilara and J.M. Vohs. Structure sensitivity in the reaction of methanol on  $\text{ZrO}_2$ . *Surf. Sci.*, 321:8–18, 1994.
- [149] M.W. Mensch, C.M. Byrd, and D.F. Cox. Reaction of methanol on stoichiometric and O-terminated  $\alpha\text{-Cr}_2\text{O}_3$  ( $10\bar{1}2$ ): interconversion of oxygenated  $\text{C}_1$  surface intermediates. *Catal. Today*, 85(2-4):279–289, 2003.
- [150] S. Kittaka, T. Umezu, H. Ogawa, H. Maegawa, and T. Takenaka. Interaction of Alcohols with Surface Hydroxyls on Chromium(III) Oxide. *Langmuir*, 14(4):832–838, 1998.
- [151] V.A. Gercher, D.F. Cox, and J.-M. Themlin. Oxygen-vacancy-controlled chemistry on a metal oxide surface: methanol dissociation and oxidation on  $\text{SnO}_2(110)$ . *Surf. Sci.*, 306:279–293, 1994.
- [152] D.R. Mullins, M.D. Robbins, and J. Zhou. Adsorption and reaction of methanol on thin-film cerium oxide. *Surf. Sci.*, 600:1547–1558, 2006.
- [153] D.F. Cox and K.H. Schulz. Methanol decomposition on single crystal  $\text{Cu}_2\text{O}$ . *J. Vac. Sci. Tech. A*, 8(3):2599–2604, 1990.
- [154] Y. Romanyshyn, S. Guimond, M. Sturm, D. G6bke, M. Naschitzki, H. Kuhlenbeck, and H.-J. Freund. Personal Information (to be published), 2007.
- [155] M. Sturm, D. G6bke, S. Guimond, H. Kuhlenbeck, and H.-J. Freund. Personal Information (to be published), 2007.
- [156] S. Kaya. *Structural and Catalytic Investigations on Vanadium Oxide Nanoparticles supported on Silica Films grown on a Mo(112) Substrate*. PhD thesis, Mathematisch-Naturwissenschaftliche Fakultät I, Humboldt-Universität Berlin, Berlin, 2007.
- [157] A. Uhl, S. Kaya, M. Baron, J.-L. Lu, Y.N. Sun, D. Stacchiola, J. Weissenrieder, Sh.K. Shaikhutdinov, and H.-J. Freund. Personal Information (to be published), 2007.

- [158] J.M. Tatibouët. Methanol oxidation as a catalytic surface probe. *Appl. Catal. A: Gen.*, 148:213–252, 1997.
- [159] S. Schauermann. *Structure Sensitive Surface Reactions on Model Catalysts: Molecular Beam Studies of Methanol and NO Dissociation on Supported Pd Nanoparticles*. PhD thesis, Mathematisch-Naturwissenschaftliche Fakultät I, Humboldt-Universität Berlin, Berlin, 2005.
- [160] P. Uvdal, M.K. Weldon, and C.M. Friend. Adsorbate symmetry and Fermi resonance of methoxide adsorbed on Mo(110) as studied by surface infrared spectroscopy. *Phys. Rev. B*, 50(16):12258–12261, 1994.
- [161] A. Serrallach, R. Meyer, and Hs.H. Günthard. Methanol and Deuterated Species: Infrared Data, Valence Force Field, Rotamers, and Conformation. *J. Molec. Spec.*, 52:94–129, 1974.
- [162] J.P. Camplin and E.M. McCash. A RAIRS study of methoxy and ethoxy on oxidised Cu(100). *Surf. Sci.*, 360:229–241, 1996.
- [163] P. Uvdal and A.D. MacKerell Jr. Vibrational spectrum of methoxy adsorbed on metal surfaces: ab initio calculations and experiments. *Surf. Sci.*, 393:141–149, 1997.
- [164] Th. Lindner, J. Somers, A.M. Bradshaw, A.L.D. Kilcoyne, and D.P. Woodruff. A Photoelectron Diffraction and NEXAFS Study of the Structure of the Methoxy Species ( $\text{CH}_3\text{O}^-$ ) on Cu(100). *Surf. Sci.*, 203:333–352, 1988.
- [165] M. Witko, K. Hermann, D. Ricken, W. Stenzel, H. Conrad, and A.M. Bradshaw. The electronic structure of the surface methoxy species on Cu(111). *Chem. Phys.*, 177(2):363–371, 1993.
- [166] S. Schauermann. Personal Information, 2008.
- [167] U. Leist, W. Ranke, and K. Al-Shamery. Water adsorption and growth of ice on epitaxial  $\text{Fe}_3\text{O}_4(111)$ ,  $\text{FeO}(111)$  and  $\text{Fe}_2\text{O}_3(\text{biphase})$ . *Phys. Chem. Chem. Phys.*, 5:2435–2441, 2003.
- [168] Y. Joseph, W. Ranke, and W. Weiss. Water on  $\text{FeO}(111)$  and  $\text{Fe}_3\text{O}_4(111)$ : Adsorption Behaviour on Different Surface Terminations. *J. Phys. Chem. B*, 104(14):3224–3236, 2000.

- [169] S. Schauermann, J. Hoffmann, V. Johánek, J. Hartmann, and J. Libuda. Adsorption, decomposition and oxidation of methanol on alumina supported palladium particles. *Phys. Chem. Chem. Phys.*, 4: 3909–3918, 2002.
- [170] C. Kuhrs, Y. Arita, W. Weiss, W. Ranke, and R. Schlögl. Understanding heterogeneous catalysis on an atomic scale: a combined surface science and reactivity investigation for the dehydrogenation of ethylbenzene over iron oxide catalysts. *Topics Catal.*, 14(1-4):111–123, 2001.
- [171] D.A. Dows. Vibrational Spectra of the Crystalline Methyl Halides. *J. Chem. Phys.*, 29(3):484–489, 1958.
- [172] Sh.K. Shaikhutdinov, M. Frank, M. Bäumer, S.D. Jackson, R.J. Oldman, J.C. Hemminger, and H.-J. Freund. Effect of carbon deposits on reactivity of supported Pd model catalysts. *Catal. Lett.*, 80(3-4): 115–122, 2002.
- [173] D.E. Starr, Sh.K. Shaikhutdinov, and H.-J. Freund. Personal Information, 2005.
- [174] M. Borasio, O. Rodríguez de la Fuente, G. Rupprechter, and H.-J. Freund. In-situ studies of methanol decomposition and oxidation on Pd(111) by PM-IRAS and XPS-spectroscopy. *Phys. Chem. B Letters*, 109(38):17791–17794, 2005.
- [175] M.J. Pilling and P.W. Seakins. *Reaction Kinetics*. Oxford University Press, Oxford, first edition, 1995.
- [176] E.S. Jang, M.Y. Jung, and D.B. Min. Hydrogenation for Low *Trans* and High Conjugated Fatty Acids. *Comp. Rev. Food Sci. Food Safety*, 4(1):22–30, 2005.
- [177] P. Sabatier. The Method of Direct Hydrogenation by Catalysis (Nobel lecture, given dec. 11th.), 1912.
- [178] P. Sabatier and J.-B. Senderens. Action du nickel sur l'éthylène. *Compt. rend.*, 124:616–618, 1897.
- [179] P. Sabatier and J.-B. Senderens. Action du nickel sur l'éthylène. Synthèse de l'éthane. *Compt. rend.*, 124:1358–1361, 1897.
- [180] Deutsche Gesellschaft für Fettwirtschaft. <http://www.dgfett.de>, 2008.

- [181] A. Farkas, L. Farkas, and E.K. Rideal. Experiments on Heavy Hydrogen: IV – The Hydrogenation and Exchange Reaction of Ethylene with Heavy Hydrogen. *Proc. Roy. Soc. London A*, 146(858):630–639, 1934.
- [182] I. Horiuti, G. Ogden, and M. Polanyi. Catalytic replacement of hydrogen by deuterium in benzene. *Trans. Faraday Soc.*, 30:663–665, 1934.
- [183] I. Horiuti and M. Polanyi. Exchange reactions of hydrogen on metallic catalysts. *Trans. Faraday Soc.*, 30:1164–1172, 1934.
- [184] R. Kuhn. Stereochemie der Kohlenstoffverbindungen. In K. Freudenberg, editor, *Stereochemie*, volume 3, page 913. Franz Deuticke-Verlag, Leipzig, Wien, 1933.
- [185] G.V. Smith and R.L. Burwell Jr. Reactions between Deuterium and Olefins in the Liquid Phase on Platinum Oxide Catalysts. *J. Am. Chem. Soc.*, 84(6):925–934, 1962.
- [186] G.H. Twigg and E.K. Rideal. The exchange reaction between ethylene and deuterium on a nickel catalyst. *Proc. Roy. Soc. A*, 171:55–69, 1939.
- [187] G.K.T. Conn and G.H. Twigg. Infra-red analysis applied to the exchange reaction between ethylene and deuterioethylene. *Proc. Roy. Soc. A*, 171:70–78, 1939.
- [188] I. Horiuti and K. Miyahara. Hydrogenation of Ethylene on Metallic Catalysts. In *National Standard Reference Data Series – National Bureau of Standards 13 (Category 6 – Chemical Kinetics)*. United States Department of Commerce (National Bureau of Standards), 1968.
- [189] C. Yoon, M.X. Yang, and G.A. Somorjai. Reactions of 1-Butene and *cis*-2-Butene on Platinum Surfaces: Structure Sensitivity of *cis*-2-Butene Isomerization. *J. Catal.*, 176(1):35–41, 1998.
- [190] I. Lee and F. Zaera. Infrared Spectroscopy Characterization of the Chemistry of C<sub>4</sub> Hydrocarbons on Pt(111) Single-Crystal Surfaces. *J. Phys. Chem. C*, 111(27):10062–10072, 2007.
- [191] R. Morales and F. Zaera. Thermal Chemistry of 1-Methyl-1-Cyclopentene and Methylene Cyclopentane on Pt(111) Surfaces: Evidence for Double-Bond Isomerization. *J. Phys. Chem. B*, 110(19):9650–9659, 2006.

- [192] F. Zaera and D. Chrysostomou. Propylene on Pt(111) II. Hydrogenation, dehydrogenation, and H-D exchange. *Surf. Sci.*, 457(1-2):89–108, 2000.
- [193] G.H. Aylward and T.J.V. Findlay. *Datensammlung Chemie in SI-Einheiten*. Wiley-VCH, Weinheim, 1999.
- [194] D.R. Stull, E.F. Westrum Jr., and G.C. Sinke. *The Chemical Thermodynamics of Organic Compounds*. John Wiley & Sons, New York, 1969.
- [195] J.W. Veldsink, M.J. Bouma, N.-H. Schoon, and A.A.C.M. Beenackers. Heterogeneous Hydrogenation of Vegetable Oils – A Literature Review. *Catal. Rev. - Sci. Eng.*, 39(3):253–318, 1997.
- [196] W.T. Koetsier. Hydrogenation of Edible Oils: Technology and Application. In F.D. Gunstone and F.B. Padley, editors, *Lipid Technologies and Applications*, pages 265–304. CRC Press, Boca Raton, 1997.
- [197] M.W. Balakos and E.E. Hernandez. Catalyst characteristics and performance in edible oil hydrogenation. *Catal. Today*, 35(4):415–425, 1997.
- [198] S.P. Pushpinder. Hydrogenation of Oils and Fats. *J. Am. Oil Chem. Soc.*, 57(11):850A–854A, 1980.
- [199] M.P. Gonzales-Marcos, J.I. Gutierrez-Ortiz, C.G.-O. De Elguea, J.I. Alvarez, and J.R. Gonzales-Velasco. Control of the product distribution in the hydrogenation of vegetable oils over nickel on silica catalysts. *Can. J. Chem. Eng.*, 76(5):927–935, 1998.
- [200] I. Lee and F. Zaera. Selectivity in Platinum-Catalyzed cis-trans Carbon-Carbon Double-Bond Isomerization. *J. Am. Chem. Soc.*, 127(35):12174–12175, 2005.
- [201] I. Lee and F. Zaera. Thermal Chemistry of C<sub>4</sub> Hydrocarbons on Pt(111): Mechanism for Double-Bond Isomerization. *J. Phys. Chem. B*, 109(7):2745–2753, 2005.
- [202] A. Cassuto and G. Tourillon. The adsorption of butene-1, isobutene, cis-2-butene and trans-2-butene on Pt(111) at 95 K: NEXAFS and UPS results. *Surf. Sci.*, 307-309:65–69, 1994.

- [203] G.C. Bond, J.J. Phillipson, P.B. Wells, and J.M. Winterbottom. Hydrogenation of Olefins, Part 1. – Hydrogenation of Ethylene, Propylene and the *n*-Butenes over Alumina-supported Platinum and Iridium. *Trans. Faraday Soc.*, 60:1847–1864, 1964.
- [204] G.C. Bond and J.M. Winterbottom. Hydrogenation of Olefins, Part 6. – Reaction of *n*-Butenes with Hydrogen and with Deuterium over Alumina-supported Palladium. *Trans. Faraday Soc.*, 65:2779–2793, 1969.
- [205] M. Salmerón and G.A. Somorjai. Desorption, Decomposition, and Deuterium Exchange Reactions of Unsaturated Hydrocarbons (Ethylene, Acetylene, Propylene, and Butenes) on the Pt(111) Crystal Face. *J. Phys. Chem.*, 86(3):341–350, 1982.
- [206] F. Zaera. The surface chemistry of hydrocarbon fragments on transition metals: towards understanding catalytic processes. *Mol. Phys.*, 100(19):3065–3073, 2002.
- [207] F. Zaera. Selectivity in hydrocarbon catalytic reforming: a surface chemistry perspective. *Appl. Catal. A: General*, 229:75–91, 2002.
- [208] B.E. Bent. Mimicking Aspects of Heterogeneous Catalysis: Generating, Isolating, and Reacting Proposed Surface Intermediates on Single Crystals in Vacuum. *Chem. Rev.*, 96(4):1361–1390, 1996.
- [209] X.C. Guo and R.J. Madix. Selective Hydrogenation and H-D Exchange of Unsaturated Hydrocarbons on Pd(100)-p(1x1)-H(D). *J. Catal.*, 155(2):336–344, 1995.
- [210] L.E. Murillo, N.A. Khan, and J.G. Chen. The effect of hydrocarbon structure and chain length on the low-temperature hydrogenation activity on Ni/Pt(111) bimetallic surfaces. *Surf. Sci.*, 594:27–42, 2005.
- [211] M.L. Burke and R.J. Madix. Effect of CO on hydrogen thermal desorption from Fe(100). *Surf. Sci.*, 237:20–34, 1990.
- [212] M.L. Burke and R.J. Madix. Migratory Insertion of Ethylene into Iron-Hydrogen Bonds and  $\beta$ -Hydride Elimination of Ethyl Groups on H-Covered Fe(100). *J. Am. Chem. Soc.*, 113(10):3675–3684, 1991.
- [213] Sh.K. Shaikhutdinov, M. Heemeier, M. Bäumer, T. Lear, D. Lennon, R.J. Oldman, S.D. Jackson, and H.-J. Freund. Structure-Reactivity Relationships on Supported Metal Model Catalysts: Adsorption and



- Reaction of Ethene and Hydrogen on Pd/Al<sub>2</sub>O<sub>3</sub>/NiAl(110). *J. Catal.*, 200(2):330–339, 2001.
- [214] Sh.K. Shaikhutdinov, M. Frank, M. Bäumer, S.D. Jackson, R.J. Oldman, J.C. Hemminger, and H.-J. Freund. Effect of carbon deposits on reactivity of supported Pd model catalysts. *Catal. Lett.*, 80(3-4): 115–122, 2002.
- [215] A.M. Doyle, Sh.K. Shaikhutdinov, S.D. Jackson, and H.-J. Freund. Hydrogenation on Metal Surfaces: Why are Nanoparticles More Active than Single Crystals? *Angew. Chem. Int. Ed.*, 42(42):5240–5243, 2003.
- [216] A.M. Doyle, Sh.K. Shaikhutdinov, and H.-J. Freund. Alkene chemistry on the palladium surface: nanoparticles vs single crystals. *J. Catal.*, 223(2):444–453, 2004.
- [217] A.M. Doyle, Sh.K. Shaikhutdinov, and H.-J. Freund. Surface-Bonded Precursor Determines Particle Size Effects for Alkene Hydrogenation on Palladium. *Angew. Chem. Int. Ed.*, 44(4):629–631, 2005.
- [218] M. Boutonnet, J. Kizling, V. Mintsä-Eya, A. Choplin, R. Touroude, G. Maire, and P. Stenius. Monodisperse Colloidal Metal Particles from Nonaqueous Solutions: Catalytic Behaviour in Hydrogenation of But-1-ene of Platinum, Palladium, and Rhodium Particles Supported on Pumice. *J. Catal.*, 103(1):95–104, 1987.
- [219] V. Mintsä-Eya, L. Hilaire, A. Choplin, R. Touroude, and F.G. Gault. The Reaction of Deuterium with Olefins on Nickel Catalysts: Evidence for Adsorbed Vinylic Species. *J. Catal.*, 82(2):267–278, 1983.
- [220] S.H. Inami, B.J. Wood, and H. Wise. Isomerization and Dehydrogenation of Butene Catalyzed by Noble Metals and Their Alloys. *J. Catal.*, 13(4):397–403, 1969.
- [221] J. Goetz, M.A. Volpe, and R. Touroude. Low-Loaded Pd/ $\alpha$ -Al<sub>2</sub>O<sub>3</sub> Catalysts: Influence of Metal Particle Morphology on Hydrogenation of Buta-1,3-diene and Hydrogenation and Isomerization of But-1-ene. *J. Catal.*, 164(2):369–377, 1996.
- [222] V. Mintsä-Eya, L. Hilaire, R. Touroude, F.G. Gault, B. Moraweck, and A. Renouprez. Exchange and Isomerization of But-1-ene on Supported Pd, Ni, and Pd-Ni Alloys. *J. Catal.*, 76(1):169–181, 1982.

- [223] N.R. Avery and N. Sheppard. The use of thermal desorption and electron energy loss spectroscopy for the determination of the structures of unsaturated hydrocarbons chemisorbed on metal single-crystal surfaces. II. *Cis*- and *trans*-but-2-ene, but-2-yne and buta-1,3-diene on Pt(111). *Proc. Roy. Soc. A*, 405(1828):27–39, 1986.
- [224] N.R. Avery and N. Sheppard. On the structure of C<sub>4</sub> hydrocarbon species resulting from the adsorption of linear butenes on a Pt(111) surface as studied by thermal desorption and electron energy loss spectroscopy. *Surf. Sci. Lett.*, 169:L367–L373, 1986.
- [225] D. Teschner, J. Borsodi, A. Woosch, Z. Révay, M. Hävecker, A. Knop-Gericke, S.D. Jackson, and R. Schlögl. The Roles of Subsurface Carbon and Hydrogen in Palladium-Catalyzed Alkyne Hydrogenation. *Science*, 320(5872):86–89, 2008.
- [226] C. Manzanares I., V.M. Blunt, and J. Peng. Spectroscopy of C-H Stretching Vibrations of Gas-Phase Butenes: *cis*-2-Butene, *trans*-2-Butene, 2-Methyl-2-butene, and 2,3-Dimethyl-2-butene. *J. Phys. Chem.*, 97(16):3994–4003, 1993.
- [227] D.C. McKean, M.W. Mackenzie, A.R. Morrisson, J.C. Lavalley, A. Janin, C. Fawcett, and H.G.M. Edwards. Vibrational spectra of *cis* and *trans* but-2-enes: assignments, isolated CH stretching frequencies and CH bond lengths. *Spectrochimica Acta Part A*, 41(3):435–450, 1985.
- [228] M.A. Chesters, C. De La Cruz, P. Gardner, E.M. McCash, P. Pudney, G. Shahid, and N. Sheppard. Infrared Spectroscopic Comparison of the chemisorbed Species from Ethene, Propene, But-1-ene and *cis*- and *trans*-But-2-ene on Pt(111) and on Platinum/Silica Catalyst. *J. Chem. Soc. Faraday Trans.*, 86(15):2757–2763, 1990.
- [229] B.J. Bandy, M.A. Chesters, M.E. Pemble, G.S. McDougall, and N. Sheppard. Low Temperature Electron Energy Loss Spectra of Acetylene Chemisorbed on Metal Single-Crystal Surfaces; Cu(111), Ni(110) and Pd(110). *Surf. Sci.*, 139:87–97, 1984.
- [230] J.M. Essen, J. Haubrich, C. Becker, and K. Wandelt. Adsorption of ethene on Pt(111) and ordered Pt<sub>x</sub>Sn/Pt(111) surface alloys: A comparative HREELS and DFT investigation. *Surf. Sci.*, 601:3472–3480, 2007.
- [231] J. Haubrich. Personal Information, 2008.

- [232] D. Zscherpel, W. Ranke, W. Weiss, and R. Schlögl. Energetics and kinetics of ethylbenzene adsorption on epitaxial FeO(111) and Fe<sub>3</sub>O<sub>4</sub>(111) films studied by thermal desorption and photoelectron spectroscopy. *J. Chem. Phys.*, 108(22):9506–9515, 1998.
- [233] F. Zaera. Hydrogenation and H-D-Exchange of Chemisorbed Ethylene on Ni(100) under Vacuum. *J. Catal.*, 121:318–326, 1990.
- [234] E.M. Stuve and R.J. Madix. Use of the  $\pi\sigma$  Parameter for Characterization of Rehybridization upon Adsorption on Metal Surfaces. *J. Phys. Chem.*, 89(15):3185–3188, 1985.
- [235] H. Öfner and F. Zaera. Isothermal Kinetic Measurements for the Hydrogenation of Ethylene on Pt(111) under Vacuum: Significance of Weakly-Bound Species in the Reaction Mechanism. *J. Phys. Chem. B*, 101(3):396–408, 1997.
- [236] W.A. Brown, R. Kose, and D.A. King. Femtomole Adsorption Calorimetry on Single-Crystal Surfaces. *Chem. Rev.*, 98(2):797–832, 1998.
- [237] F. Zaera and G.A. Somorjai. Role of Hydrogen in Low- and High-Pressure Hydrocarbon Reactions. In Z. Paál and P.G. Menon, editors, *Hydrogen Effects in Catalysis: Fundamentals and Practical Applications*, pages 425–447. Marcel Dekker, New York, 1988.
- [238] F. Zaera and D. Chrysostomou. Propylene on Pt(111) I. Characterization of surface species by infra-red spectroscopy. *Surf. Sci.*, 457(1-2): 71–88, 2000.
- [239] Z. Ma and F. Zaera. Organic chemistry on solid surfaces. *Surf. Sci. Rep.*, 61(5):229–281, 2006.
- [240] M. Wilde, K. Fukutani, M. Naschitzki, and H.-J. Freund. Hydrogen absorption in oxide-supported palladium nanocrystals. *Phys. Rev. B*, 77(11):3412–3415, 2008.
- [241] M. Wilde, K. Fukutani, W. Ludwig, B. Brandt, J.-H. Fischer, S. Schauer mann, and H.-J. Freund. Influence of carbon deposition on the hydrogen distribution in Pd nanoparticles and their reactivity in olefin hydrogenation. *Angew. Chem.*, in press.
- [242] N.R. Daly, A. McCormick, and R.E. Powell. The Metastable Spectra of *cis*- and *trans*-Butenes. *Org. Mass. Spec.*, 1:167–168, 1968.

- [243] G.G. Meisels, J.Y. Park, and B.G. Giessner. Carbon Skeletal Rearrangement of Butene Ions. *J. Am. Chem. Soc.*, 91(6):1555–1556, 1969.
- [244] G.G. Meisels, J.Y. Park, and B.G. Giessner. Ionization and Dissociation of C<sub>4</sub>H<sub>8</sub> Isomers. *J. Am. Chem. Soc.*, 92(2):254–258, 1970.
- [245] D.F. Ogletree, M.A. Van Hove, and G.A. Somorjai. LEED intensity analysis of the structures of clean Pt(111) and of CO adsorbed on Pt(111) in the c(4 x 2) arrangement. *Surf. Sci.*, 173:351–365, 1986.
- [246] D. Ambrose and C.H.S. Sprake. Thermodynamic Properties of Organic Oxygen Compounds. XXV. Vapor Pressures and Normal Boiling Temperatures of Aliphatic Alcohols. *J. Chem. Thermodyn.*, 2:631–645, 1970.
- [247] F. Nakao. Determination of the ionization gauge sensitivity using the relative ionization cross-section. *Vacuum*, 25(9/10):431–435, 1975.
- [248] H. Dannelun, I. Lundström, and L.-G. Petersson. The relative ionization gauge sensitivity of some unsaturated hydrocarbons. *Appl. Surf. Sci.*, 29:361–366, 1987.
- [249] J.R. Young. Measuring Hydrocarbon Gas Pressures with an Ionization Gauge. *J. Vac. Sci. Technol.*, 10(1):212–214, 1973.
- [250] J.E. Bartmess and R.M. Georgiadis. Empirical methods for determination of ionization gauge relative sensitivities for different gases. *Vacuum*, 33(3):149–153, 1983.

# List of Figures

2.1	Elementary processes of gas-surface interactions. . . . .	8
2.2	Potential energy diagrams for nonactivated and activated ad- sorption. . . . .	8
2.3	Different bonding modes of a diatomic model adsorbate on metals. . . . .	14
2.4	The $(\sqrt{3}\times\sqrt{3})R30^\circ$ overlayer structure of CO on Pd(111). . . .	16
2.5	Elementary processes on model catalysts. . . . .	19
3.1	The molecular beam setup, schematically. . . . .	24
3.2	The setup of the manipulator and the sampleholder. . . . .	25
3.3	The components of the scattering chamber. . . . .	27
3.4	The scattering geometry. . . . .	28
3.5	General idea of molecular beam formation. . . . .	29
3.6	The two principles of molecular beam formation. . . . .	30
3.7	The setup of the supersonic beam used in this study (Fenn-type). . . .	34
3.8	The setup of the effusive beams (both beams have identical construction). . . . .	37
3.9	The beam profiles of the supersonic and effusive beams. . . . .	37
3.10	Principle of the beam monitor (accumulation detector). . . . .	39
3.11	The setup of a QMS mass spectrometer. . . . .	41
3.12	The principle of quadrupole mass spectrometry. . . . .	42
3.13	The principle of IRAS spectroscopy. . . . .	49
3.14	The calculation of IRAS spectra (example: CO on clean Pt(111), $\approx 115$ K). . . . .	49
3.15	Physical foundations of IRAS spectroscopy. . . . .	50
3.16	Block diagram of the experiment time control. . . . .	55
4.1	Preparation of the Pd/Fe <sub>3</sub> O <sub>4</sub> /Pt(111) model catalyst, sche- matically. . . . .	58
4.2	Surface structure of Fe <sub>3</sub> O <sub>4</sub> in STM and LEED. . . . .	59
4.3	Bulk structure of Fe <sub>3</sub> O <sub>4</sub> . . . . .	60

4.4	Effect of methanol exposure/annealing on the Fe <sub>3</sub> O <sub>4</sub> surface oxygen. . . . .	62
4.5	Characterization of Fe <sub>3</sub> O <sub>4</sub> and Pd/Fe <sub>3</sub> O <sub>4</sub> by IRAS of adsorbed CO. . . . .	64
4.6	Experimental observation of stabilization of Pd/Fe <sub>3</sub> O <sub>4</sub> . . . . .	66
4.7	Long-term stability of the Pd/Fe <sub>3</sub> O <sub>4</sub> system and removal of carbon deposits. . . . .	69
4.8	Abstract: oxidation behaviour of Pd/Fe <sub>3</sub> O <sub>4</sub> and influence on activity. . . . .	72
5.1	The methanol molecule. . . . .	74
5.2	Possible methanol decomposition pathways and products on metal surfaces; see discussion in the text for references. . . . .	76
5.3	Methanol decomposition pathways and products on oxides. . . . .	81
5.4	Coverage series of deuterated methanol on Fe <sub>3</sub> O <sub>4</sub> . . . . .	87
5.5	IRAS peak assignments for deuterated methanol and methoxy (adsorbed). . . . .	88
5.6	IRAS spectra on Fe <sub>3</sub> O <sub>4</sub> as a function of annealing temperature. . . . .	92
5.7	Models of surface-O-D-group decomposition. . . . .	96
5.8	Repeated TPRS experiments of CD <sub>3</sub> OD on Fe <sub>3</sub> O <sub>4</sub> , overview. . . . .	97
5.9	Repeated TPRS experiments of CD <sub>3</sub> OD on pristine Fe <sub>3</sub> O <sub>4</sub> : signal evolution. . . . .	98
5.10	Coverage series of deuterated methanol on Pd/Fe <sub>3</sub> O <sub>4</sub> . . . . .	110
5.11	Coverage series of deuterated methanol on oxidized Pd/Fe <sub>3</sub> O <sub>4</sub> . . . . .	113
5.12	IRAS spectra of CD <sub>3</sub> OD on pristine and oxidized Pd/Fe <sub>3</sub> O <sub>4</sub> as a function of annealing temperature. . . . .	116
5.13	Repeated TPRS experiments of CD <sub>3</sub> OD on Pd/Fe <sub>3</sub> O <sub>4</sub> , overview. . . . .	120
5.14	Repeated TPRS experiments of CD <sub>3</sub> OD on Pd/Fe <sub>3</sub> O <sub>4</sub> : signal evolution. . . . .	121
5.15	Carbon-accumulation on Pd/Fe <sub>3</sub> O <sub>4</sub> from methanol-decomposition followed by IRAS of adsorbed CO. . . . .	124
5.16	Measurement of carbon formation rate from methanol on Pd/Fe <sub>3</sub> O <sub>4</sub> . . . . .	126
5.17	Evaluation of the carbon formation rate (see fig. 5.16). . . . .	127
5.18	Measurement in the CO-formation rate from methanol on Pd/Fe <sub>3</sub> O <sub>4</sub> . . . . .	132
5.19	Evaluation of the CO-formation rate (see fig. 5.18). . . . .	133
6.1	The molecules <i>cis</i> - and <i>trans</i> -2-butene. . . . .	141
6.2	Possible reaction mechanisms for the exchange reaction. . . . .	145
6.3	The Horiuti-Polanyi mechanism, formulated for <i>cis</i> -2-butene. . . . .	146

6.4	The double bond migration pathway in the Horiuti-Polanyi mechanism. . . . .	146
6.5	Steric repulsion and stabilities of <i>cis</i> - and <i>trans</i> -2-butene. . . .	151
6.6	Stabilities of different conformers of the 2-butyl surface group. . .	152
6.7	Exposure series of <i>cis</i> -2-butene on Fe <sub>3</sub> O <sub>4</sub> (115 K) and peak assignment. . . . .	158
6.8	TPRS experiment of <i>cis</i> -2-butene from Fe <sub>3</sub> O <sub>4</sub> with and without deuterium. . . . .	161
6.9	Repeated TPRS experiments of <i>cis</i> -2-butene from Fe <sub>3</sub> <sup>18</sup> O <sub>4</sub> . . . .	162
6.10	Scheme of isothermal pulsed molecular beam experiments. . . .	164
6.11	Adsorption behaviour of <i>cis</i> -2-butene on Fe <sub>3</sub> O <sub>4</sub> at 200 K. . . .	165
6.12	IRAS exposure series <i>cis</i> -2-butene on Pd/Fe <sub>3</sub> O <sub>4</sub> at 115 K. . . .	167
6.13	TPRS of <i>cis</i> -2-butene with & without coadsorbed D <sub>2</sub> from Pd/Fe <sub>3</sub> O <sub>4</sub> . . . . .	170
6.14	Evolution of TPRS signals from the clean Pd/Fe <sub>3</sub> O <sub>4</sub> with exposure. . . . .	171
6.15	Carbon-accumulation on Pd/Fe <sub>3</sub> O <sub>4</sub> from 2-butene-decomposition followed by IRAS of adsorbed CO. . . . .	174
6.16	Repeated TPRS experiments of <i>cis</i> -2-butene from Pd/Fe <sub>3</sub> O <sub>4</sub> . . .	176
6.17	Repeated TPRS experiments of <i>cis</i> -2-butene + D <sub>2</sub> from Pd/Fe <sub>3</sub> O <sub>4</sub> (peak temperature: 485 K). . . . .	179
6.18	Repeated TPRS experiments of <i>cis</i> -2-butene + D <sub>2</sub> from Pd/Fe <sub>3</sub> O <sub>4</sub> (peak temperature: 360 K). . . . .	180
6.19	The conversion products of <i>cis</i> -2-butene. . . . .	182
6.20	Scheme of isothermal pulsed molecular beam experiments. . . .	184
6.21	Reaction rates ( <i>cis</i> -2-butene + D <sub>2</sub> ) of different products on clean Pd/Fe <sub>3</sub> O <sub>4</sub> , 200 K. . . . .	185
6.22	Formation rates of <i>trans</i> -2-butene- <i>d</i> 1 at different temperatures on clean Pd/Fe <sub>3</sub> O <sub>4</sub> . . . . .	186
6.23	Evolution of reaction rates during isothermal experiment on D <sub>2</sub> -beam switching. . . . .	188
6.24	Reaction rates ( <i>cis</i> -2-butene + D <sub>2</sub> ) on clean and C-precovered Pd/Fe <sub>3</sub> O <sub>4</sub> . . . . .	190
6.25	Reaction rates ( <i>cis</i> -2-butene + D <sub>2</sub> ) on Pd/Fe <sub>3</sub> O <sub>4</sub> C-precovered at 360 K. . . . .	191
6.26	D <sub>2</sub> TPD experiments from Pd/Fe <sub>3</sub> O <sub>4</sub> : exposure series and effect of carbon-deposition. . . . .	199
6.27	Isothermal experiments with <i>cis</i> - and <i>trans</i> -2-butene + D <sub>2</sub> on clean Pd/Fe <sub>3</sub> O <sub>4</sub> at different temperatures. . . . .	205
6.28	Isothermal experiments with <i>cis</i> - and <i>trans</i> -2-butene + D <sub>2</sub> on Pd/Fe <sub>3</sub> O <sub>4</sub> , pulse averages. . . . .	206

6.29	IRAS spectra of <i>cis</i> - and <i>trans</i> -2-butene on Pd/Fe <sub>3</sub> O <sub>4</sub> . . . . .	208
6.30	TPRS experiments of <i>cis</i> - and <i>trans</i> -2-butene on Pd/Fe <sub>3</sub> O <sub>4</sub> . . . . .	210
6.31	TPRS experiments of <i>cis</i> - and <i>trans</i> -2-butene <i>plus</i> D <sub>2</sub> on clean Pd/Fe <sub>3</sub> O <sub>4</sub> . . . . .	211



# List of Tables

3.1	Approximative formula for the flow properties in the zone of silence. . . . .	32
5.1	Assignment of the methanol CD <sub>3</sub> OD vibrational modes. . . . .	89
A.1	Metals used for physical vapour deposition (PVD). . . . .	238
A.2	Liquid chemicals applied in the experiments. . . . .	238
A.3	Gaseous chemicals applied in the experiments. . . . .	239
A.4	Effusive beam intensities. . . . .	241
A.5	Supersonic beam intensities. . . . .	241
A.6	Cracking fractions of CD <sub>3</sub> OD in masses of other products. . .	242
A.7	C-13 contributions of 2-butene in masses of other products. . .	243



# Selbständigkeitserklärung

Hiermit erkläre ich, diese Dissertation selbständig, nur unter Verwendung der angegebenen und ohne unerlaubte Hilfe oder Hilfsmittel angefertigt zu haben.

Berlin, d. 28. Oktober 2008.